

NASA
Reference
Publication

May 1991

77
20,000

P-137

Atlas of the
Earth's Radiation Budget
as Measured by Nimbus-7:
May 1979 to May 1980

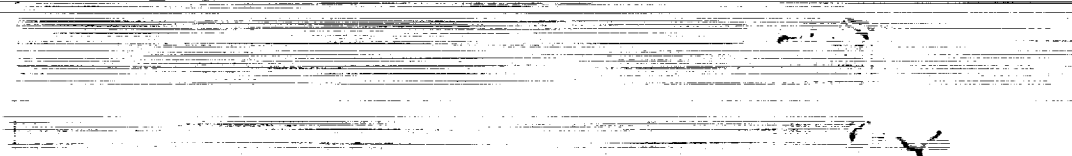
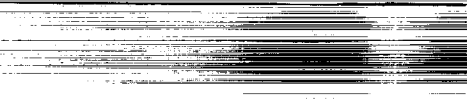
H. Lee Kyle,
Richard R. Hucek,
and Brenda J. Vallette

(NASA-RP-1263) ATLAS OF THE EARTH'S
RADIATION BUDGET AS MEASURED BY NIMBUS-7:
MAY 1979 TO MAY 1980 (NASA) 137 p CSCL 048

NP1-24720

Unclas
H1/47 0020000

NASA



**NASA
Reference
Publication
1263**

1991

**Atlas of the
Earth's Radiation Budget
as Measured by Nimbus-7:
May 1979 to May 1980**

H. Lee Kyle
*Goddard Space Flight Center
Greenbelt, Maryland*

Richard R. Hucek
and Brenda J. Vallette
*Research and Data Systems Corporation
Greenbelt, Maryland*



National Aeronautics and
Space Administration
Office of Management
Scientific and Technical
Information Program

CONTENTS

<u>Section</u>	<u>Page</u>
1. INTRODUCTION	1
1.1 The New Nimbus-7 ERB Scanner Products	1
1.2 The Nimbus-7 Bispectral THIR/TOMS Cloud Data Set	2
1.3 Arrangement of the Atlas	3
2. THE EARTH'S MEAN ANNUAL RADIATION BUDGET	4
2.1 The Radiation Budget	4
2.2 The Effect of Climate on the Regional Net Radiation	7
3. THE SEASONAL CYCLE	9
3.1 General Characteristics	9
3.2 The Seasonal Maps	10
4. DISCUSSION OF THE MONTHLY AVERAGED MAPS	11
4.1 Global and Hemispherical Averages	11
4.2 The Monthly Maps	13
5. REFERENCES	14
6. ANNUAL MAPS FOR THE PERIOD FROM JUNE 1979 TO MAY 1980	17
7. SEASONAL MAPS FOR THE PERIOD FROM JUNE 1979 TO MAY 1980	25
8. MONTHLY MAPS FOR THE PERIOD FROM MAY 1979 TO MAY 1980	54
9. ACRONYMS, INITIALS, AND ABBREVIATIONS	133

1. INTRODUCTION

The Sun is the primary energy source of the Earth's climate and also of its biosphere. There are strong feedback mechanisms by which the Earth's climate interacts with the top-of-the-atmosphere insolation to modify the energy that various regions absorb from the Sun. Important parameters affecting the absorbed energy include the regional cloud fraction, the predominant cloud type, and the surface albedo. In addition, the surface temperature influences the cloud types and whether snow or ice can remain on the surface for any length of time. In recent decades, several satellite experiments have been undertaken to better understand the Earth's radiation budget and how climate does and/or might affect it (House et al., 1986). This atlas presents 13 months (May 1979 to May 1980) of Earth Radiation Budget (ERB) and cloud observations taken by the experiments on the Nimbus-7 satellite. Maps included here give monthly, seasonal, and annual albedo, Outgoing Longwave Radiation (OLR), net radiation, surface temperature, and noon-time cloud cover. In addition, noon minus midnight OLR differences are examined as are the effects of clouds on the radiation budget parameters.

On October 24, 1978, the Nimbus-7 satellite was launched into a Sun-synchronous, near-polar orbit. The orbital period is 104 minutes, giving 13.85 orbits per day. The equator crossings are near noon local time on the ascending node and near midnight on the descending node. The Nimbus-7 spacecraft carried eight experiments to measure numerous atmospheric and climate parameters. The three instruments of interest here are the Earth Radiation Budget Experiment (ERBE), the Temperature Humidity Infrared Radiometer (THIR), and the Total Ozone Mapping Spectrometer (TOMS).

Concurrent Nimbus-7 ERB and cloud data sets are used in this study. They have the advantage of being developed from simultaneous measurements by instruments on the same satellite platform. Furthermore, the data sets were designed as complementary climate products and are presented on the same global grid system. The ERB grid consists of 2,070 roughly equal area (500-km x 500-km) regions, termed target areas, which cover the surface of the globe. There are 40 latitude zones, each 4.5° in width, within which the number of target areas

varies as a function of latitude. The equatorial zones each have 80 target areas 4.5° of longitude in length, but the two polar zones have only three target areas, each 120° of longitude in length. This grid system is illustrated in Kyle et al. (1986).

Both the Nimbus-7 ERB and cloud data sets are based on one near-noon and one near-midnight measurement for most of the globe. Thus, some errors may occur in the estimated diurnal averages. However, the cloud and ERB measurements are made simultaneously and refer to the same scenes.

1.1 The New Nimbus-7 ERB Scanner Products

The Nimbus-7 ERBE measured the total solar irradiance (0.2 to $> 50 \mu\text{m}$), Earth's albedo (0.2 to $4 \mu\text{m}$), and OLR (5 to $> 50 \mu\text{m}$). From these the net radiation was derived. The terrestrial fluxes were measured by two sets of instruments. There are low-resolution, wide-field-of-view (WFOV) sensors that are still operating, and a higher-resolution scanner, which took 20 months of data (through June 20, 1980), including the FGGE year. The ERBE is described in detail by Jacobowitz et al. (1984).

The ERB products used here cover 13 months (May 1979 through May 1980). They were derived from the narrow-field-of-view (NFOV) measurements made by the ERB scanner. These measurements were recently reprocessed (Kyle, 1990) utilizing a Maximum Likelihood Estimation (MLE) algorithm similar to that recently described by Wielicki and Green (1989). The original scanner products had been determined to have a number of defects. These include an algorithm problem, which caused the albedo to be 10% (3 albedo units) too large (Arking and Vemury, 1984), and a calibration error that reduced the longwave flux by about 3 W/m^2 (Kyle et al., 1985). The first few months of measurements were not reprocessed with this improved scene identification algorithm, primarily because of the numerous data gaps in the period. When active, the ERB scanner tended to interfere with another, short-lived Nimbus-7 experiment. Thus, during the first 6 months, the scanner was frequently commanded into the nonscan position.

The new 13-month ERB MLE products include daily and monthly averaged top of the atmosphere (TOA) albedo, longwave, and net radiation. The MLE

algorithm checks for the presence of clouds, and both mean and clear-sky values are given. The scene identification algorithm does make some misidentifications. Most of the errors occur at large satellite zenith angles. The effect on the longwave flux is minimal, but the albedo is increased by about 3% (one albedo unit).

Several factors affect the scanner's temporal sampling. The first is the satellite's sun-synchronous orbit. This means that, at best, most regions of the Earth can be seen only once near noon and once near midnight during each day. Kyle et al. (1990) have shown, by comparisons with the diurnally sampled ERBE measurements (Barkstrom, et al., 1989), that in the monthly mean these sampling times yield results accurate to about 1% in the longwave. The errors over land tend to be larger than this, but over oceans they are frequently even smaller. In the mean, the albedo errors are similar, but with larger regional errors.

During the period in question, the Nimbus-7 satellite did not have sufficient power to run all of the experiments at the same time. Because of this, the ERB instrument ran on a 3-day-on/1-day-off schedule. Thus, in most months there were about 23 measurement days. A final problem affected only the shortwave. The ERB scanner has four telescopes, each with shortwave and longwave sensors. In December 1978, one of the shortwave sensors became noisy and, thereafter, the data from that channel were not ordinarily used. Therefore, in the MLE processing there were only 75% as many daytime shortwave measurements as longwave.

The MLE algorithm produces a flux estimate from each valid shortwave or longwave measurement. Thus, despite the reduced number of shortwave measurements available, a reasonable coverage of the globe occurs on most days for both the shortwave and longwave. Both diurnal sampling limitations and regional gaps can be partially overcome by averaging over several days.

We will consider radiation budget parameters for both average conditions (clear and cloudy), as well as the clear-sky estimates. Parameters of interest include the diurnally averaged albedo, OLR, net radiation, and the reflected shortwave radiation. The parameters are all valid at the TOA and are all

broadband estimates. Therefore, they fully represent the regional spectrally integrated energy exchange between the Sun, Earth, and deep space.

1.2 The Nimbus-7 Bispectral THIR/TOMS Cloud Data Set

The Nimbus cloud data set was formed by merging two independent cloud estimates. The 11.5 μm measurements made by the THIR were used to make the first estimate. The procedure utilized variations in the radiance-equivalent blackbody temperatures to judge if a cloud was present and, if so, what its altitude was. This allows the formation of uniform daytime and nighttime cloud data sets. The second method utilizes 0.37 μm TOMS reflectances to determine the presence or absence of clouds. This method can be used only during daylight. The algorithms are described in detail in Stowe et al. (1988). The bispectral cloud-cover algorithm has been designed to use the strengths of each of the THIR infrared (IR) and TOMS ultraviolet (UV) cloudiness algorithms and to eliminate their weaknesses.

The THIR algorithm does a good job of detecting mid-level and high-altitude clouds but sometimes misses low-altitude clouds, which may have little thermal contrast with the surface. The 0.37 μm algorithm judges clouds based solely upon their reflectance in the UV. It is somewhat less sensitive than the IR algorithm but is capable of detecting low-altitude clouds as easily as high-altitude clouds. During daytime, the two data sets are merged to form an improved daytime cloud estimate. In the merge algorithm, the THIR estimate is given preference for mid- and high-altitude clouds, but for low-altitude clouds, the TOMS 0.37 μm estimates are weighted more highly. The primary cloud data set consists of the merged daytime cloud estimates plus the THIR daytime and nighttime estimates. The first year (April 1979-March 1980) of the cloud estimates is analyzed in detail in Stowe et al. (1989).

The THIR instrument operated as a simple cross-track scanner. The channel used accepted radiances between 10.5 μm and 12.5 μm . The Earth footprint had a diameter of 6.7 km at nadir, which grew to 13 x 24 km at a nadir angle of 50° (where measurements from neighboring orbits overlap at the equator). Since the THIR instrument required little power, it operated continuously. The THIR cloud algorithm utilized the

11.5 μm radiances plus concurrent surface temperature and snow/ice data from the Air Force three-dimensional nephelometer data set. In addition, monthly climatological atmospheric temperature lapse rates were utilized to define the cloud-top altitude.

The TOMS reflectivity algorithm utilized an average UV (0.36 μm and 0.38 μm channel) reflectivity. An important atmospheric correction here is the removal of the Rayleigh scattering, which is a straightforward computation. At these wavelengths, there is very little difference in land and ocean reflectivities, which are uniformly small. Clouds stand out as bright objects against a dark background. The TOMS footprint varied from (50 km)² at nadir to 150 x 200 km at the extreme off-nadir position. In both the THIR and TOMS algorithms, when choice was available, the smallest nadir angles were chosen. The TOMS instrument also operated continuously.

The cloudiness estimates used in this study are from the archived data set (Hwang et al., 1988; Stowe et al., 1988) and are near-noon daily values on a (500-km)² quasi-equal-area world grid. The bispectral cloud estimates (UV and IR) are used in this study. In particular, we will work with the total cloud amount and the included surface temperature maps.

1.3 Arrangement of the Atlas

In this atlas, the annual averages (June 1979 to May 1980) are presented first to give a general picture of the different global climate areas and an idea of the relationship between the various parameters. The net Earth radiation (NR) is given by

$$\begin{aligned} \text{NR} &= (1-A)I_s - F(\text{LW}). \\ &= \text{absorbed} - \text{emitted}. \\ A &= \text{diurnally averaged albedo.} \\ I_s &= \text{diurnally averaged (solar) insolation.} \\ F(\text{LW}) &= \text{diurnally averaged outgoing.} \\ &\quad \text{longwave radiation.} \end{aligned} \quad (1)$$

The measured quantities are the reflected shortwave $F(\text{SW})$, the emitted longwave, and the solar irradiance. The albedo and $F(\text{SW})$ are related by

$$F(\text{SW}) = AI_s. \quad (2)$$

Both the albedo and OLR are strongly influenced by clouds. In addition, clear-sky OLR over dry

continental regions is strongly influenced by the surface temperature. Over moist and ocean regions, the amount of water vapor in the atmosphere is generally linked to the surface temperature. This sets up a feedback mechanism that somewhat weakens the correlation between the surface temperature and the clear-sky OLR. However, the surface temperature does affect both cloud type and amount. The atlas, therefore, includes surface temperature and cloud maps.

The effect of the clouds on the radiation parameters is often discussed as cloud forcing (CF) terms (Ramanathan, 1987), where

$$\begin{aligned} \text{CF} &= F(\text{clear}) - F(\text{average}). \\ F(\text{clear}) &= \text{clear sky flux.} \\ F(\text{average}) &= \text{mean observed flux also called} \\ &\quad \text{the all-sky value.} \end{aligned} \quad (3)$$

and

$$\text{CF}(\text{NR}) = \text{CF}(\text{SW}) + \text{CF}(\text{LW}).$$

The shortwave forcing, $\text{CF}(\text{SW})$, is almost always negative, while the longwave forcing, $\text{CF}(\text{LW})$, is generally positive.

Since both mean sky and clear longwave and shortwave observations are included in the Nimbus-7 scanner products, the cloud forcing terms can be directly computed from the observations. In this atlas, only the net cloud forcing maps are given, but the shortwave and longwave forcing terms are discussed in terms of their latitude band averages.

Therefore, seven parameters are shown:

Parameter	MAPS		
	Annual	Seasonal	Monthly
Diurnal OLR	YES	YES	YES
Noon-Midnight OLR	YES	YES	YES
Diurnal Albedo	YES	YES	YES
Diurnal Net Radiation	YES	YES	YES
Diurnal Surface Temperature	YES	YES	YES
Local Noon Total Cloud	YES	YES	YES
Net Cloud Forcing	YES	YES	NO

After the annual averages are examined (Section 2 and the Maps on pages 18 through 24), seasonal (Section 3) and monthly (Section 4) variations are treated. In the seasonal and monthly sections, there are numerous maps that are arranged by parameter and season (month). This is done so that the reader can most easily follow the seasonal (monthly) changes in a given parameter. Sections 3 and 4 give a compact review of the combined parameter set as the seasons change.

2. THE EARTH'S MEAN ANNUAL RADIATION BUDGET

2.1 The Radiation Budget

The Earth's climate is dominated by the fact that the mean annual, top-of-the-atmosphere, insolation is over twice as large in the tropics as in the polar regions. In addition, a higher percentage of the incident solar irradiance is absorbed at low latitudes. As a result, the regions between approximately $\pm 36^\circ$ latitude show a positive annual net radiation, while the higher latitudes show a negative balance that must be made up by the transport of energy from the warmer regions by atmospheric and ocean currents.

The annual zonal mean ERB parameters are shown in Figure 1 for the period June 1979 to May 1980. On a reduced scale, the net radiation (bottom curve) mimics the top of the atmosphere (TOA) insolation (top curve) with only minor deviations. The diurnally averaged OLR is about 100 W/m^2 larger in the tropics than at the poles (less for north pole, more for south pole). The diurnally averaged reflected shortwave is nearly independent of latitude, but is slightly higher at the poles. This indicates that the regional albedo is much lower in the tropics than at the higher latitudes with the polar regions being the brightest. While the insolation shows a north/south symmetry, slight but significant asymmetries appear in the other quantities. The OLR is nearly 50 W/m^2 lower at the south pole than at the north pole in accordance with the lower Antarctic temperatures. The reflected radiation, however, is slightly larger at the south pole. The OLR asymmetry is the larger so that the net radiation is algebraically lower by about 20 W/m^2 at the north pole than at the south pole. In the tropics, a slight peak in the reflected shortwave about 6° north of the equator indicates the mean

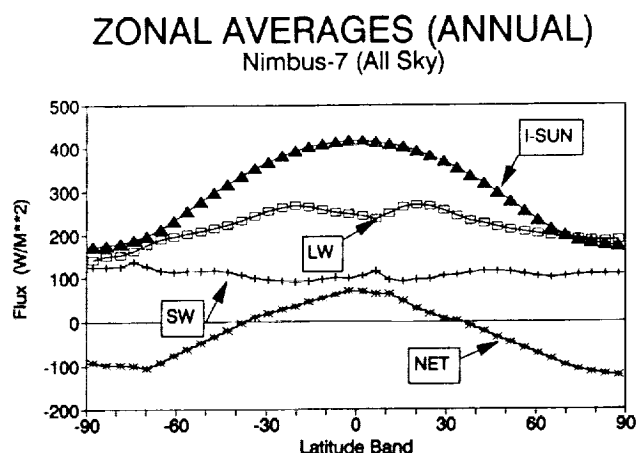


Figure 1. Nimbus-7 scanner (MLCE) annually and zonally averaged (June 1979 through May 1980) emitted longwave (LW), reflected shortwave (SW), net radiation (NR), and top-of-the-atmosphere insolation, I(sun).

position of the intertropical convergence zone. A dip in the OLR occurs at the same position. Slight OLR maxima occur in the subtropical high-pressure zones, at about $\pm 20^\circ$ of latitude, indicating the cloud minima present. The Sahara-Arabian deserts are strong contributors to the northern hemisphere maximum. In the southern hemisphere, stable high-pressure regions at about 10°S latitude in the Atlantic and Eastern Pacific combine with the southern deserts in Australia, Southern Africa, and South America to produce the southern OLR maximum (see Map 1, page 18).

The annual maps of OLR (averaged noon-midnight) albedo, net radiation, local noon cloud cover, and the mean of the noon and midnight surface temperatures are given, respectively, in Maps 1 through 6). Map 7 shows the effects of clouds on the net radiation. This is the so-called net cloud forcing (Ramanathan, 1987; Ramanathan, et al., 1989).

Map 1 (page 18) shows the mean annual (June 1979 to May 1980) global average (noon and midnight) of the Nimbus-7-derived OLR. Map 2 shows the corresponding noon minus midnight OLR differences. Note the large differences of over 40 W/m^2 in the Sahara and Arabian deserts but the small noon versus midnight range over the oceans. Larger day/night differences are found in some of the seasonal and monthly maps. The annual albedo is given on page 20, while the noontime cloud cover appears on page 22. The net radiation, page 21, will be discussed shortly. Complex tropical and mid-latitude patterns dominate the OLR and albedo maps. Map 5, page 22,

shows that these patterns basically represent the mean cloud fields. The clouds reduce the OLR and increase the albedo. Even at high latitudes the clouds are important. However, the deserts, and particularly the Sahara-Arabian Desert, are exceptions. In these relatively cloud-free regions, the low heat capacity and high reflectivity of the surface are dominant factors.

Three major cloud belts with mean annual cloud cover often in excess of 70% appear in Map 5. The north and south circumpolar belts, together with the polar snow and ice fields, are the principle causes of the high polar albedos. The tropical cloud belt is broken and has three centers: the Indonesian maritime continent, northern South America, and the Congo basin in Africa. The OLR map shows local minima over these three cloud centers, while the albedo map shows local maxima. Low cloud regions in the tropical Pacific and Atlantic Oceans show OLR maxima and albedo minima.

The Sahara-Arabian desert shows quite low cloud cover, but both the OLR and albedo are high due to the surface characteristics. The other large deserts show similar behavior except that their surface reflectivity is usually less than that of the Sahara-Arabian desert.

Interestingly, the Nimbus-7 annual (June 1979 to May 1980) net radiation (page 21) shows quite a distinct low latitude pattern. Two global maxima regions, with the net radiation greater than 80 W/m^2 , appear, like Siamese twins, along the equator in the Western Pacific and in the Indian Ocean. These are surrounded by large tropical ocean regions where the net radiation exceeds 60 W/m^2 . The tropical Atlantic also shows net radiation values greater than 60 W/m^2 . On the whole, there is a distinct break in the net radiation going from ocean to continental regions, with lower values present over land. However, note the 60 W/m^2 contour over central Africa. Just north of these strong energy maxima appear energy sinks with values less than -20 W/m^2 in the Sahara and Arabian deserts. These desert minima coincide with local OLR and albedo maxima (Maps 1 and 3).

Comparison with the cloud map (page 22) indicates that in the tropics high cloud fractions and high net radiation values are associated. However, low-altitude cloud fields can sharply reduce the net

radiation. This occurs along the west coasts of South America and Southern Africa.

In general, a good correlation does exist between the net radiation and the mean annual surface temperature. Map 6, page 23, shows the mean annual surface temperatures for June 1979 to May 1980 as derived from the Nimbus-7 cloud data set (Stowe et al., 1988). They represent the average of the noon and midnight temperatures corresponding to the Nimbus-7 over flight times. Over land, shelter temperatures are represented. The general resemblance between the surface temperature and net radiation pattern is to be expected, since the Sun is the primary heat source for the surface.

Both the surface temperature and the net radiation are low in the polar regions. The higher north polar temperatures cause the OLR to be higher in the north than in the south. This is a major factor behind the slightly lower net radiation in the Arctic compared to the Antarctic. Both the net radiation and surface temperature peak in the tropics. Further, over the tropical oceans both the sea-surface temperatures and the net radiation increase westward from the west coasts of Africa and South America. This trend is strongest in the southern hemisphere. Over the tropical continental regions, the relationship between surface temperature and net radiation is weaker than over the oceans. For instance, in Africa the net radiation maximum is in central Africa and straddles the equator. However, the temperature maxima is in West Africa a little north of the equator.

Radiation budget annual global averages from several satellite experiments are shown in Table 1 (taken from Kyle et al., 1991). The Nimbus-7 and ERBE results are shown at the bottom. The original Nimbus-7 algorithms (Jacobowitz et al., 1984a,b) contained a number of defects (Kyle et al., 1985). The results from the revised Nimbus-7 algorithms are shown below the original results. The revised Nimbus-7 WFOV results are shown for both years 1979/80 and 1985/86. The slight difference between the two years may be partially real (Cess, 1990), but some of the difference may be due to experimental error. The fact that the Nimbus-7 NFOV albedo is about 1% higher than the WFOV result is at least partially due to cloud identification problems in the version of the MLE program used by the Nimbus-7 team.

Table 1. Radiation Budget Annual Global Averages (from Kyle et al., 1991)							
Source	Solar Constant (W/m ²)	I _s ^(a) Solar Insolation (W/m ²)	F _{sw} Reflected ^(b) (W/m ²)	A (%)	OLR (W/m ²)	Net Radiation	
						Stated (W/m ²)	Formula ^(c) (W/m ²)
Raschke et al. (1973) N-3 Data	1360.7	340.18	96.61	28.4	240.7	2.79	2.87
Ellis & Vonder Haar (1976) Satellite Composite				30	236		
Nimbus-6 WFOV Campbell & Vonder Haar (1980)	1391			31	230		
Jacobowitz et al. (1979) (Adjusted results to scanner)	1391			31	234		
NOAA SR Gruber & Winston (1978); Ohring & Gruber (1983)				31	234		
Nimbus-7 Original Jacobowitz et al. (1984b) WFOV NFOV	1371.5	342.88	104.9 113.5	30.6 33.1	228.8 232.7	10.9 -3.4	9.18 -3.32
Nimbus-7 Reprocessed 6/79-5/80 (MATRIX) WFOV (MLE) NFOV 2/85-1/86 (MATRIX) WFOV	1371.5	342.88	102.7 104.7 103.0	29.95 30.55 30.03	236.2 236.0 235.0		3.98 2.21 4.92
ERBE (N9 ERBS) 2/85-1/86 (5° scanner)	1365	341.25	102.1	29.92	234.0	5.19	5.16
^(a) Calculated as (solar constant)/4 ^(b) Calculated using given albedo and solar constant ^(c) Calculated by $NR = I_s - F_{sw} - OLR$							

A few points should be kept in mind in studying the table. A non-time-varying solar constant was used by all investigators, but each investigator adopted their own specific value for the solar constant. In the case of the Nimbus-7 and ERBE experiments, a solar sensor was included in the instrument package, and the values shown in the table were measured during the first year of the experiment. It is now known that the total solar irradiance varied in phase with the solar activity with a range of over 0.1% between 1979 and 1989 (see, for instance, Hickey et al., 1988; Kyle, 1990). During active solar periods, short-term (a few days to weeks) variations of up to 0.2% or 0.3% can occur. The error introduced by ignoring these variations is small compared to the other experimental errors. Because of the different solar constants chosen, the percentage differences in the calculated albedos may not be the same as those in the measured reflected shortwave fluxes. Next, the stated net radiation is either given by the investigators or obtained by summing the target area values. Both OLR and albedo measurements must be present if the net radiation is to be calculated. Often nonconcurrent gaps appear in both.

2.2 The Effect of Climate on the Regional Net Radiation

The Nimbus-7 data set contains evidence showing that regional climate does affect the regional radiation budget components including the net radiation. The net radiation is affected by the surface temperature and reflectivity and by the atmospheric dynamics, particularly the clouds. The surface albedo increases markedly both in snow-covered regions and in arid or semi-arid regions. This reduces the absorbed solar energy. Clouds increase the albedo, but they normally also decrease the emitted longwave radiation. Thus, the effect of clouds depends strongly on the cloud type. Fairly low, thick clouds affect the absorbed shortwave more than the OLR and, hence, reduce the net radiation. Thin, medium or high altitude clouds can reduce the OLR more than they do the absorbed shortwave and, thus, increase the net radiation. But cloud types depend strongly on the regional climate. The surface temperature and available water are among the important surface characteristics affecting cloud types.

The persistent circumpolar cloud belts (see page 22) sharply reduce the net radiation absorbed by the polar

and circumpolar oceans. This has been pointed out by Ardanuy et al. (1989, 1990) using Nimbus-7 data and Ramanathan et al. (1989) and Harrison et al. (1990) using ERBE mean and clear-sky measurements for April, July, and October 1985 and January 1986. Ramanathan (1987) introduced the term cloud radiative forcing for the difference (clear sky minus mean) results. Thus, the shortwave cloud forcing is almost always negative and longwave cloud forcing is generally positive. The net cloud forcing is the sum of the shortwave and longwave cloud forcing values.

Figure 2 shows the annual mean (June 1979 to May 1980), zonally averaged cloud forcing values derived from the ERB data set. The cloud belt around the Antarctic continent reduces the solar energy absorbed by the southern ocean by nearly 80 W/m^2 . The clouds also reduce the OLR by about 40 W/m^2 so the net cloud forcing is about -40 W/m^2 . Over the Antarctic continent, the shortwave, longwave, and net cloud forcing are all shown as small but positive in the figure. However, the present MLE algorithm does not accurately identify clouds over snow. Thus, the values shown over the Antarctic continent should not be given too much weight. The very high albedo in the polar regions, however, is a dominant factor. Thus, whether it is caused by clouds or ice and snow, it still sharply reduces the absorbed solar energy. Thus, in Figure 1 no sharp break appears in the mean zonal curves at the Antarctic Ocean/land boundary.

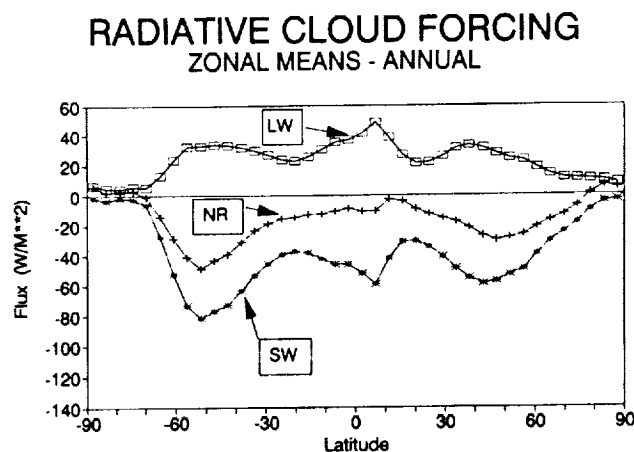


Figure 2. Nimbus-7 (MLCE) annually and zonally averaged longwave (LW), shortwave (SW), and net radiation (NR) cloud forcing values.

A somewhat shallower net radiation forcing minimum appears between 40°N and 60°N latitude. This is produced primarily by the dense cloud systems over

the northern Atlantic and Pacific Oceans. In the tropics, both the longwave and shortwave cloud forcing are large. But, they tend to cancel, thus the net cloud forcing is small and is algebraically often greater than -10 W/m^2 .

A strong equator-to-pole temperature gradient is shown in Map 6, page 23. This is basically caused by the fact that much less top-of-the-atmosphere solar irradiance is received in the polar regions than in the tropics (see Figure 1). In the mean, our global cloud system acts to strengthen this gradient by causing a larger percentage of insolation to be converted to net radiation in the tropics than at the poles. The high albedo of the polar snow and ice fields also strongly reduces the solar energy absorbed at high latitudes. At the high latitudes, the cloud fields act to moderate the seasonal extremes. They tend to make the summers cooler and the winters warmer.

The annual net cloud forcing map for June 1979 to May 1980 is shown on page 24. In very cloudy regions (see page 22), few clear observations were made, and this reduces the accuracy of the time averages. Because of its 90-km^2 nadir footprint, the Nimbus-7 ERB could identify very few clear sky areas in some regions. The principle data gaps occur in the southern circumpolar cloud belt and in the Northern Pacific. Missing values are indicated by dots. Reduced clear sky sampling, of course, occurs in all cloudy regions.

At high latitudes over the oceans, net cloud forcing values of -30 W/m^2 to -60 W/m^2 are common, but over the continents the absolute values are smaller and numbers between 0 W/m^2 and -15 W/m^2 are common. Positive cloud forcing is shown near both poles. In the tropics and subtropics, both positive and negative cloud forcing patterns appear over both land and ocean. In the ocean along the west coasts of South America, Southern Africa, and off Baja California, negative cloud forcing appears. The map shows a local minimum of -50 W/m^2 off Southwest Africa and one of -56.7 W/m^2 off the coast of South America. However, the dense equatorial cloud field north of Australia (page 22) shows essentially zero cloud forcing. This is also a region of high sea-surface temperature (page 23).

Off Southern California and along the west coasts of South America and Southern Africa, the low stratus

clouds produce strong negative shortwave forcing but only relatively weak positive longwave forcing. Thus, fairly strong negative net cloud forcing occurs. Further west, high clouds produce strong shortwave and longwave forcing terms that tend to cancel. Dhuria and Kyle (1990) showed that north of Australia the high clouds consist of a mixture of optically thick and optically thin clouds. The thick clouds yield strongly negative net cloud forcing. The more plentiful thin clouds yield positive cloud forcing and the mixture is often neutral.

Over land, net cloud forcing tends to be slightly negative, but at mid and high latitudes during the winter (see Maps, pages 50 and 52) and at all times over arid regions, positive values are common. The sharpest contrast over land occurs in East Asia. Here, in the annual map (page 24), a positive cloud forcing maximum of 6.4 W/m^2 in Central Asia contrasts with a deep negative of -60 W/m^2 over South China. These two cloud forcing extremes are reflected, in a reduced form, in the annual net radiation map (page 21). In Map 7, page 24, a broken belt of positive cloud forcing extends from Central Asia southeastward to the west coast of Africa. Much of this region is arid or semiarid. Over the Sahara and Arabian Deserts the dominant factors are the high albedo and low heat capacity of the surface. Thus, the mean net radiation (page 21) is normally negative over these deserts despite the positive cloud forcing.

Both the Nimbus-7 radiation budget data and the derived cloud forcing maps give strong evidence of the close tie between the regional climate and the regional net radiation budget. The high latitude cloud fields work together with the regional snow and ice to sharply reduce the absorbed solar radiation. Over the warm tropical oceans, clouds again reduce the absorbed radiation, but the high cloud tops cause a compensating reduction in the OLR. At times, high thin clouds appear to actually increase the net radiation (Dhuria and Kyle, 1990). Low clouds predominate over the relatively cool tropical waters off the west coasts of Southern Africa, South America, and Baja California. These clouds reduce the net radiation, and, thus, act as a mechanism for keeping down the sea-surface temperature. Over Central Africa, the cloud cover is above average (page 22), but so is the net radiation (page 21). The cloud forcing there is small (page 24). The somewhat lower clouds over South China do, however, cause a sharp reduction in the net

radiation. In the warm, humid regions, cloud cover is above average, but the net cloud forcing is small and may at times be positive. In cool and cold regions, cloud tops are frequently low and the cloud forcing is generally strongly negative.

3. THE SEASONAL CYCLE

3.1 General Characteristics

The changes in the top-of-the-atmosphere insolation drive the seasonal changes in the ERB parameters. At the December solstice the Sun is 23.5° south of the equator, while at the June solstice it is 23.5° north of the equator. Further, because of the eccentricity of the Earth's orbit, the solar irradiance at the Earth is about 6% larger in December and January than in June and July.

The seasonally and zonally averaged Nimbus-7 insolation, reflected shortwave, emitted longwave, and net radiation are shown in Figures 3, 4, 5, and 6. At the solstices (Figures 3 and 5), these parameters are markedly different from the annual averages (Figure 1). In December to February the insolation is 450 W/m^2 or greater from 10°S latitude to the South Pole. However, north of the equator, the insolation drops steadily to zero just beyond the Arctic Circle. The reflected shortwave drops from over 300 W/m^2 at the bright South Pole to zero in the sunless Arctic. Note the steady decline in the shortwave signal from the South Pole to 36°S latitude even though the insolation increases slightly. This is caused by the decrease in the regional albedos as the Antarctic ice and clouds give way to the relatively clear southern oceans. The high reflectivity in the South keeps the net radiation slightly negative in the Antarctic even when the insolation is large. In this season, the net radiation is positive from 14°N to 66°S latitude. At the North Pole, the net radiation drops to about -170 W/m^2 .

At the equinoxes (Figures 4 and 6), the situation more closely resembles the annual mean (Figure 1) than do the solstice periods. However, the seasons are chosen so that the Sun is north of the equator most of the time in March to May and south of it most of the time in September to November. This causes a tilt to the north or to the south following the insolation. In June, July, and August, it is summer in the Arctic, but the Earth is furthest from the Sun

so that the insolation is slightly smaller than in December to February. In the June to August season, the net radiation is positive from 70°N latitude to 10°S latitude.

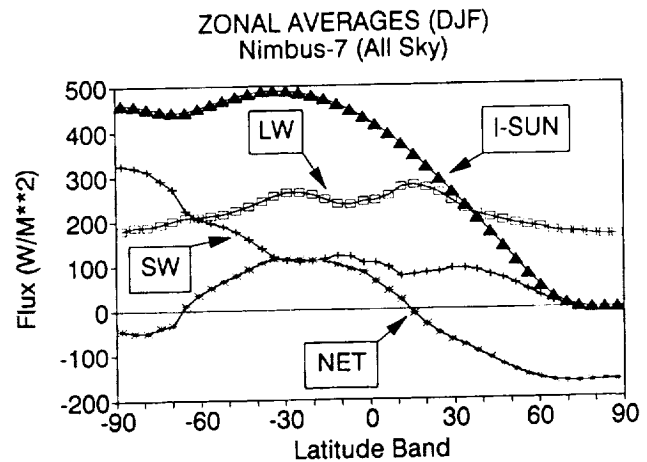


Figure 3. Nimbus-7 (MLCE) zonally averaged insolation, $I(\text{sun})$, longwave (LW), reflected shortwave (SW), and net radiation (NR) for the season, December (1979) through February (1980).

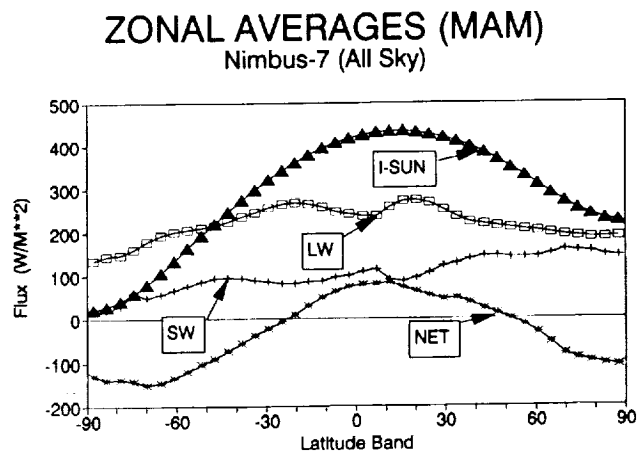


Figure 4. Zonally averaged Earth radiation budget parameters for March 1980 through May 1980 (see Figure 3).

The seasonal variations in the effects of clouds on the radiation parameters are summarized in Figures 7, 8, 9, and 10. Here are given the zonally averaged shortwave, longwave, and net radiation cloud forcing values. These show over the southern circumpolar ocean net cloud forcing values of about -100 W/m^2 in December to January, but positive values of about 20 W/m^2 appear in the southern winter season (June to August). Likewise in the high northern latitudes, strong net negative cloud forcing in the summer changes to slightly positive cloud forcing in the winter.

In the high latitude winter when the insolation becomes small (see Figures 3 and 5), the positive longwave cloud forcing is dominant. Note that in all seasons the net cloud forcing is small over the tropics. Seasonal cloud forcing values from 1985/86, derived from the follow-on ERBE, have recently been discussed by Harrison et al. (1990) and Kyle et al. (1991). The results are qualitatively similar.

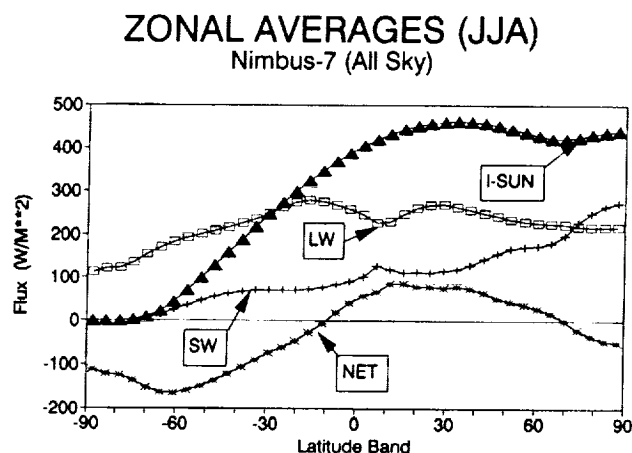


Figure 5. Zonally averaged Earth radiation budget parameters for June 1979 through August 1979 (see Figure 3).

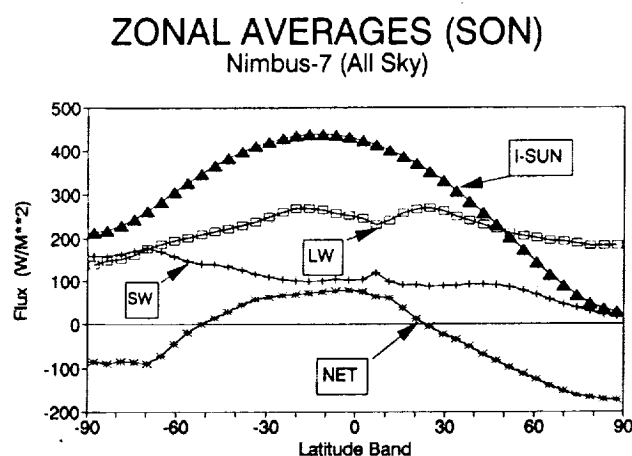


Figure 6. Zonally averaged Earth radiation budget parameters for September 1979 through November 1979 (see Figure 3).

3.2 The Seasonal Maps

The seasonally averaged parameter maps are shown on pages 26 through 53. The four seasonal maps for each parameter are grouped together starting with the June to August solstice season. Driven by the seasonal cycle of the solar insolation (Figures 3 through 6), the tropical cloud belt moves northward in June to August (page 42) bringing the summer

monsoons to the Northern Hemisphere (India and Southeast Asia, Central Africa, and Central America and Northern South America). In the monsoon areas, the albedo increases and the OLR decreases in step with the clouds. The surface temperature (page 46) is high in the monsoon regions, but note the maximum in the dry Sahara.

RADIATIVE CLOUD FORCING ZONAL MEANS - DJF

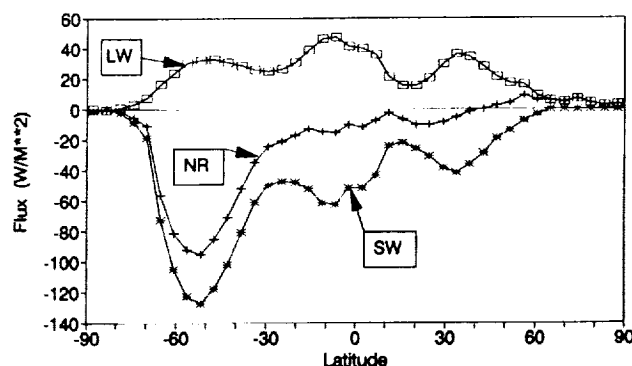


Figure 7. Zonally averaged longwave (LW), shortwave (SW), and their sum (the net radiation, NR) Nimbus-7 ERB cloud forcing results for the season (December 1979 through February 1980).

RADIATIVE CLOUD FORCING ZONAL MEANS - MAM

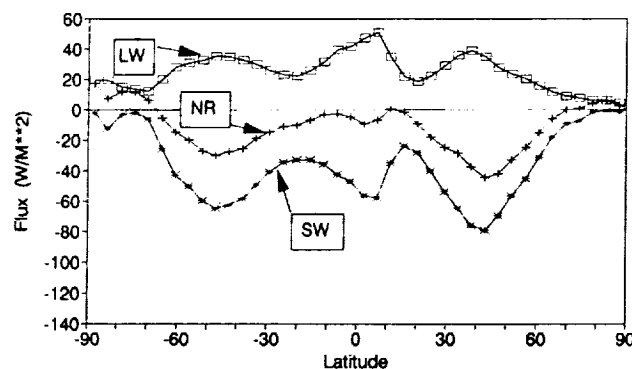


Figure 8. Zonally averaged cloud forcing results for March through May 1980 (see Figure 7).

In December to February the Intertropical Convergence Zone (ITCZ) has followed the Sun southward and the monsoon clouds are over Brazil, South-Central Africa, and the Java-New Guinea region (page 44). The OLR and albedo maps are strongly influenced by changing cloud patterns. The net radiation and surface temperature fields follow the Sun, but are not as strongly tied to the cloud fields as are the OLR and albedo.

RADIATIVE CLOUD FORCING ZONAL MEANS - JJA

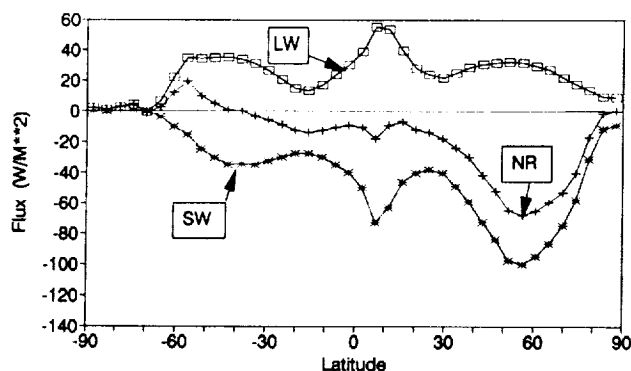


Figure 9. Zonally averaged cloud forcing parameters for June through August 1979 (see Figure 7).

RADIATIVE CLOUD FORCING ZONAL MEANS - SON

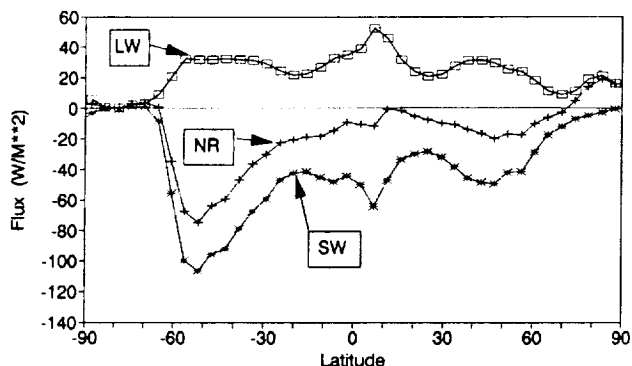


Figure 10. Zonally averaged cloud forcing parameters for September through November 1979 (see Figure 7).

Seasonally, the net radiation patterns are more complex in the summer than in the winter hemisphere. In December to February at about 30°S latitude (page 40), large ocean regions with net radiation greater than 120 W/m² contrast with desert regions in South Africa and Australia where the net radiation is less than 90 W/m². Along the coast of Argentina a high net radiation region actually extends beyond 50°S latitude. In the June to August season, Map 20, similar patterns occur around 30°N latitude. Note the low net radiation off Baja California between two high net radiation regions. This is caused by low stratus clouds, which normally occur here. In the Sahara-Arabian Desert, some regions have negative net radiation values even in the summer.

In the winter hemisphere, the net radiation contours are relatively straight. But, note the local minima

over the Sahara and South China in December to February. In June to August, the ocean regions off the west coasts of both South America and South Africa are also relatively poor heat absorbers. The low net radiation in South China and in the coastal regions is caused by low clouds. These reduce the absorbed solar energy but have less effect on the OLR.

The more persistent seasonal patterns carry over clearly to the annual maps (Maps 1 through 7) but some seasonal extremes are hard to identify in the annual means. In the tropics and subtropics, the low net radiation over the Sahara, South China, and off the west coasts of Southern Africa, South America, and Baja California are easily found in the annual maps. However, the summer subtropical maxima are greatly smoothed in the annual maps. In the mean, the steady input of solar energy along the equator is a dominant factor. In addition, considerably greater (noon-midnight) OLR differences appear over the oceans in the seasonal and monthly maps than do in the annual map.

4. DISCUSSION OF THE MONTHLY AVERAGED MAPS

4.1 Global and Hemispherical Averages

The Earth would rarely be in instantaneous radiation balance even if the global mean annual net radiation were exactly zero. The global monthly mean OLR, albedo, net radiation, noontime cloud cover, and the average (noon and midnight) surface temperature for June 1979 to May 1980 are given in Table 2. Assuming that the annual mean net radiation is zero means that we should subtract the annual mean value from each month. This would lead to a net global deficit of about -10 W/m² in June and July and a net surplus of 7 W/m² to 8 W/m² in December to February. Note that the global albedo is brightest in November to January, when the Earth is closest to the Sun, and lowest in August and September. In the radiation balance, this is partially offset by the mean OLR, which has the opposite trend. Interestingly, the global surface temperature and the OLR (not the net radiation) are in phase. The connecting link appears to be in the great continental land masses in the Northern Hemisphere.

Table 2
Nimbus-7 Scanner (MLE)
Global Monthly Mean Earth Radiation Budget Parameters
June 1979 to May 1980

Month/Year	OLR (W/m ²)	Albedo (%)	NR (W/m ²)	Noon Cloud Cover (%)	Average Temperature (noon and midnight) (°K)
January 1980	233.0	31.3	10.5	51.2	13.2
February 1980	234.4	30.6	9.7	51.6	13.4
March 1980	234.6	30.2	7.3	49.9	13.9
April 1980	234.5	30.4	2.7	51.8	14.9
May 1980	237.2	30.7	-4.9	52.0	15.7
June 1979	238.3	30.7	-7.9	50.8	16.2
July 1979	239.8	30.1	-7.7	51.6	16.4
August 1979	239.7	29.5	-3.7	51.5	16.2
September 1979	238.0	29.3	2.0	51.0	15.7
October 1979	236.0	30.3	4.7	51.2	14.4
November 1979	233.5	31.7	6.1	53.5	13.9
December 1979	232.5	31.7	9.2	51.5	13.4
Annual	236.0	30.6	2.3	51.5	14.8

Hemispherically the imbalance in the parameters can be much worse. Figure 11 shows that the Southern Hemisphere net radiation varies from $+90 \text{ W/m}^2$ in December to -90 W/m^2 in June, while in the Northern Hemisphere it goes from -80 W/m^2 in December to $+75 \text{ W/m}^2$ in June. Figures 12a and 12b show that seasonally the hemispherically mean ocean temperatures vary by only a few degrees Kelvin, but the mean land temperatures in the Northern Hemisphere vary by about 22°K . The large size of the Northern Hemisphere land masses make them a dominant factor in the climate of this hemisphere. In the Southern Hemisphere, the mean land temperature varies by only about 13°K from July to January. The mean hemispherical OLR monthly averages (Figure 13) move essentially in phase with the surface temperature. The large seasonal OLR variations in the Northern Hemisphere correspond to the cycle and amplitude of the land surface temperature changes in this hemisphere.

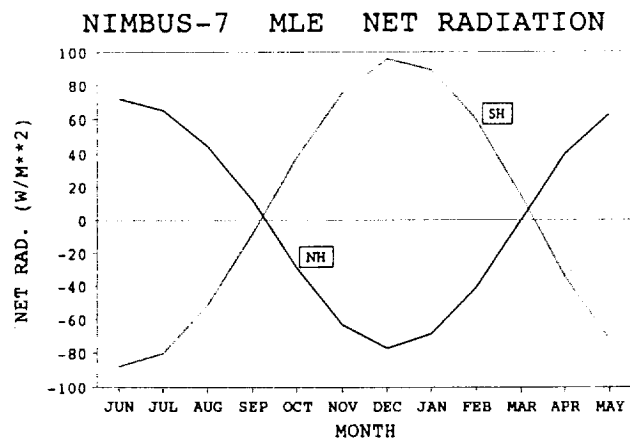


Figure 11. Hemispherical, monthly averages of the net radiation for June 1979 through May 1980.

The mean hemispherical cycles of the albedo and the total noontime cloud amounts are shown in Figures 14 and 15. Each hemisphere is brightest during its summer solstice and has more clouds in the summer than in the winter. There is not, however, a close connection between hemispherical albedo and cloud amount. Over land, arid sections normally have a much larger albedo than do clear moist regions. Also, snow covered regions are about equally bright whether cloud covered or clear. Finally, the amount of shortwave flux reflected from clouds varies both with the amount of insolation and with cloud type as well as amount. Thus, the difference in the total cloud and albedo curves is not surprising.

Nevertheless, clouds are a dominant factor in the global albedo and in most regional albedos.

There is a fair amount of year-to-year variation in the monthly averaged parameters. For instance, the northern hemispheric cloud and albedo peaks in November 1979 are not noticeable in some years.

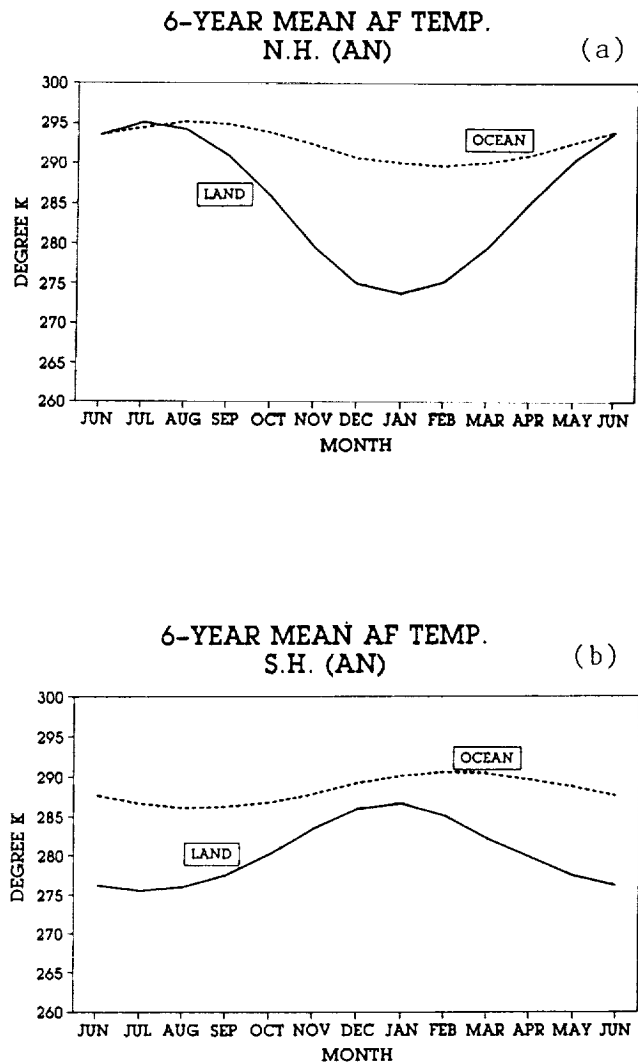


Figure 12. Hemispherical, monthly averages of the Air Force 3-D nephanalysis near noon surface temperatures. Means for the 6 Years April 1979 through March 1985 are shown (a) Northern Hemisphere and (b) Southern Hemisphere. Land and ocean regions are summed separately to show the larger seasonal temperature changes over the continents. Over land, shelter temperatures are shown.

4.2 The Monthly Maps

The monthly averages are shown on pages 55 through 132 for six parameters: diurnal OLR, noon-midnight,

OLR, diurnal albedo, net radiation, total noon cloud cover, and the average (noon and midnight) surface temperature. The net radiative cloud forcing is not given at the monthly level. The maps are arranged by parameter and then by month (May 1979 to May 1980). In the monthly maps, only the region from 60°S to 60°N latitude is shown.

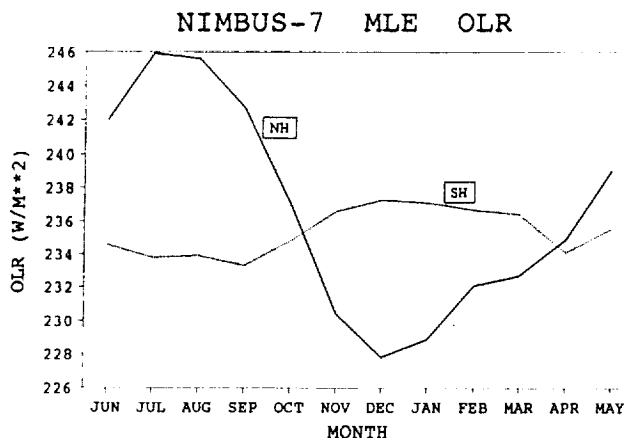


Figure 13. Hemispherical, monthly averages of the outgoing longwave radiation (OLR) for June 1979 through May 1980. The Northern Hemisphere, with its large continental land areas has the larger seasonal changes.

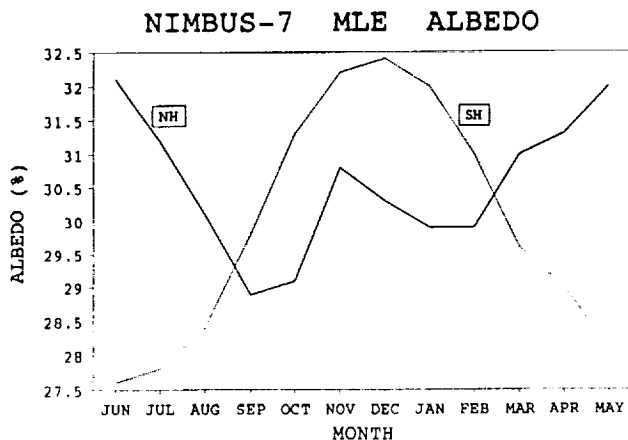


Figure 14. Hemispherical, monthly averages of the albedo June 1979 through May 1980. The presence or absence of solar irradiance on the bright polar regions is a major cause of the seasonal changes. The brightening of the Northern Hemisphere in November is caused by nonpolar cloud fields. This fall brightening is variable from year to year.

The monthly maps show more detail of the seasonal changes than do the seasonal maps. Note particularly the monthly (noon-midnight) OLR patterns over the oceans. In the annual mean (page 19), little diurnal activity appears over the ocean. However, in the

monthly maps, numerous ocean regions appear with OLR differences of 8 W/m² or larger. Both negative and positive differences are almost equally common, and the patterns shift markedly from month to month and from season to season. These patterns indicate varying diurnal cloud cycles; the large heat capacity of the ocean keeps the surface temperature from having a significant diurnal range. Additional discussion on diurnal OLR variations can be found in Gruber and Chen (1988). They found that over the ocean, regional OLR maxima can occur at any time of the day. Over the tropical oceans, the largest diurnal amplitudes tend to occur during the rainy seasons when cloud activity is large.

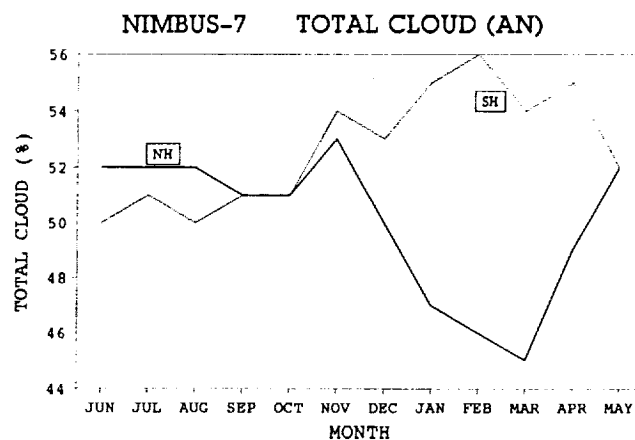


Figure 15. Hemispherical, monthly averages of the total ascending node (noontime) cloud cover in percent.

Over land, the maxima tend to occur early in the afternoon (about 1 or 2 PM). But in monsoon areas, morning maxima are not uncommon. The Nimbus-7 observes most regions only twice a day at fixed local times. Thus, it frequently misses the regional OLR maxima and minima. The (noon-midnight) OLR maps do, however, in most cases, give a qualitative picture of the diurnal variations.

5. REFERENCES

Ardanuy, P. E., L. L. Stowe, A. Gruber, and M. Weiss, 1989: Shortwave, Longwave, and Net Cloud-Radiative Forcing as Determined From Nimbus-7 Observations, *IRS '88: Current Problems in Atmospheric Radiation*, Proceedings of the International Radiation Symposium, Lille France, August 18-24, 1988 (A. Deepak Publishing, Hampton, Virginia), pp. 232-235.

Ardanuy, P. E., L. L. Stowe, A. Gruber, and M. Weiss, 1990: Shortwave, Longwave, and Net Cloud-Radiative Forcing as Determined From Nimbus-7 Observations, submitted to *J. Geophys. Res.*

Arking, A. and S. K. Vemury, 1984: The Nimbus-7 ERB Data Set: A Critical Analyses, *J. Geophys. Res.*, **89**, pp. 5089-5097.

Barkstrom, B., E. Harrison, G. Smith, R. Green, J. Kibler, R. Cess, and the ERBE Science Team, 1989: Earth Radiation Budget Experiment (ERBE) Archival and April 1985 Results, *Bull. Amer. Meteor. Soc.*, **70**, pp. 1254-1262.

Campbell, G. G. and T. H. Vonder Haar, 1980: An Analysis of Two Years of Nimbus-6 Radiation Budget Measurements, *Atmos. Sci. Pap.*, **320**, Colorado State University, Ft. Collins, p. 83.

Cess, R. D., 1990: Interpretation of an Eight-Year Record of Nimbus-7 Wide-Field-of-View Infrared Measurements, December 1989, submitted to *J. Geophys. Res.*

Dhuria, H. L. and H. L. Kyle, 1990: Cloud Types and the Tropical Earth Radiation Budget, *J. Climate*, **3**, 1409-1434.

Ellis, J. and T. H. Vonder Haar, 1976: Zonal Average Earth Radiation Budget Measurements From Satellites for Climate Studies, *Atmos. Sci. Pap.*, **240**, Colorado State University, Ft. Collins.

Gruber, A. and T. S. Chen, 1988: Diurnal Variation of Outgoing Longwave Radiation, *J. Climatology*, **8**, 1-16.

Gruber, A. and J. S. Winston, 1978: Earth-Atmosphere Radiative Heating Based on NOAA Scanning Radiometer Measurements, *Bull. Amer. Meteorol. Soc.*, **59**, 1570-1573.

Harrison, E. F., P. Minnis, B. R. Barkstrom, V. Ramanathan, R. D. Cess, and G. G. Gibson, 1990: Seasonal Variation of Cloud Radiative Forcing Derived From the Earth Radiation Budget Experiment, *J. Geophys. Res.*, **95**, 18,687-18703.

Hickey, J. R., B. M. Alton, H. L. Kyle, and D. Hoyt, 1988: Total Solar Irradiance Measurements by ERB/Nimbus-7: A Review of Nine Years, *Space Science Reviews*, **48**, 321-342.

House, F. B., A. Gruber, G. E. Hunt, and A. T. Mecherikunnel, 1986: History of Satellite Missions and Measurements of the Earth Radiation Budget (1957-1984), *Rev. Geophys.*, **24**, 357-377.

Hwang, P. H., L. L. Stowe, H. Y. M. Yeh, H. L. Kyle, and Nimbus-7 Cloud Data Processing Team, 1988: The Nimbus-7 Global Cloud Climatology, *Bull. Amer. Meteor. Soc.*, **69**, 743-752.

Jacobowitz, H., W. L. Smith, H. B. Howell, F. W. Nagle, and J. R. Hickey, 1979: The First 19 Months of Planetary Radiation Budget Measurements From the Nimbus-6 ERB, *J. Atmos. Sci.*, **36**, 501-507.

Jacobowitz, H., H. V. Soule, H. L. Kyle, F. B. House, and the Nimbus-7 ERB Experiment Team, 1984a: The Earth Radiation Budget (ERB) Experiment: An Overview, *J. Geophys. Res.*, **89**, 5021-5038.

Jacobowitz, H., R. J. Tighe, and the Nimbus-7 ERB Experiment Team, 1984b: The Earth Radiation Budget Derived From the Nimbus-7 ERB Experiment, *J. Geophys. Res.*, **89**, 4997-5010.

Kyle, H. L., 1990: "The Nimbus-7 Earth Radiation Budget (ERB) Data Set and Its Uses," A Chapter in Long-Term Monitoring of the Earth's Radiation Budget, Bruce R. Barkstrom (editor), *Proc. SPIE 1299*, 27-39.

Kyle, H. L., P. E. Ardanuy, and E. J. Hurley, 1985: The Status of the Nimbus-7 ERB Earth Radiation Budget Data Set, *Bull. Amer. Meteor. Soc.*, **66**, 1378-1388.

Kyle, H. L., A. Mecherikunnel, P. Ardanuy, L. Penn, B. Groveman, G. G. Campbell, and T. H. Vonder Haar, 1990: Comparison of Two Major Earth Radiation Budget Data Sets, *J. Geophys. Res.*, **95**, D7, 9951-9970.

Kyle, H. L., A. Mecherikunnel, C. R. Kondragunta, and R. R. Hucek, 1991: The Earth's Annual Net Radiation Budget in 1979/80 and 1985/86, submitted to *J. Climate*.

Kyle, H. L., K. L. Vasanth, and the Nimbus-7 ERB Experiment Team, 1986: Some Characteristic Differences in the Earth's Radiation Budget Over Land and Ocean Derived From the Nimbus-7 ERB Experiment, *J. Climate Appl. Meteor.*, **25**, 958-981.

Ohring, G. and A. Gruber, 1983: Satellite Radiation Observations and Climate Theory, *Advan. Geophys.*, **25**, 237-301.

Ramanathan, V., 1987: The Role of Earth Radiation Budget Studies in Climate and General Circulation Research, *J. Geophys. Res.*, **92**, 4075-4095.

Ramanathan, V., R. D. Cess, E. F. Harrison, P. Minnis, B. R. Barkstrom, E. Ahmad, and D. Hartmann, 1989: Cloud-Radiative Forcing and Climate: Results From the Earth Radiation Budget Experiment, *Science*, **243**, 57-63.

Raschke, E., T. H. Vonder Haar, W. R. Bandeen, and M. Pasternack, 1973: The Annual Radiation Balance of the Earth-Atmosphere System During 1969-70 from Nimbus-3 Measurements, *J. Atmos. Sci.*, **30**, 341-364.

Stowe, L. L., C. G. Wellemeyer, T. F. Eck, H. Y. M. Yeh, and the Nimbus-7 Cloud Data Processing Team, 1988: Nimbus-7 Global Cloud Climatology, Part I: Algorithms and Validation, *J. Climate*, **1**, 445-470.

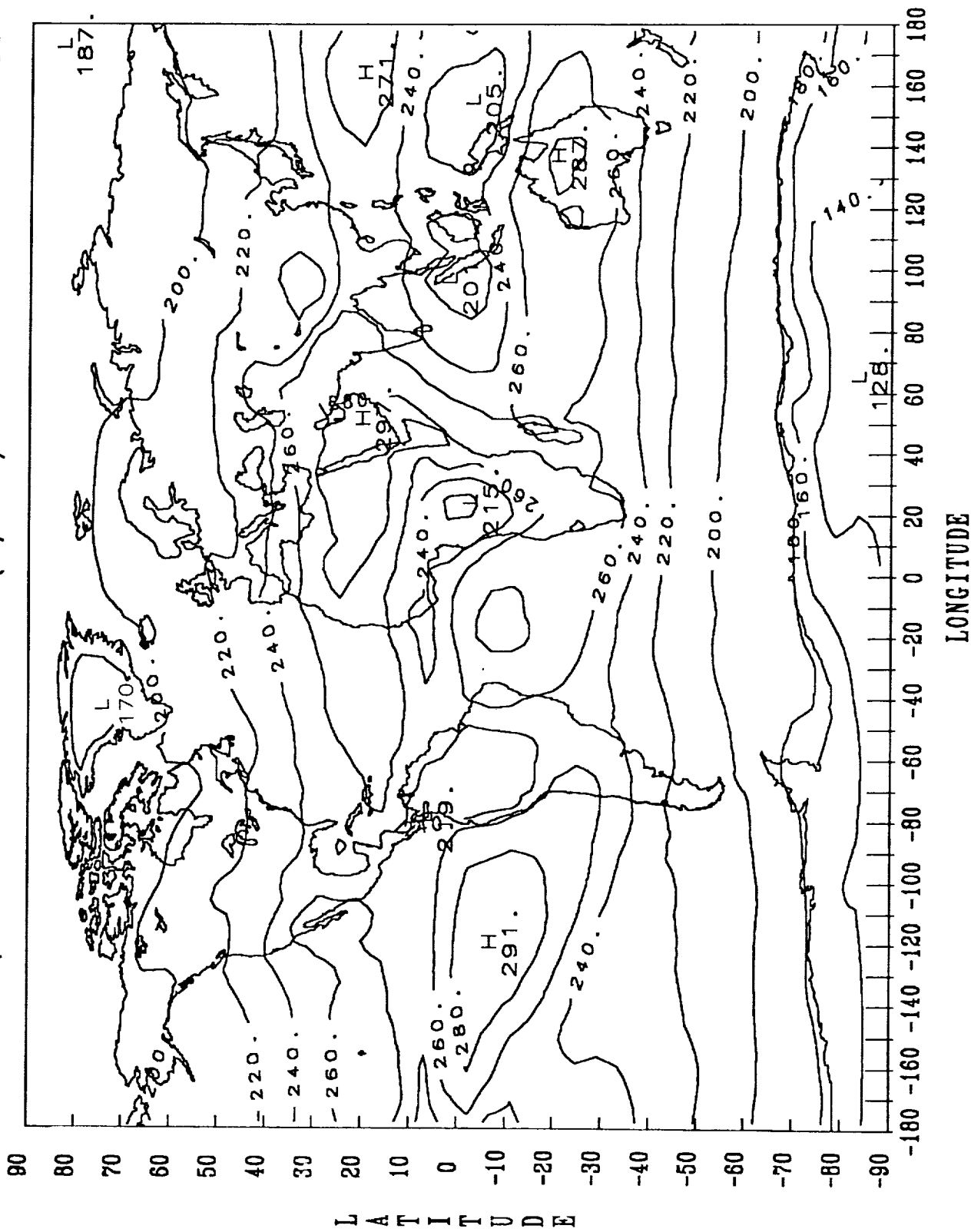
Stowe, L. L., H. Y. M. Yeh, T. F. Eck, C. G. Wellemeyer, H. L. Kyle, and the Nimbus-7 Cloud Data Processing Team, 1989: Nimbus-7 Global Cloud Climatology, Part II: First Year Results, *J. Climate*, **2**, 671-709.

Wielicki, B. A. and R. N. Green, 1989: Cloud Identification for ERBE Radiative Flux Retrieval, *J. Appl. Meteor.*, **28**, 1131-1146.

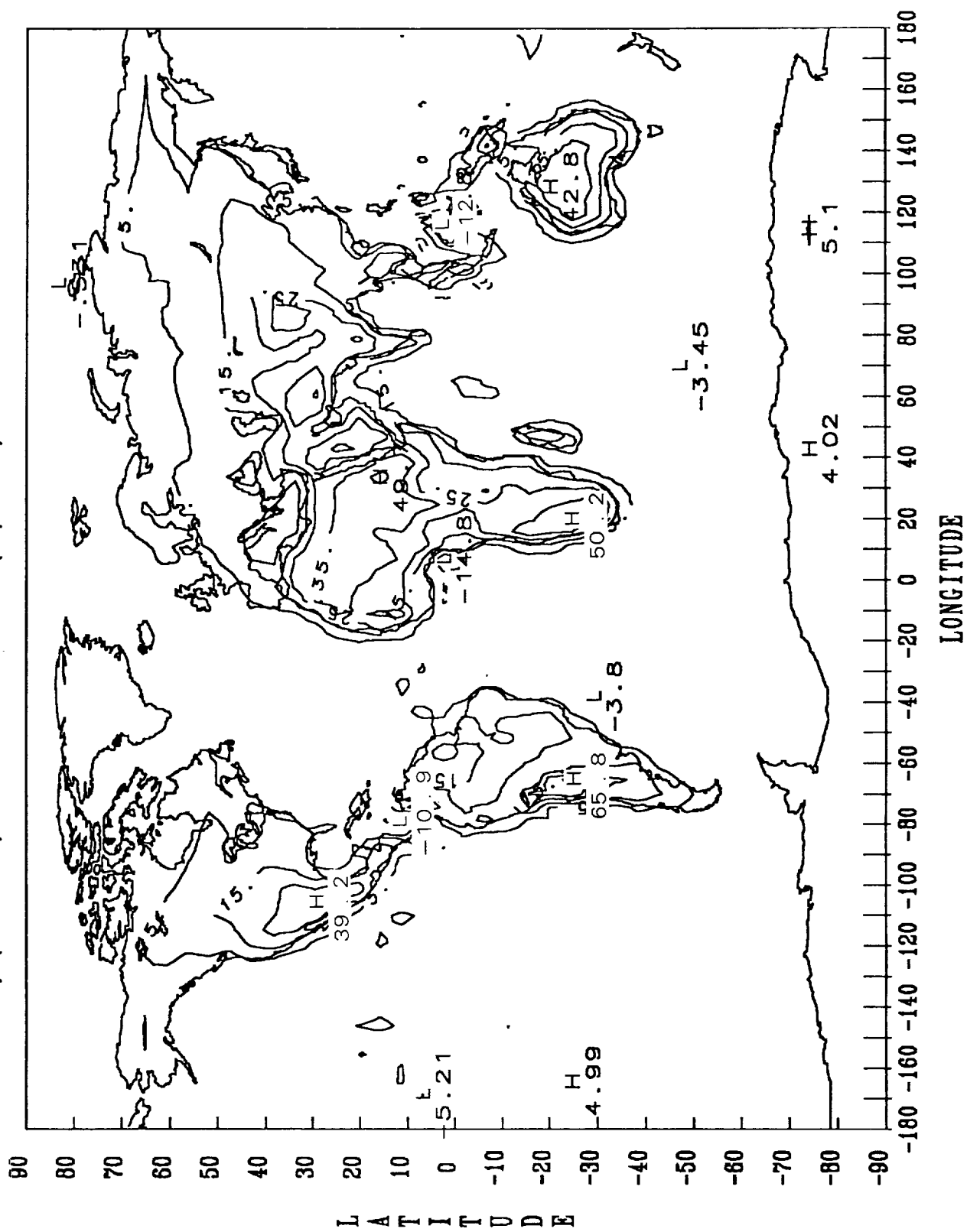
6. ANNUAL MAPS FOR THE PERIOD FROM JUNE 1979 TO MAY 1980

ANNUAL MAPS		
PARAMETER	CONTOUR STEP SIZE	PAGE
Diurnal OLR	20 W/m ²	18
Noon-Midnight OLR Difference	10 W/m ²	19
Diurnal Albedo	10% (20% or below dashed)	20
Net Radiation	20 W/m ² (negative values dashed)	21
Total Noon Cloud Cover	15% (30% or below dashed)	22
Average (Noon and Midnight) Surface Temperature	5°K (every other contour labelled)	23
Net Radiation Cloud Forcing	15 W/m ² (zero and positive values dashed; every other contour labelled)	24

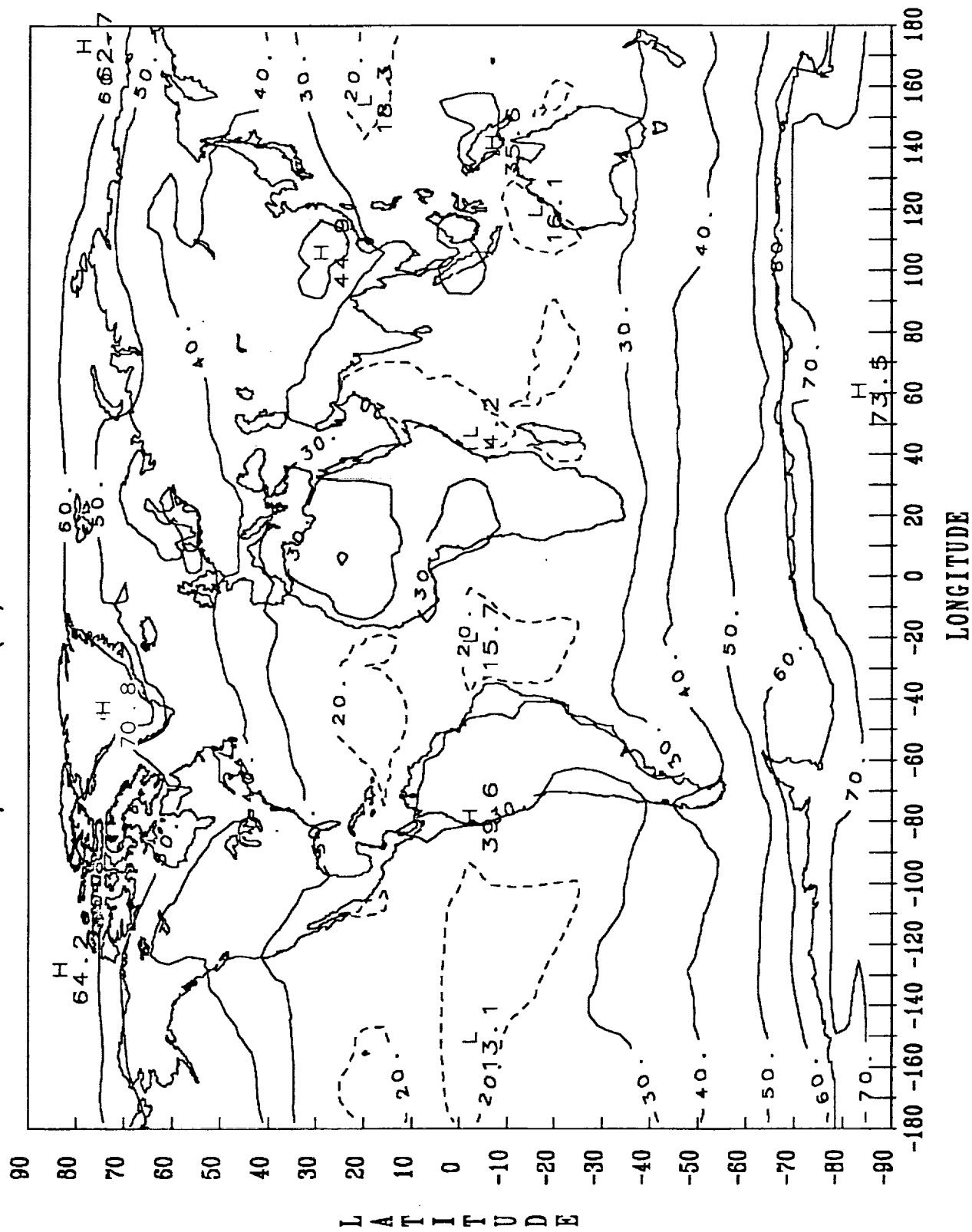
NIMBUS 7/EMITTED RADIATION (W/M*²M) JUNE 1979 - MAY 1980



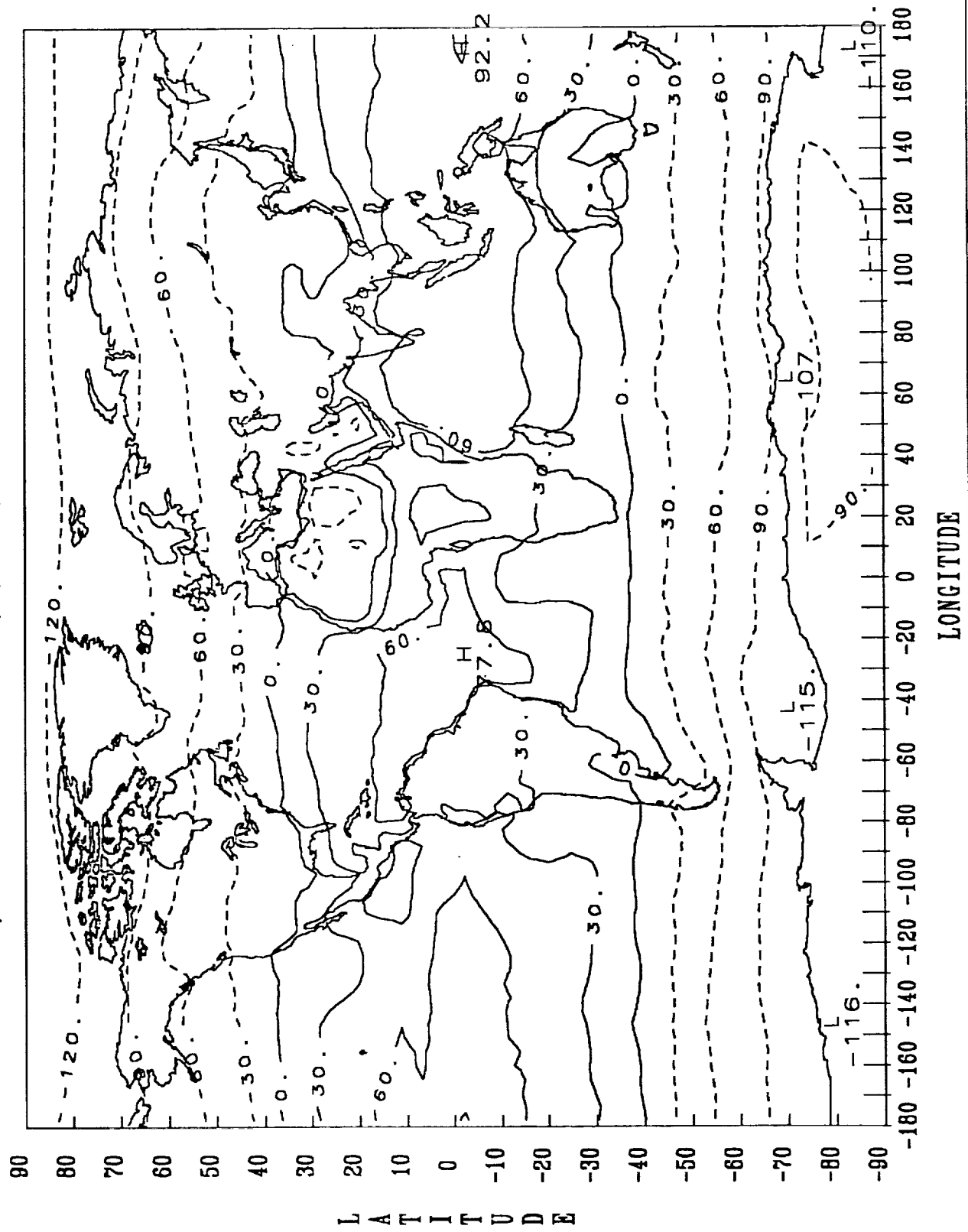
NIMBUS 7/(AN-DN) EMITTED DIF (W/M-M) JUNE 1979 - MAY 1980



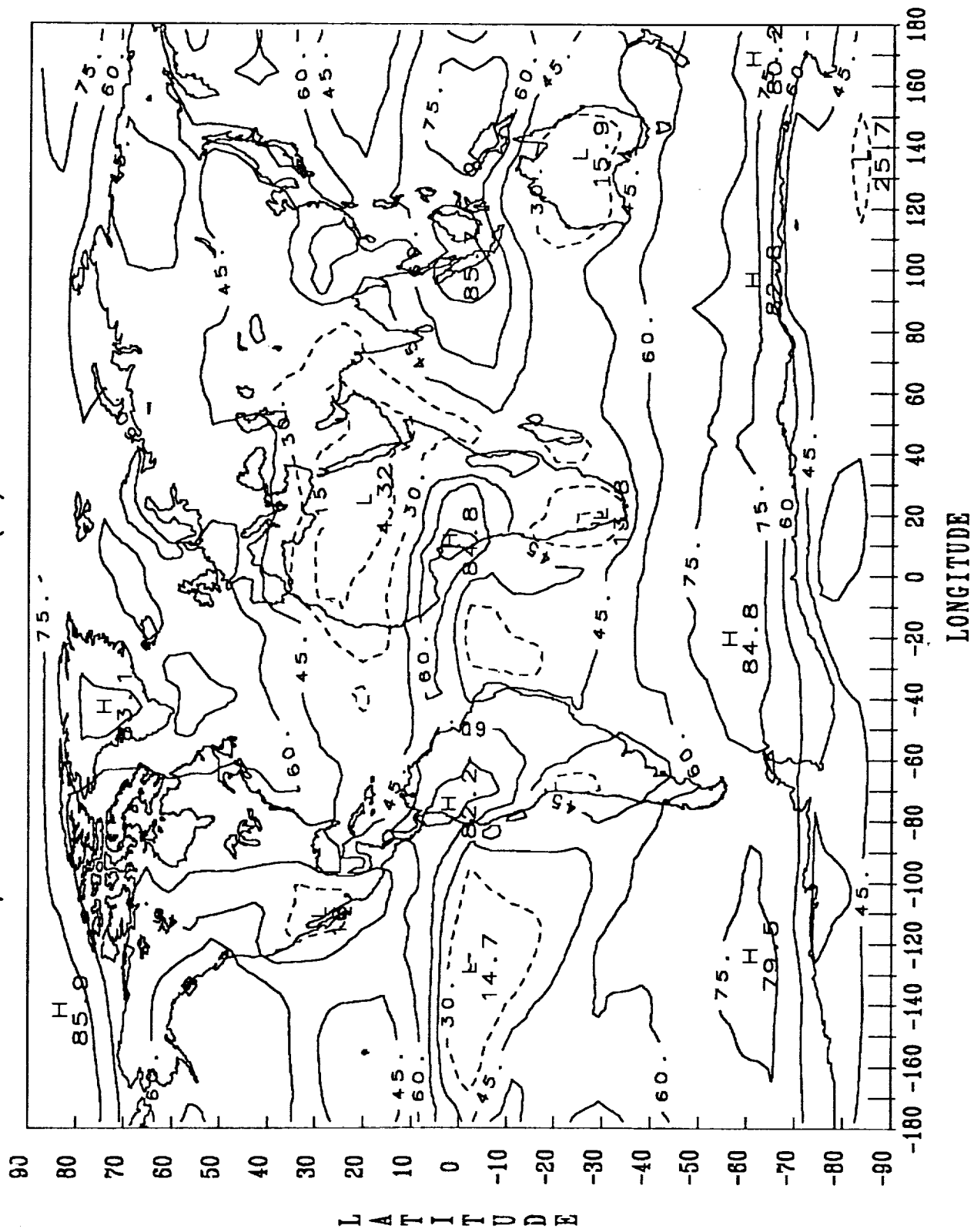
NIMBUS 7/ALBEDO (%) JUNE 1979 - MAY 1980



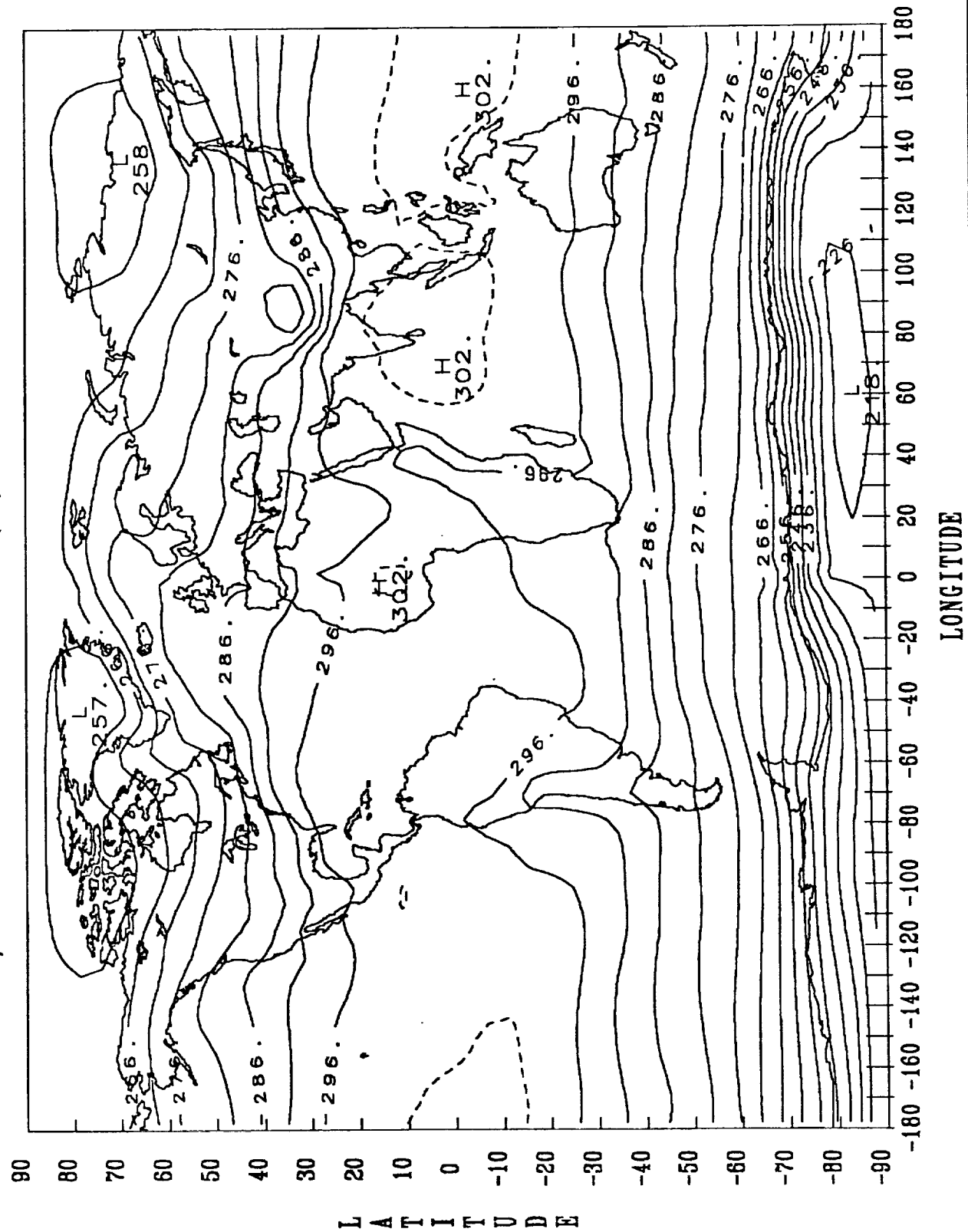
NIMBUS 7/NET RADIATION (W/M*M) JUNE 1979 - MAY 1980



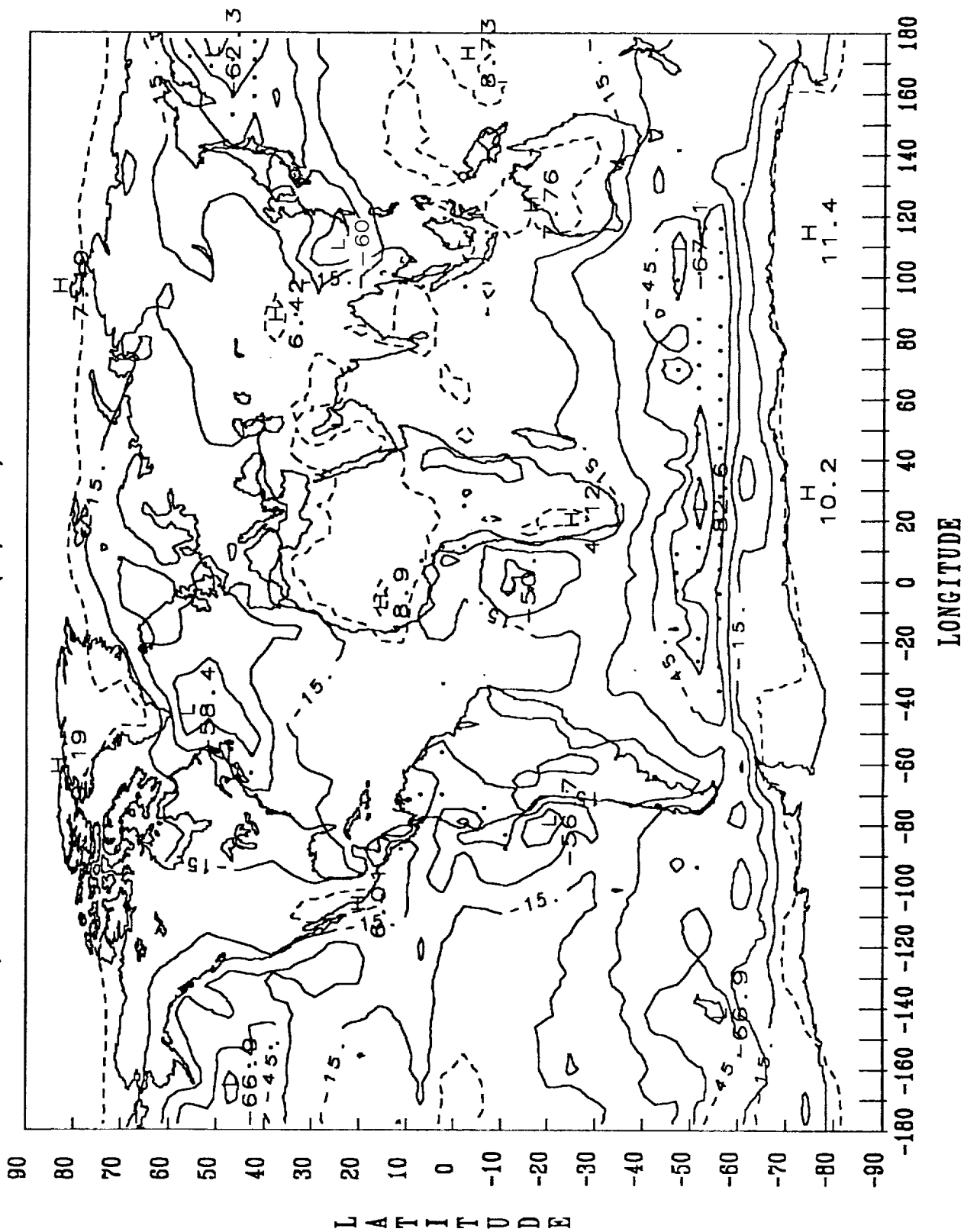
NIMBUS 7/TOTAL NOON CLOUD (%) JUN 1979 - MAY 1980



NIMBUS 7/SURFACE TEMPERATURE (K) JUNE 1979 - MAY 1980



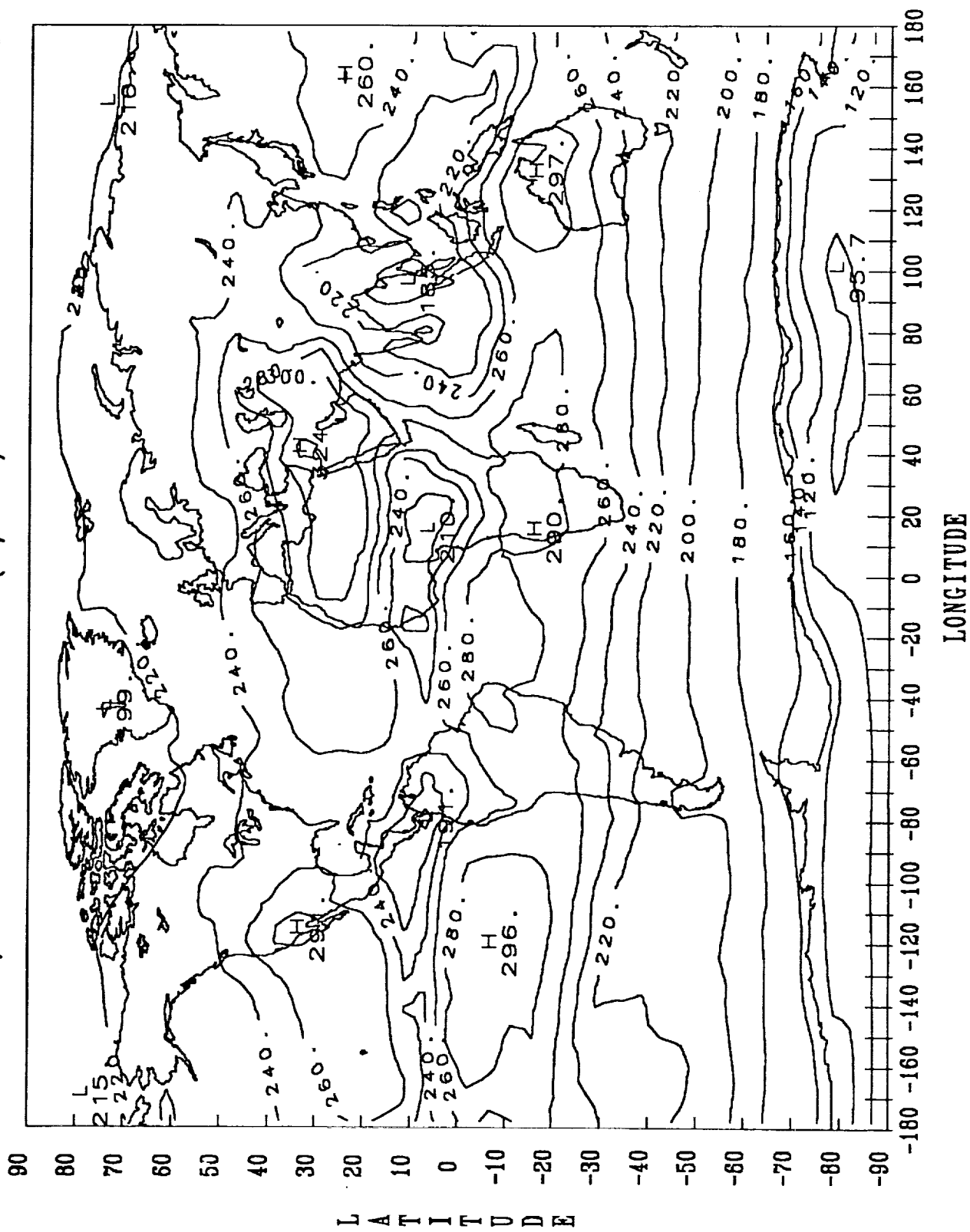
NIMBUS 7/NET CLOUD FORCING (W/M-M) JUNE 1979 - MAY 1980



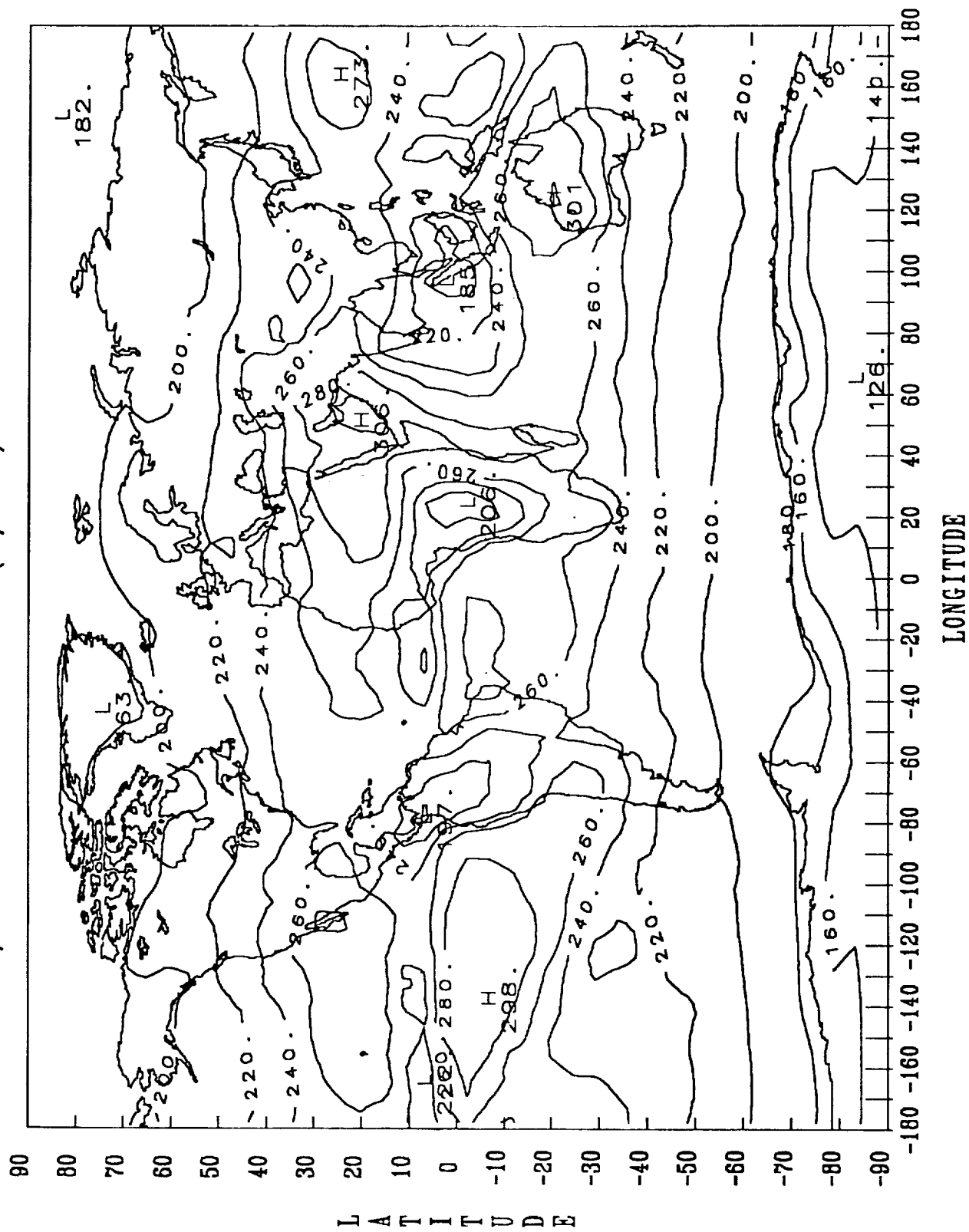
7. SEASONAL MAPS FOR THE PERIOD FROM JUNE 1979 TO MAY 1980

SEASONAL MAPS		
The maps are arranged by parameter and then by season as follows:		
SOLSTICE: June to August EQUINOX: September to November SOLSTICE: December to February EQUINOX: March to May		
PARAMETER	CONTOUR STEP SIZE	PAGE
Diurnal OLR	20 W/m ²	26
Noon-Midnight OLR Difference	10 W/m ² (negative values dashed)	30
Diurnal Albedo	10% (20% or below dashed)	34
Net Radiation	30 W/m ² (negative values dashed)	38
Noon Cloud Cover	15% (30% or below dashed)	42
Average (Noon and Midnight) Surface Temperature	5°K (every other contour labelled; values of 301°K or larger dashed)	46
Net Radiation Cloud Forcing	20 W/m ² (every other contour labeled; zero and positive contours dashed)	50

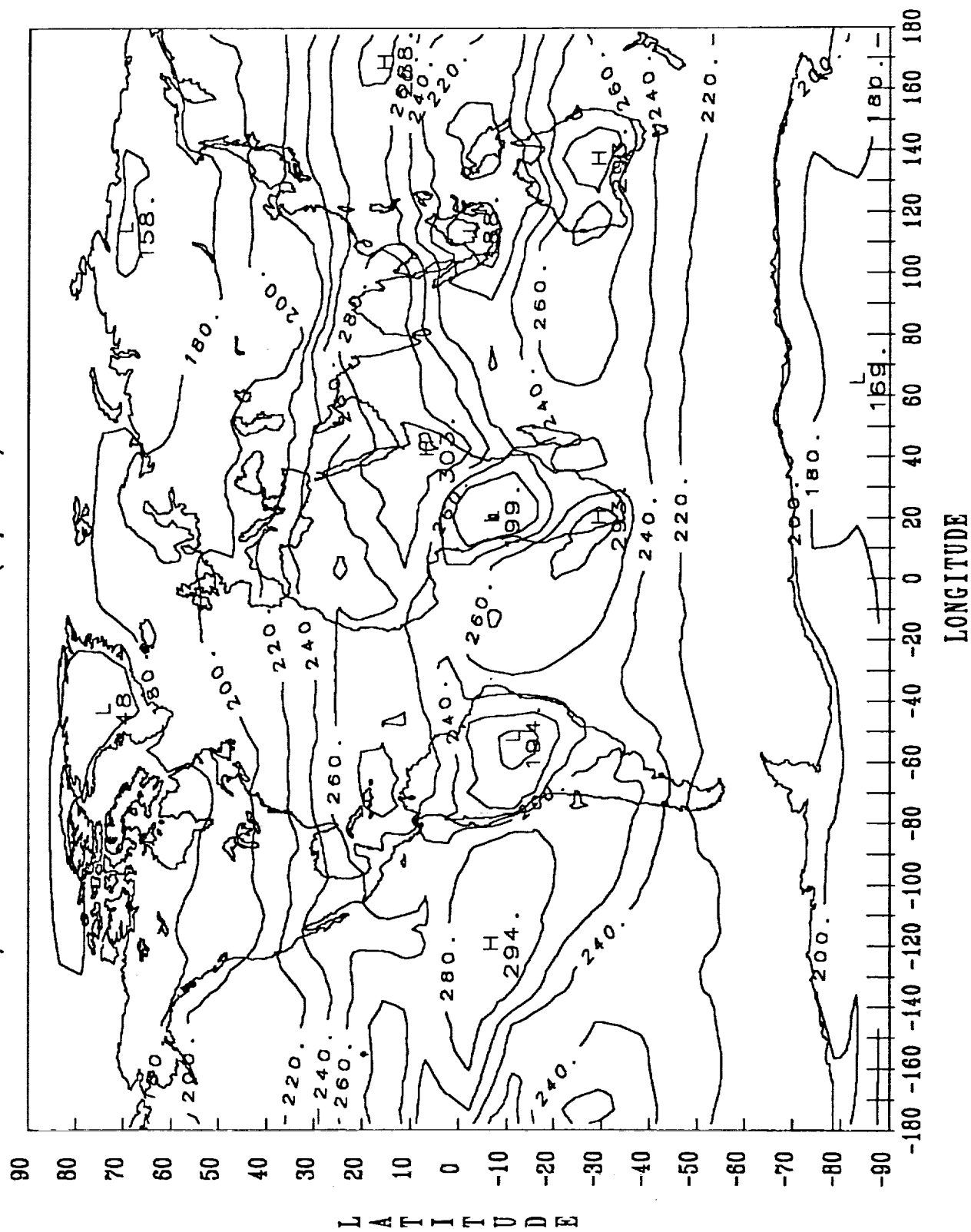
NIMBUS 7/EMITTED RADIATION (W/M*²M) JUNE 1979 - AUG 1979



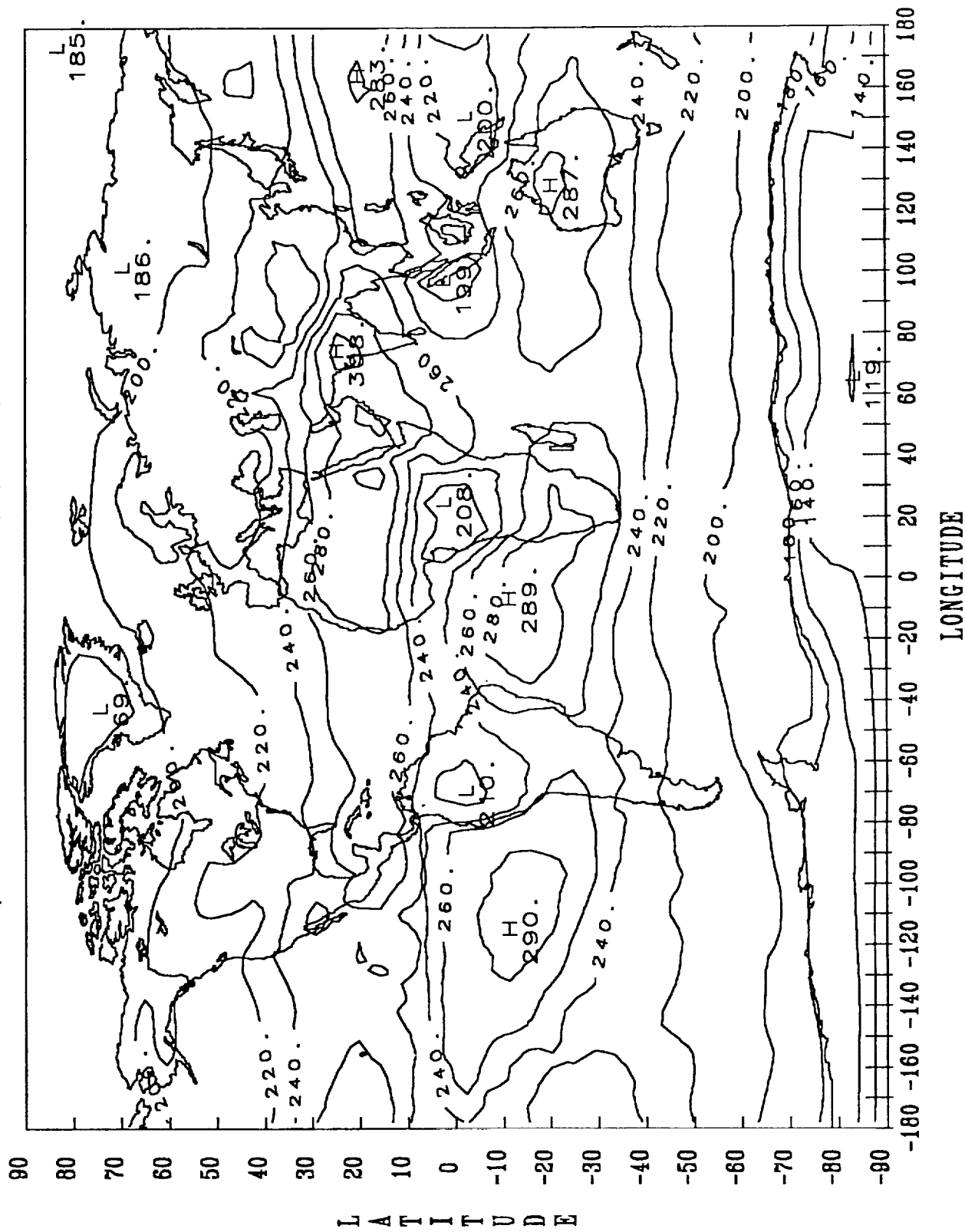
NIMBUS 7/EMITTED RADIATION (W/M²M) SEP 1979 - NOV 1979



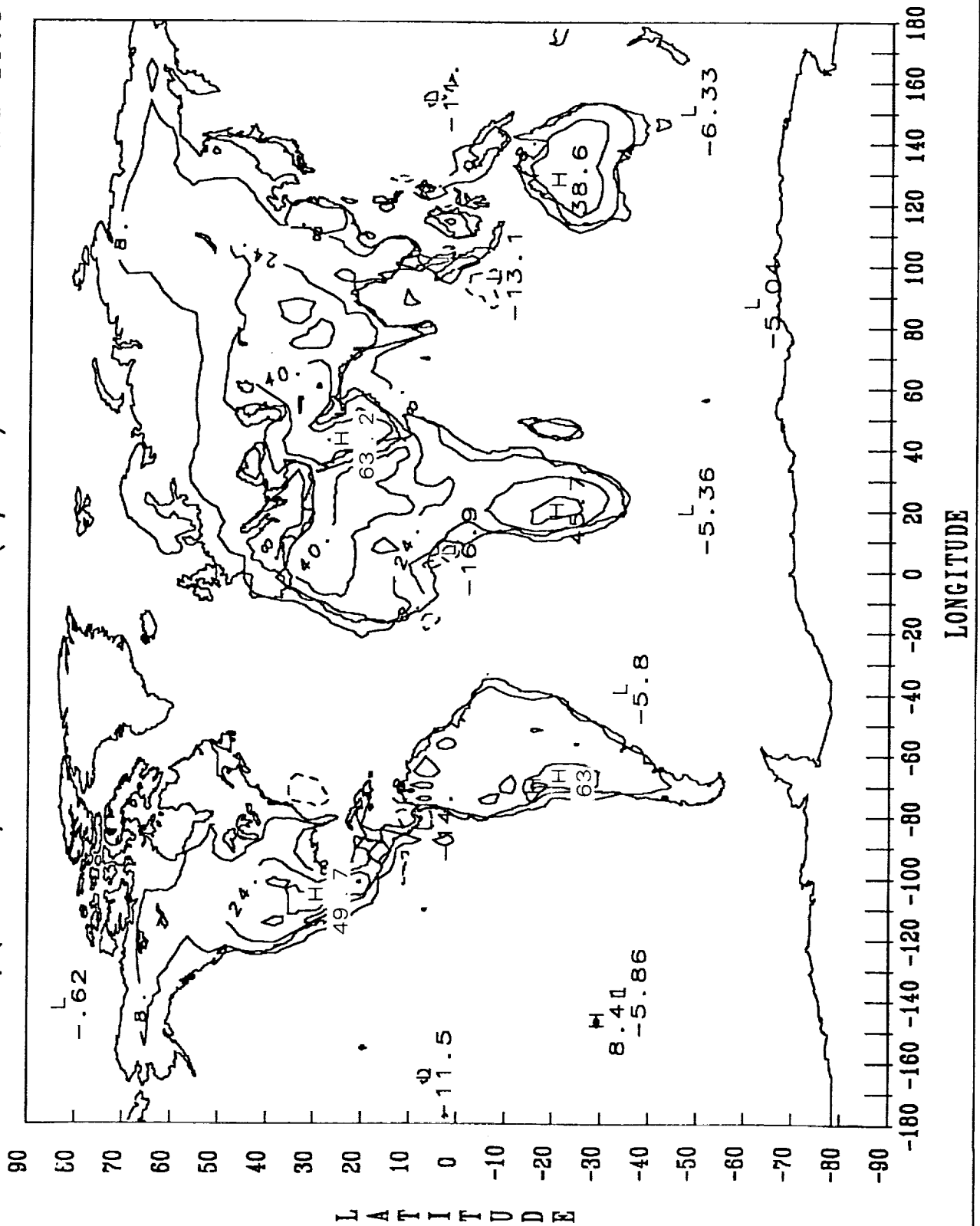
NIMBUS 7/EMITTED RADIATION (W/M*²M) DEC 1979 - FEB 1980



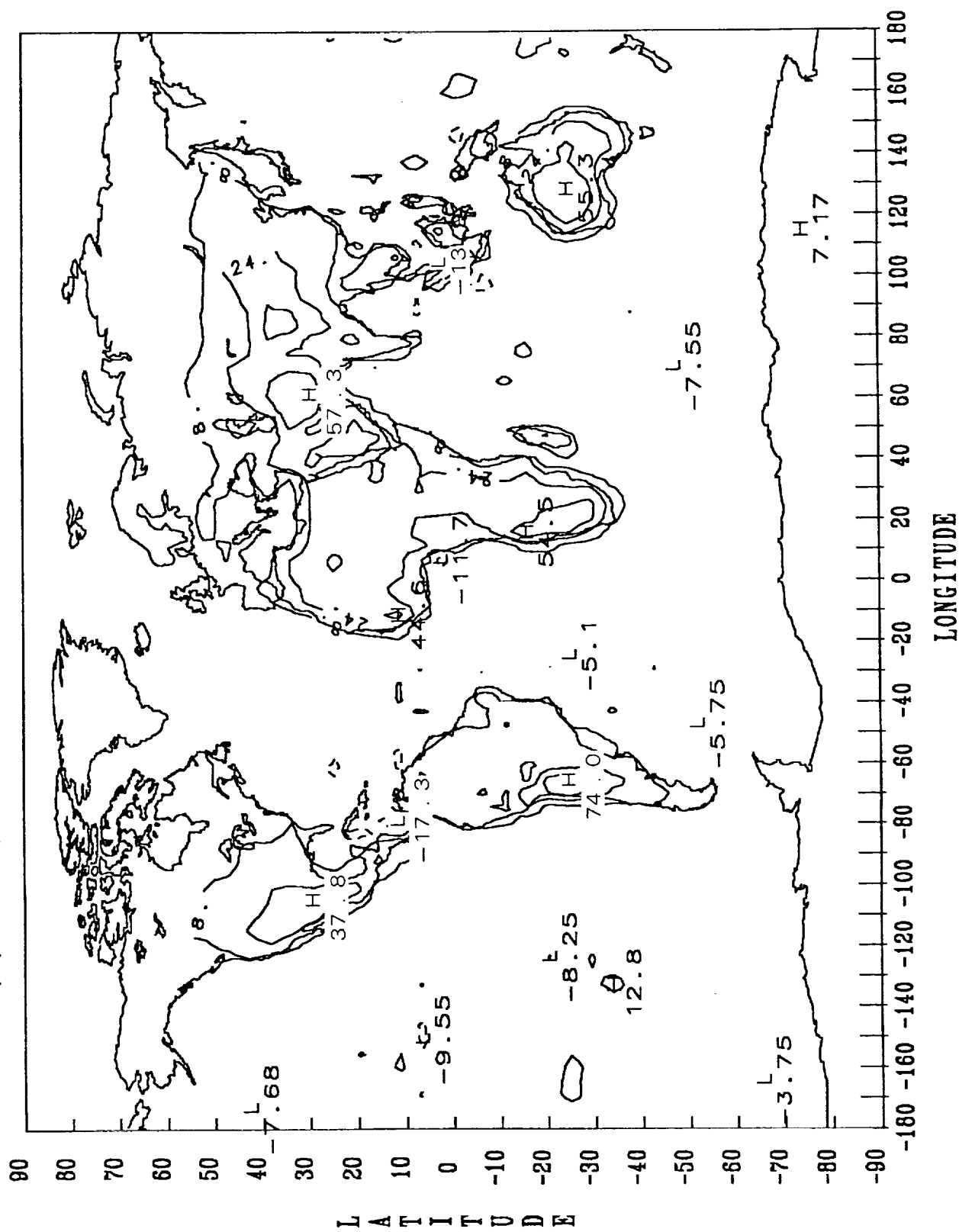
NIMBUS 7/EMITTED RADIATION (W/M* μ M) MAR - MAY 1980



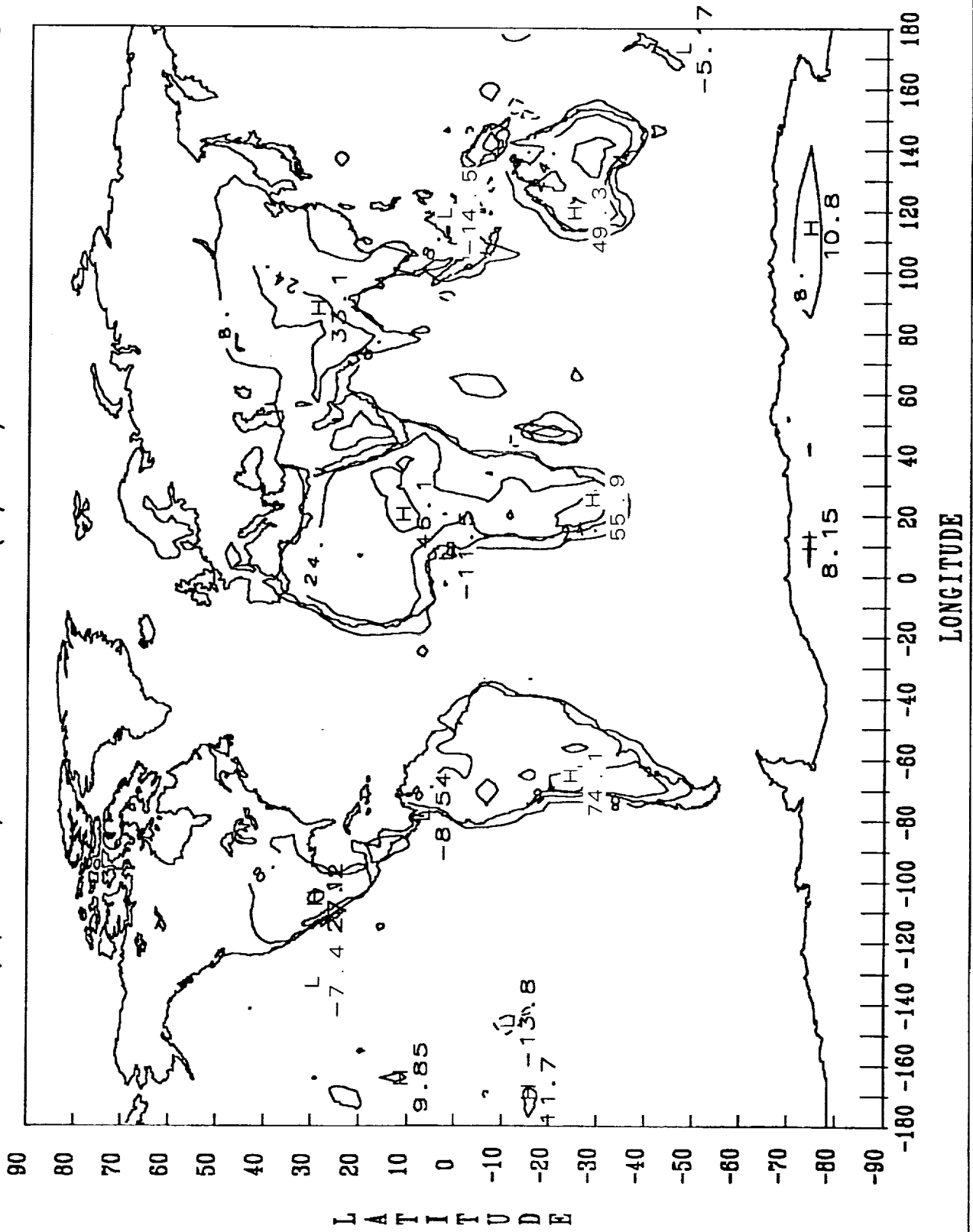
NIMBUS 7/(AN-DN) EMITTED DIF (W/M-M) JUNE 1979 - AUG 1979



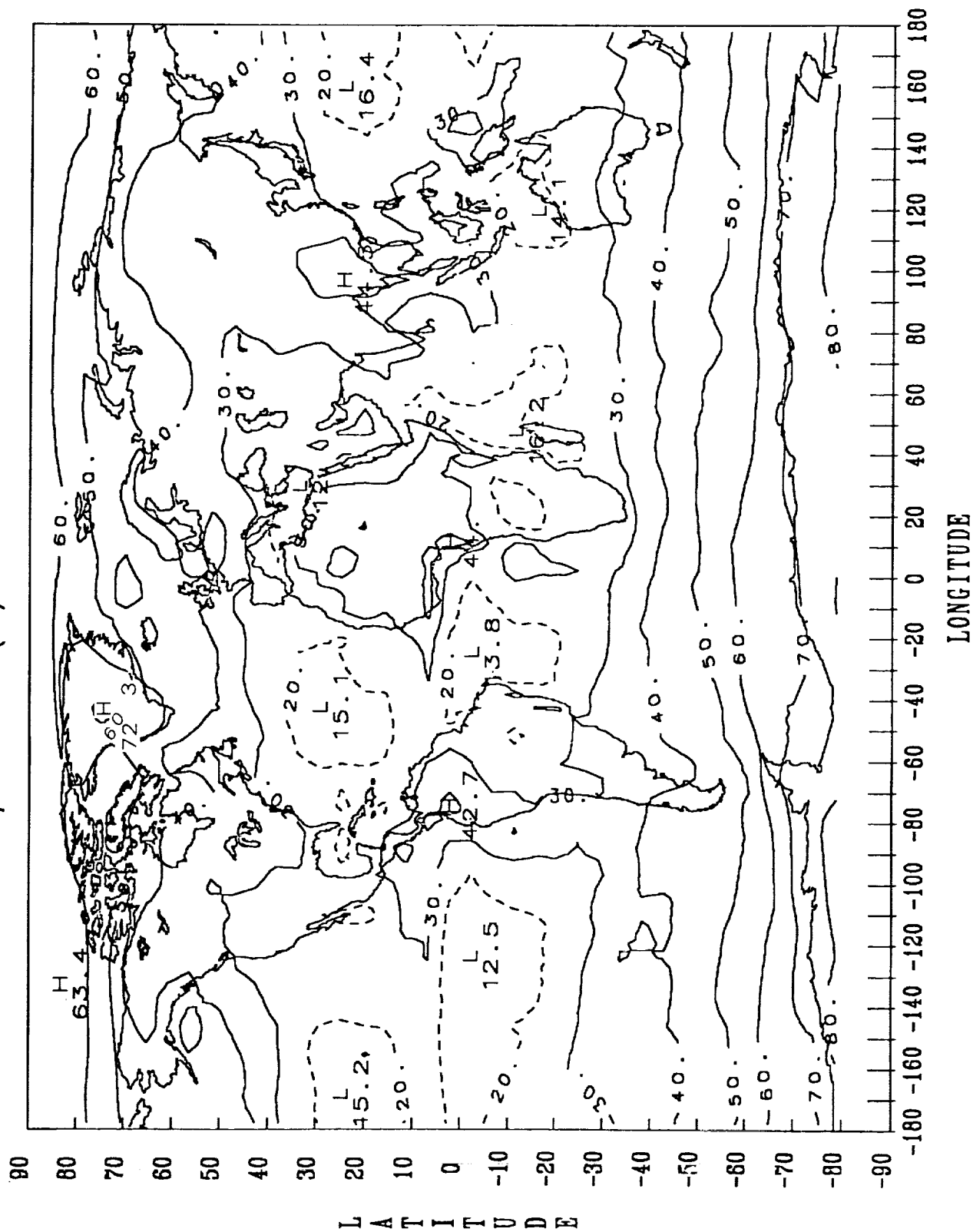
NIMBUS 7/(AN-DN) EMITTED DIF (W/M-M) SEPT 1979 - NOV 1979



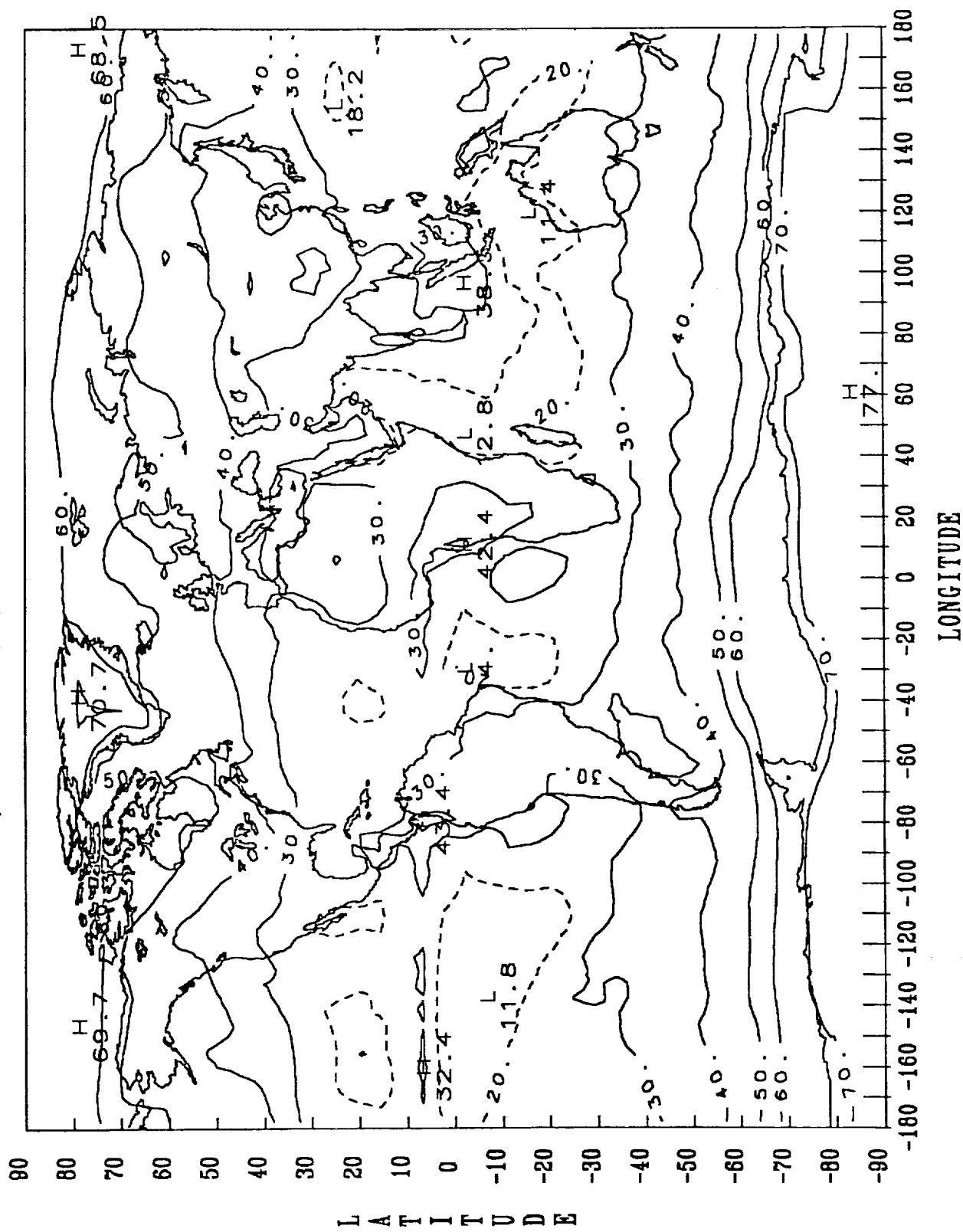
NIMBUS 7/(AN-DN) EMITTED DIF (W/M-M) DEC 1979 - FEB 1980



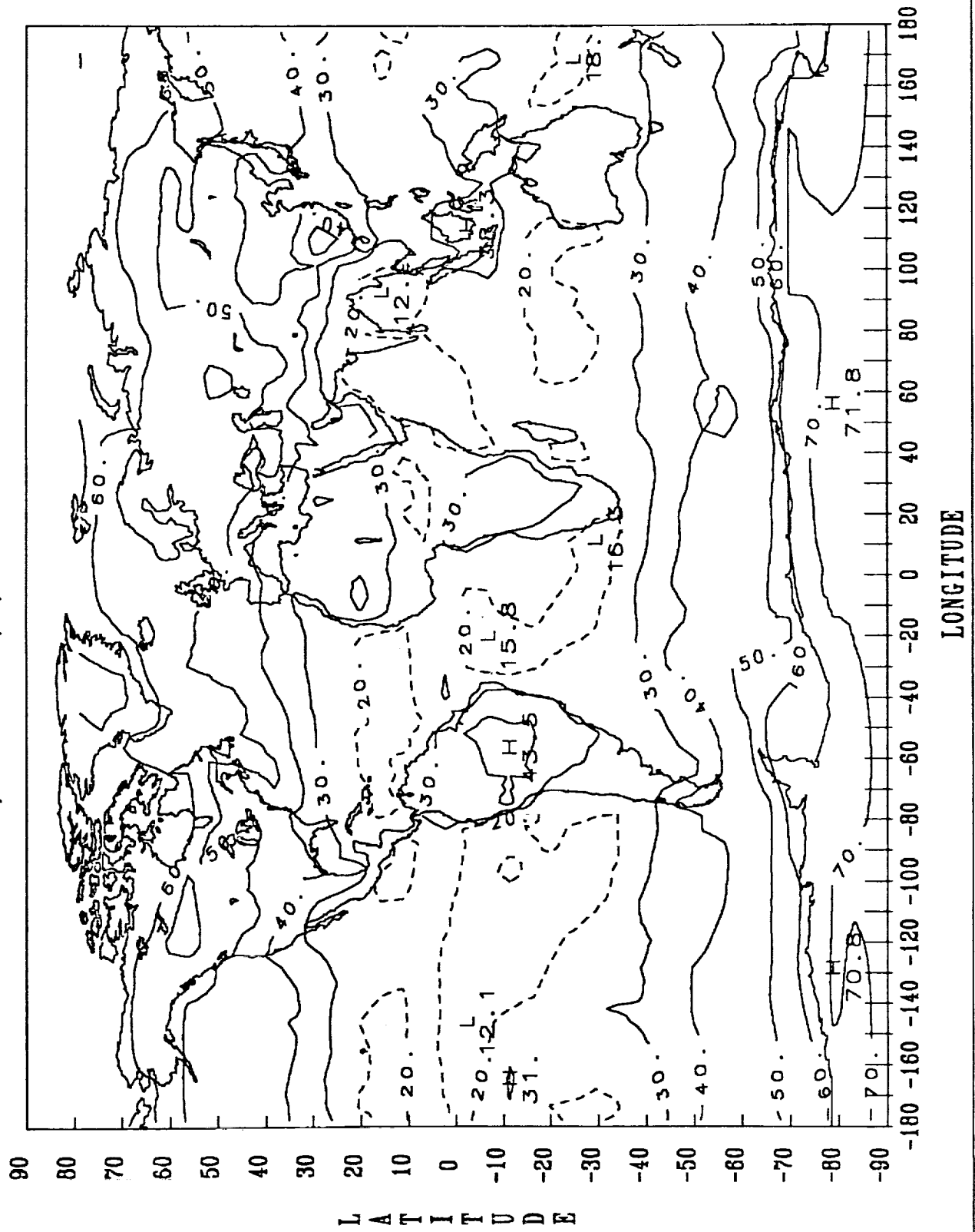
NIMBUS 7/ALBEDO (%) JUNE 1979 - AUG 1979



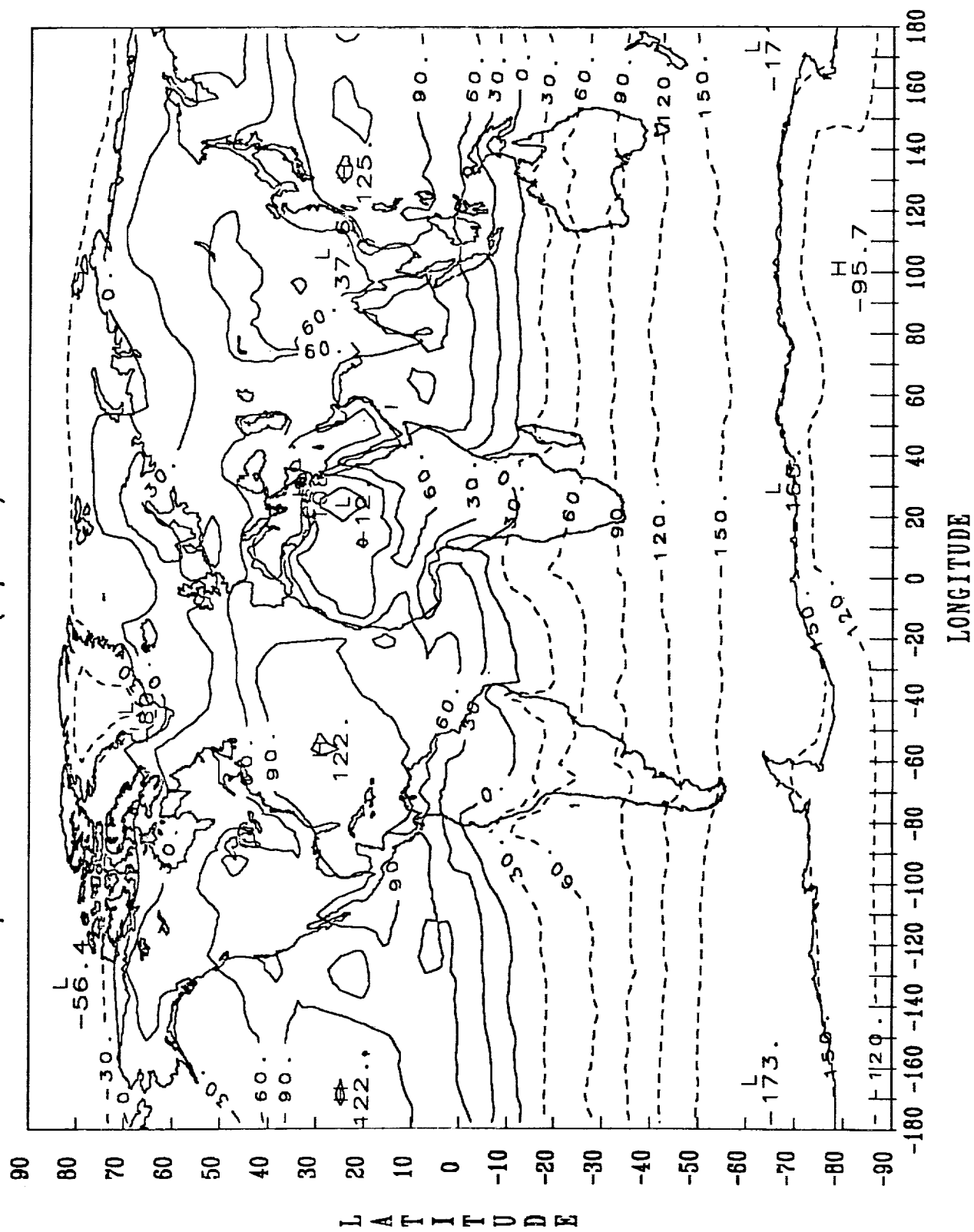
NIMBUS 7/ALBEDO (%) SEPT 1979 - NOV 1979



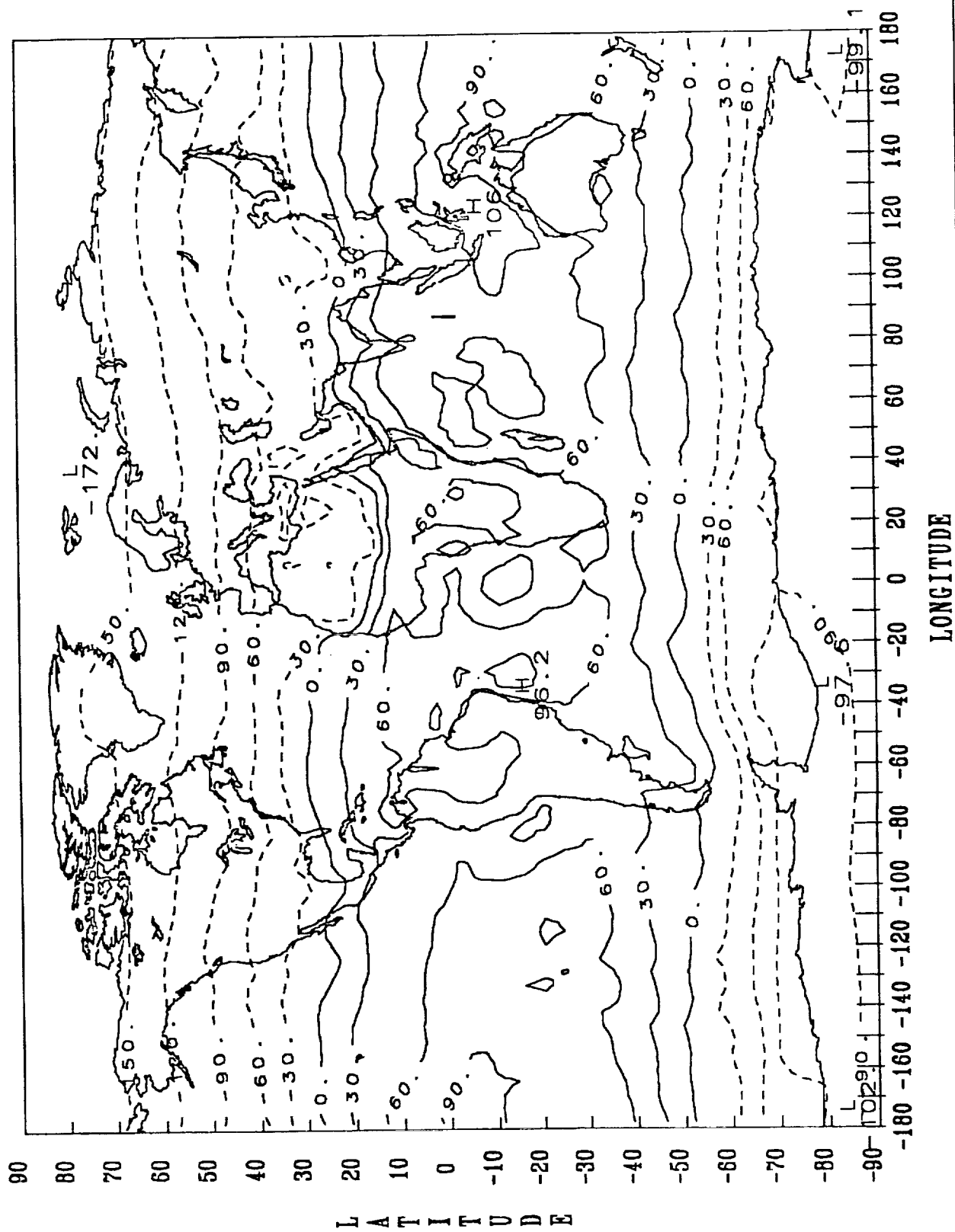
NIMBUS 7/ALBEDO (%) DEC 1979 - FEB 1980



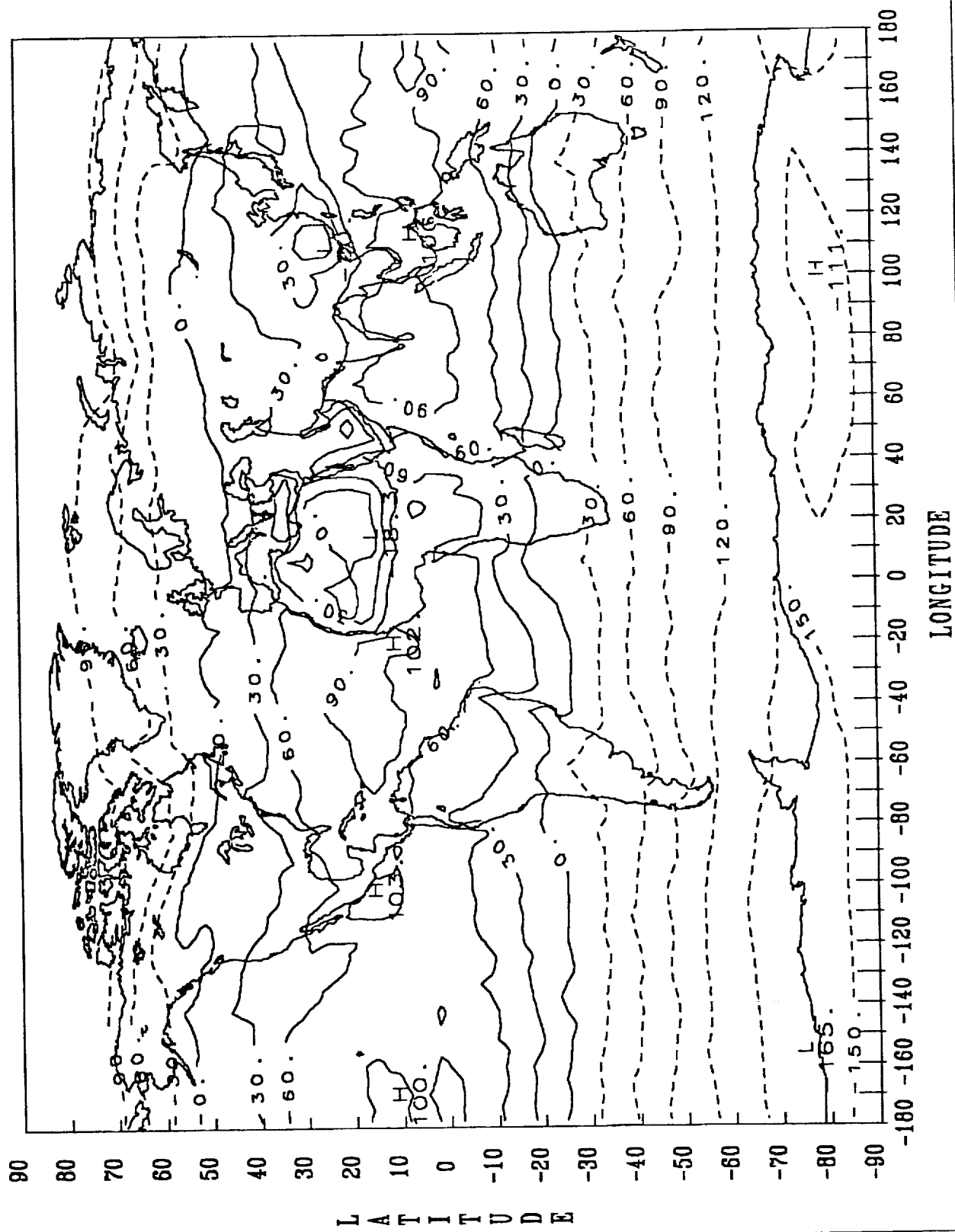
NIMBUS 7/NET RADIATION (W/M*M) JUNE 1979 - AUG 1979



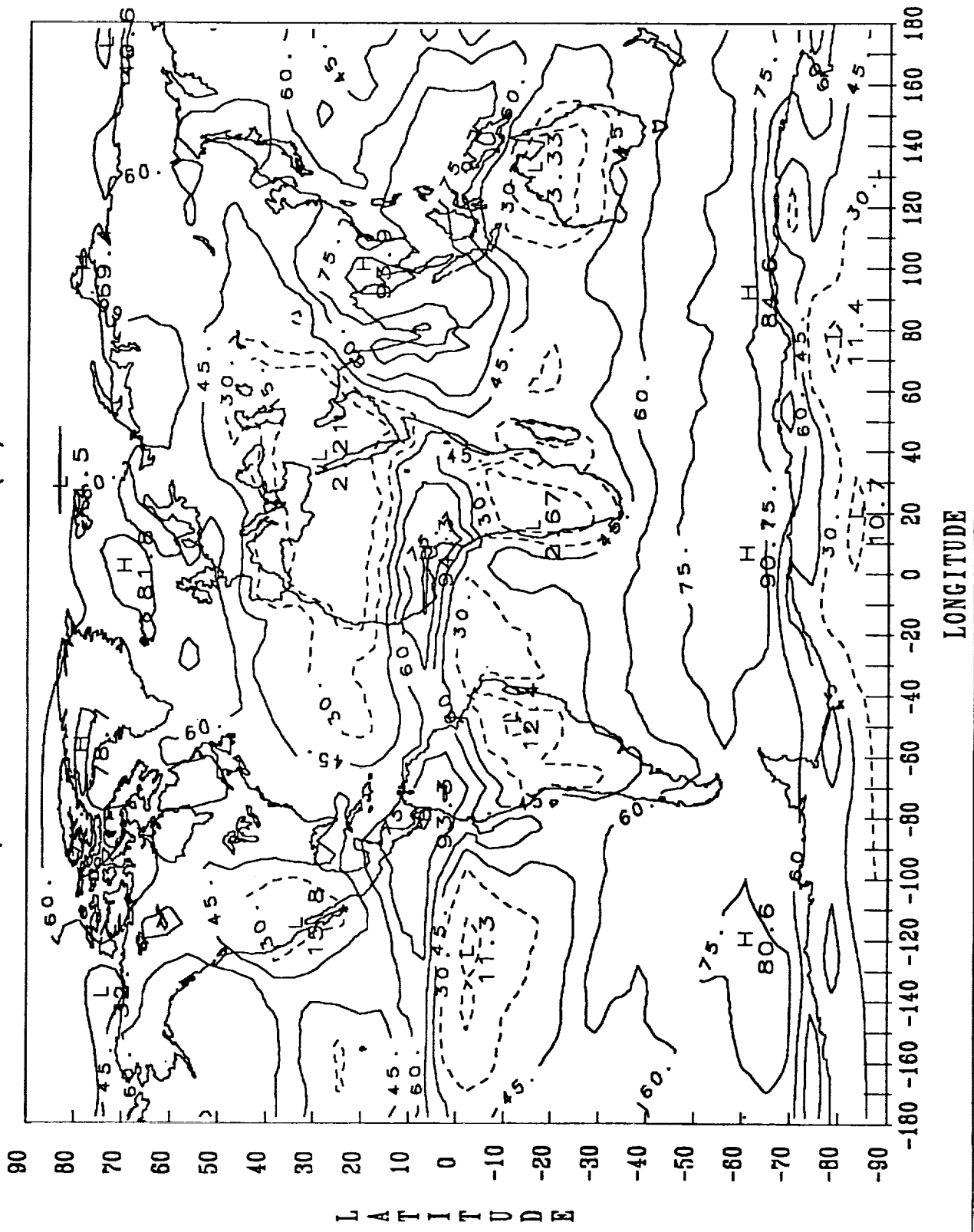
NIMBUS 7/NET RADIATION (W/M²M) SEPT 1979 - NOV 1979



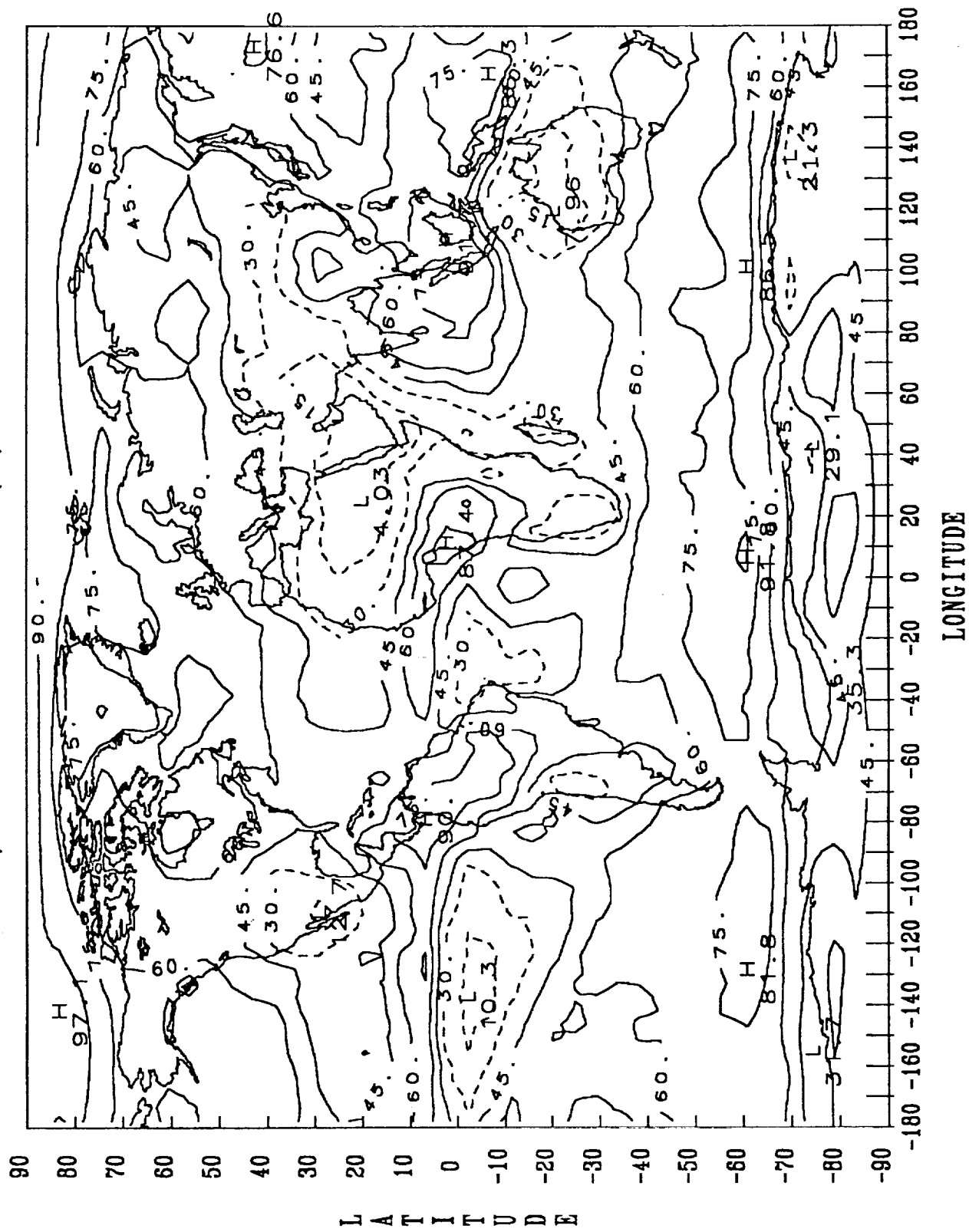
NIMBUS 7/NET RADIATION (W/M²M) MAR 1980 - MAY 1980



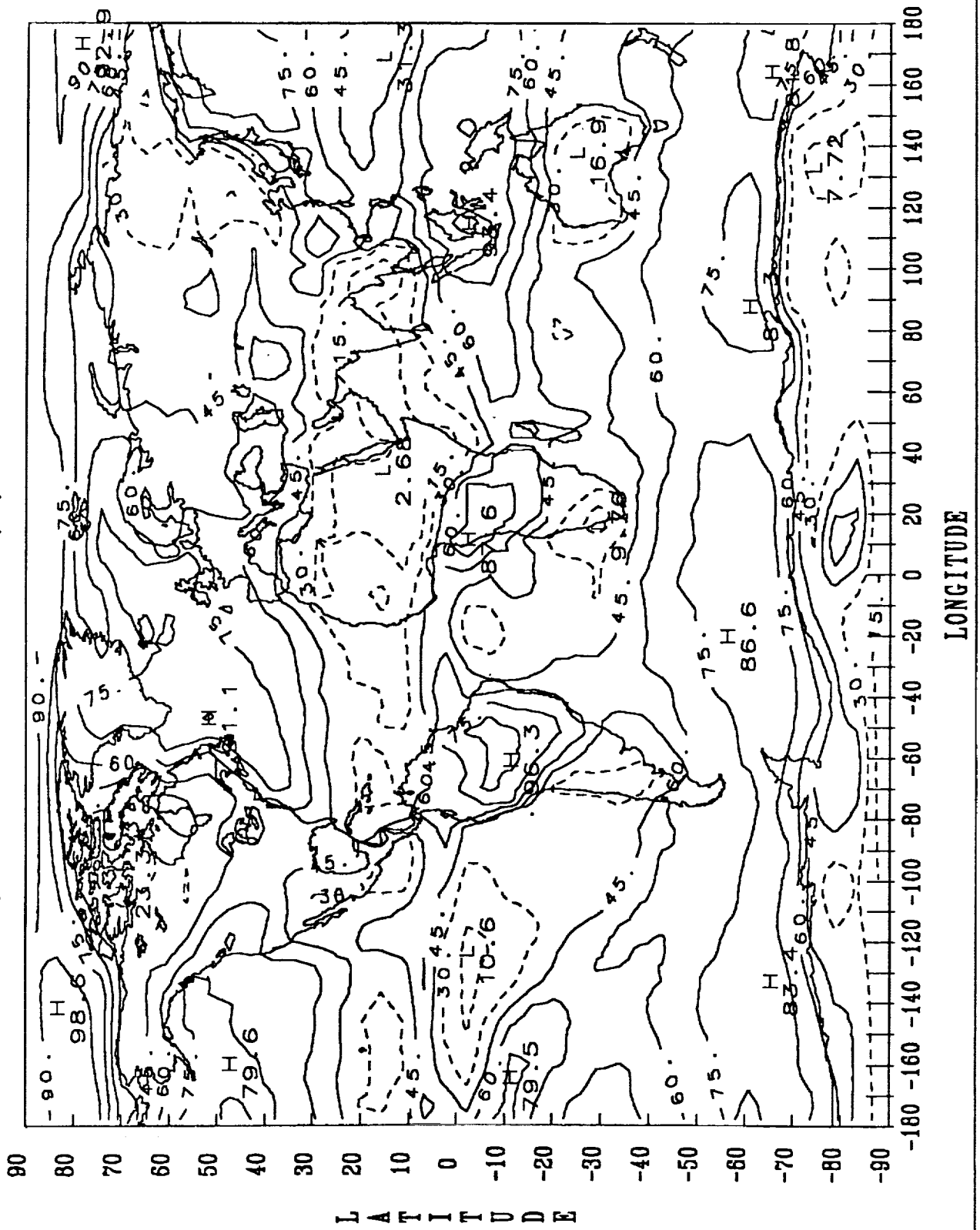
NIMBUS 7/TOTAL NOON CLOUD (%) JUN - AUG 1979



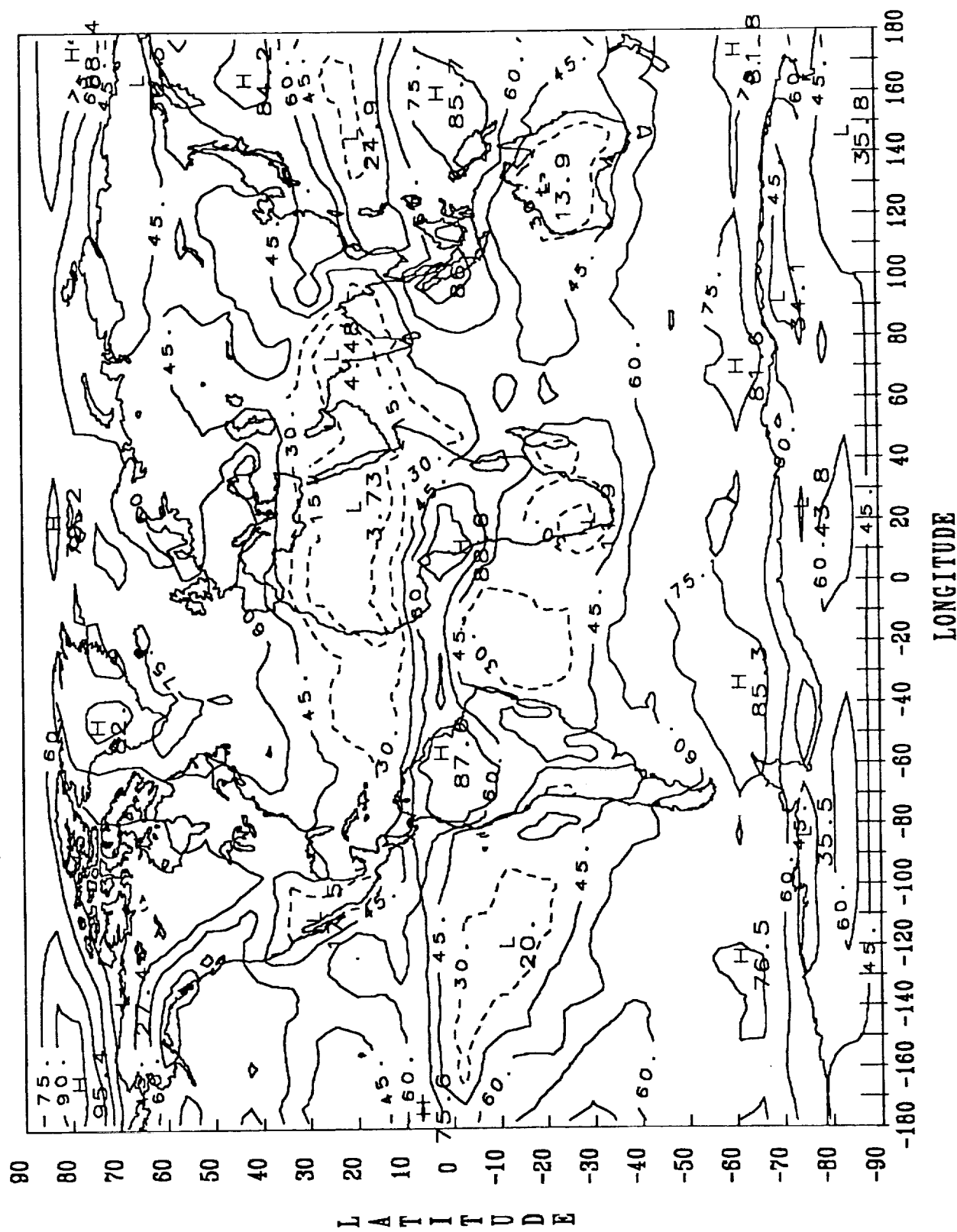
NIMBUS 7/TOTAL NOON CLOUD (%) SEP - NOV 1979



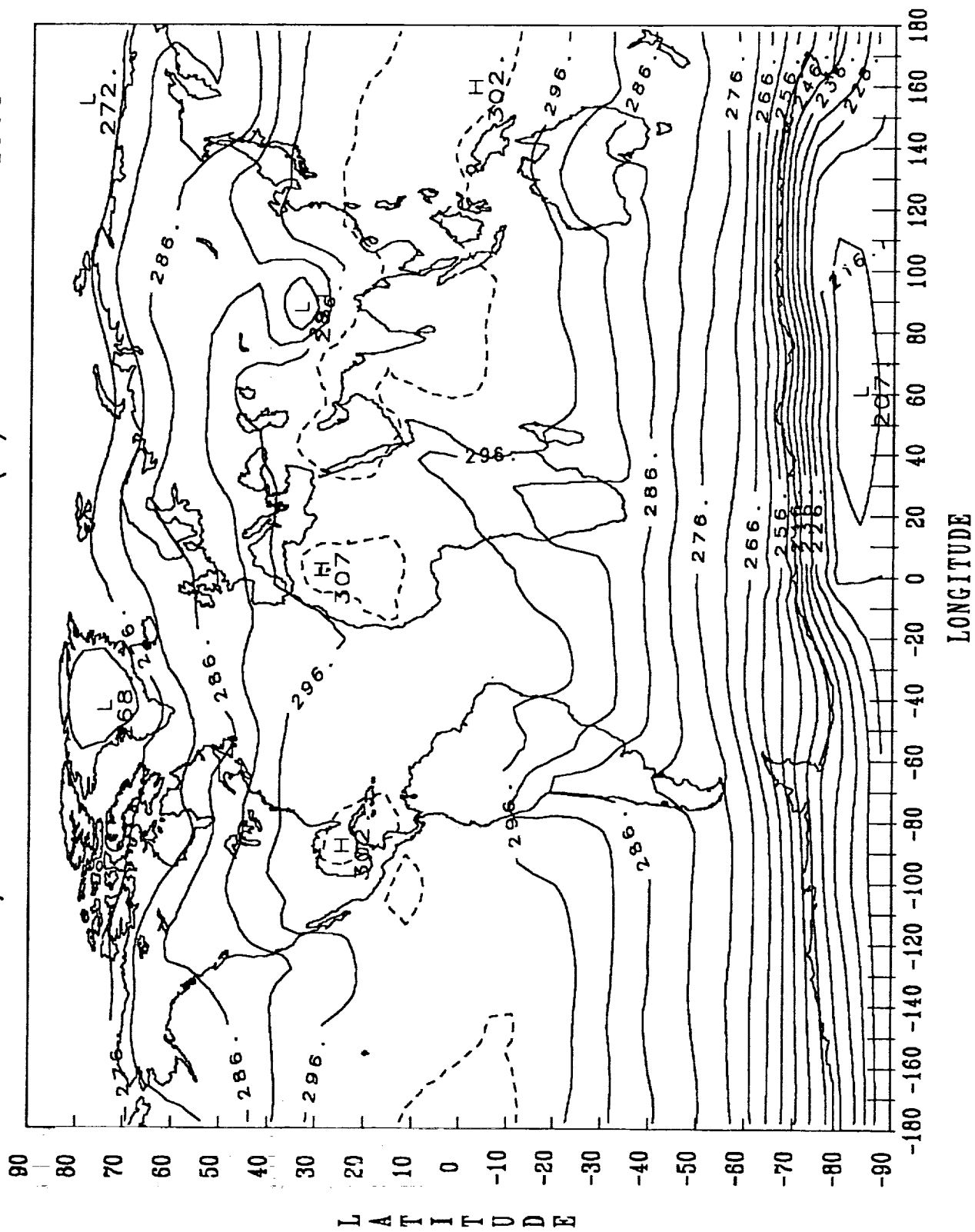
NIMBUS 7/TOTAL NOON CLOUD (%) DEC 1979 - FEB 1980



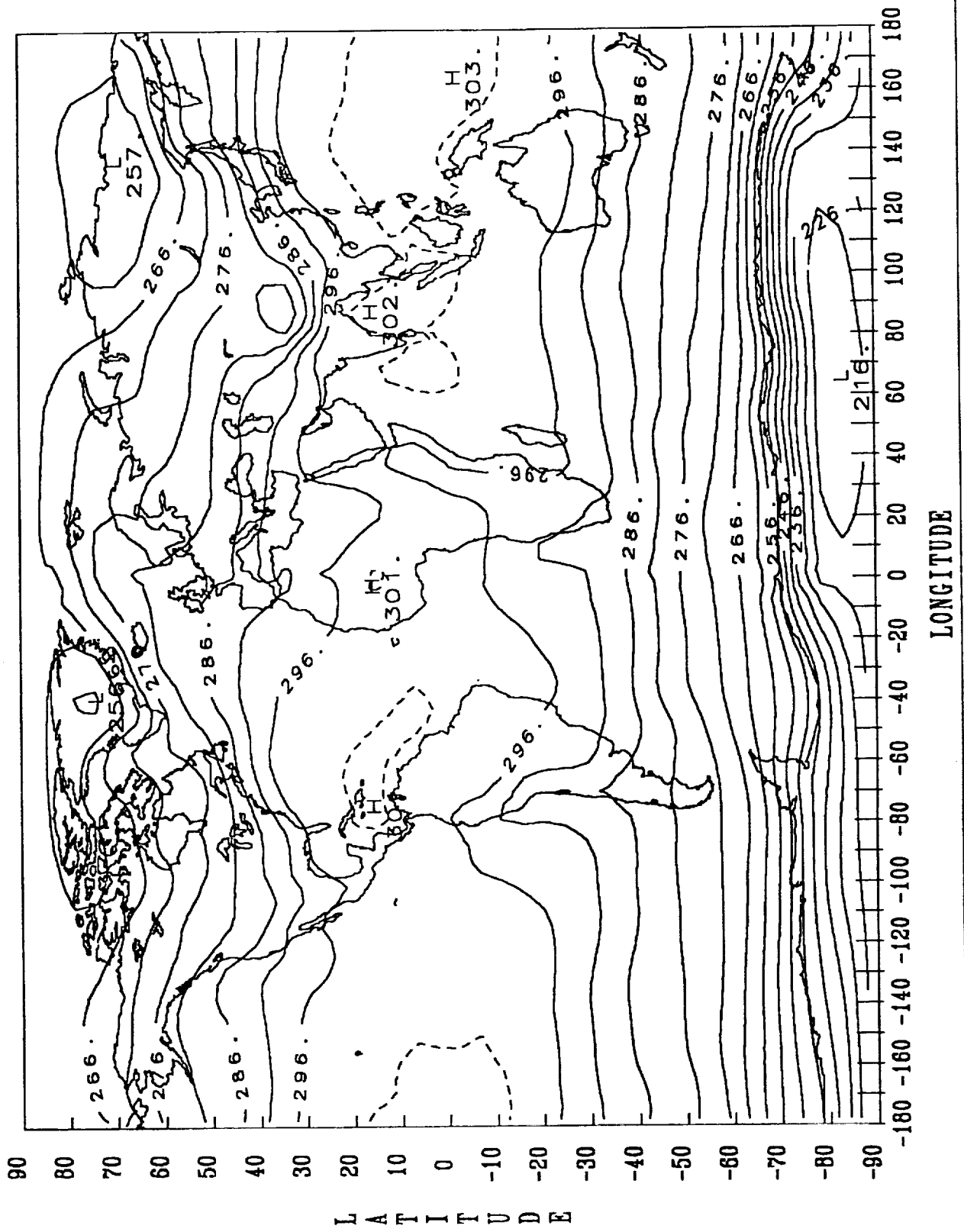
NIMBUS 7/TOTAL NOON CLOUD (%) MAR - MAY 1980



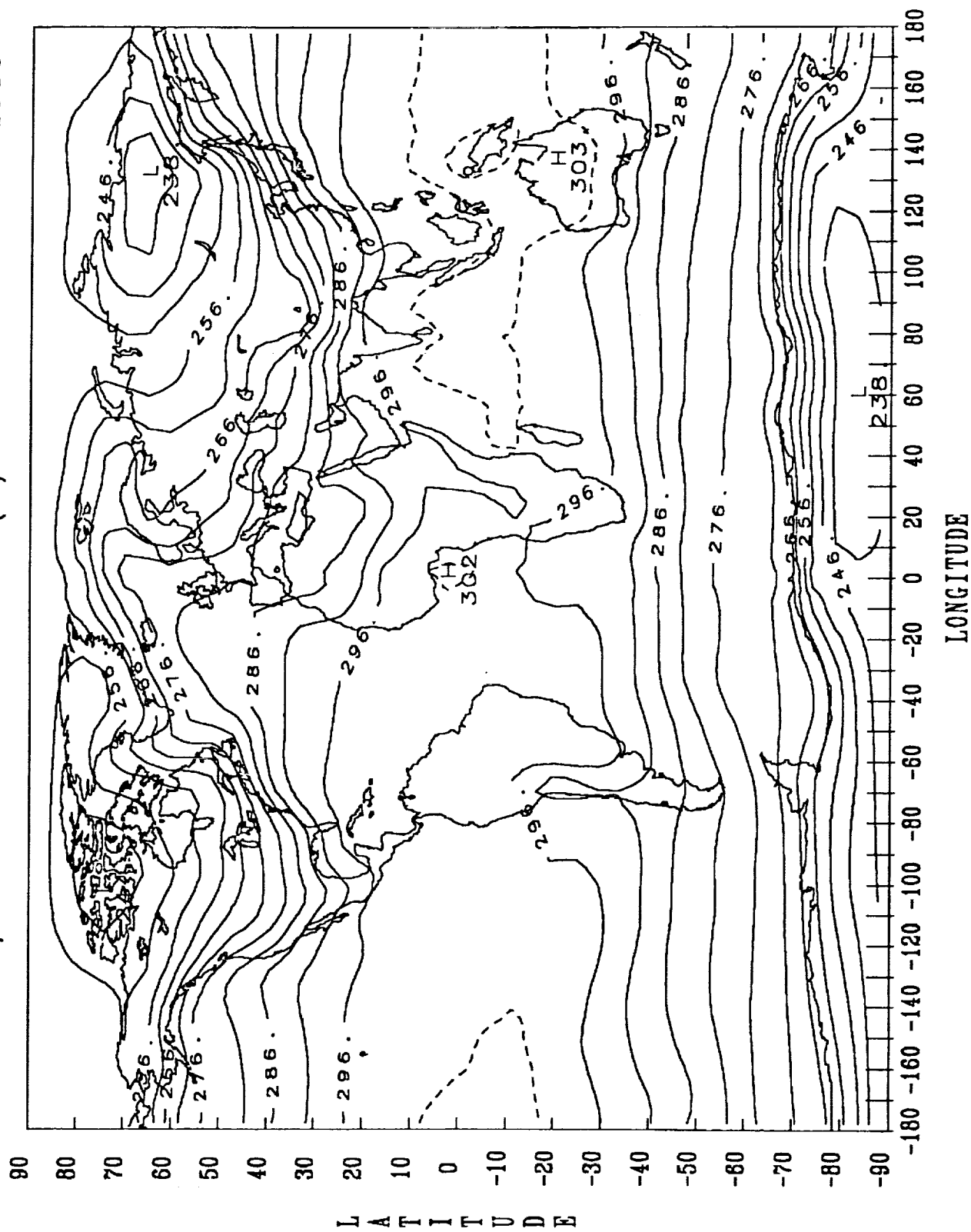
NIMBUS 7/SURFACE TEMPERATURE (K) JUNE - AUG 1979



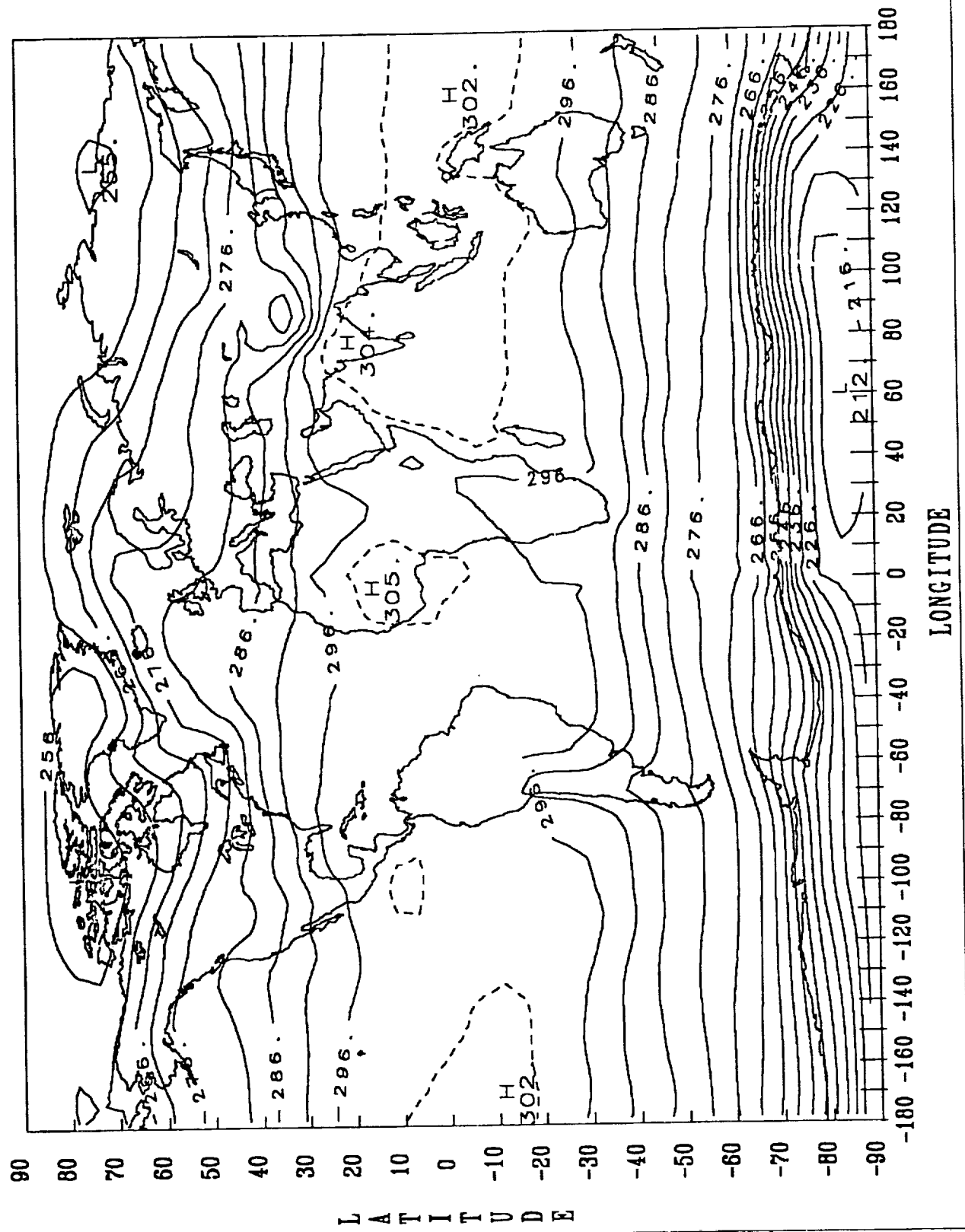
NIMBUS 7/SURFACE TEMPERATURE (K) SEP - NOV 1979



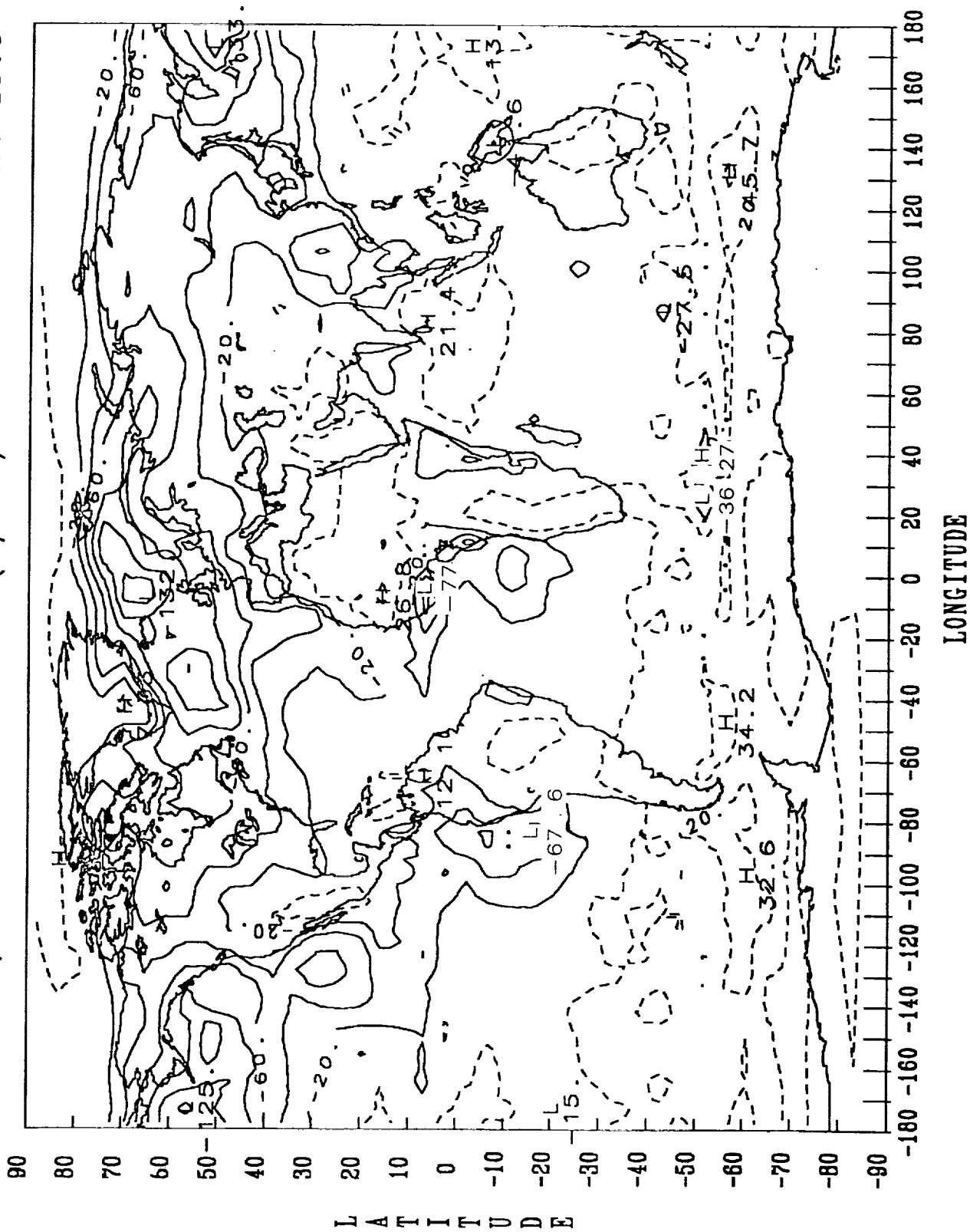
NIMBUS 7/SURFACE TEMPERATURE (K) DEC 1979 - FEB 1980



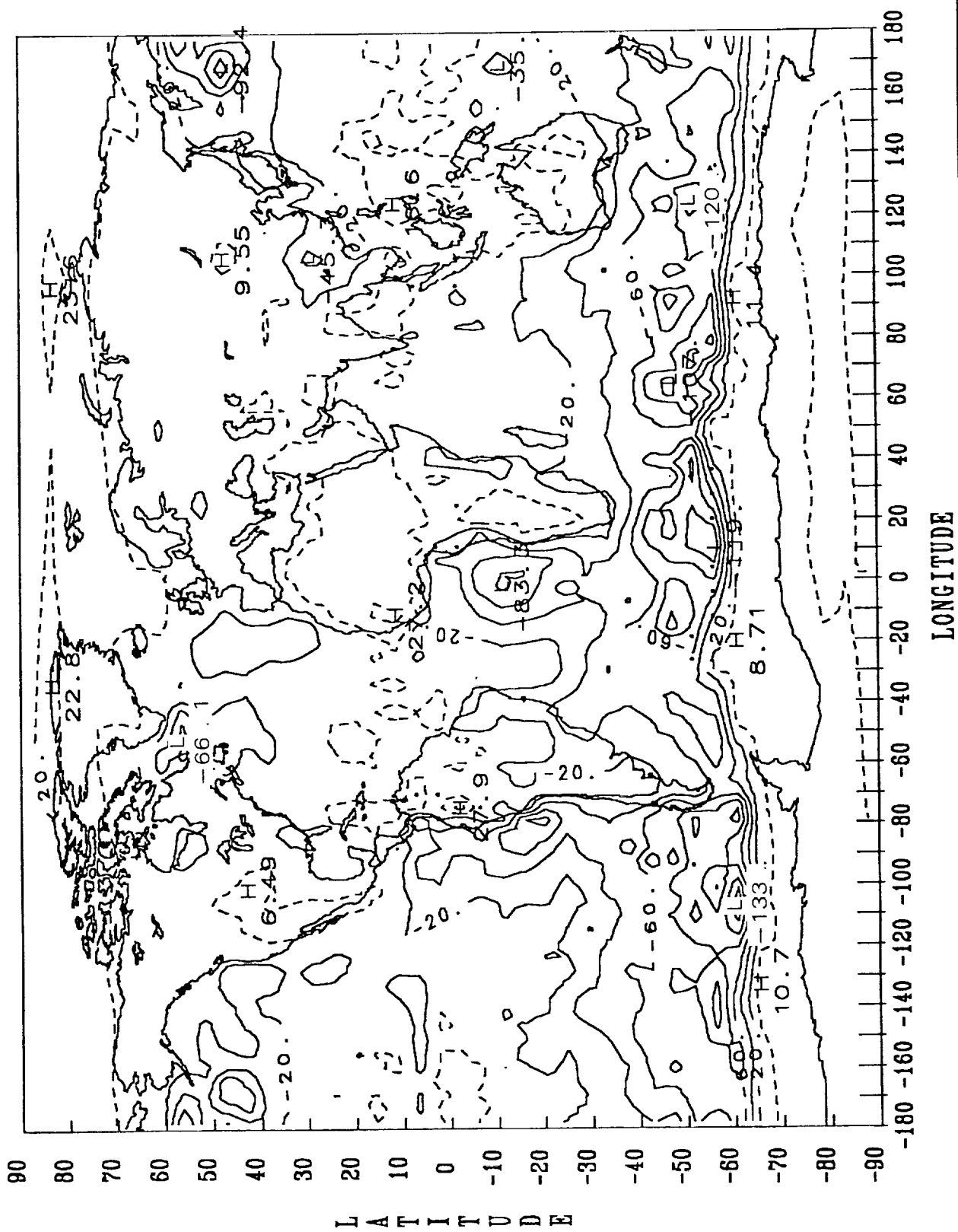
NIMBUS 7/SURFACE TEMPERATURE (K) MAR - MAY 1980



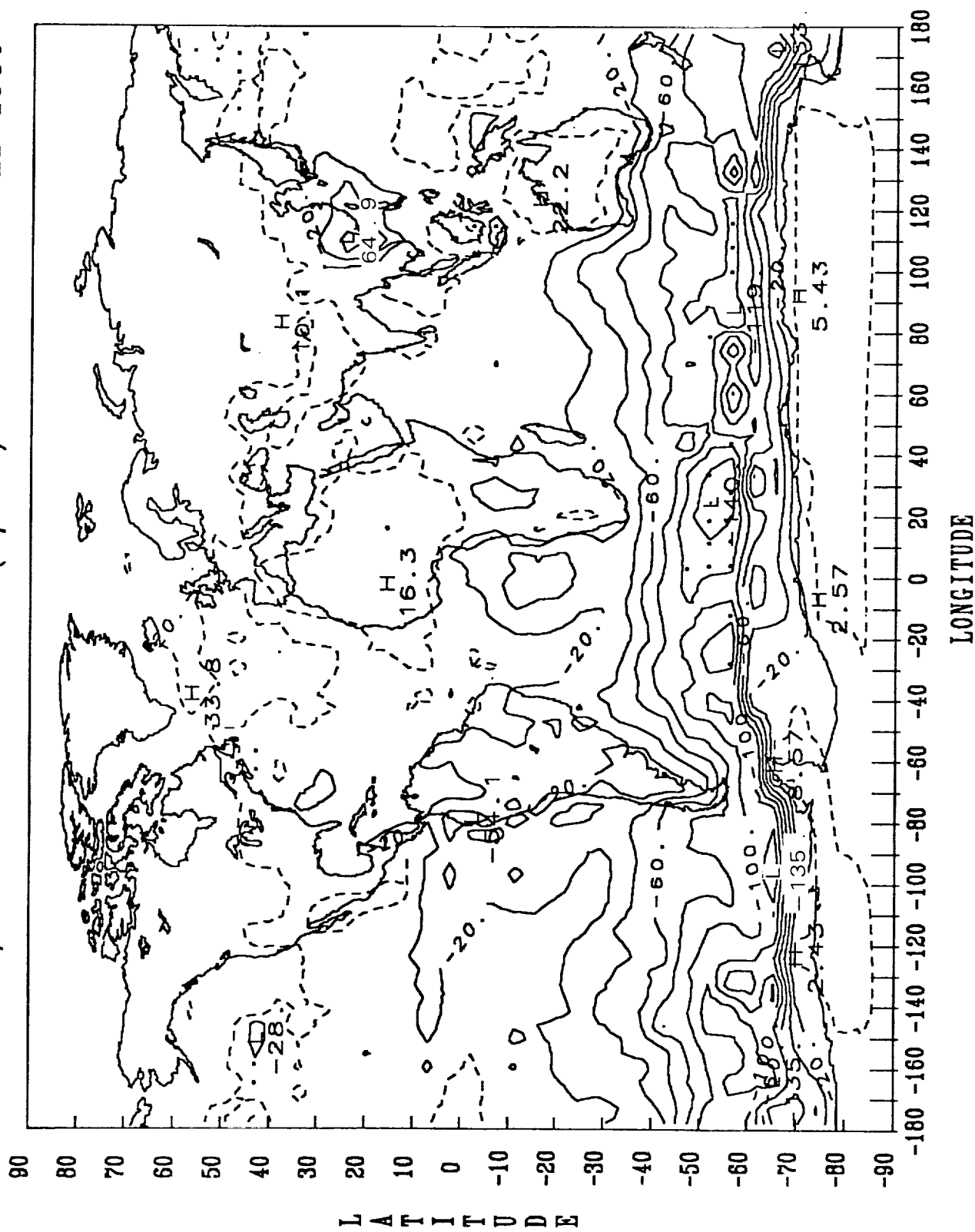
NIMBUS 7/NET CLOUD FORCING (W/M-M) JUNE 1979 - AUG 1979



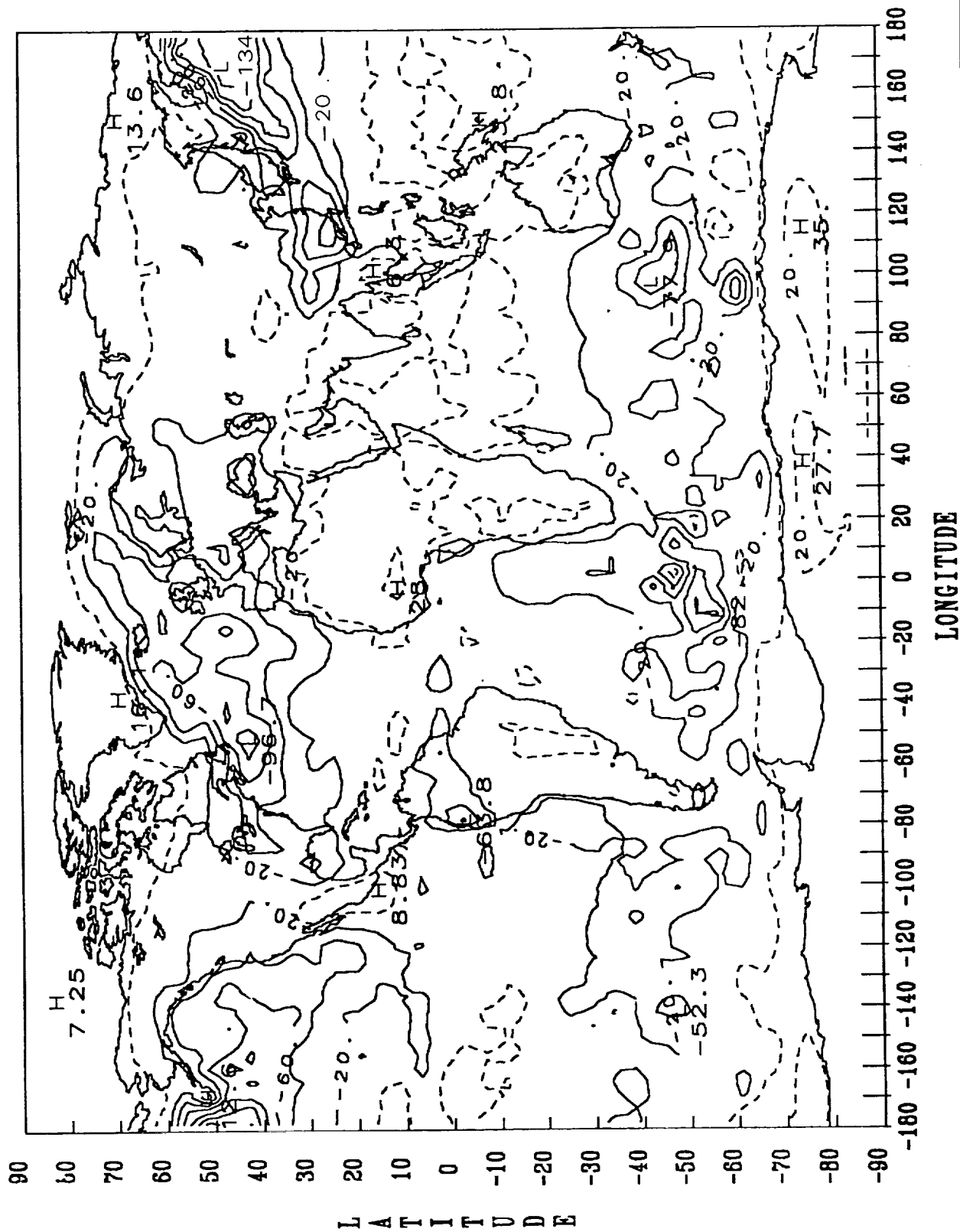
NIMBUS 7/NET CLOUD FORCING (W/M-M) SEP - NOV 1979



NIMBUS 7/NET CLOUD FORCING (W/M-M) DEC 1979 - FEB 1980



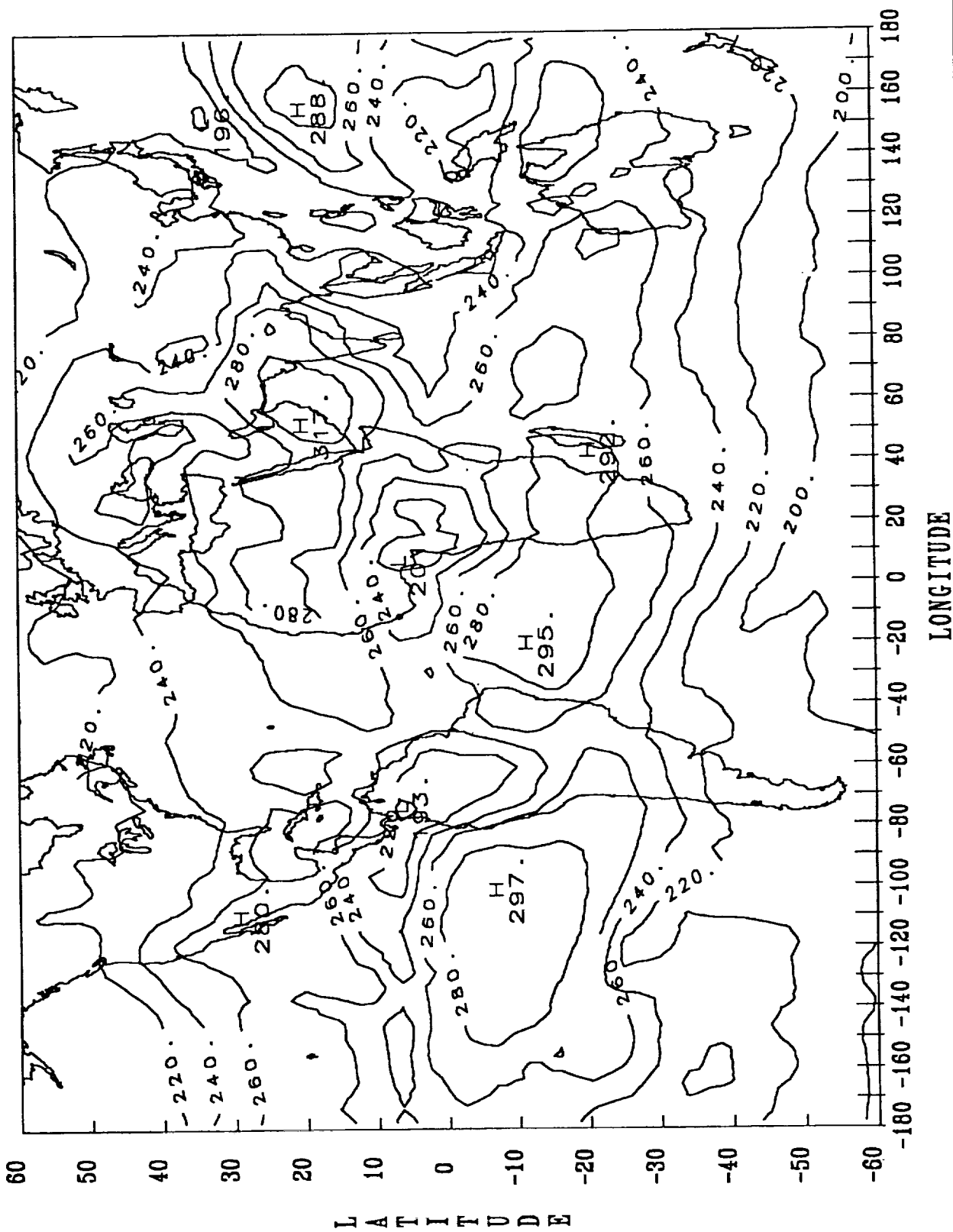
NIMBUS 7/NET CLOUD FORCING (W/M-M) MAR 1980 - MAY 1980



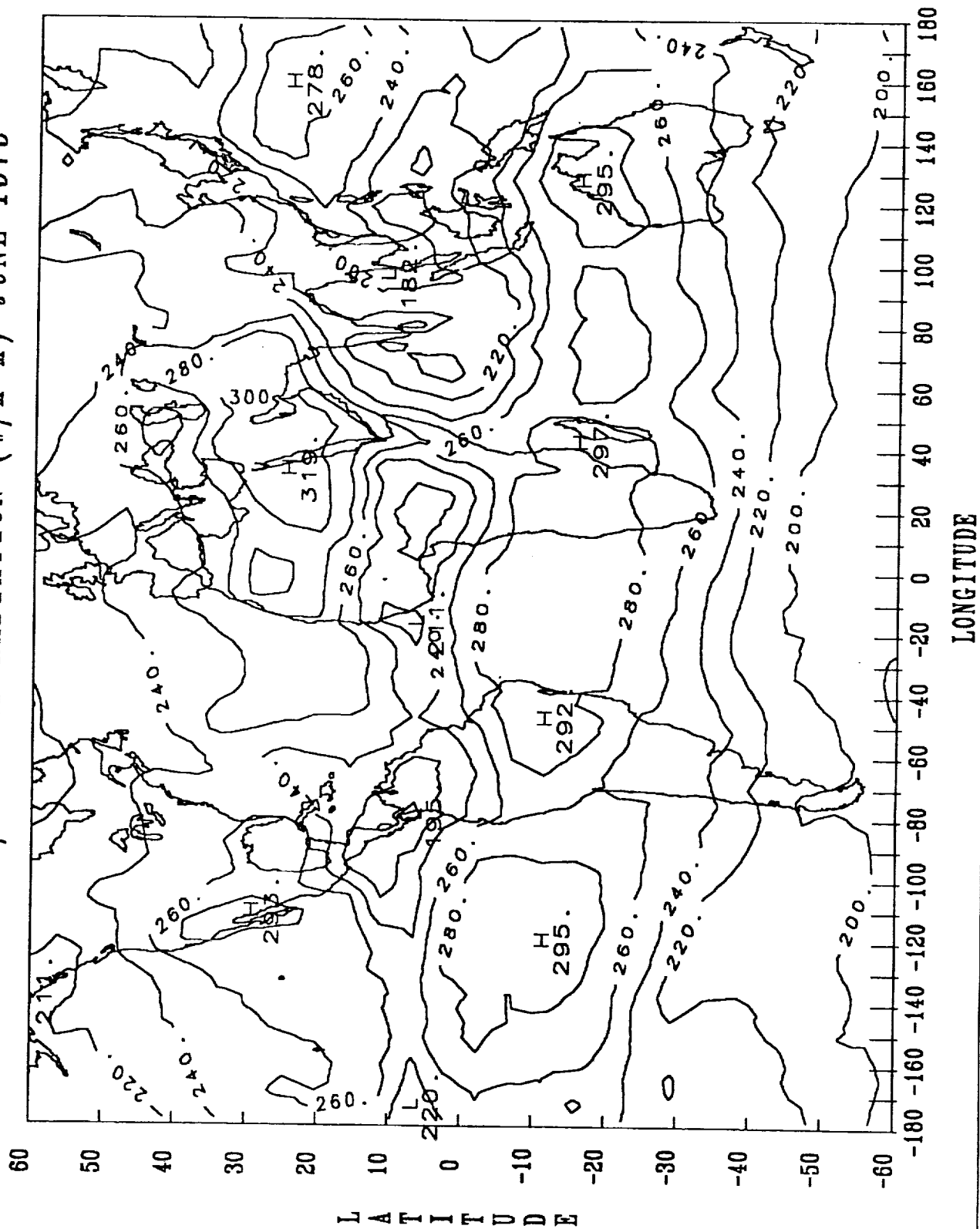
8. MONTHLY MAPS FOR THE PERIOD FROM MAY 1979 TO MAY 1980

MONTHLY MAPS		
The maps are arranged by parameter and then by month (May 1979 to May 1980). These maps include the region 60°S to 60°N latitude only.		
PARAMETER	CONTOUR STEP SIZE	PAGE
Diurnal OLR	20 W/m ²	55
Noon-Midnight OLR Difference	16 W/m ² (negative values dashed)	68
Diurnal Albedo	10% (20% or below dashed)	81
Net Radiation	30 W/m ² (negative values dashed)	94
Noon Cloud Cover	15% (30% or below dashed)	107
Average (Noon and Midnight) Surface Temperature	5°K (values of 301°K or larger dashed)	120

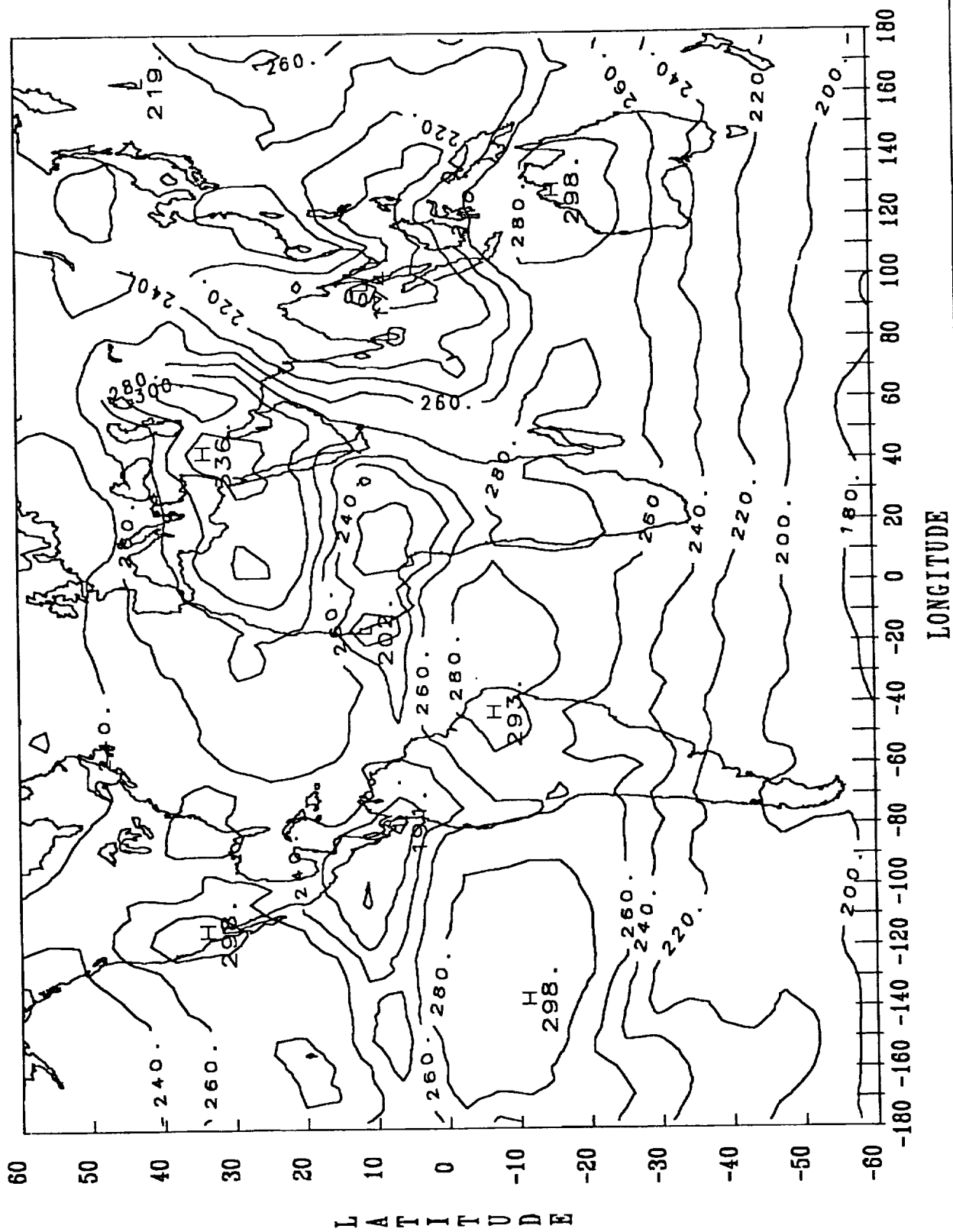
NIMBUS 7/EMITTED RADIATION (W/M* μ M) MAY 1979



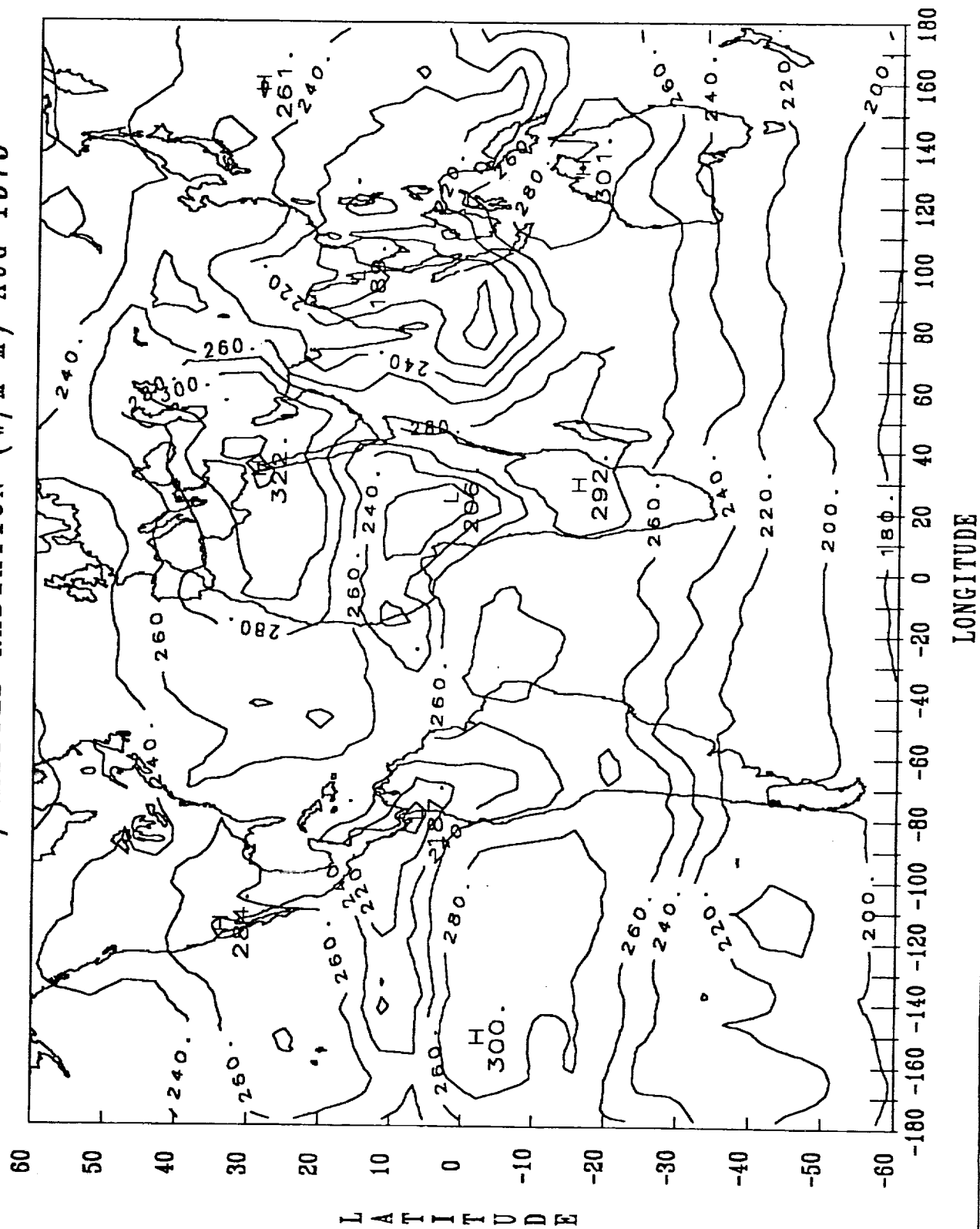
NIMBUS 7/EMITTED RADIATION (W/M*²M) JUNE 1979



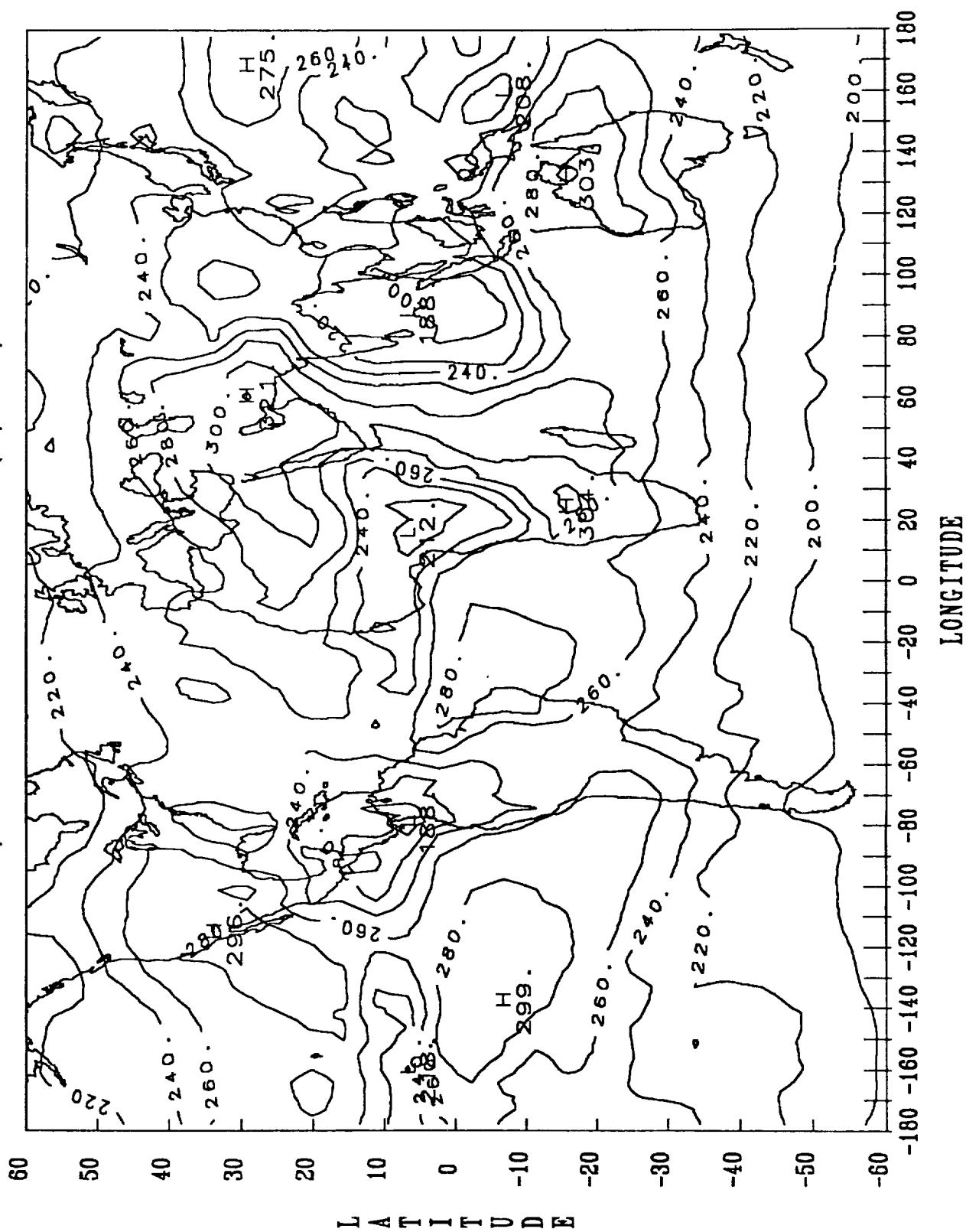
NIMBUS 7/EMITTED RADIATION (W/M* μ M) JULY 1979



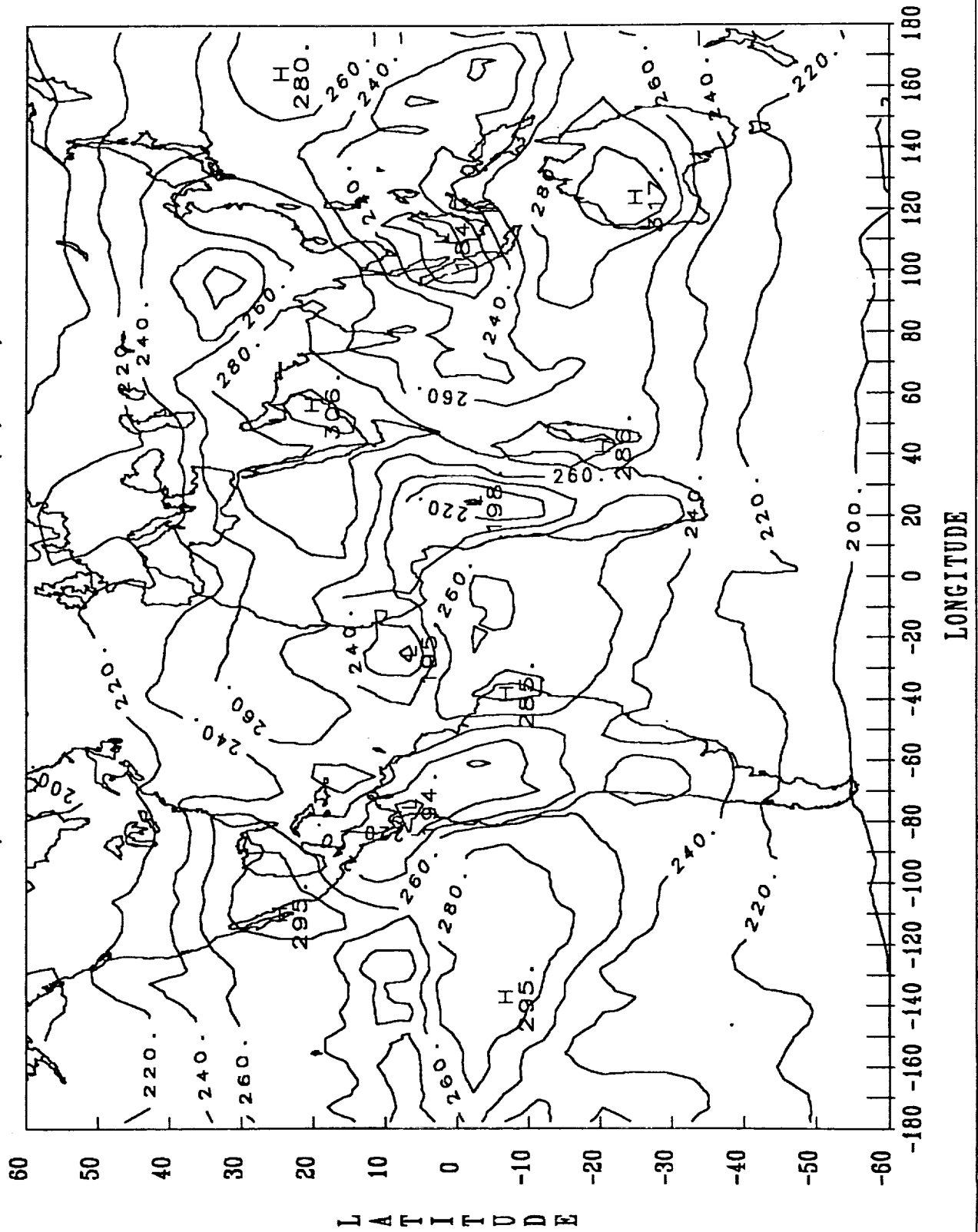
NIMBUS 7/EMITTED RADIATION (W/M*²M) AUG 1979



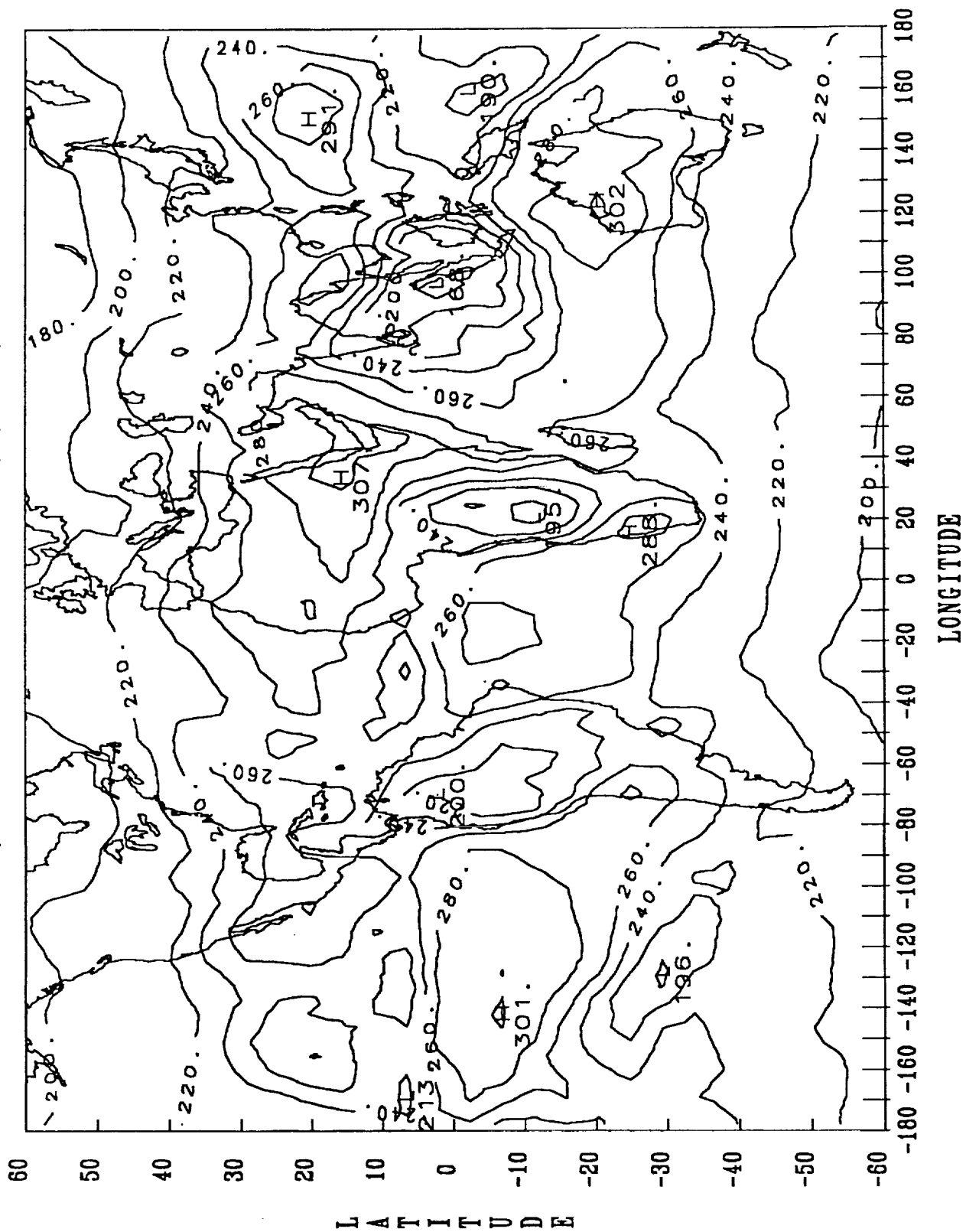
NIMBUS 7/EMITTED RADIATION (W/M*²M) SEP 1979



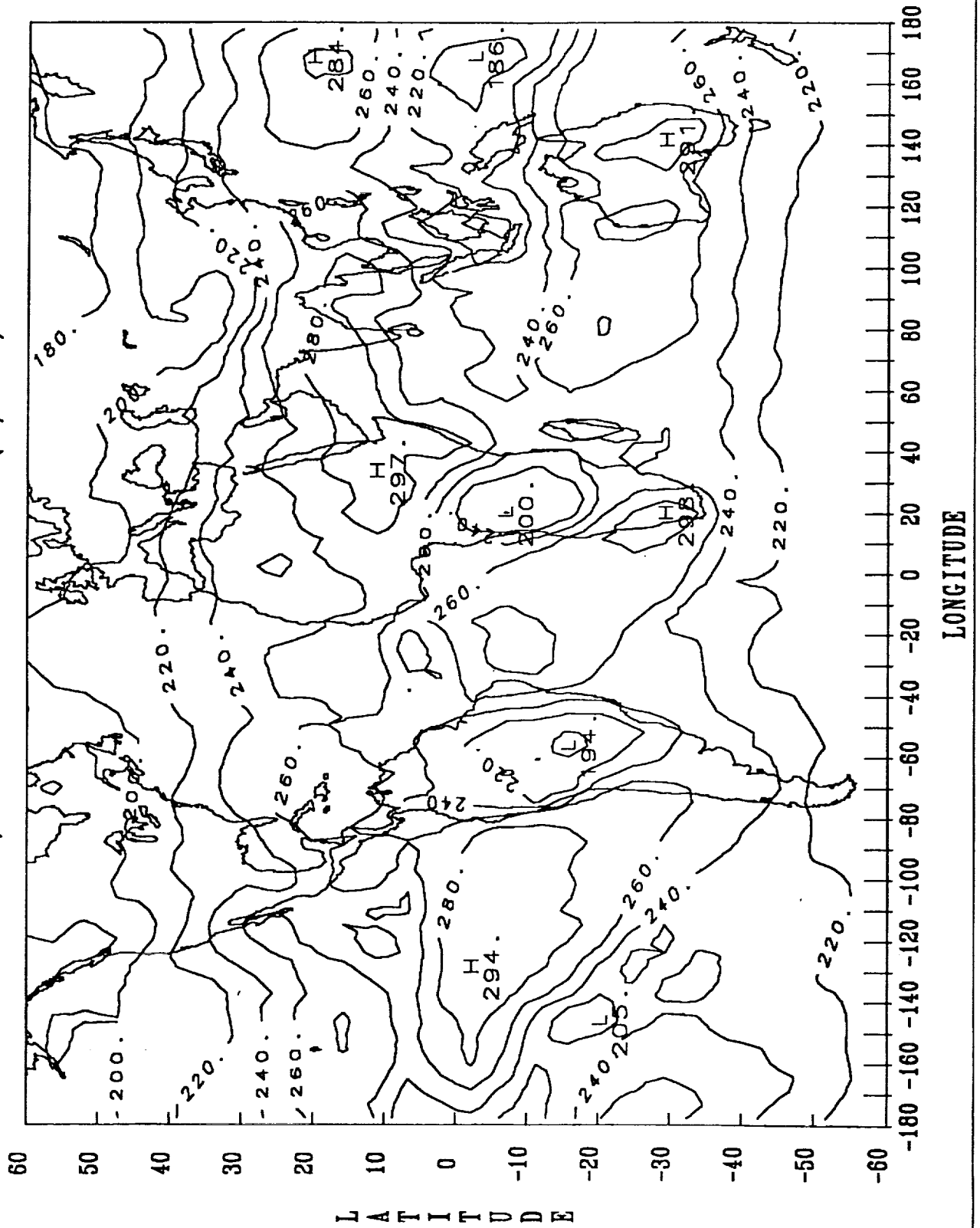
NIMBUS 7/EMITTED RADIATION (W/M*H) OCT 1979



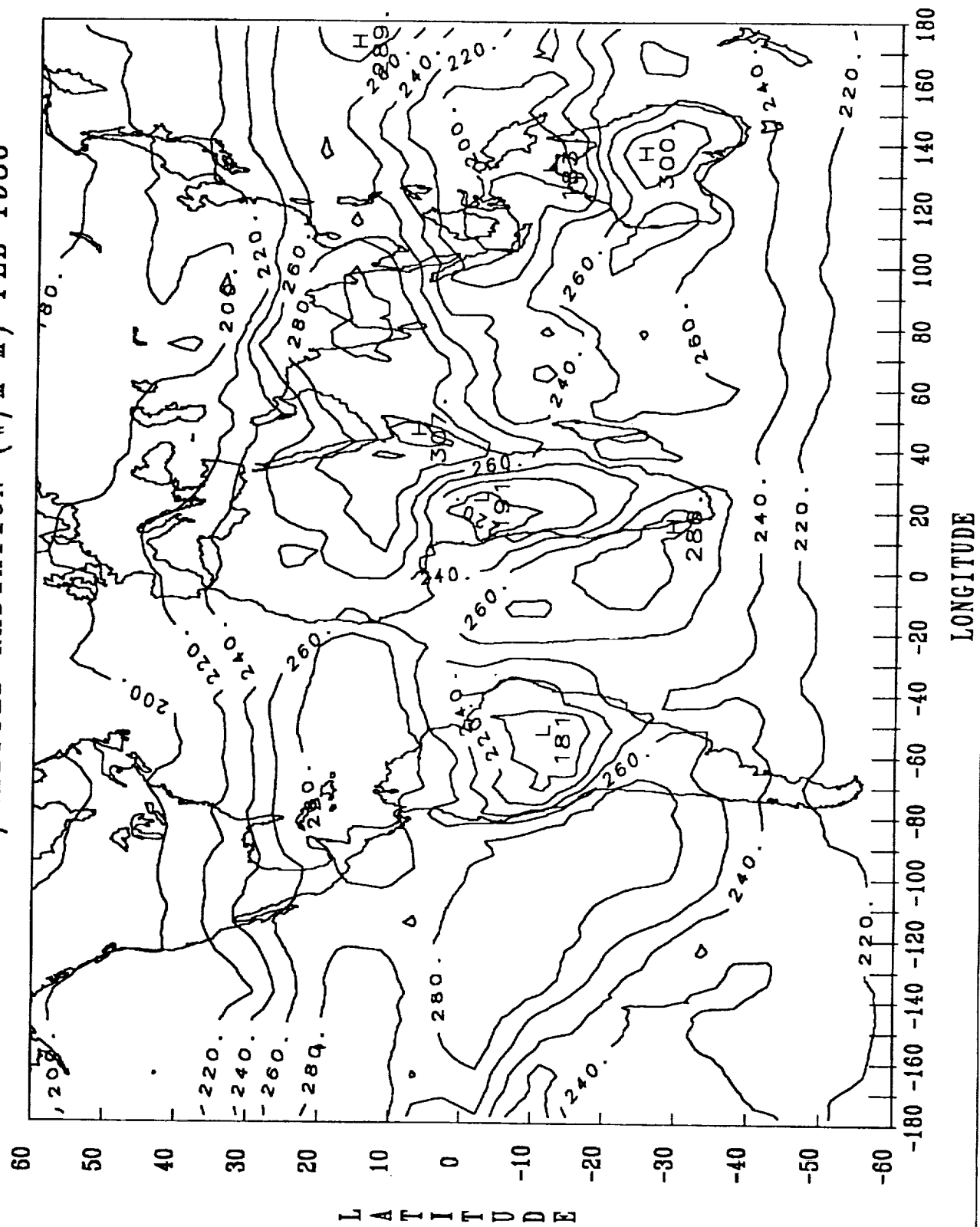
NIMBUS 7/EMITTED RADIATION (W/M²M) NOV 1979



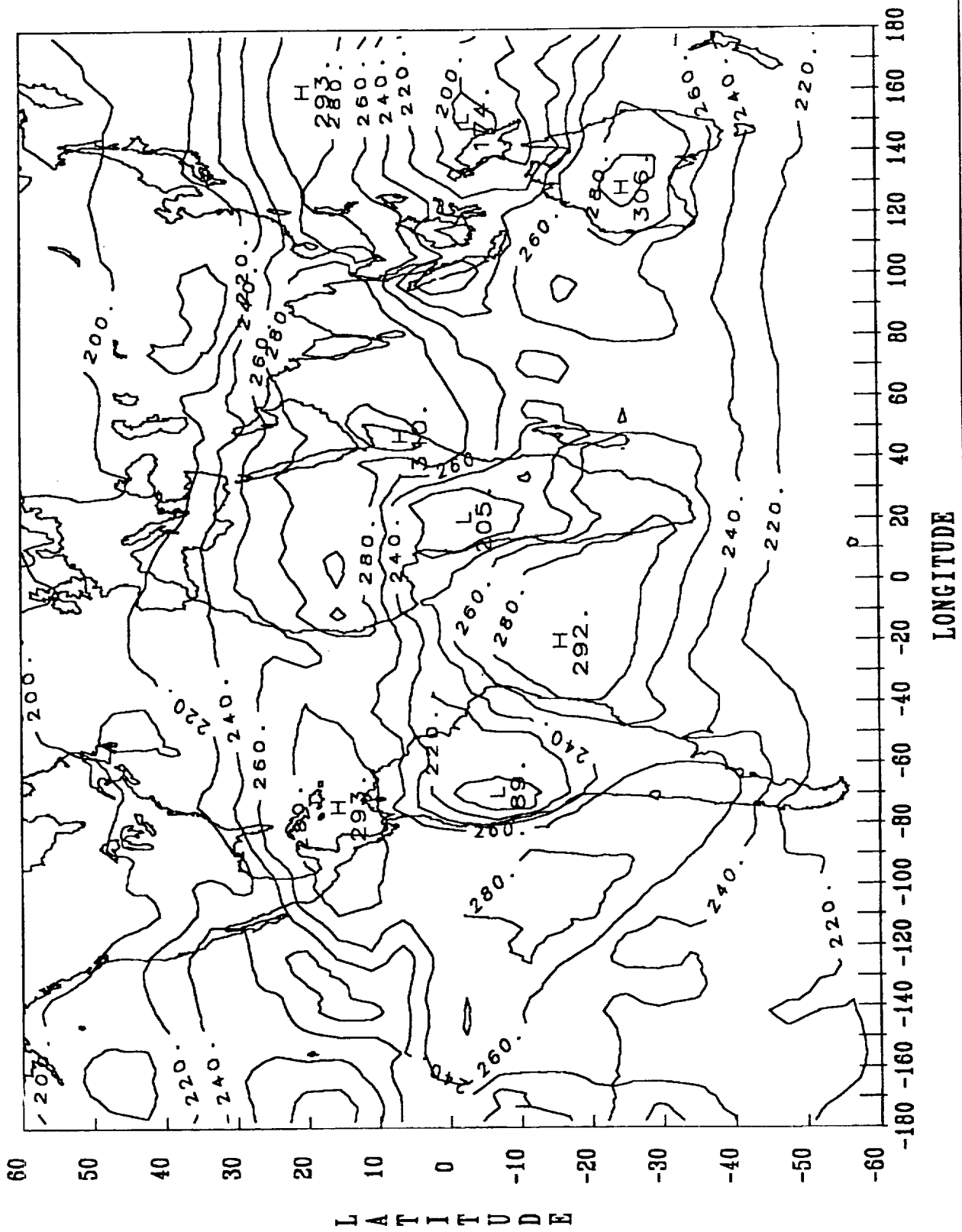
NIMBUS 7/EMITTED RADIATION (W/M²M) DEC 1979



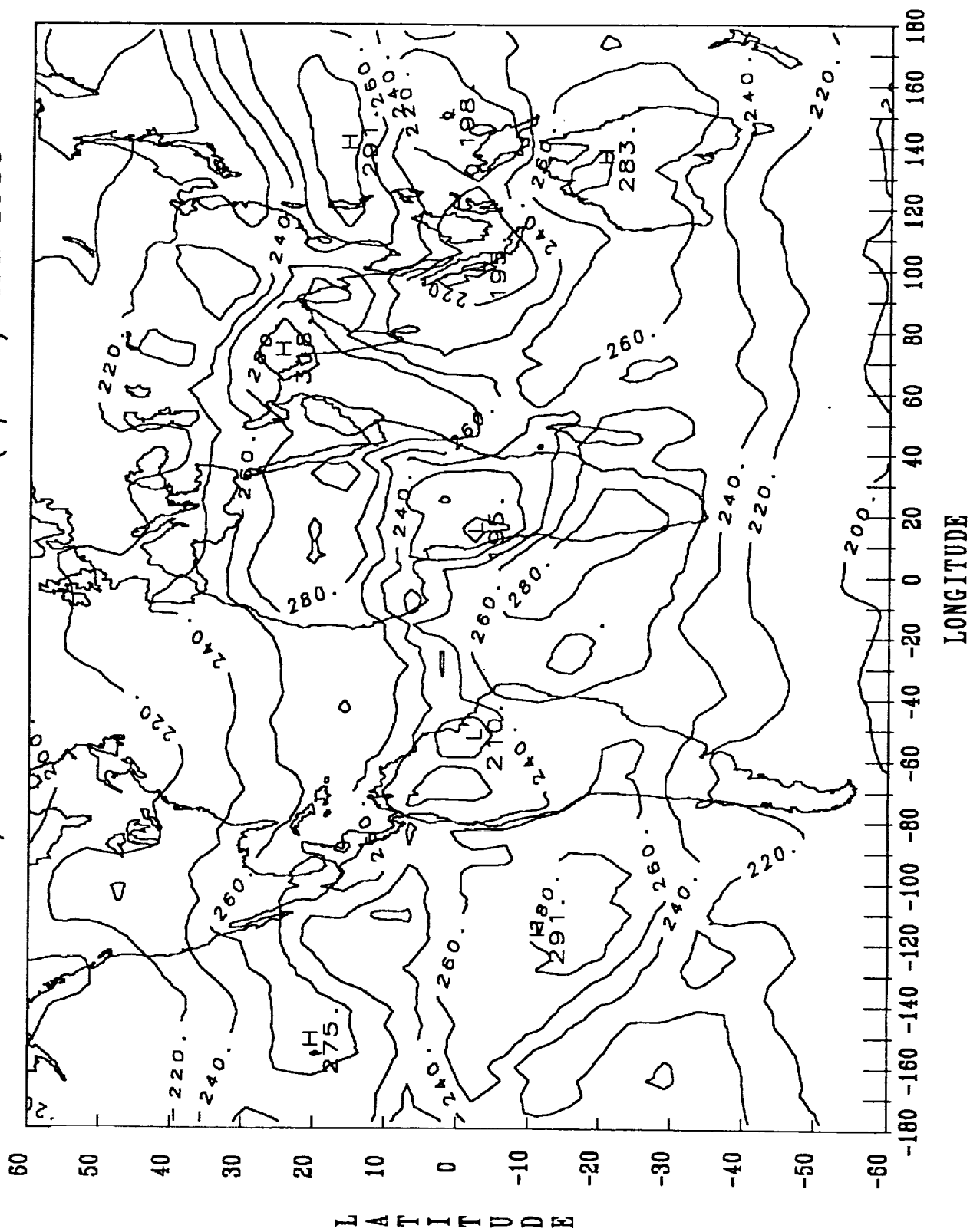
NIMBUS 7/EMITTED RADIATION (W/M* μ M) FEB 1980



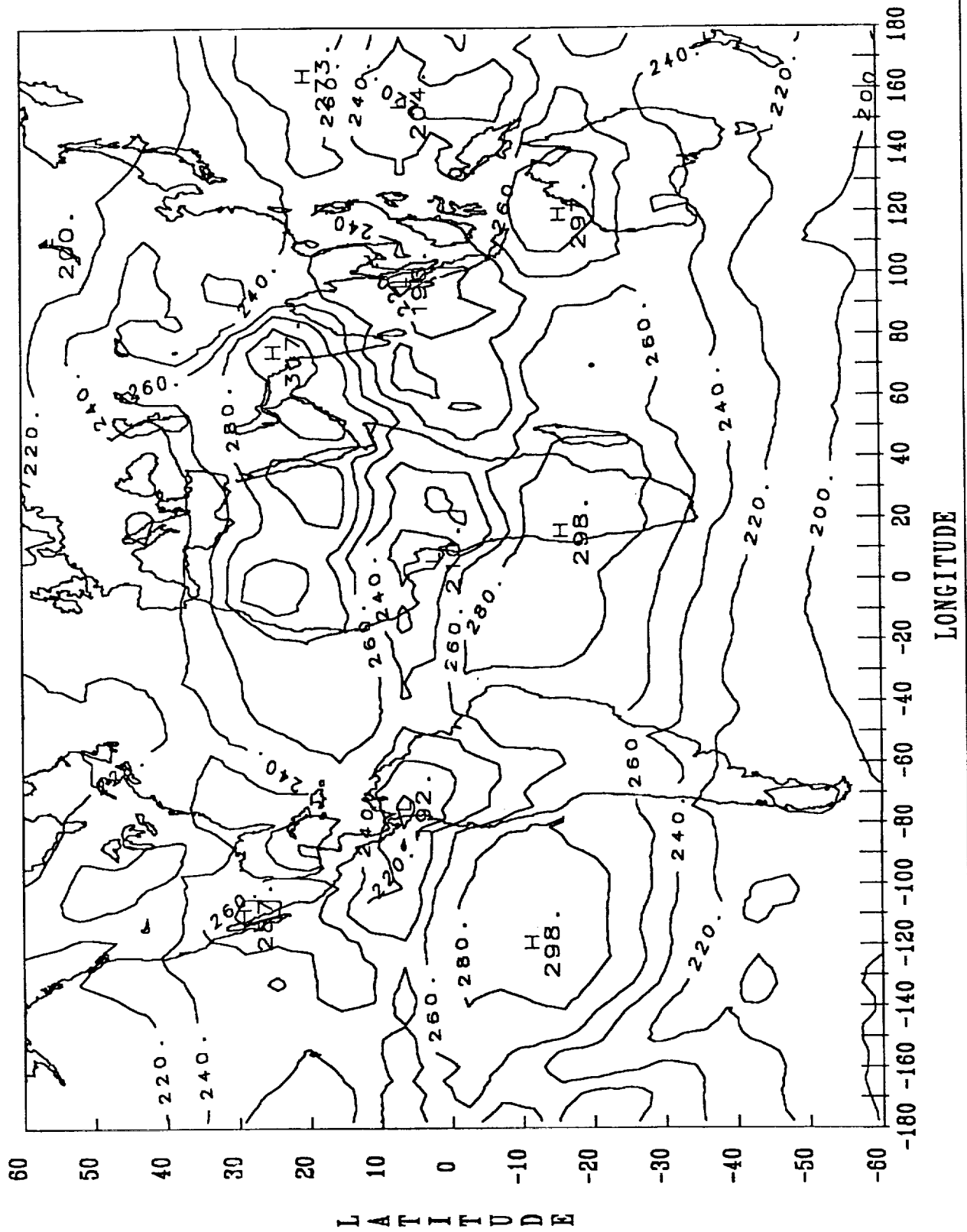
NIMBUS 7/EMITTED RADIATION (W/M²M) MAR 1980



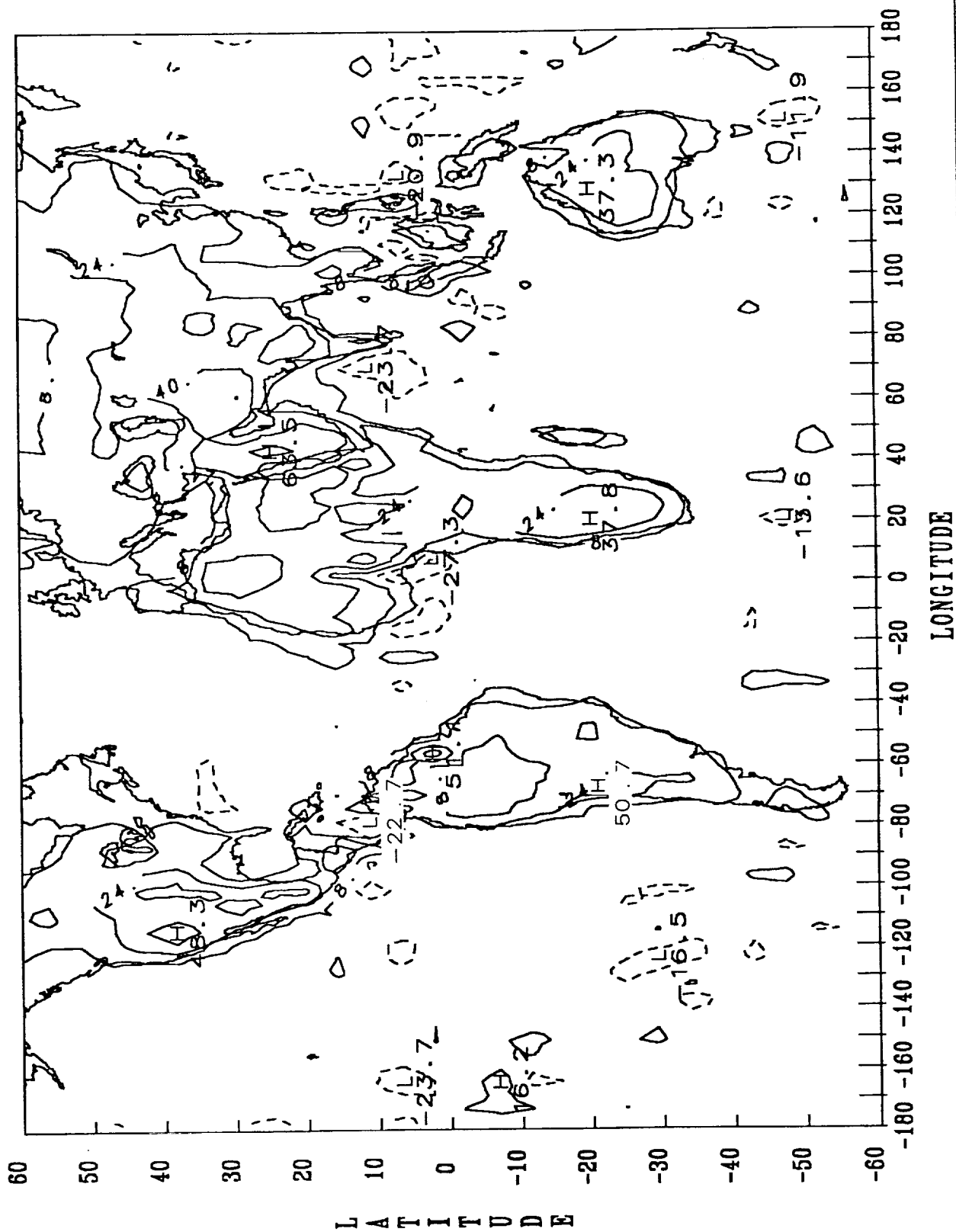
NIMBUS 7/EMITTED RADIATION (W/M*W) APR 1980



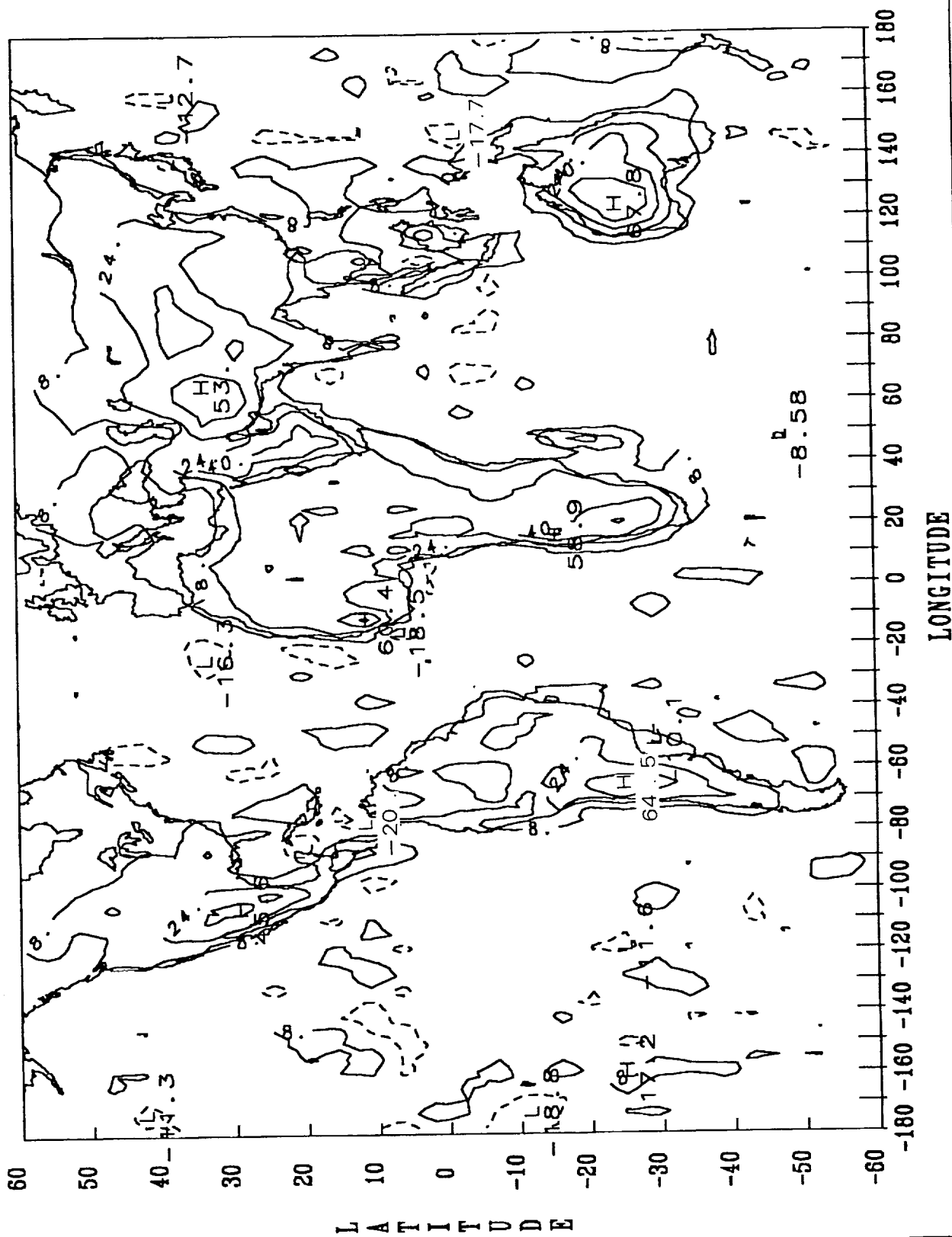
NIMBUS 7/EMITTED RADIATION (W/M* μ M) MAY 1980



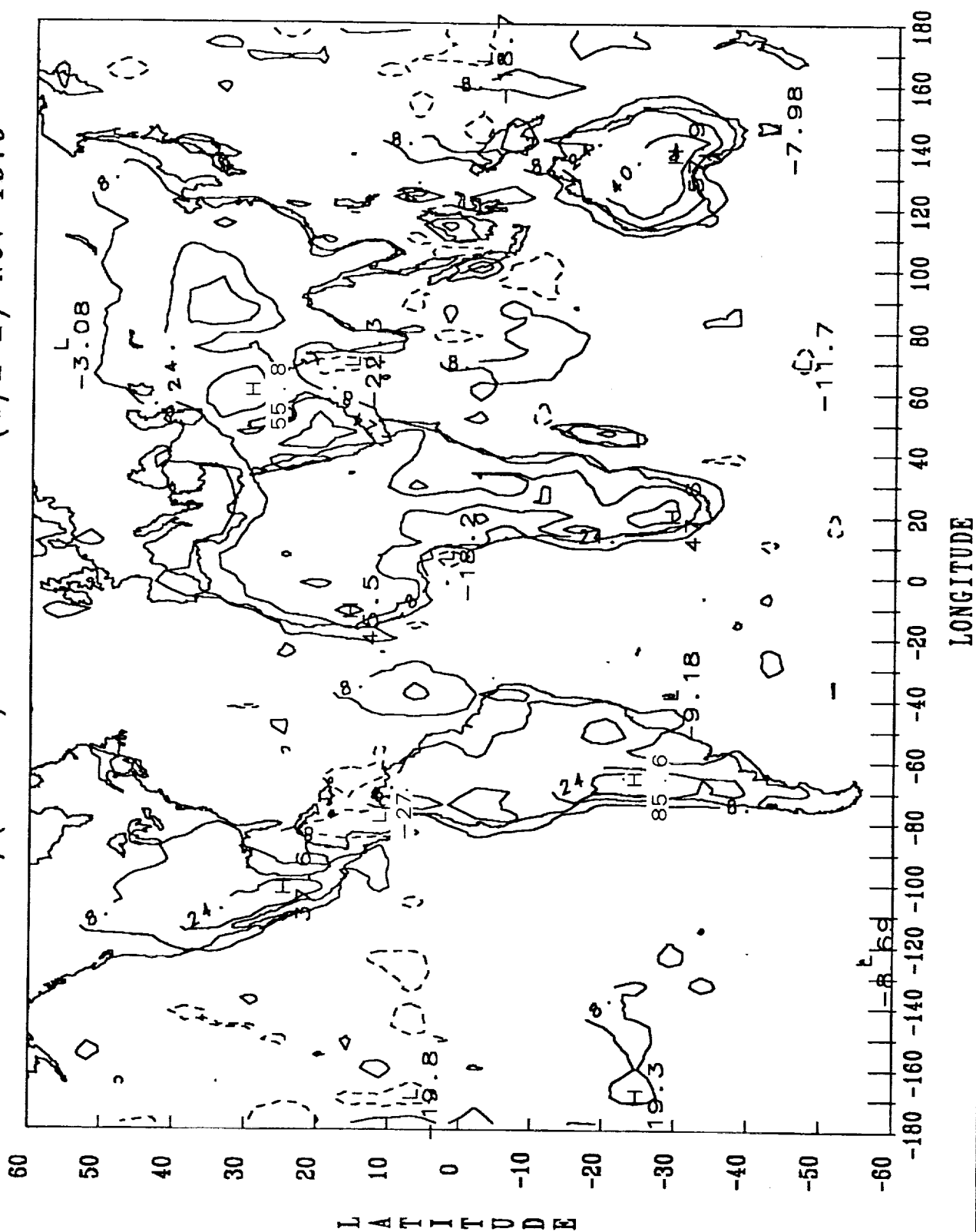
NIMBUS 7/(AN-DN) EMITTED DIF (W/M-M) JUNE 1979



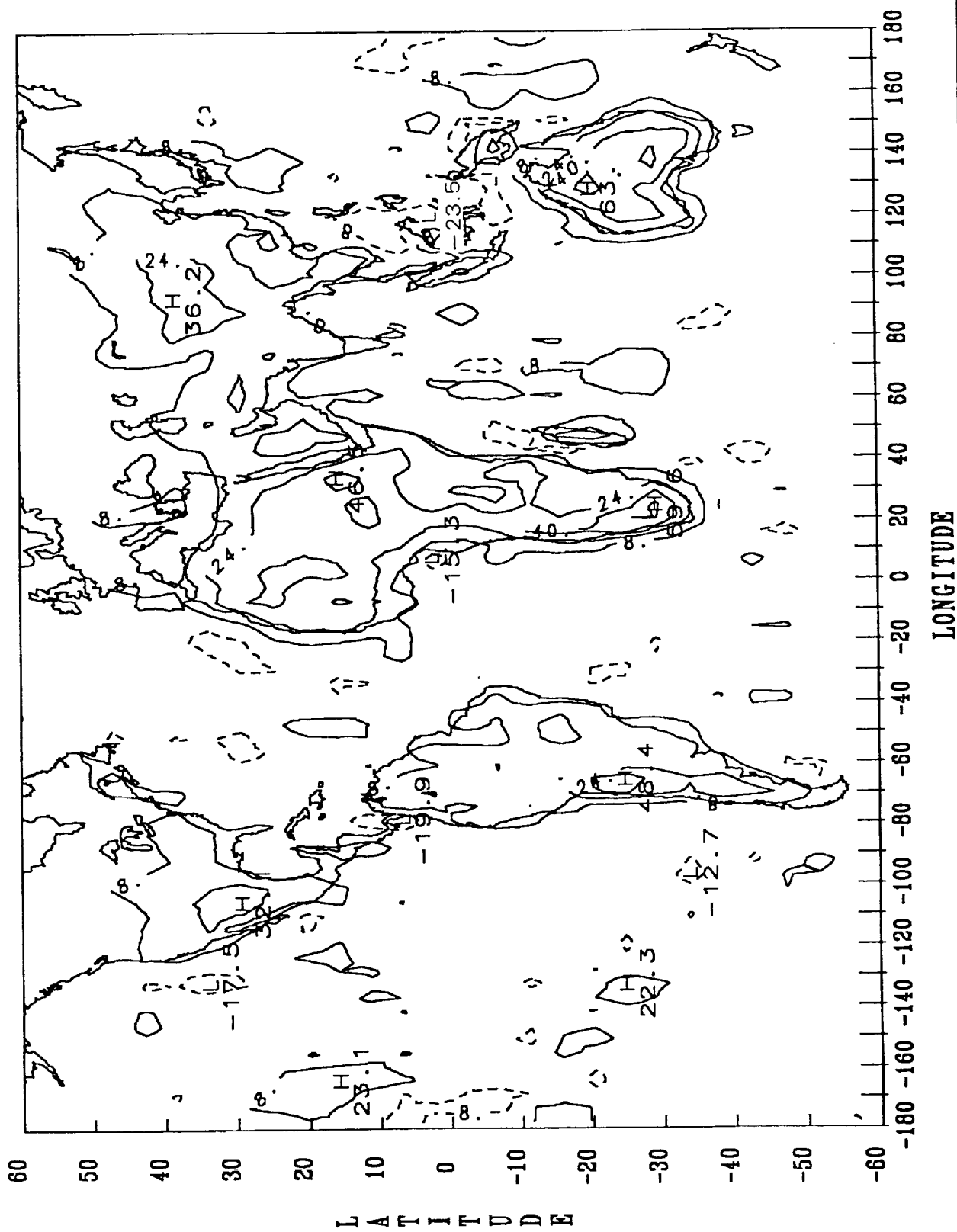
NIMBUS 7/(AN-DN) EMITTED DIF (W/M-M) OCT 1979



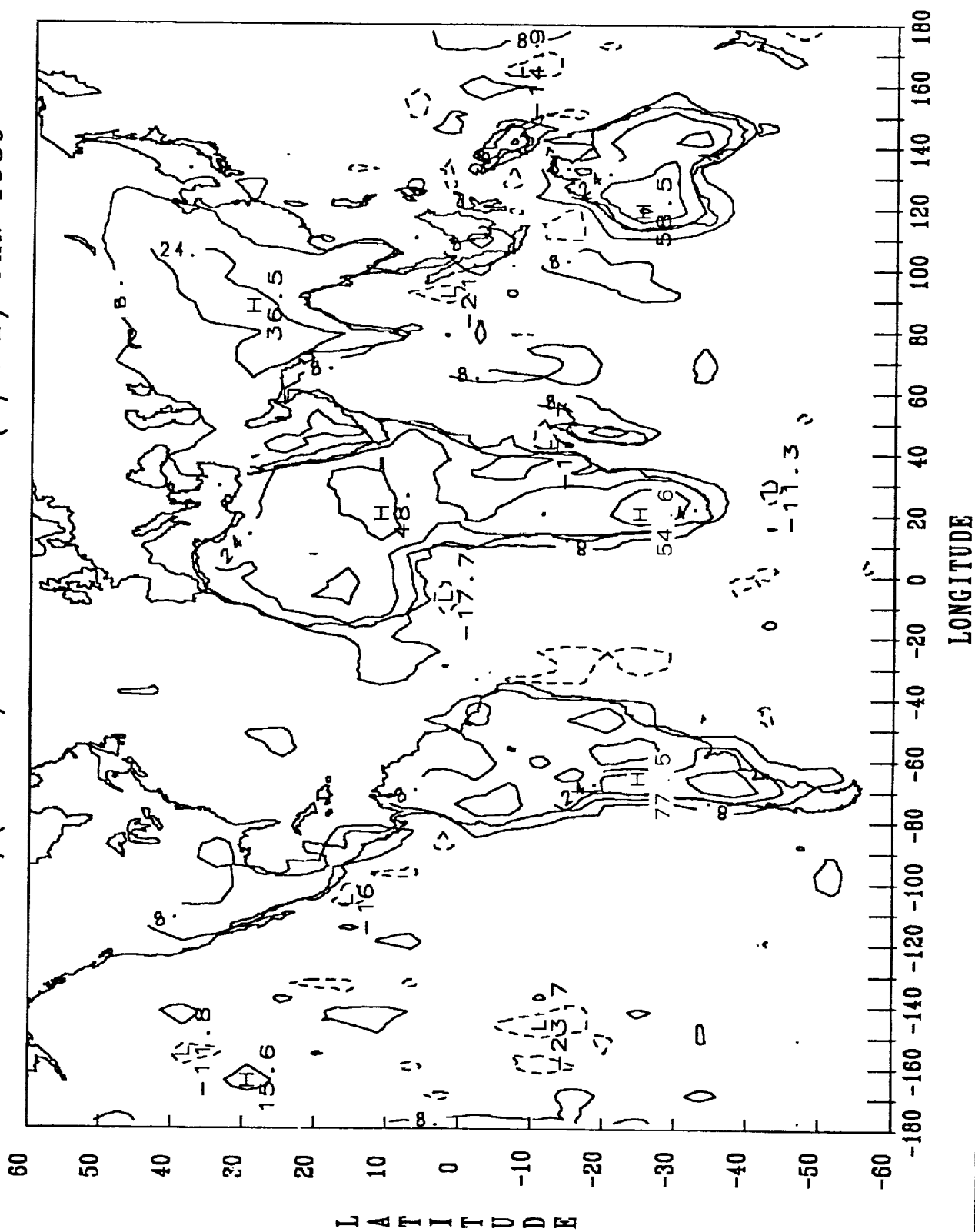
NIMBUS 7/(AN-DN) EMITTED DIF (W/M-M) NOV 1979



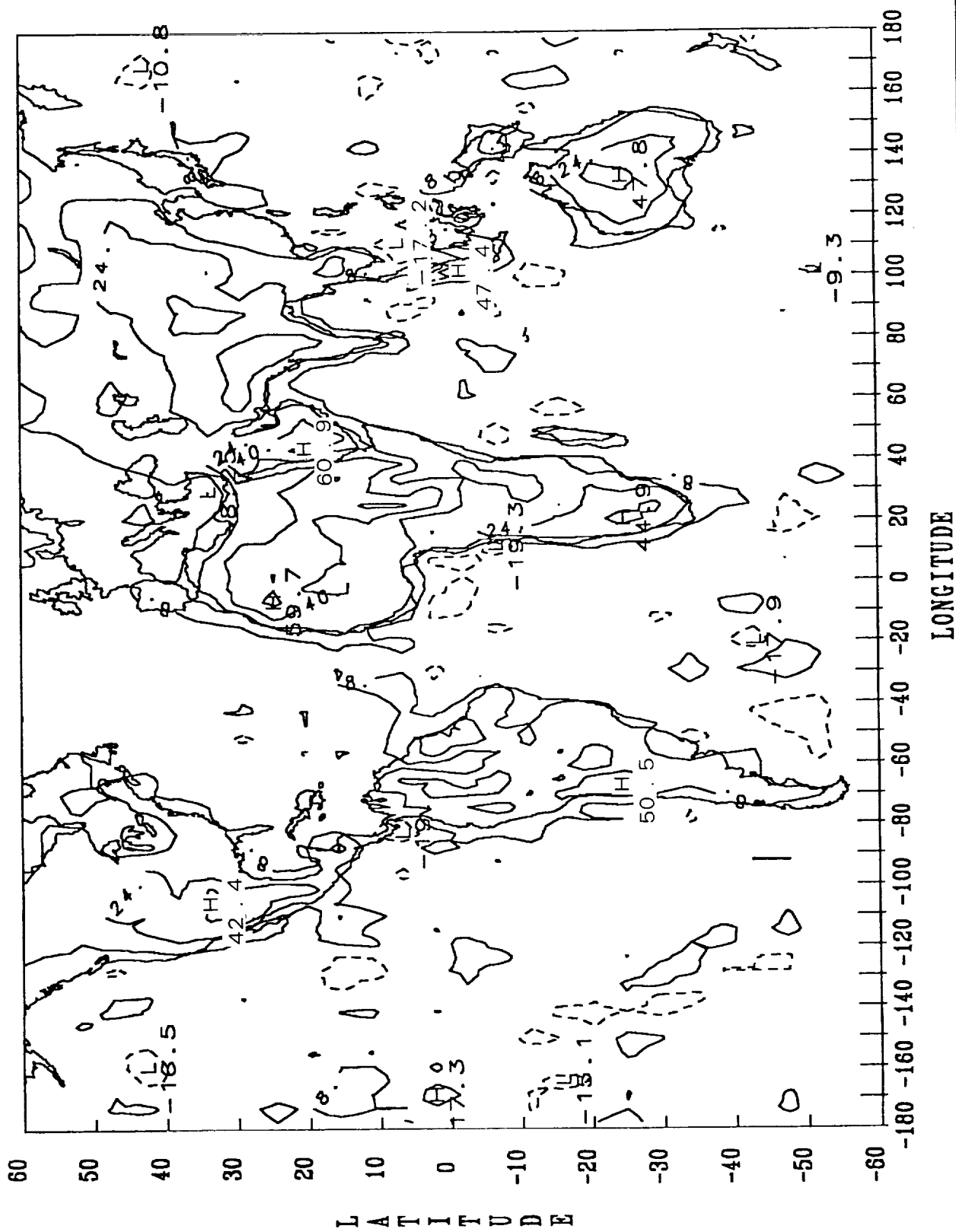
NIMBUS 7/(AN-DN) EMITTED DIF (W/M-M) DEC 1979



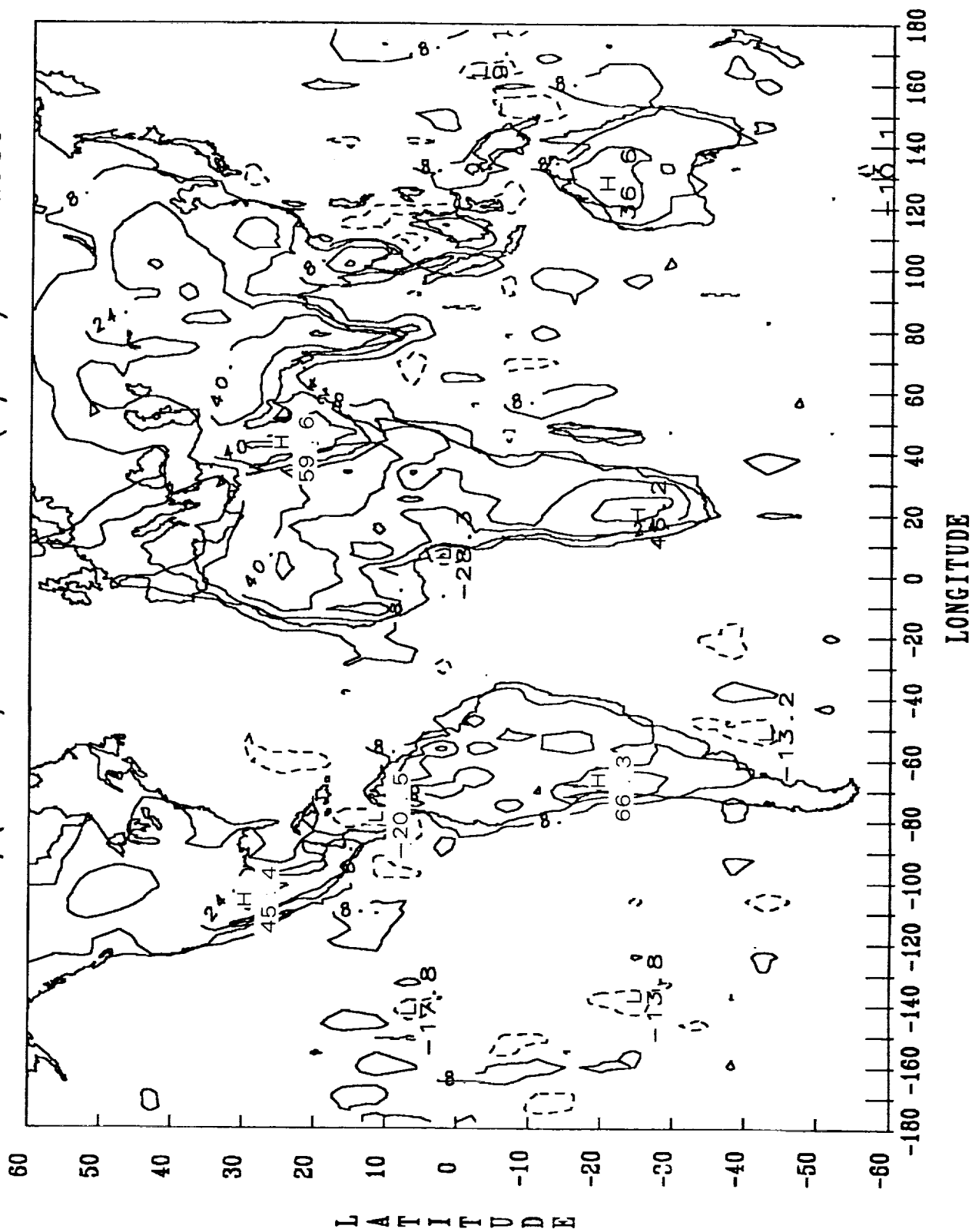
NIMBUS 7/(AN-DN) EMITTED DIF (W/M-M) JAN 1980



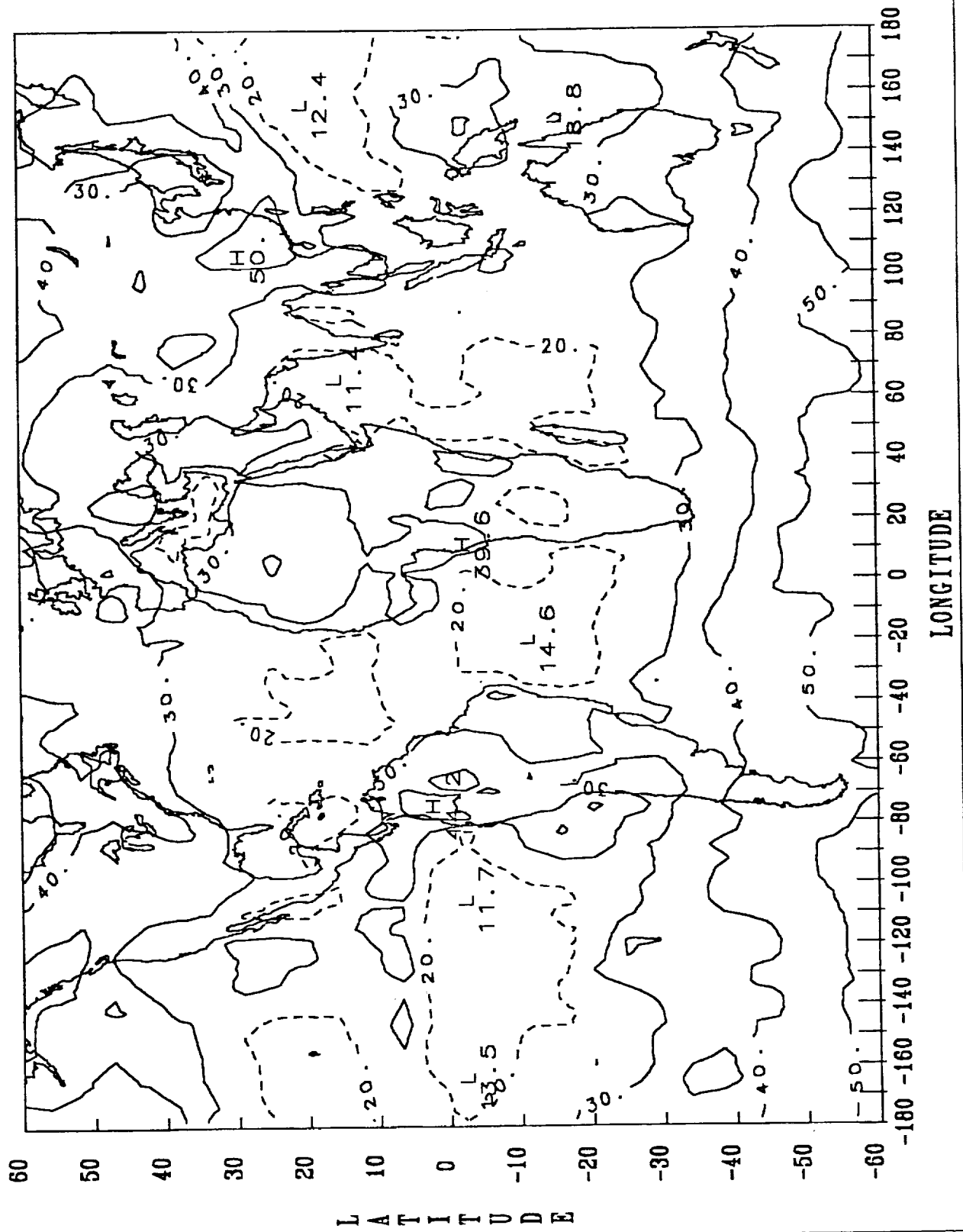
NIMBUS 7/(AN-DN) EMITTED DIF (W/M-M) APR 1980



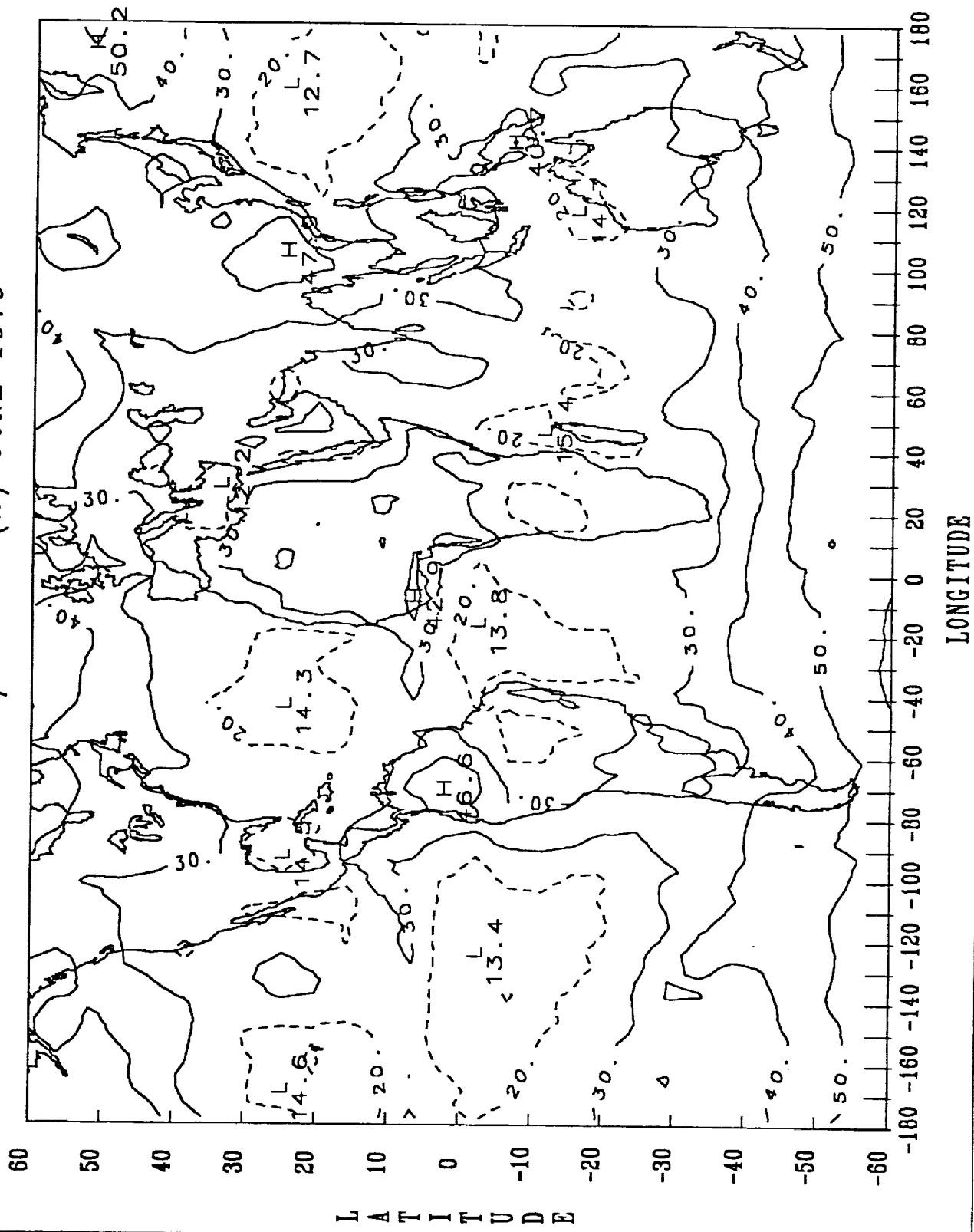
NIMBUS 7/(AN-DN) EMITTED DIF (W/M-M) MAY 1980



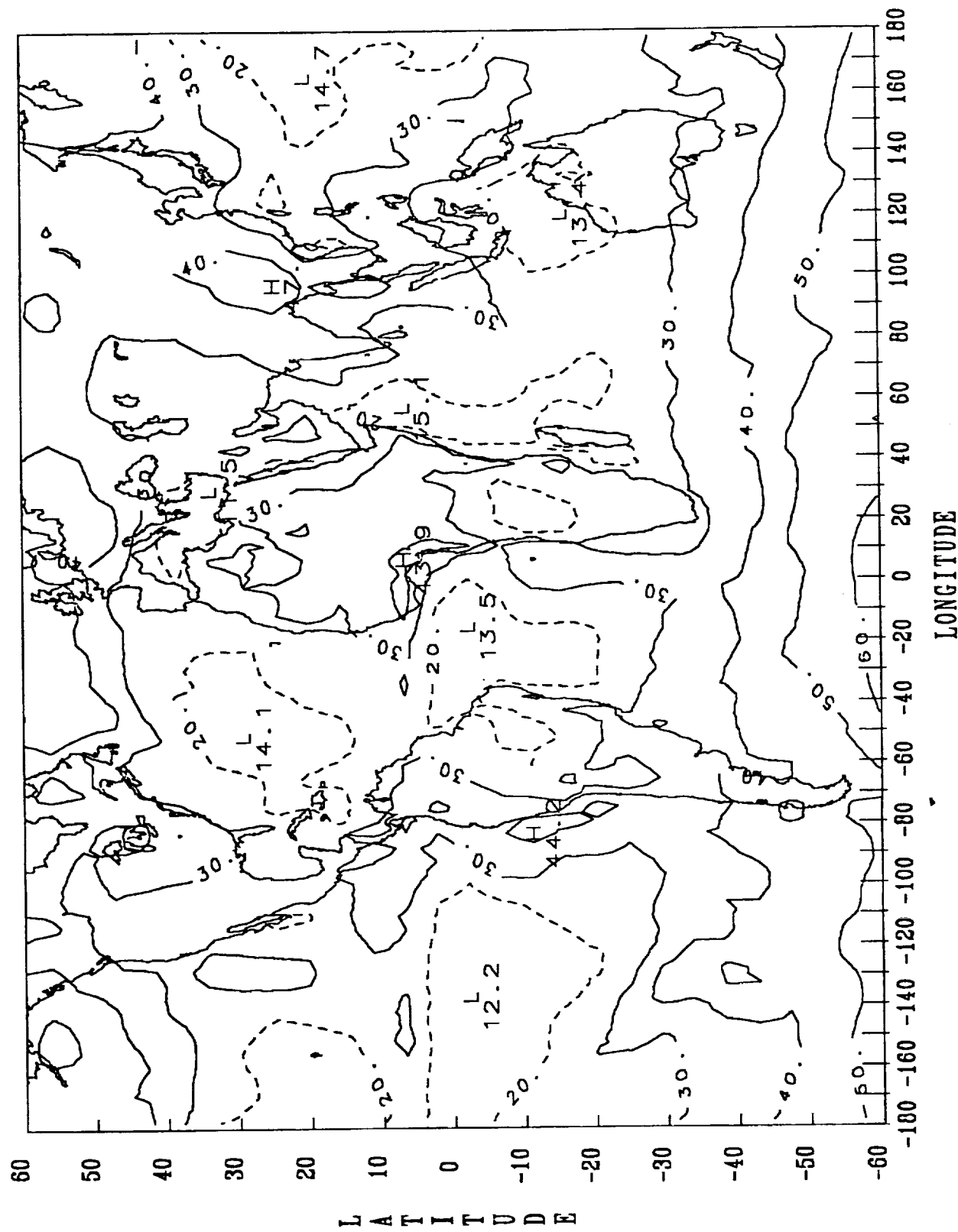
NIMBUS 7/ALBEDO (%) MAY 1979



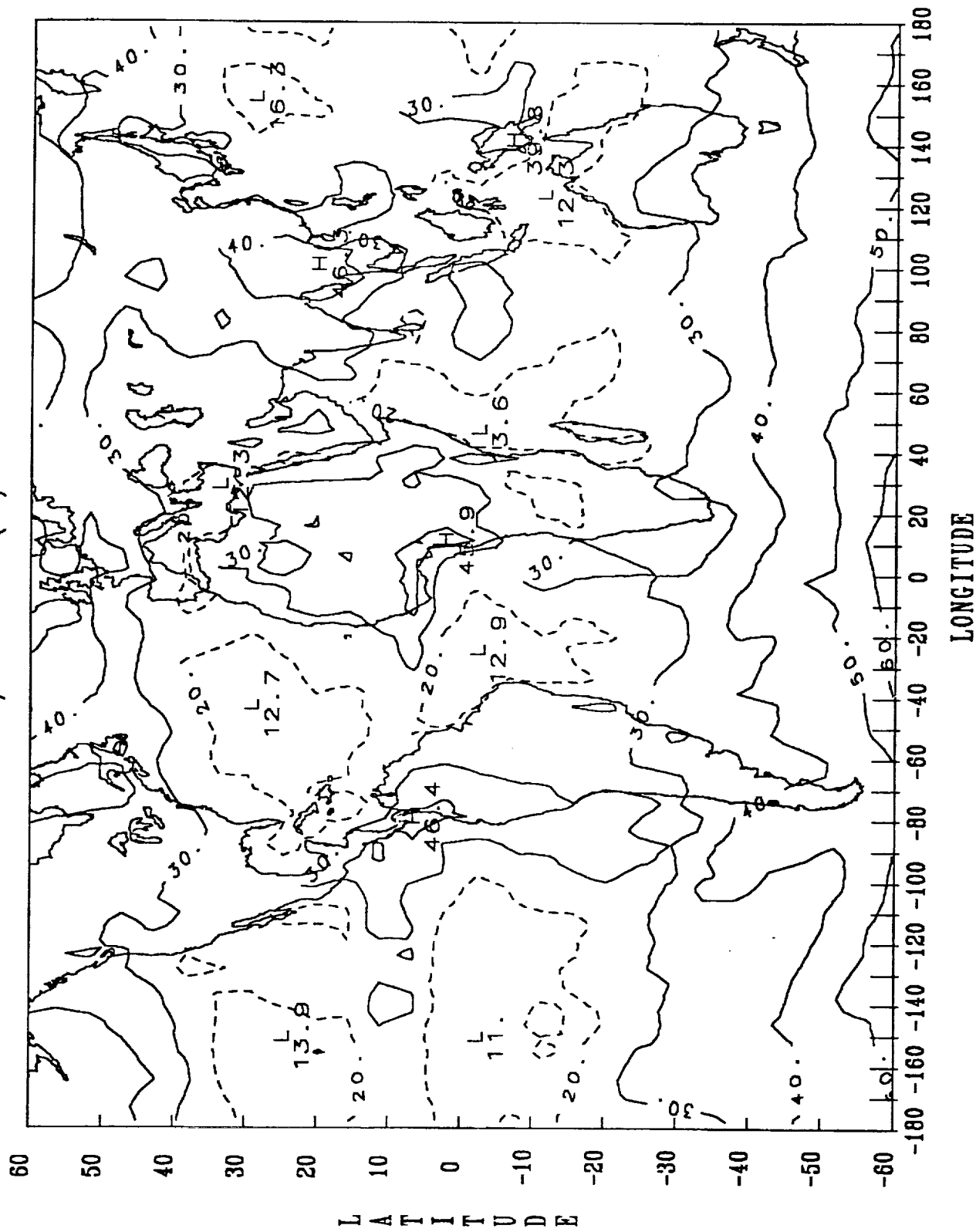
NIMBUS 7/ALBEDO (%) JUNE 1979



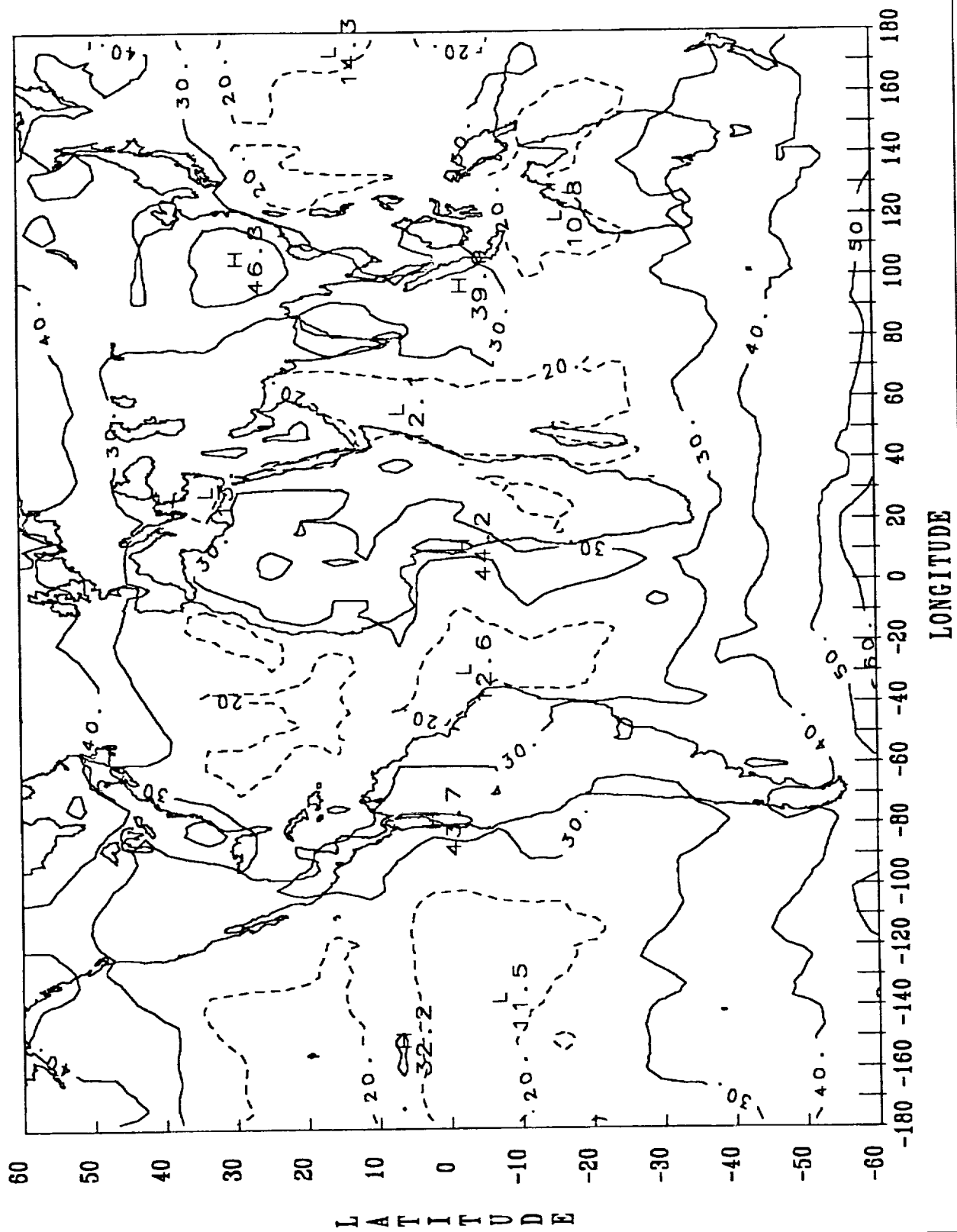
NIMBUS 7/ALBEDO (%) JULY 1979



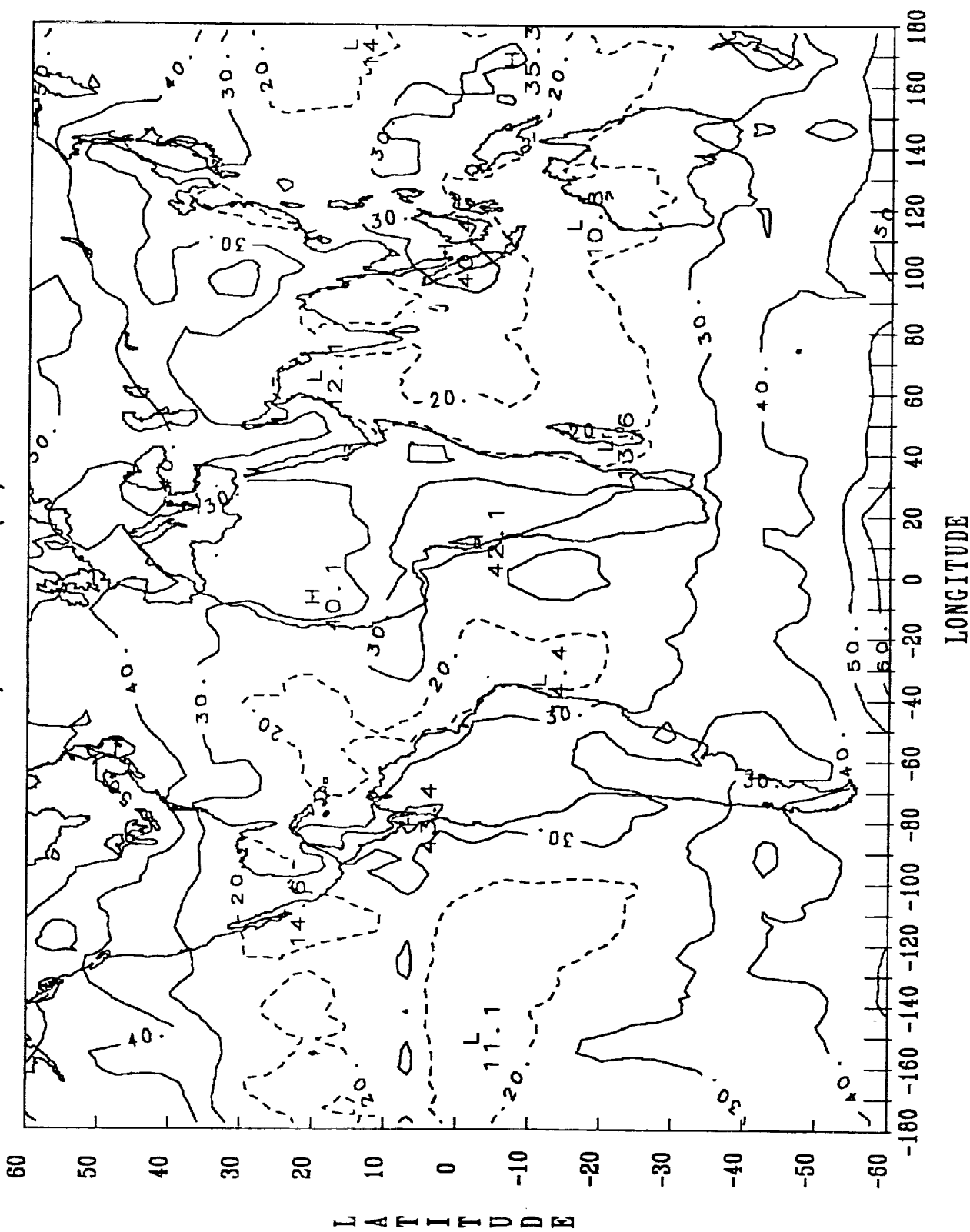
NIMBUS 7/ALBEDO (%) AUG 1979



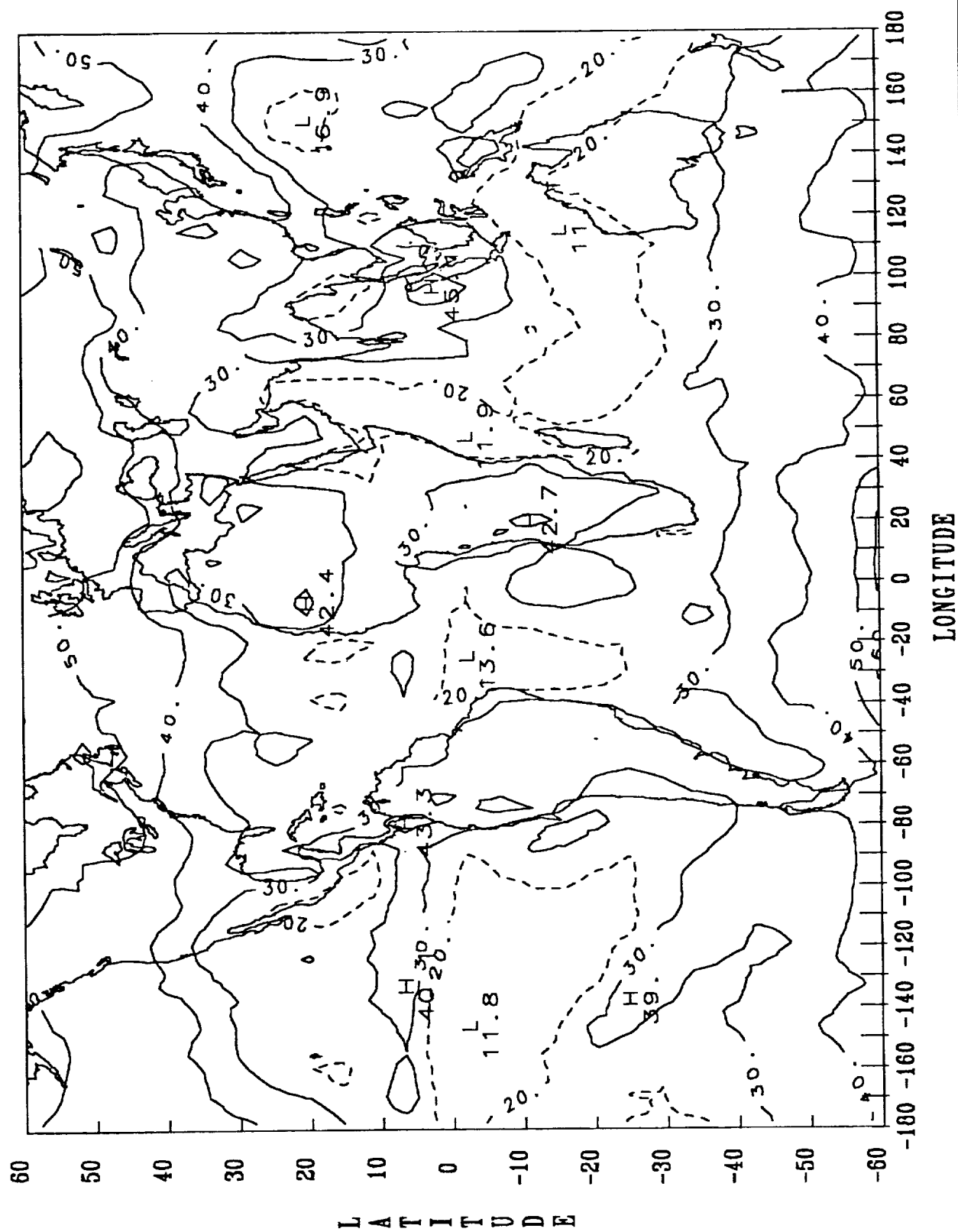
NIMBUS 7/ALBEDO (%) SEPT 1979



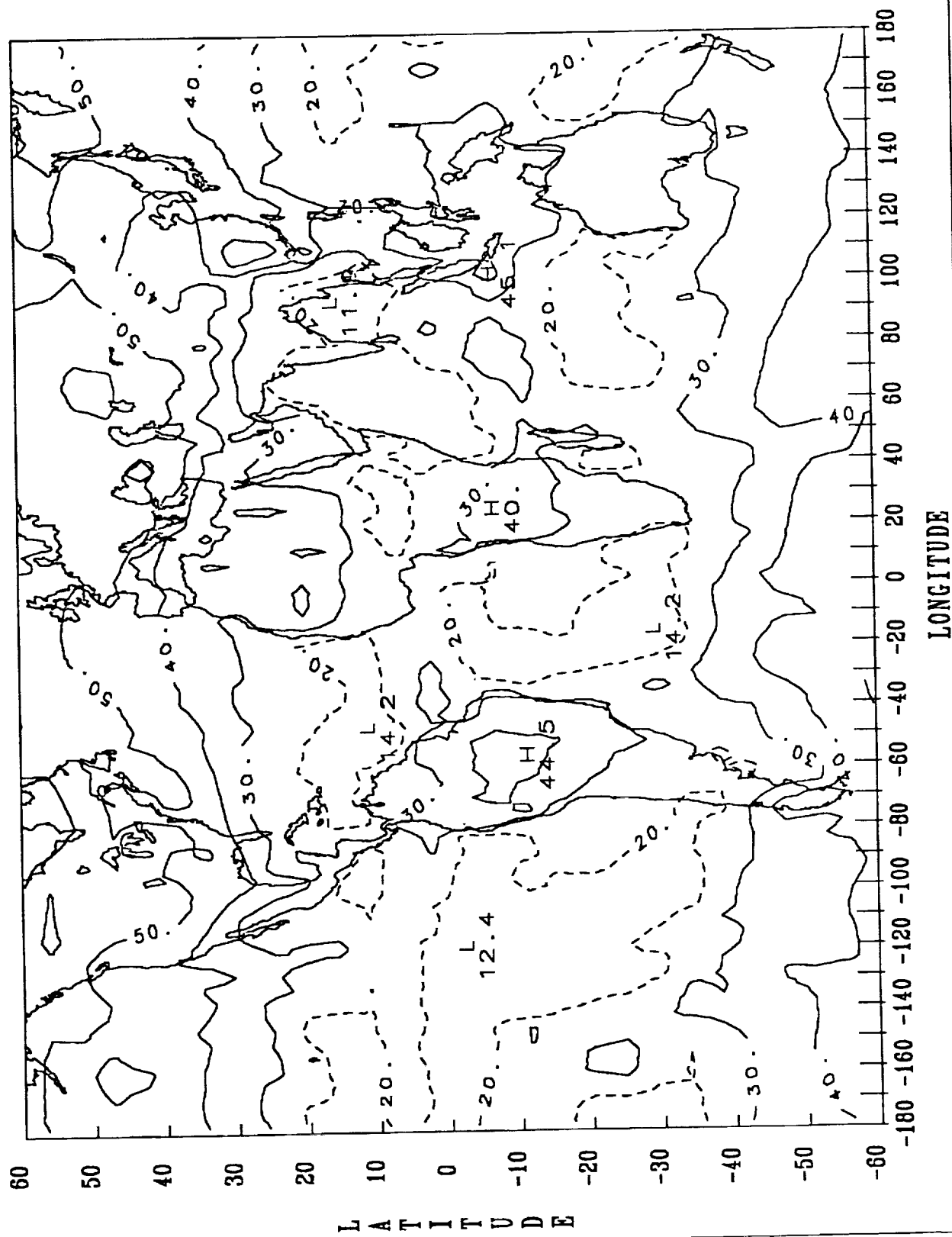
NIMBUS 7/ALBEDO (%) OCT 1979



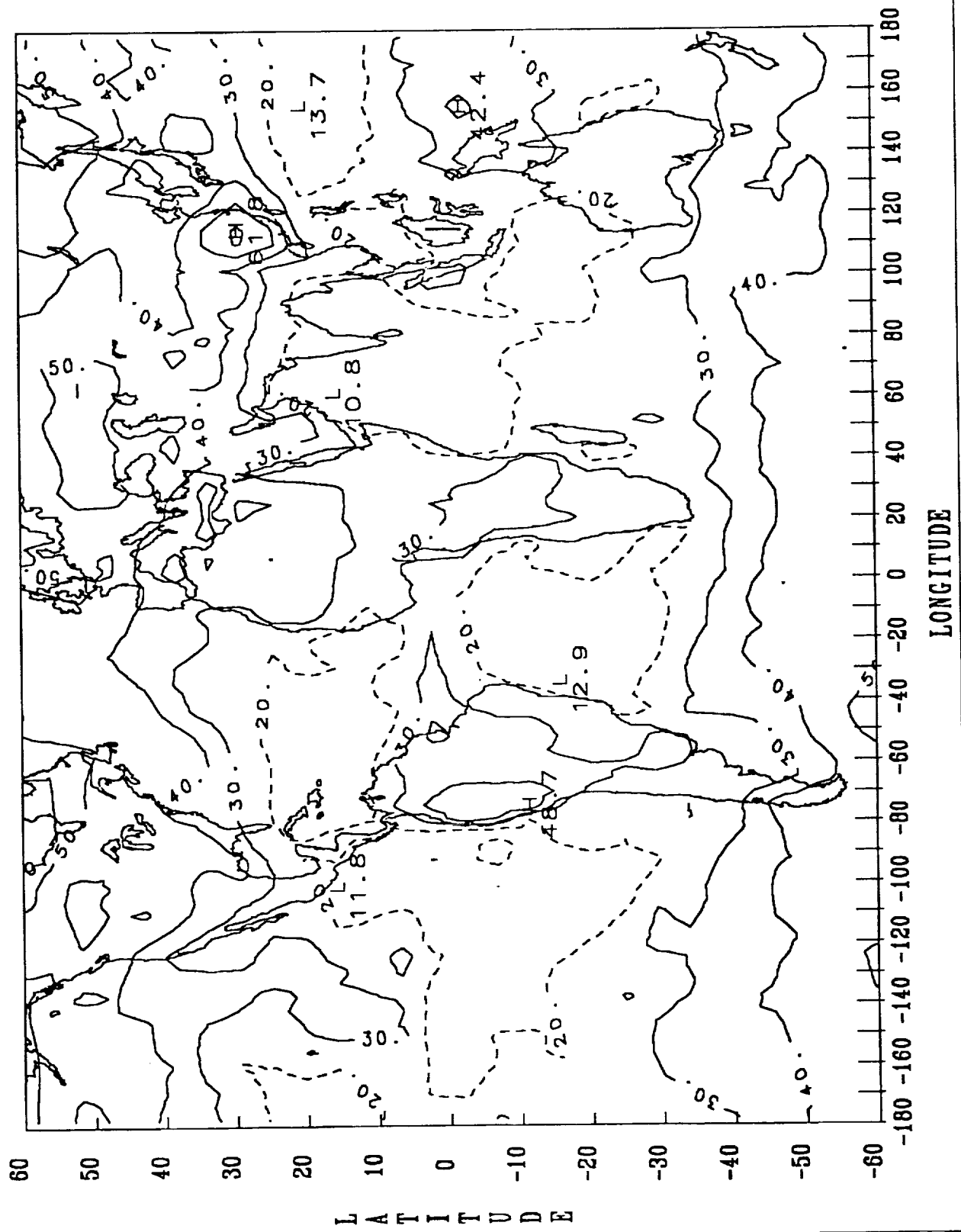
NIMBUS 7/ALBEDO (%) NOV 1979



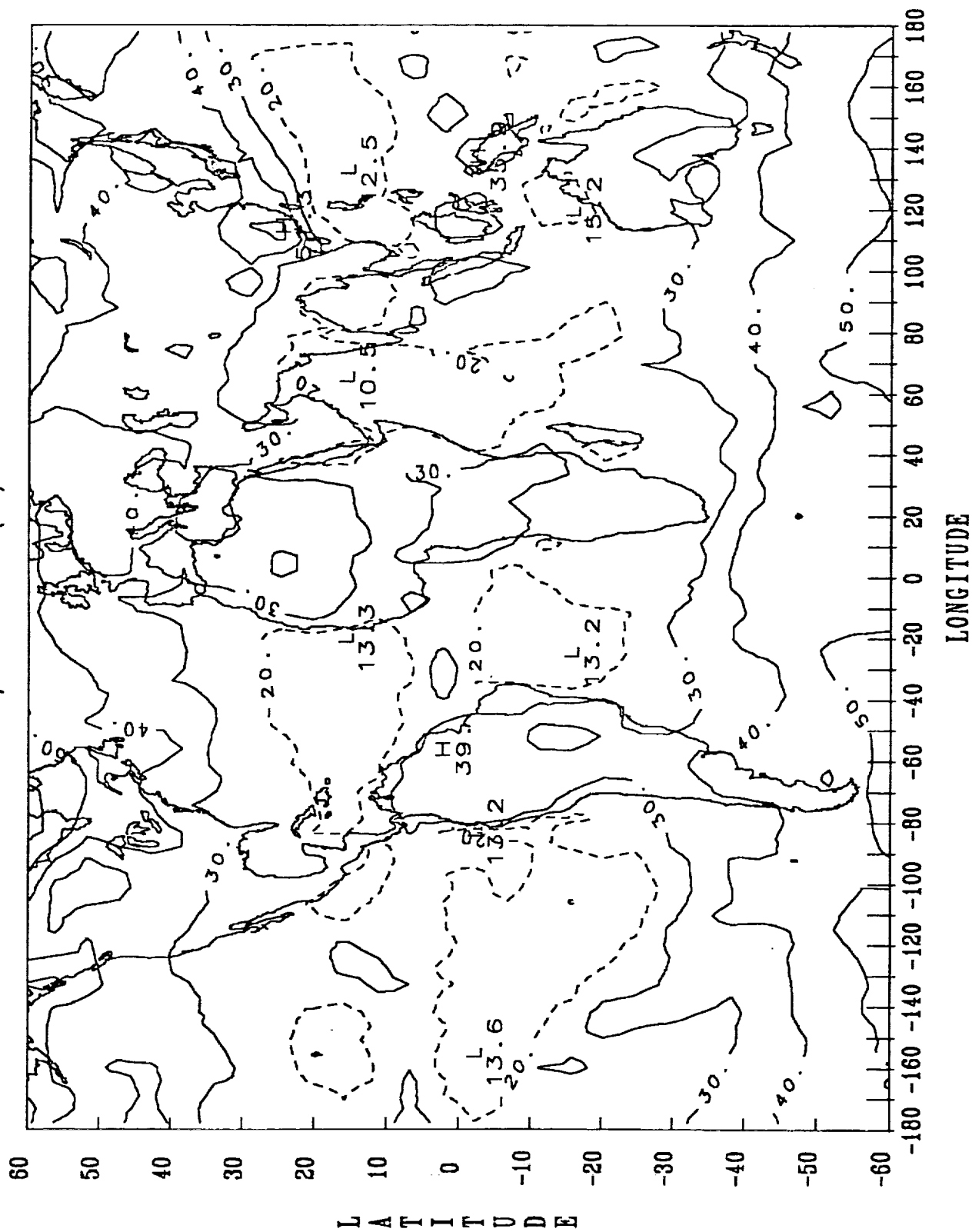
NIMBUS 7/ALBEDO (%) JAN 1980



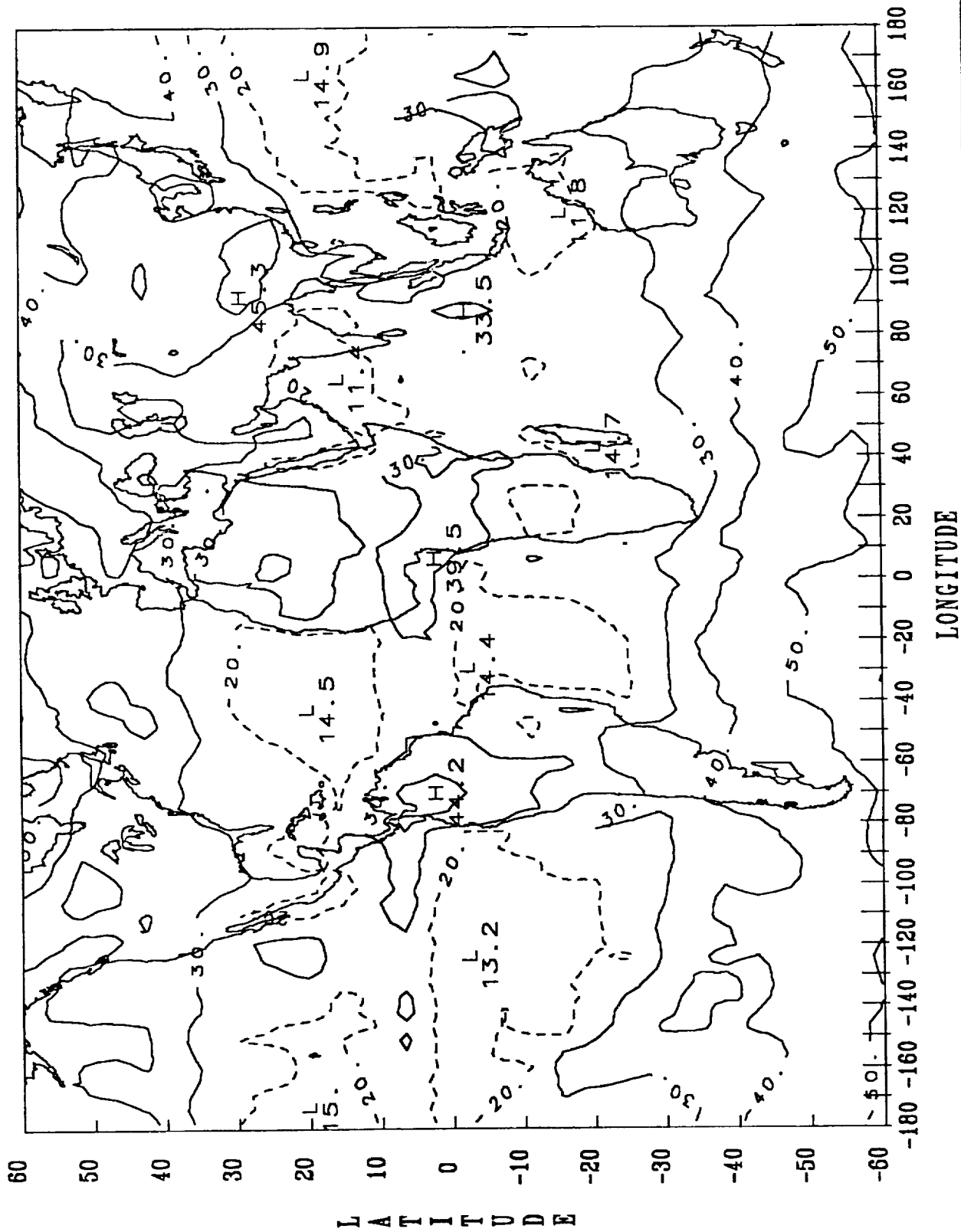
NIMBUS 7/ALBEDO (%) MAR 1980



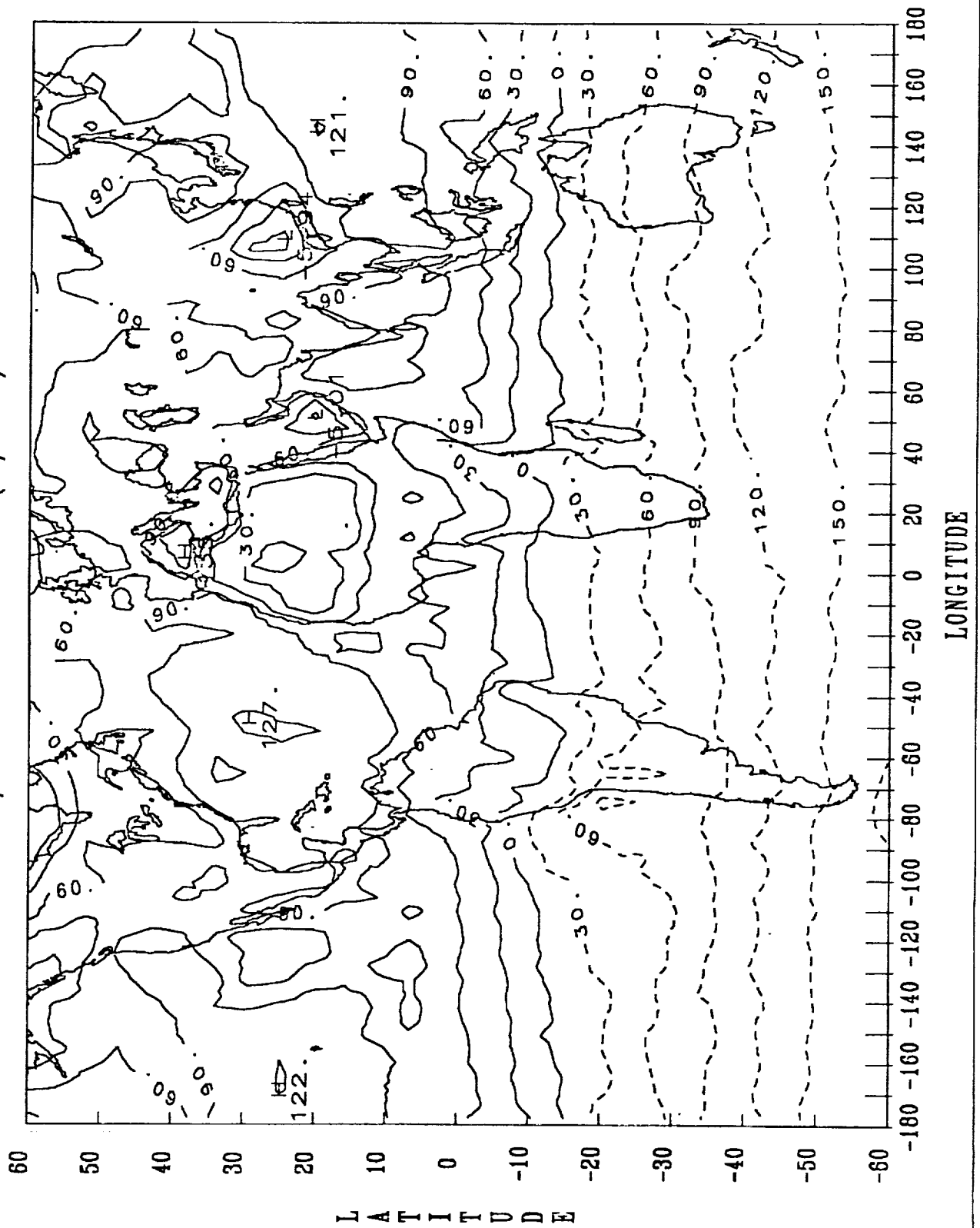
NIMBUS 7/ALBEDO (%) APR 1980



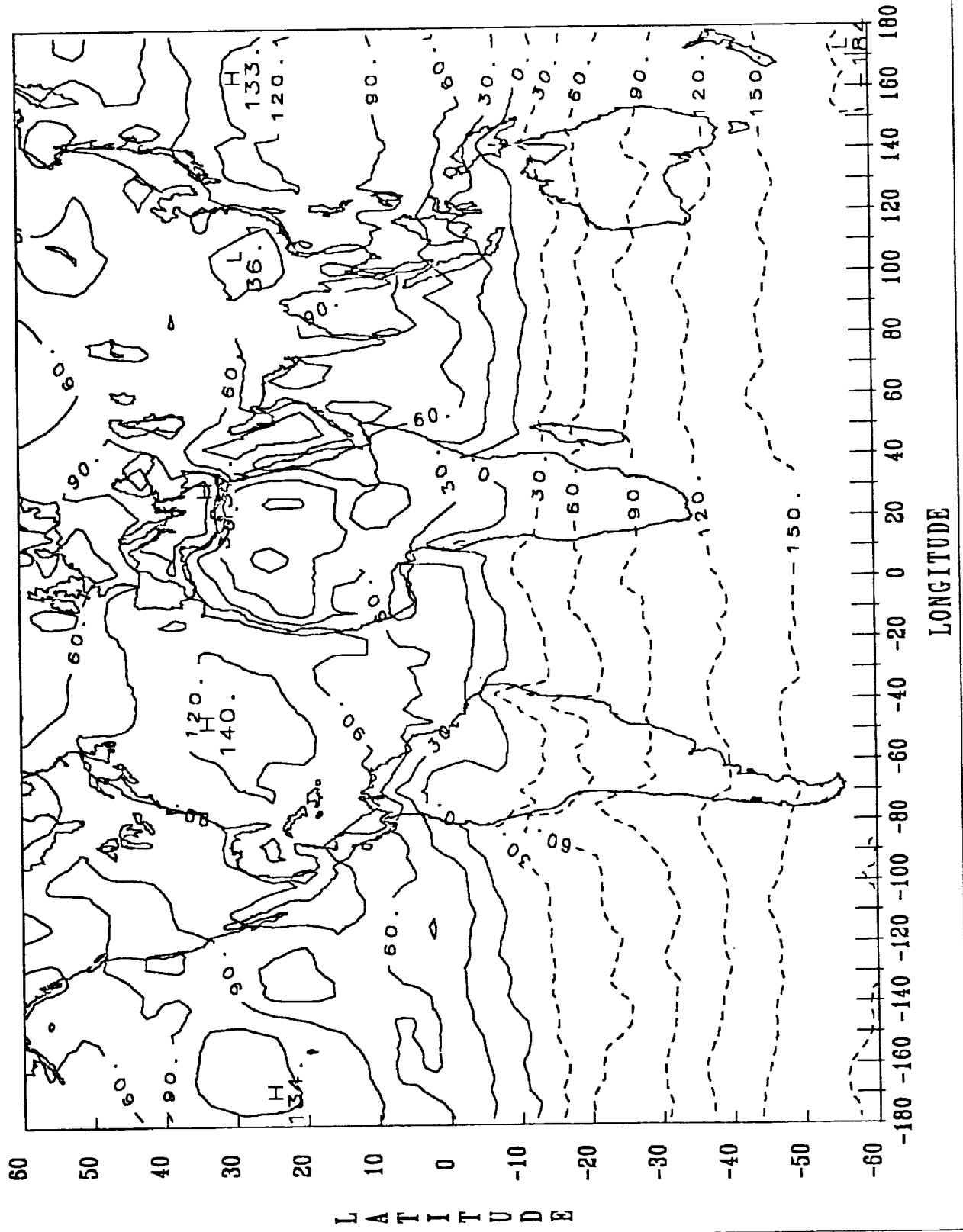
NIMBUS 7/ALBEDO (%) MAY 1980



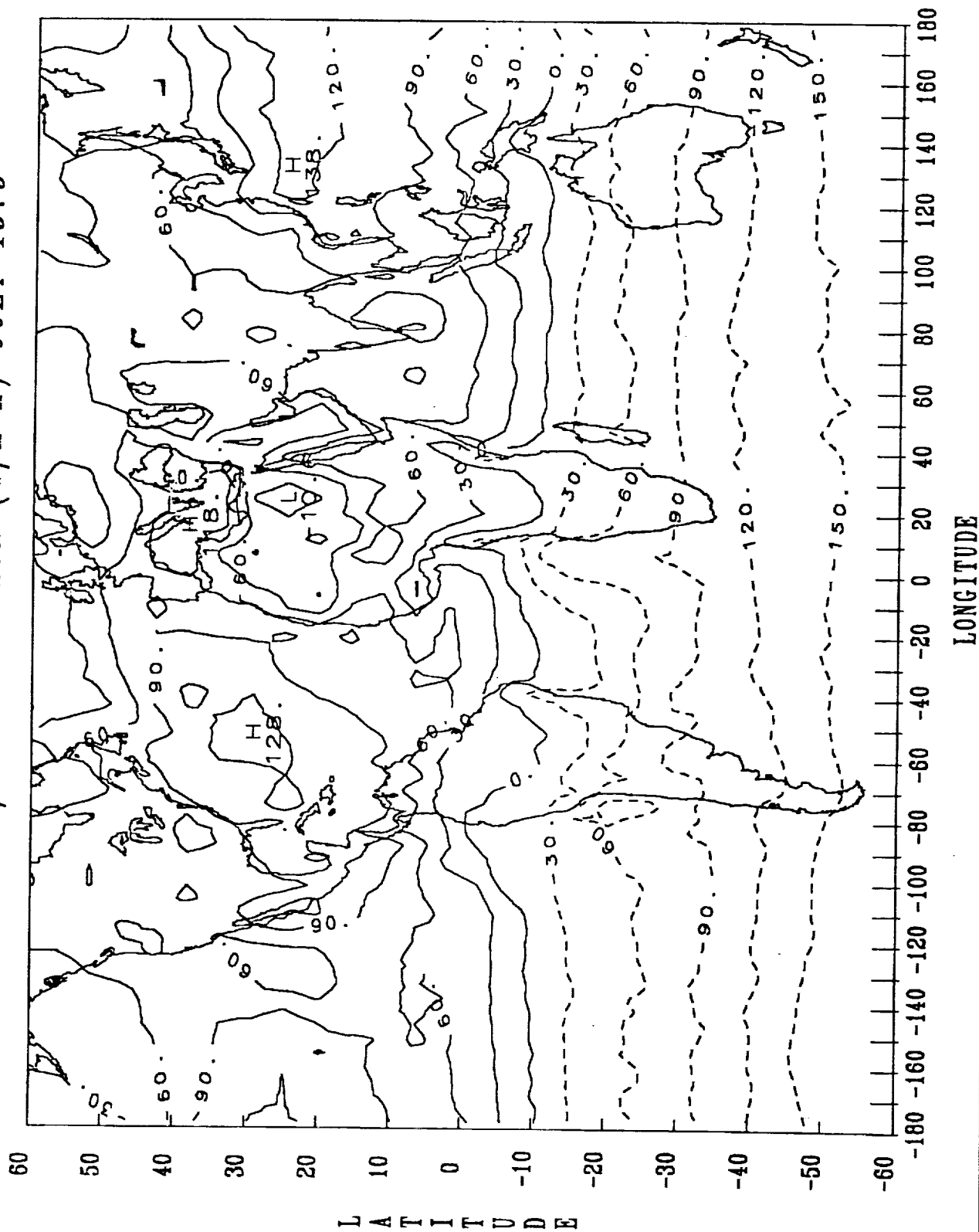
NIMBUS 7/NET RADIATION (W/M*M) MAY 1979



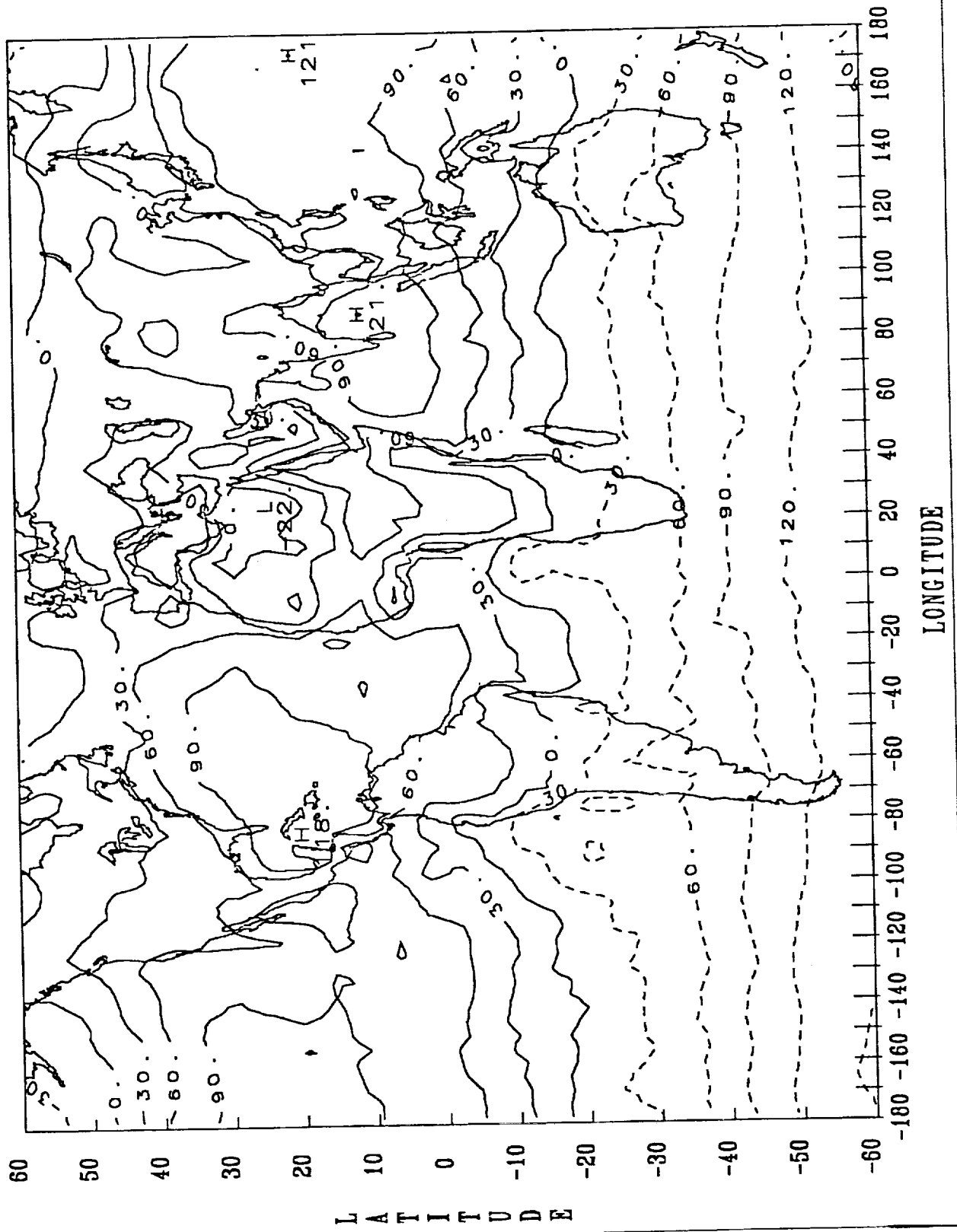
NIMBUS 7/NET RADIATION (W/M²M) JUNE 1979



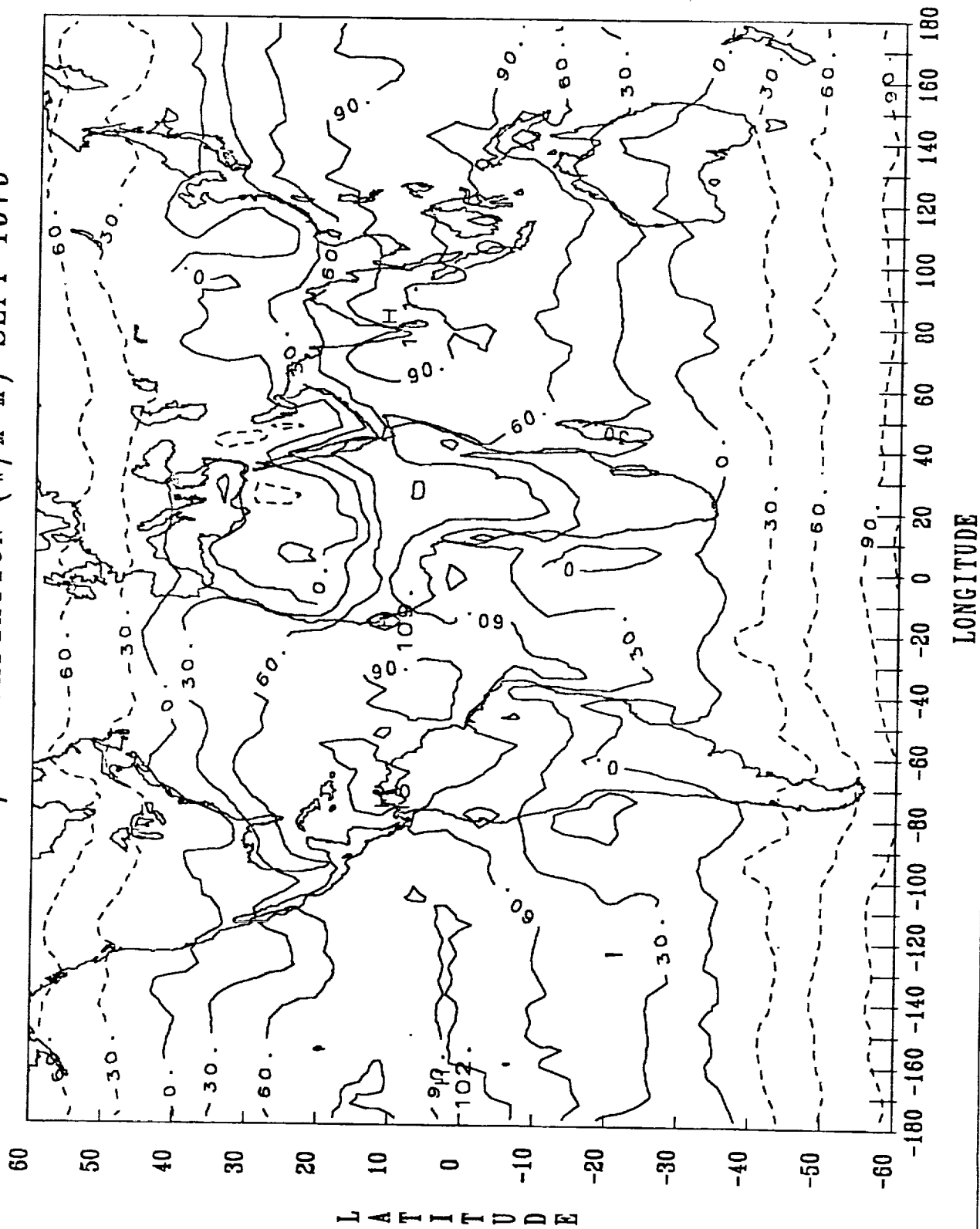
NIMBUS 7/NET RADIATION (W/M*M) JULY 1979



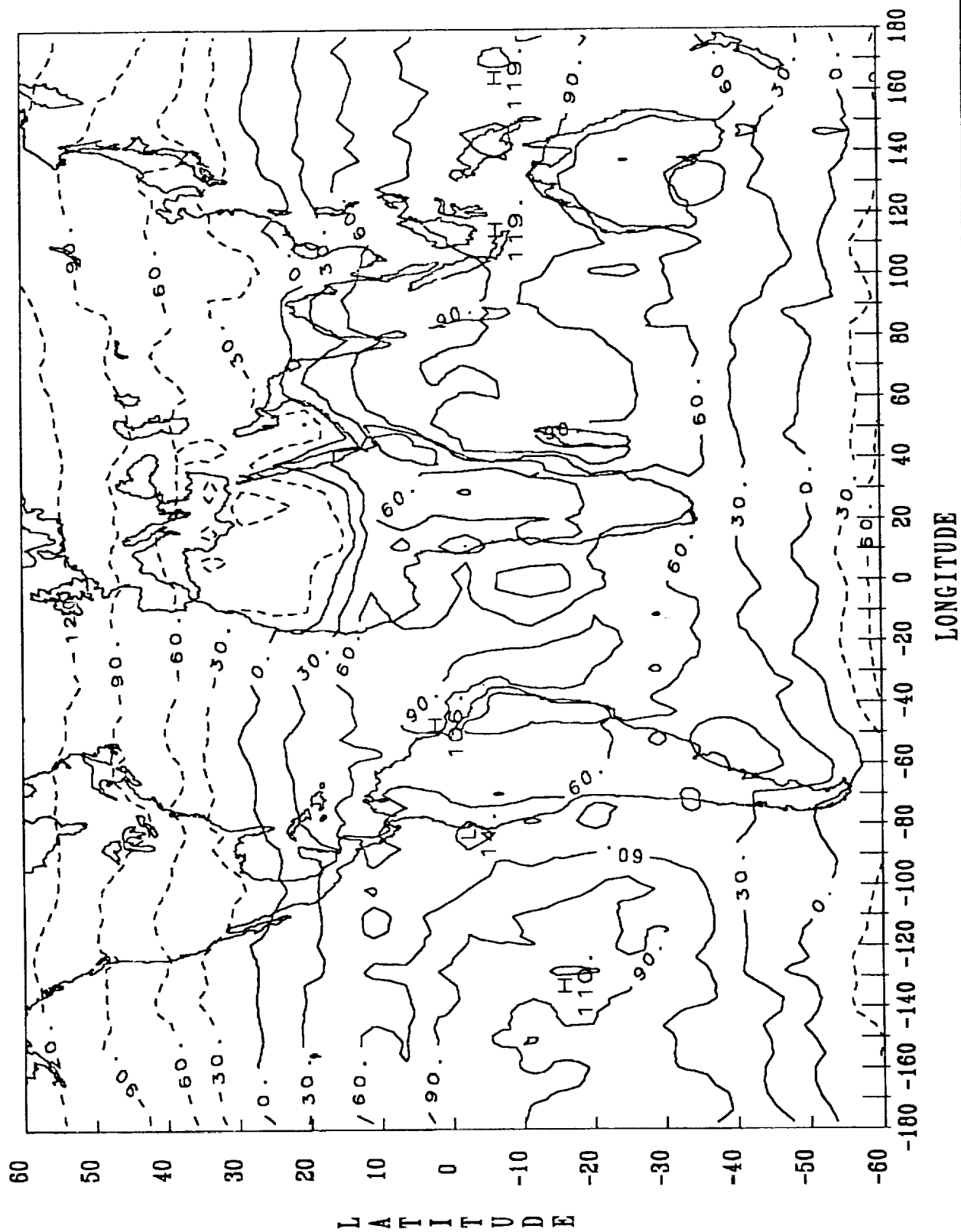
NIMBUS 7/NET RADIATION (W/M*M) AUG 1979



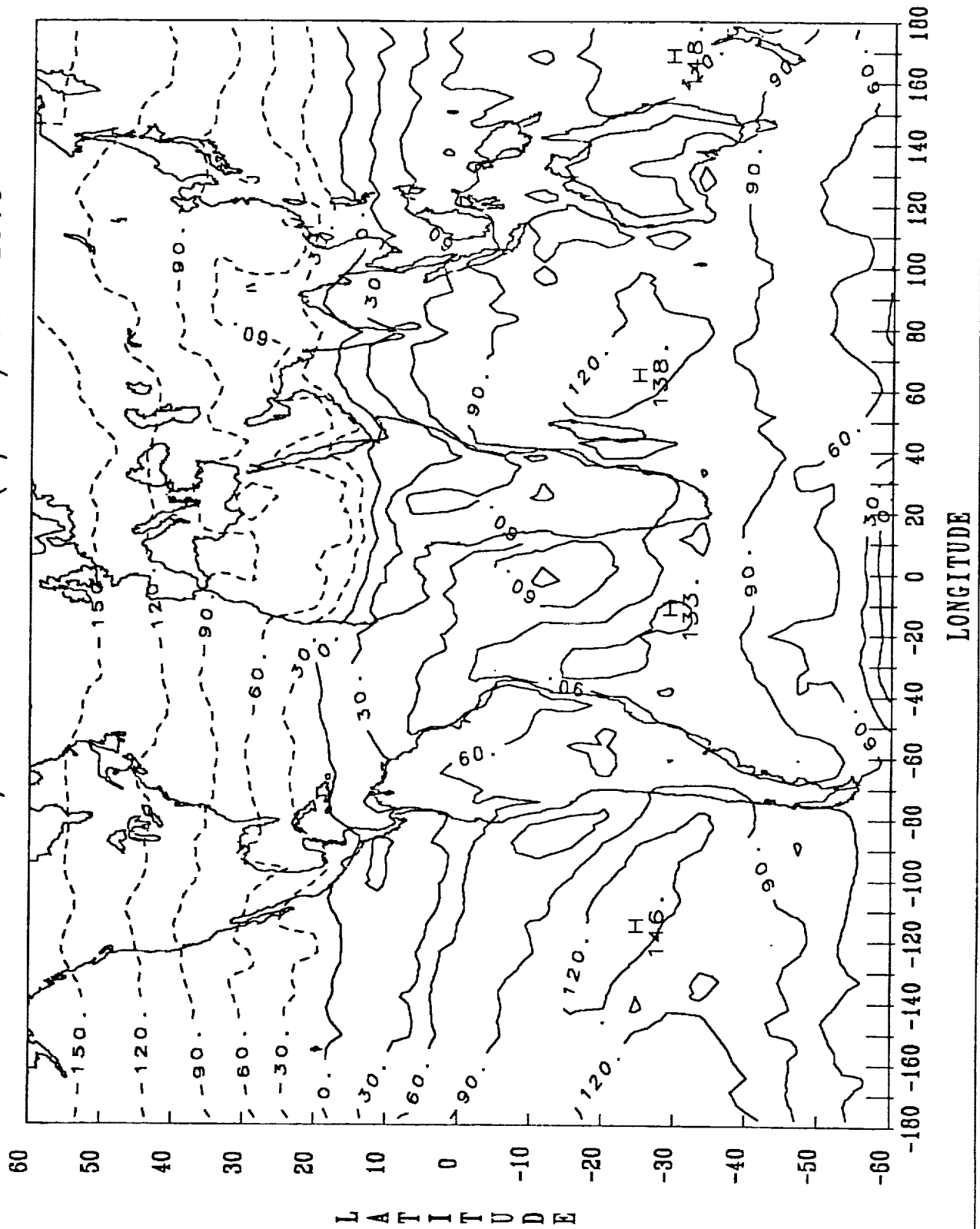
NIMBUS 7/NET RADIATION (W/M²M) SEPT 1979



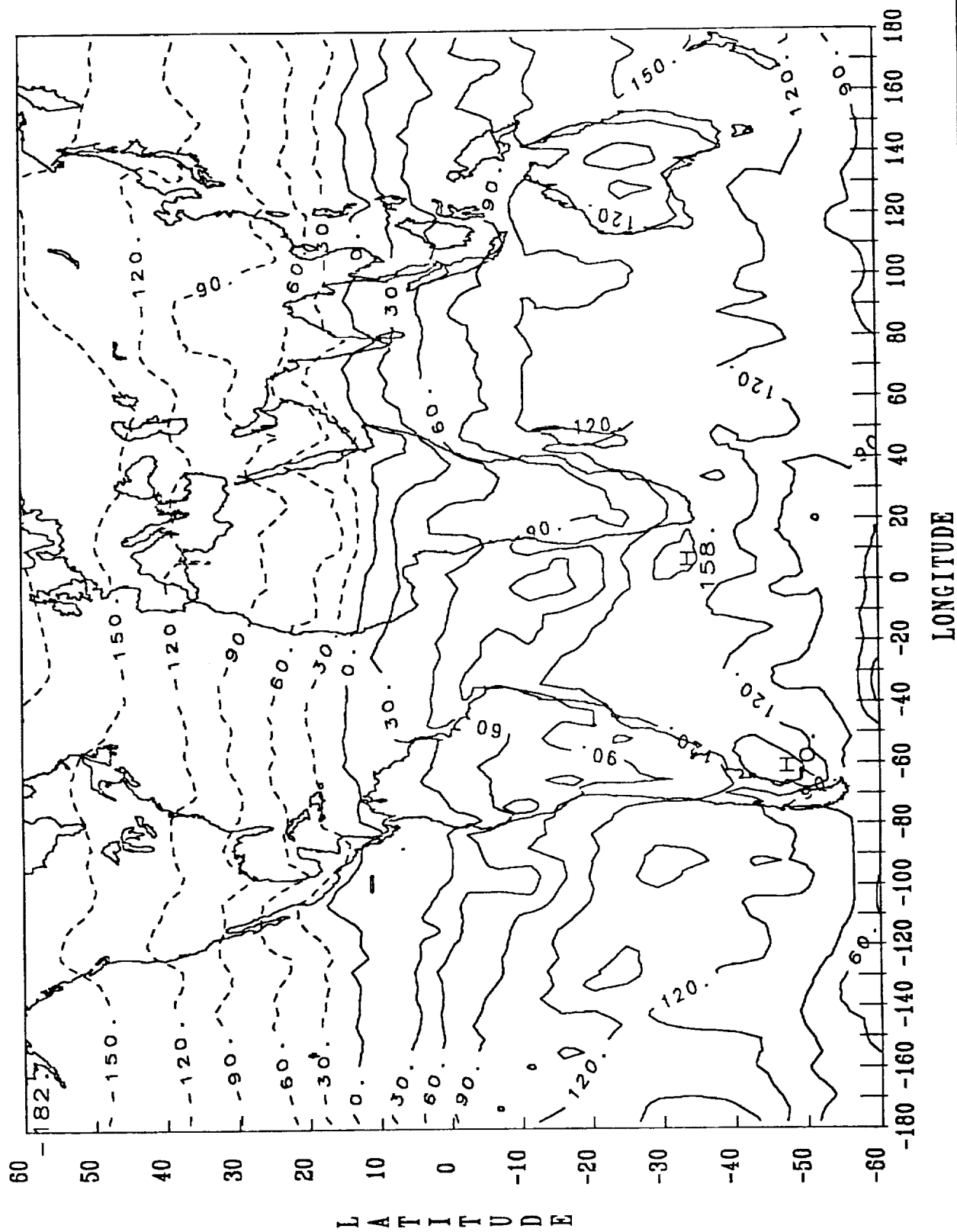
NIMBUS 7/NET RADIATION (W/M*M) OCT 1979



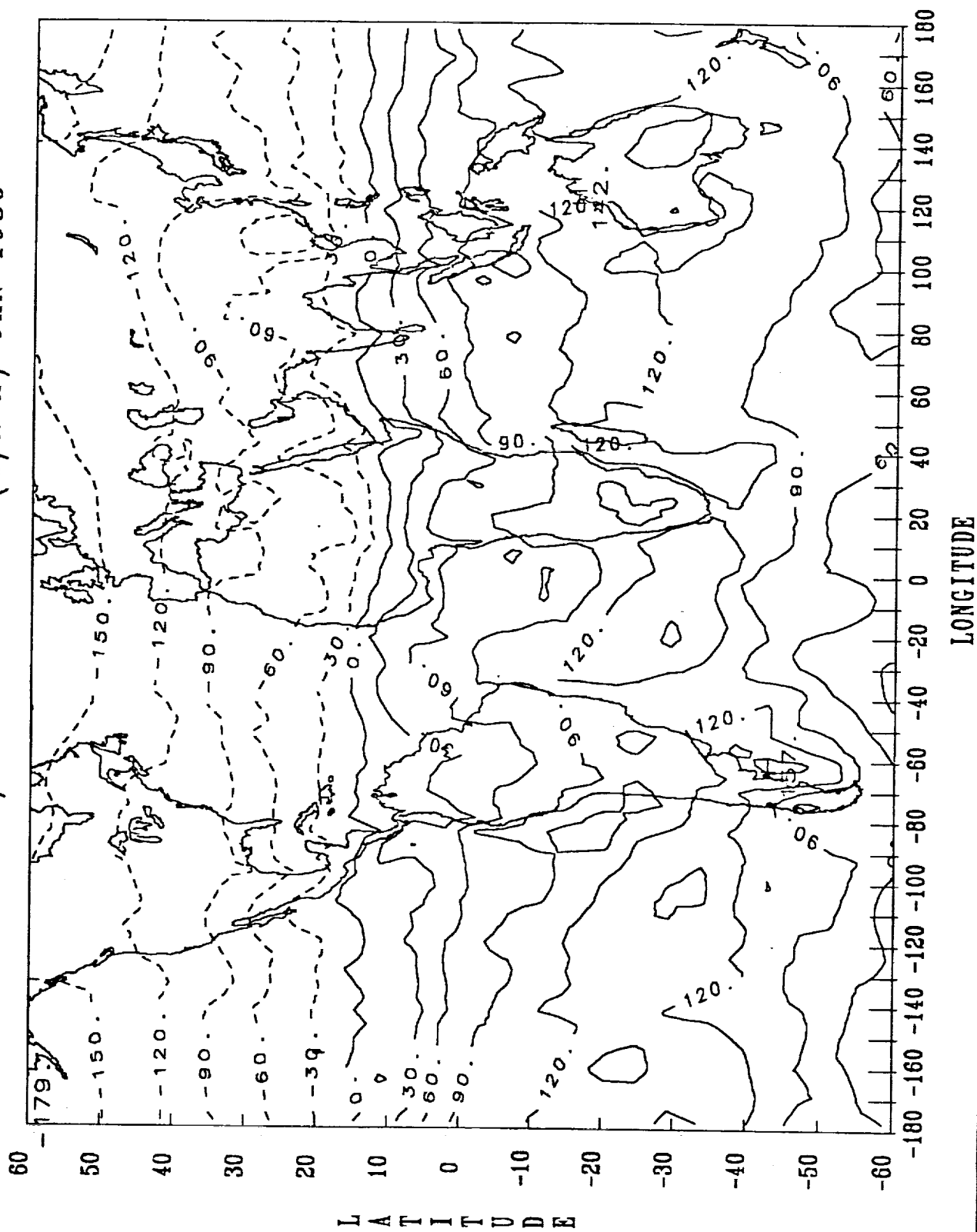
NIMBUS 7/NET RADIATION (W/M²M) NOV 1979



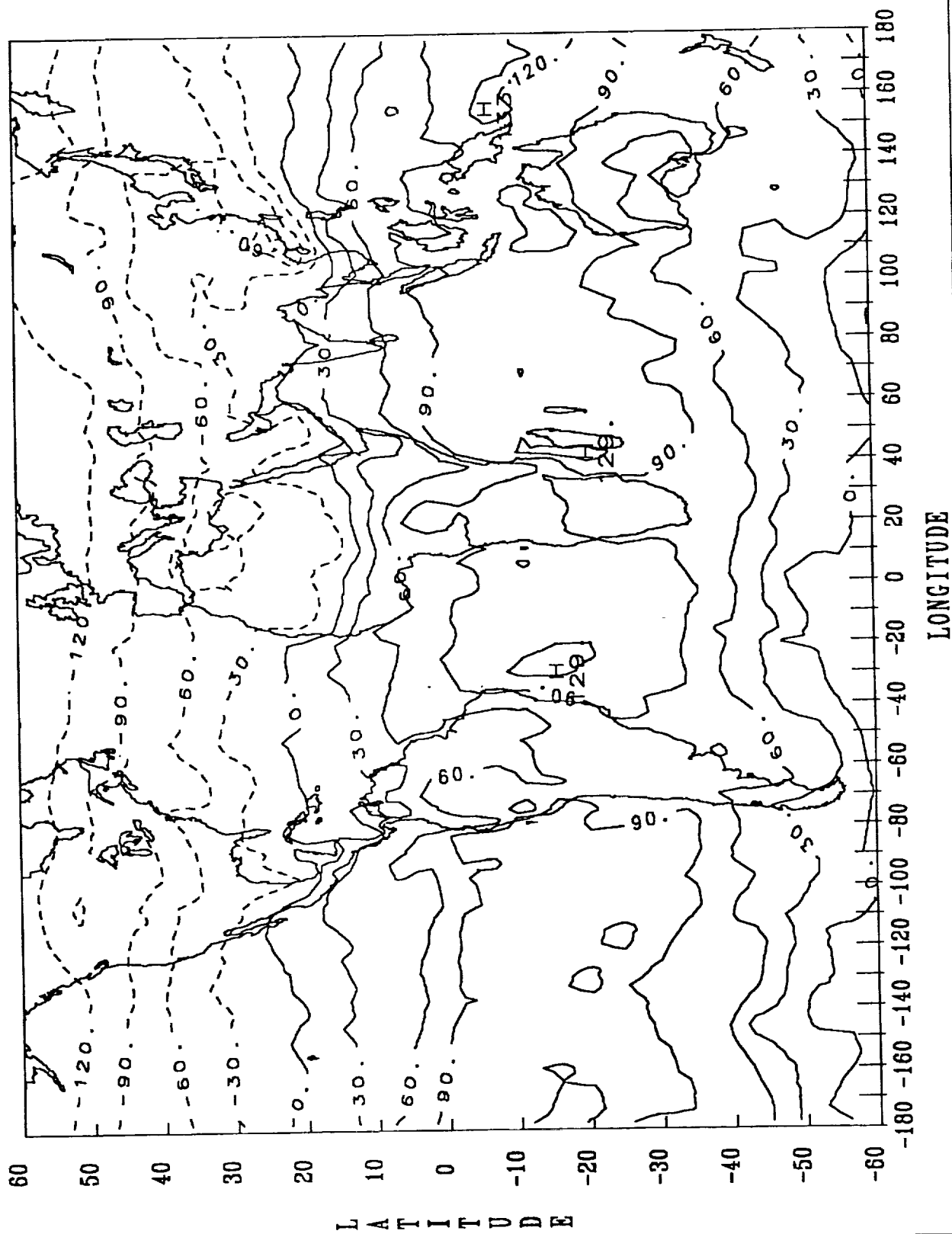
NIMBUS 7/NET RADIATION (W/M*M) DEC 1979



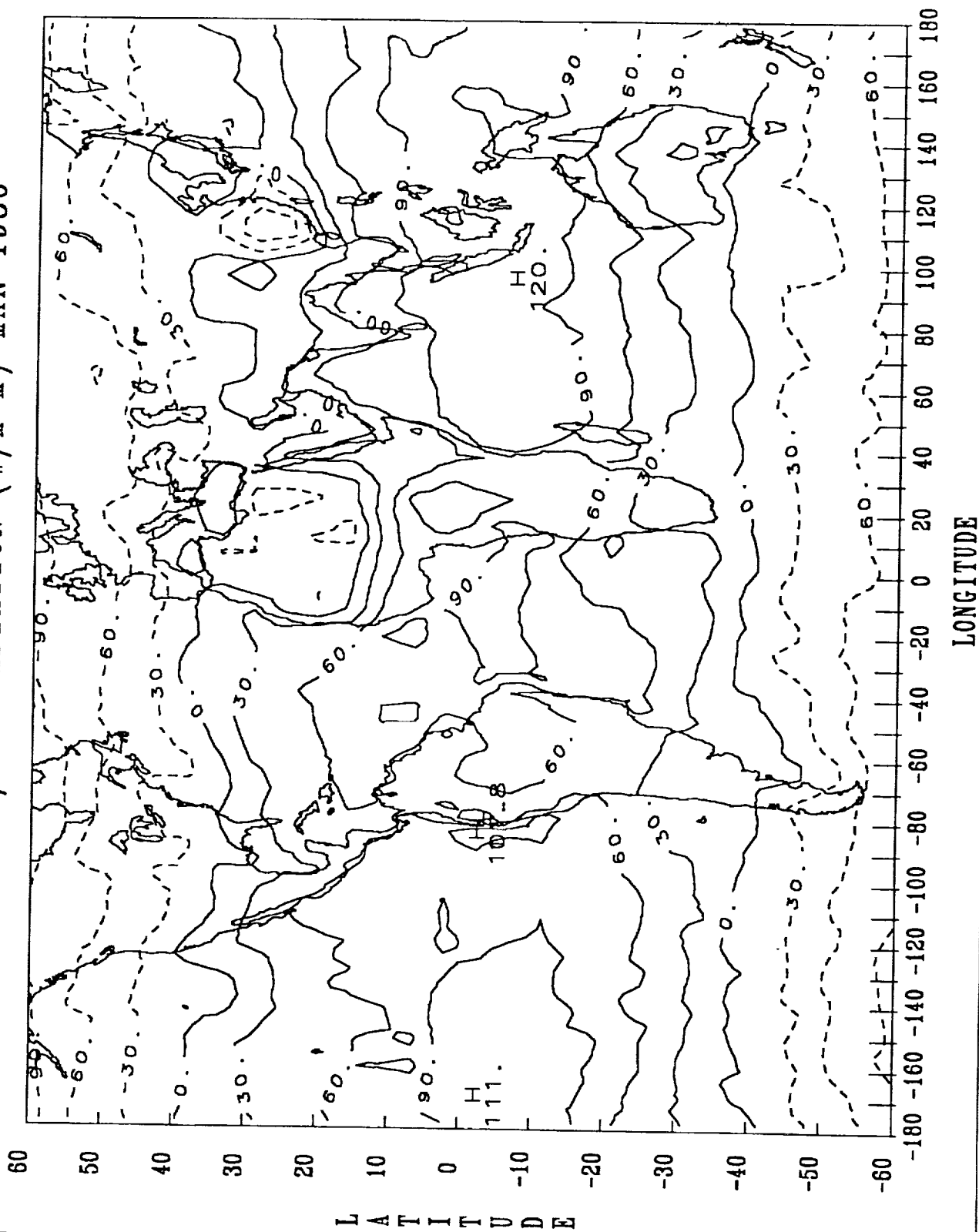
NIMBUS 7/NET RADIATION (W/M²M) JAN 1980



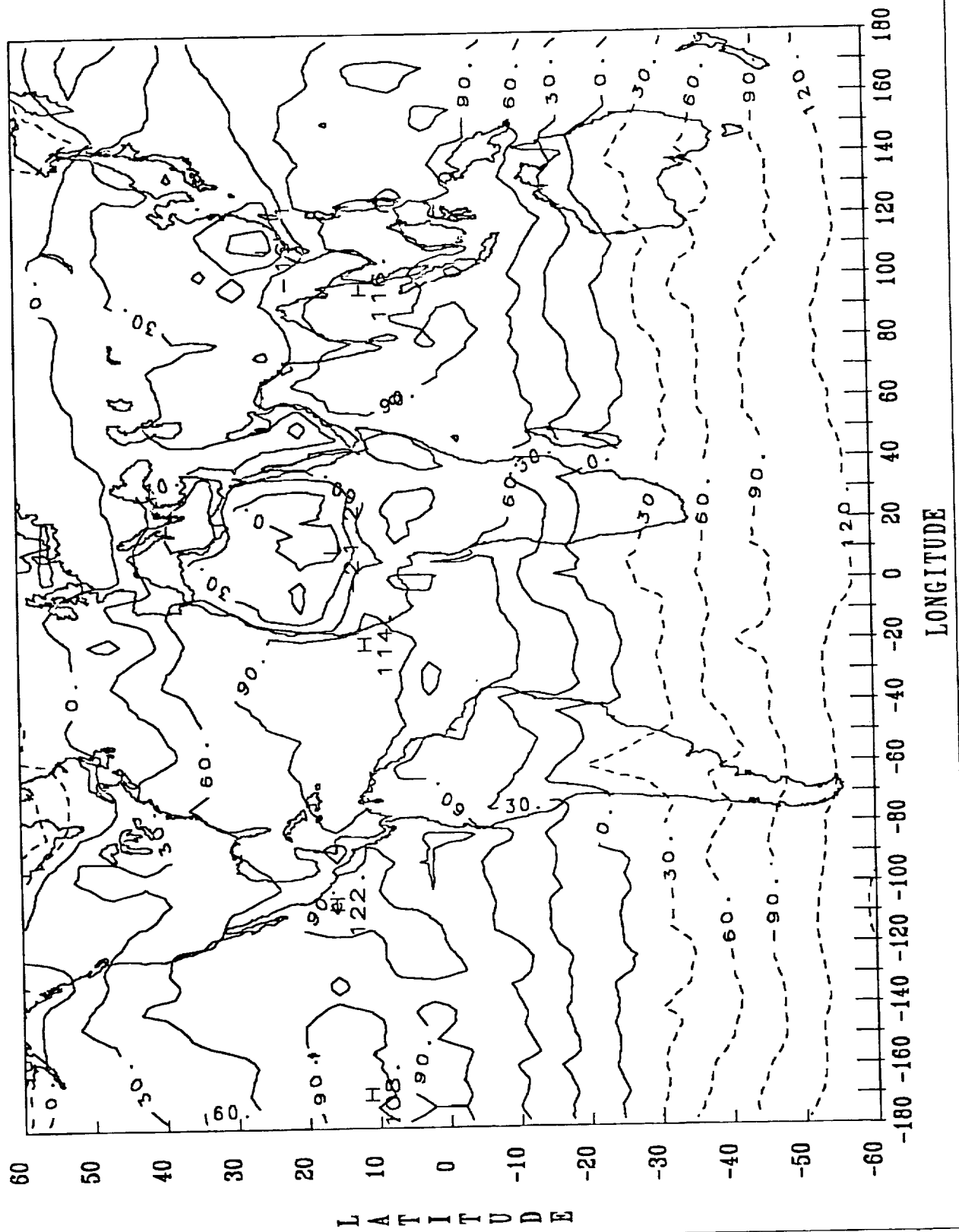
NIMBUS 7/NET RADIATION (W/M²M) FEB 1980



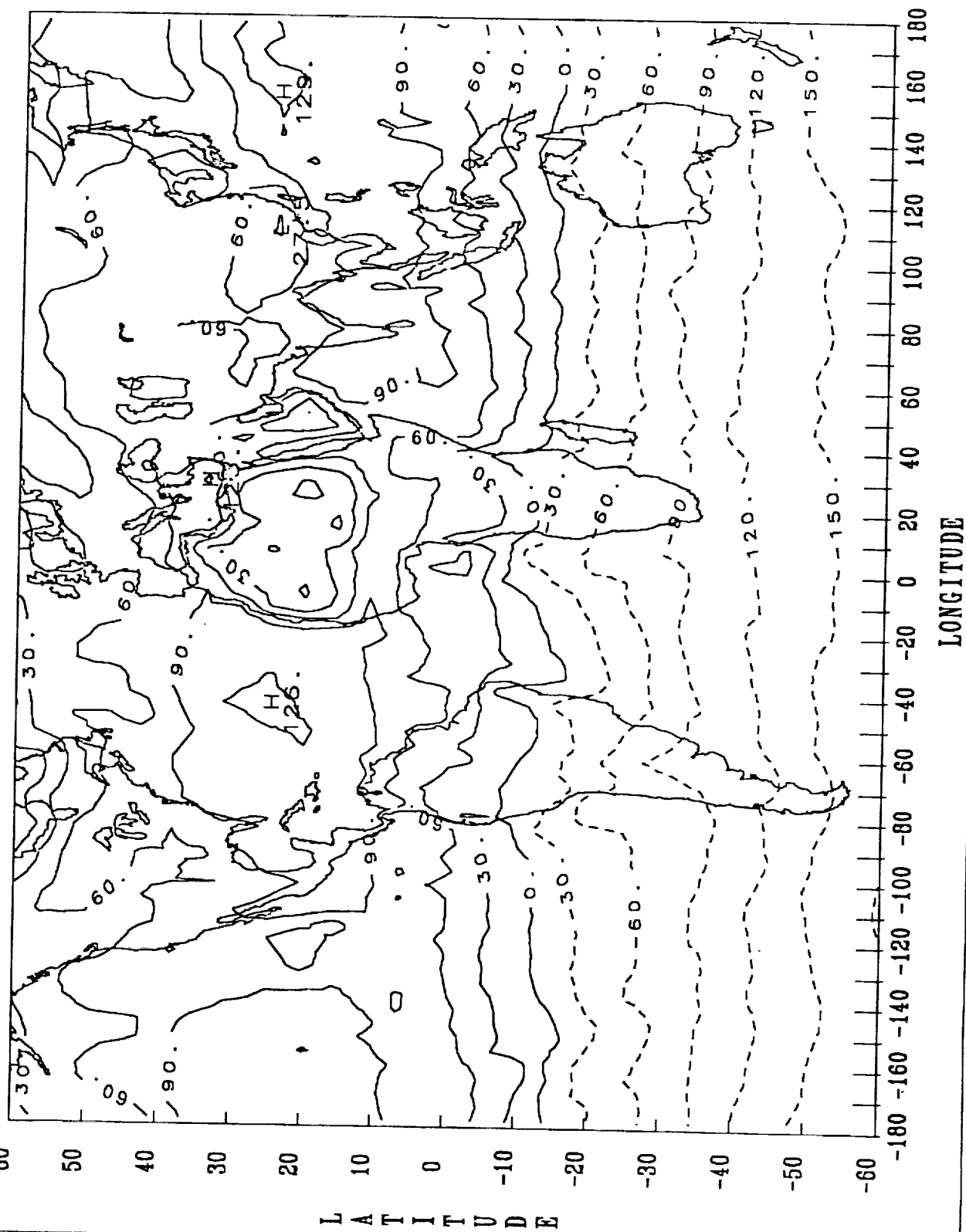
NIMBUS 7/NET RADIATION (W/M²M) MAR 1980



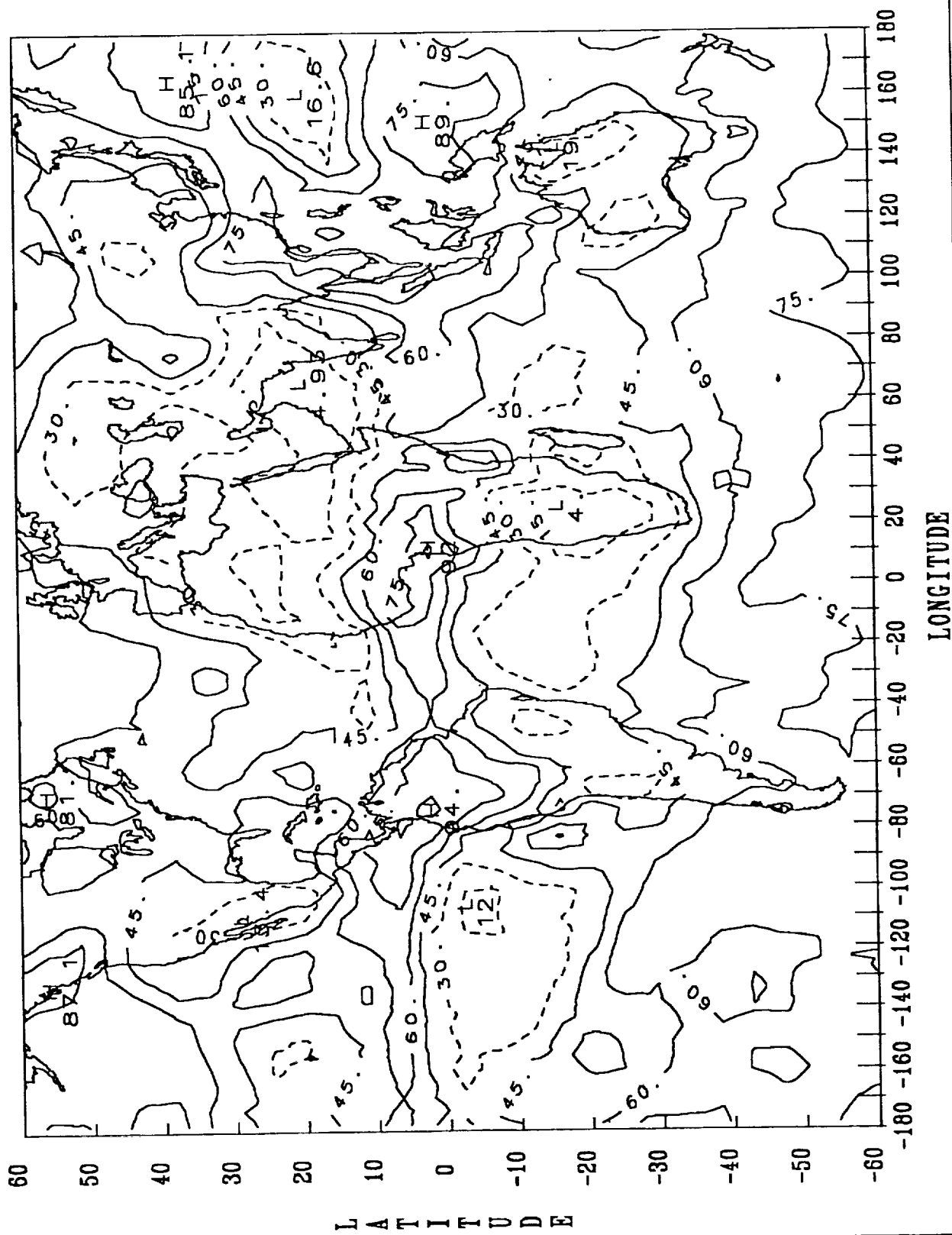
NIMBUS 7/NET RADIATION (W/M*M) APR 1980



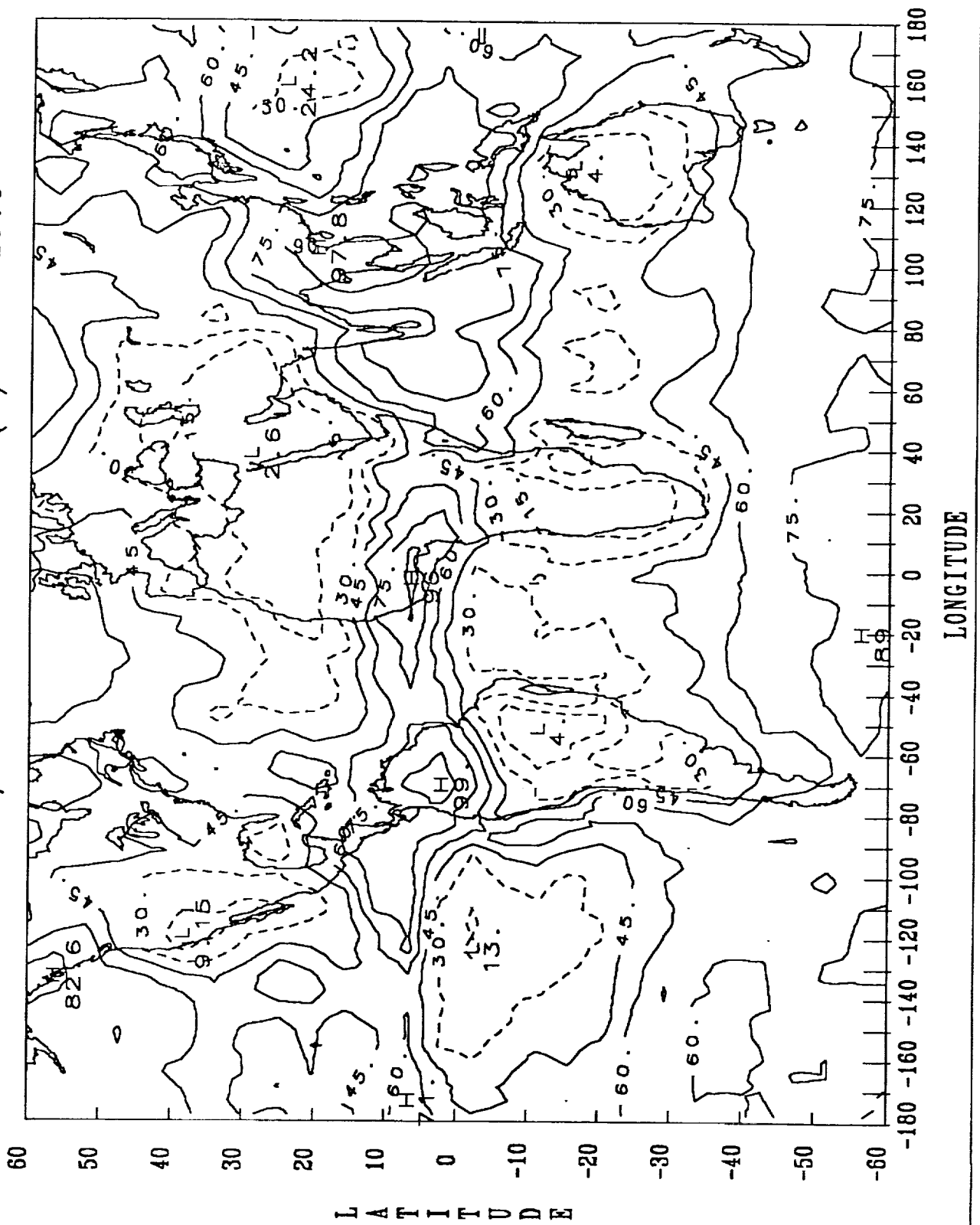
NIMBUS 7/NET RADIATION (W/M*²M) MAY 1980



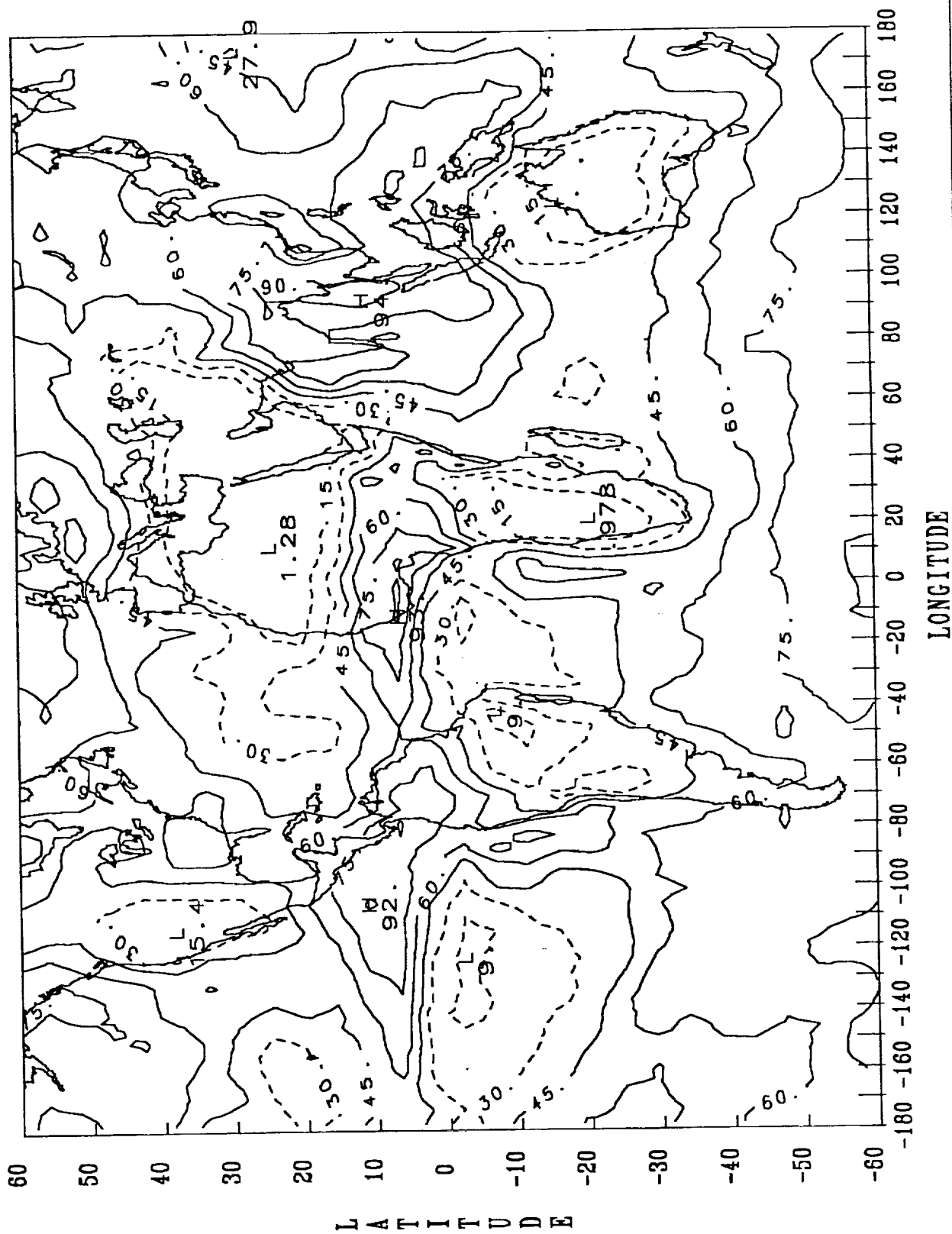
NIMBUS 7/TOTAL NOON CLOUD (%) MAY 1979



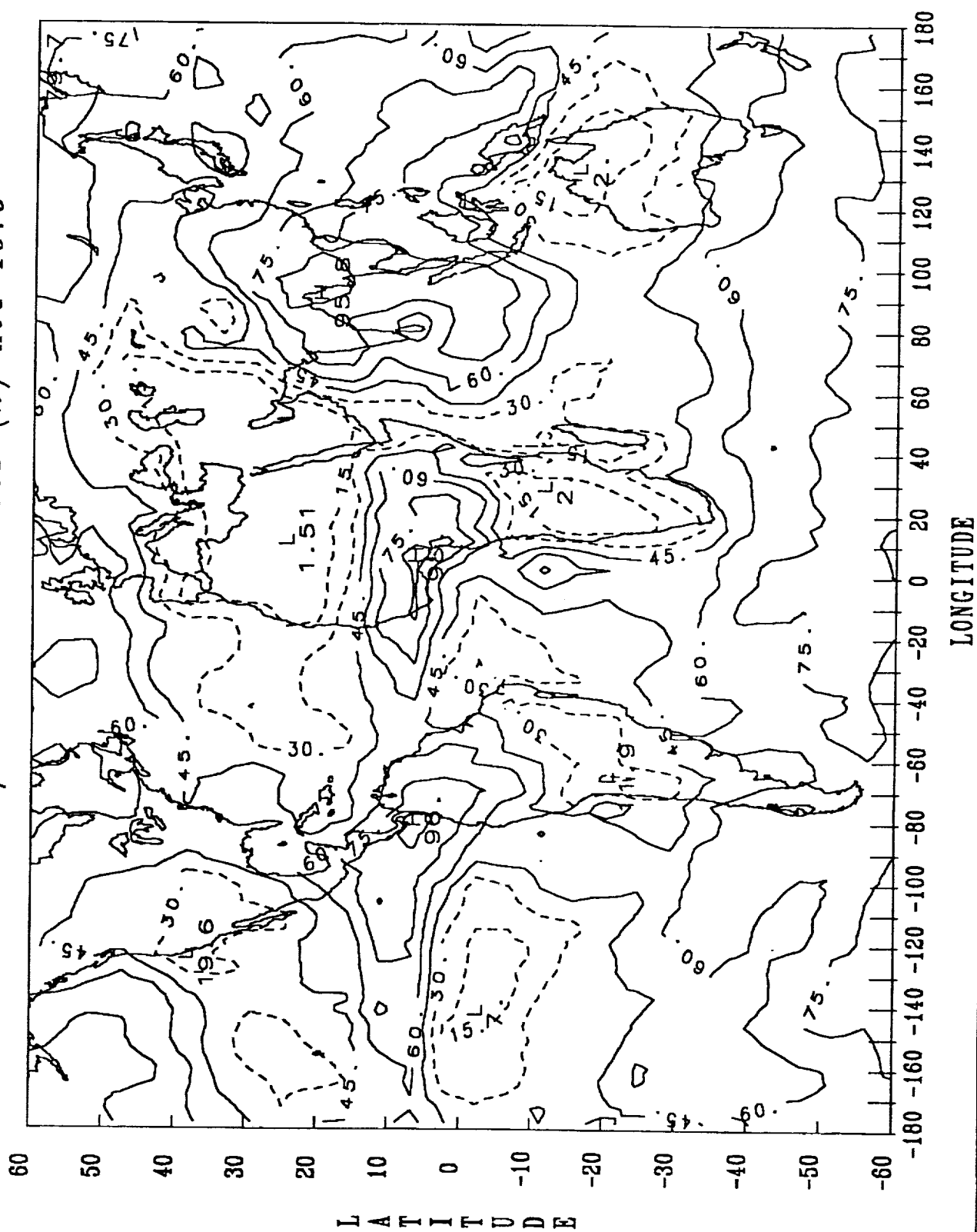
NIMBUS 7/TOTAL NOON CLOUD (%) JUNE 1979



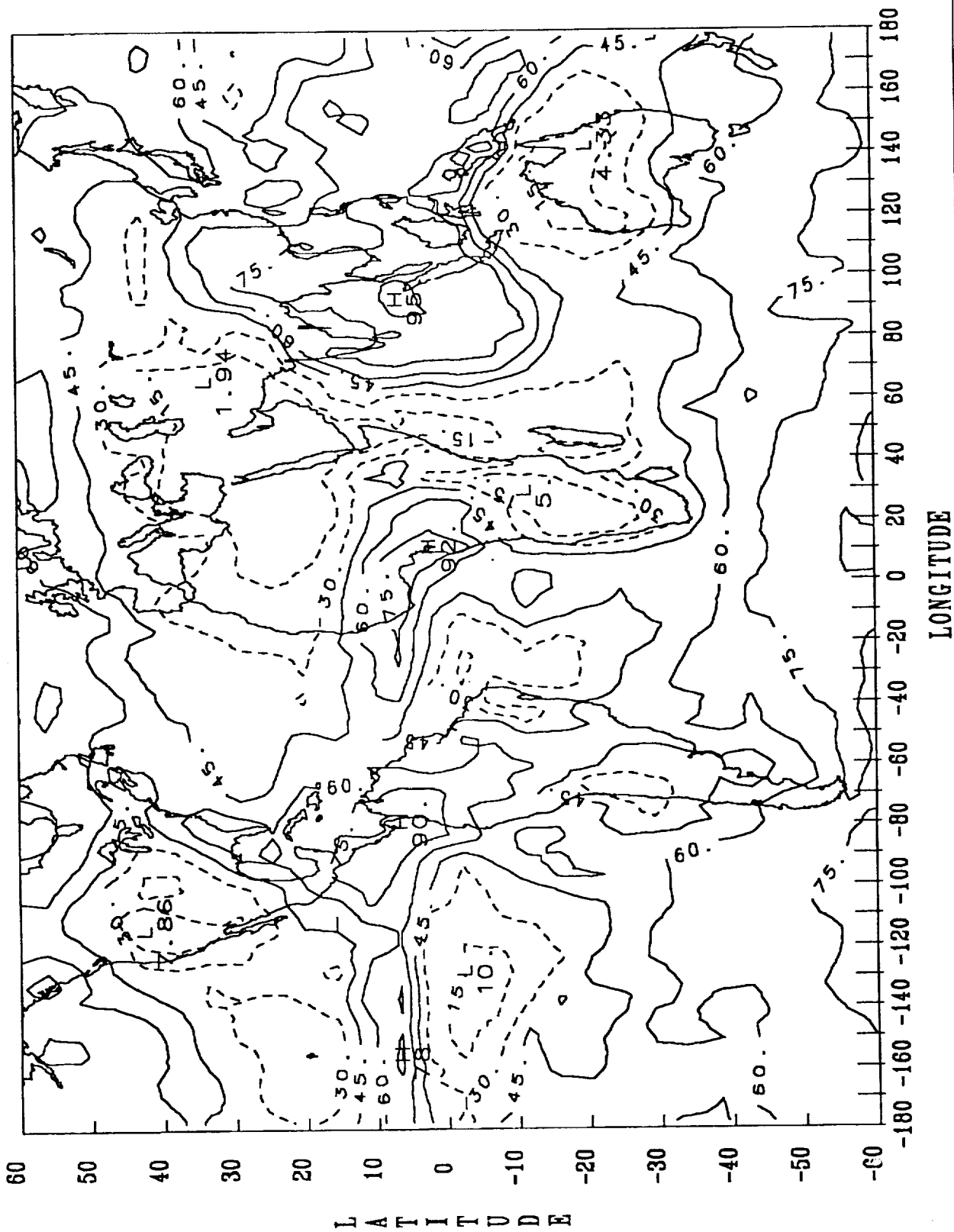
NIMBUS 7/TOTAL NOON CLOUD (%) JULY 1979



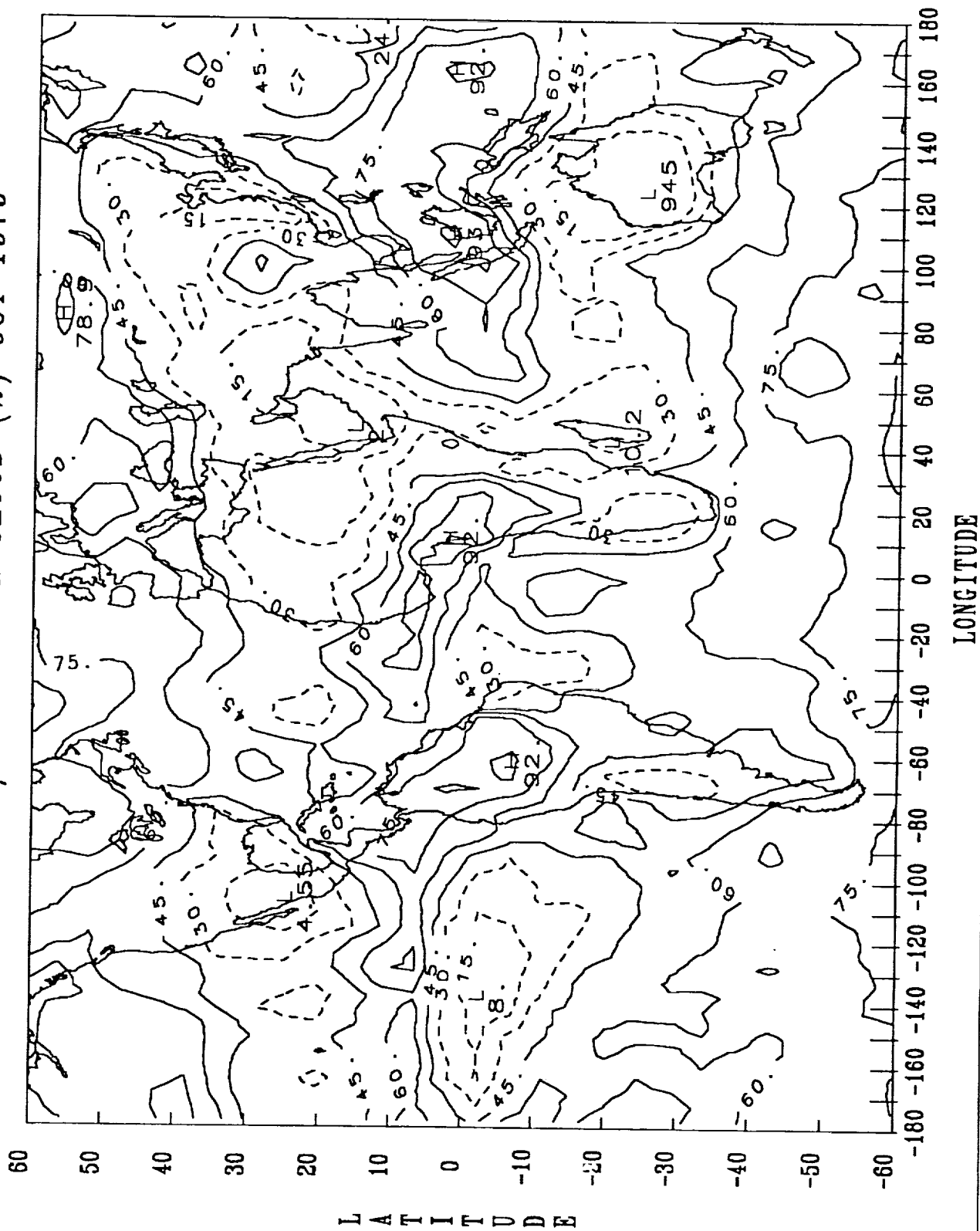
NIMBUS . / TOTAL NOON CLOUD (%) AUG 1979



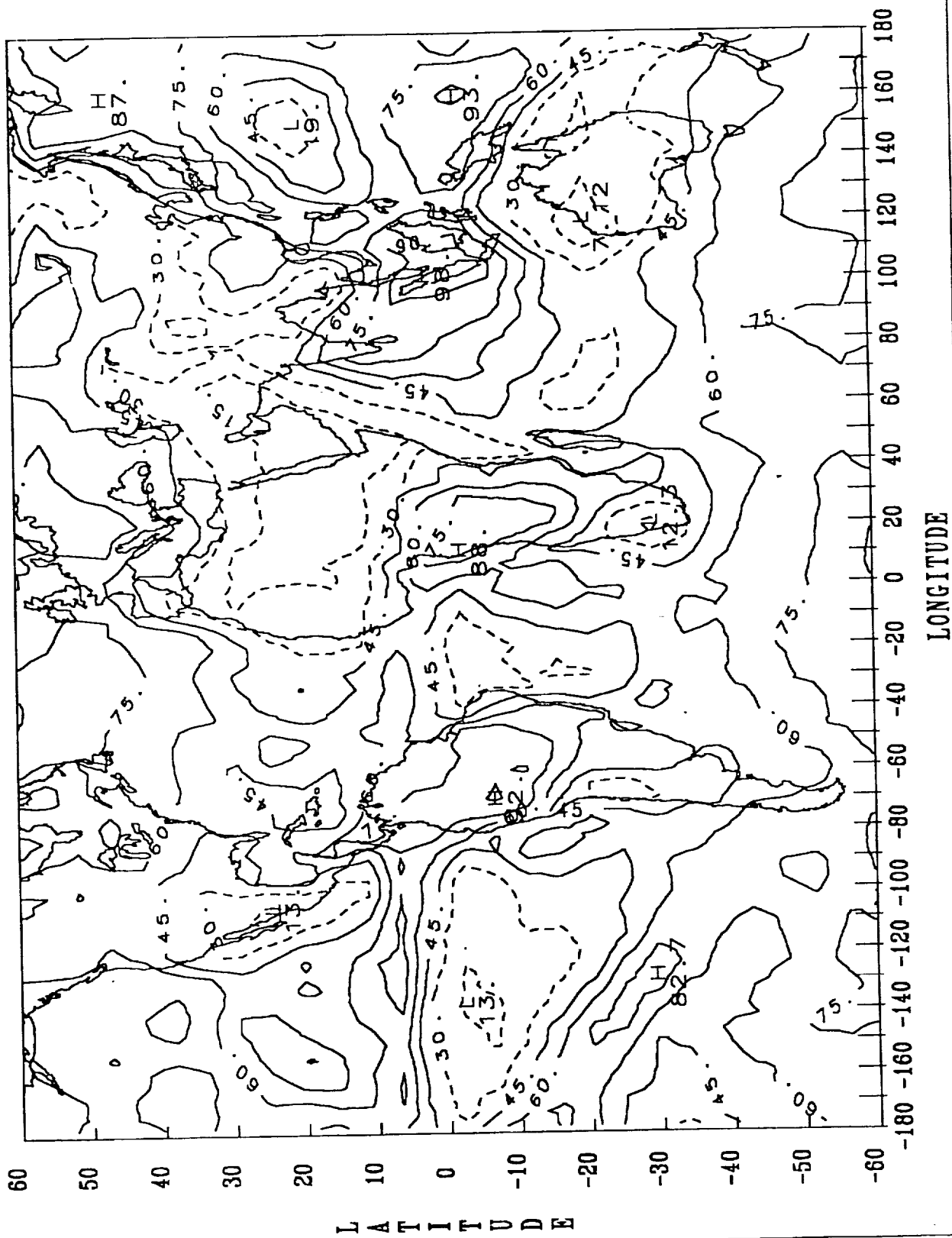
NIMBUS 7/TOTAL NOON CLOUD (%) SEP 1979



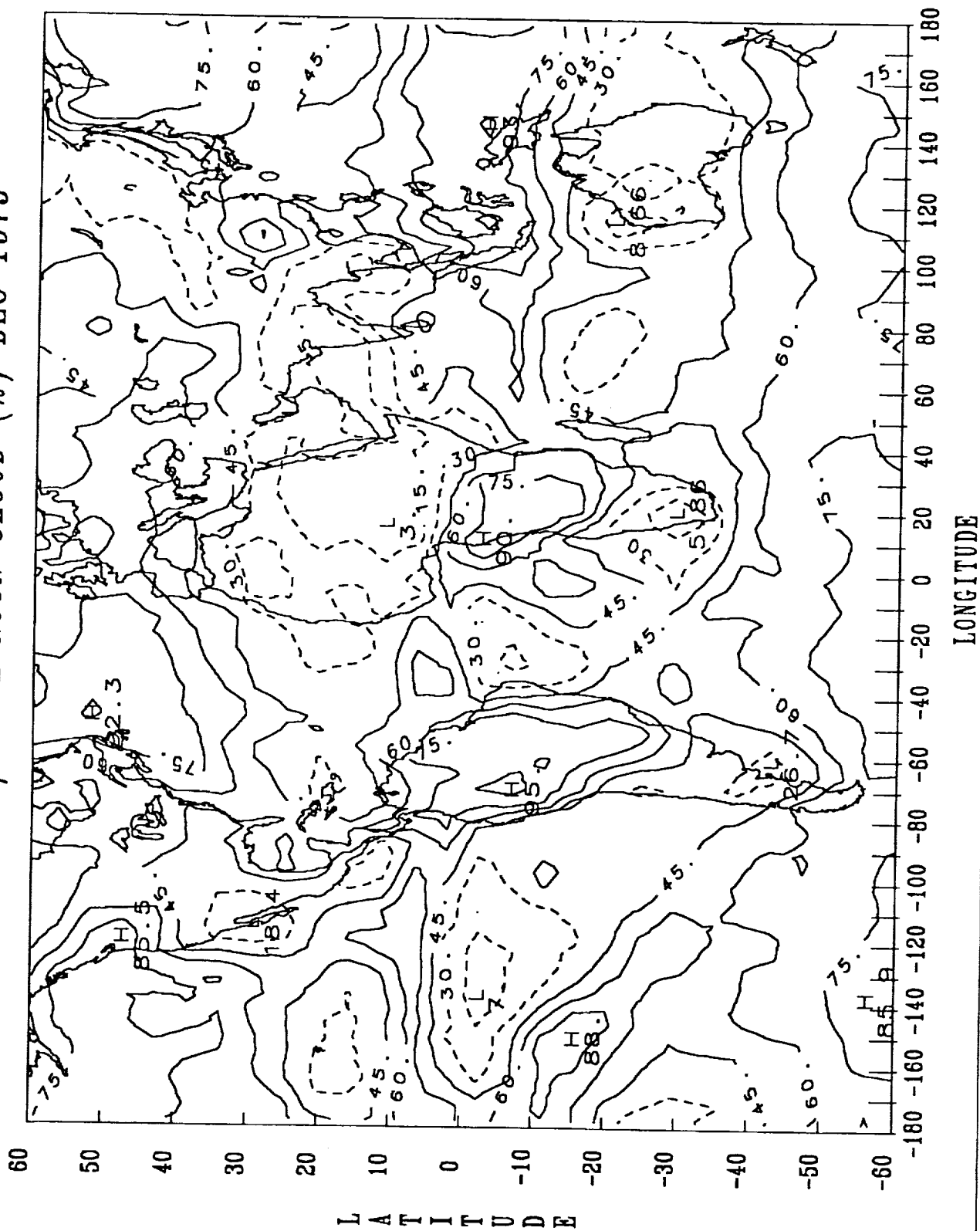
NIMBUS 7/TOTAL NOON CLOUD (%) OCT 1979



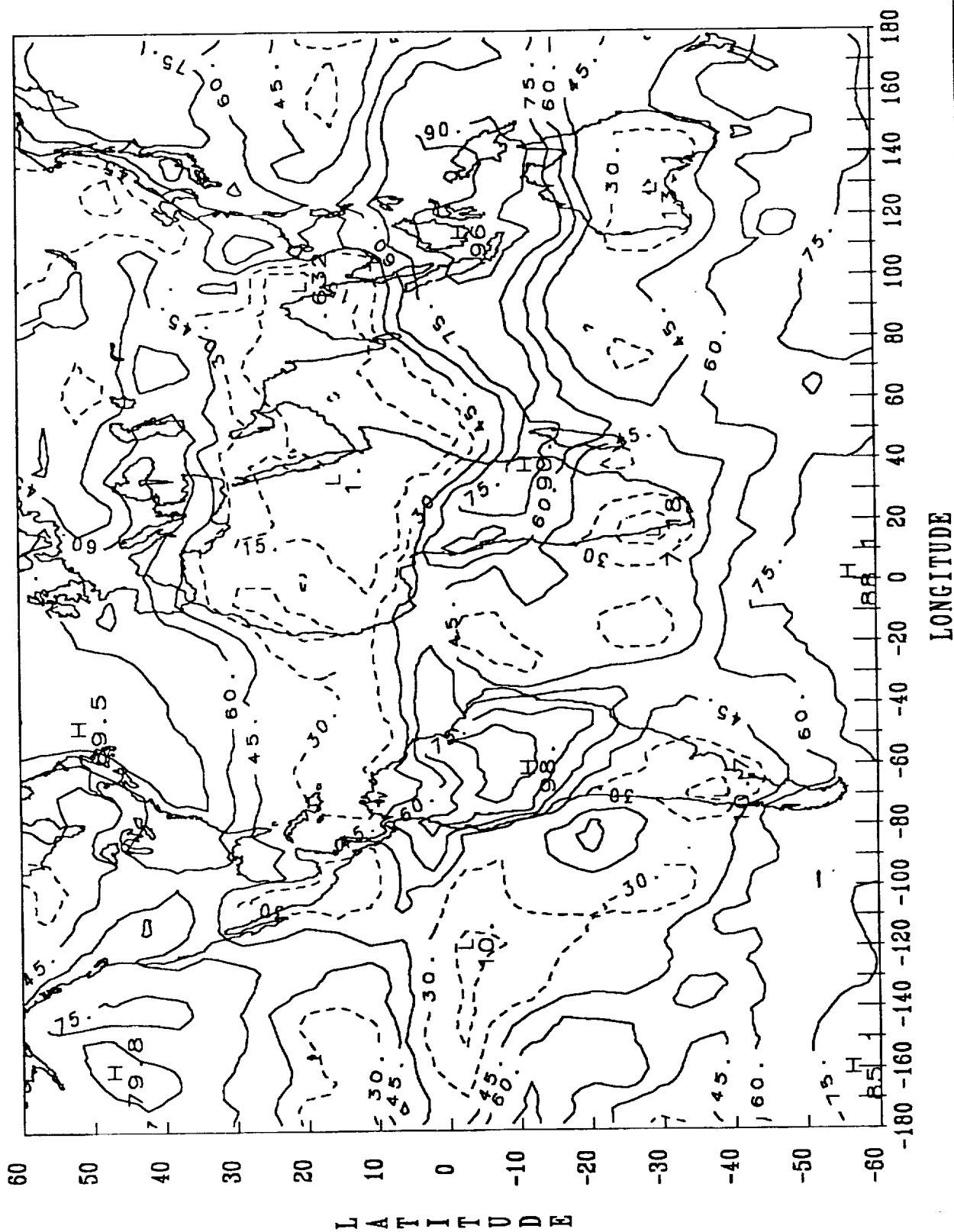
NIMBUS 7/TOTAL NOON CLOUD (%) NOV 1979



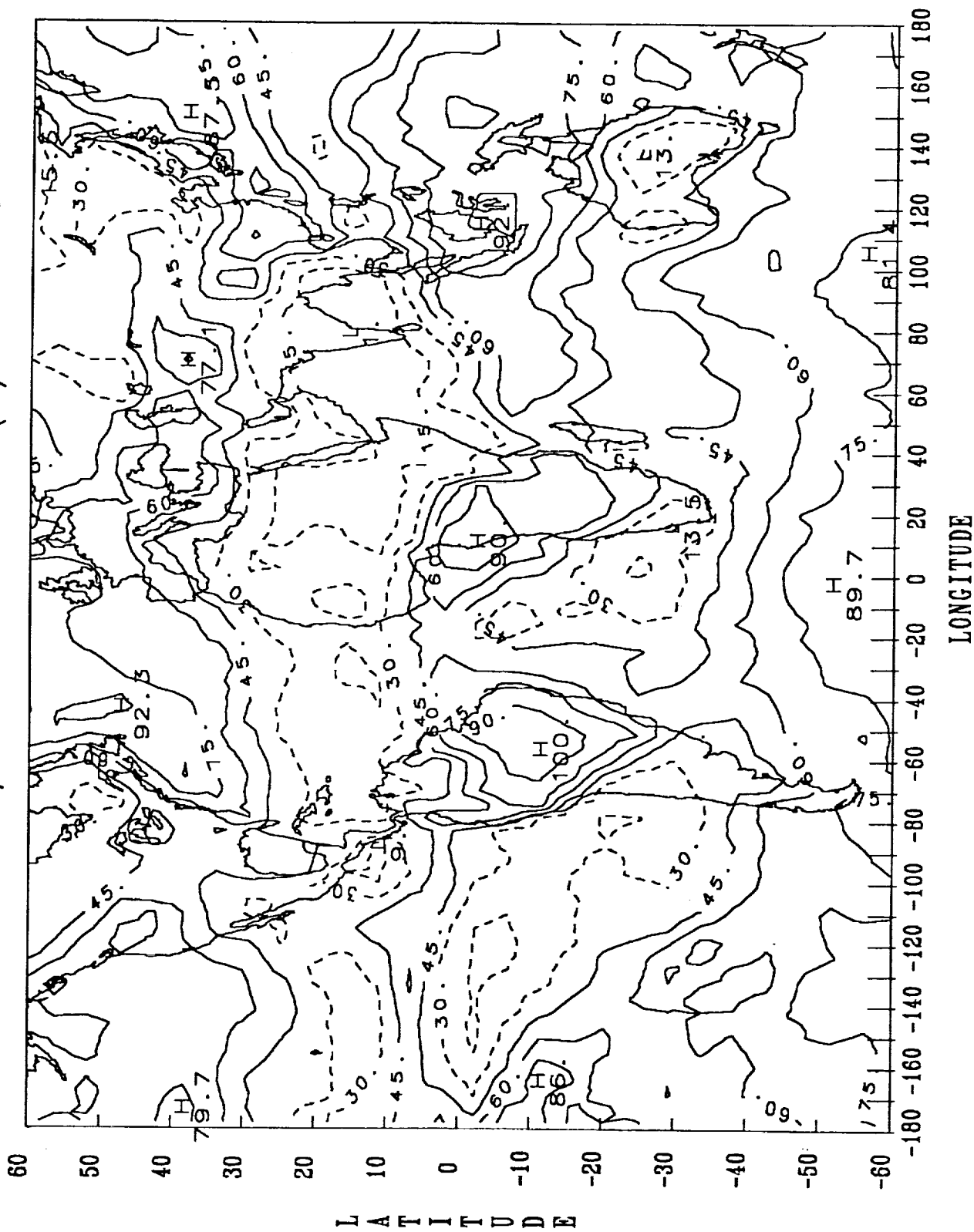
NIMBUS 7/TOTAL NOON CLOUD (%) DEC 1979



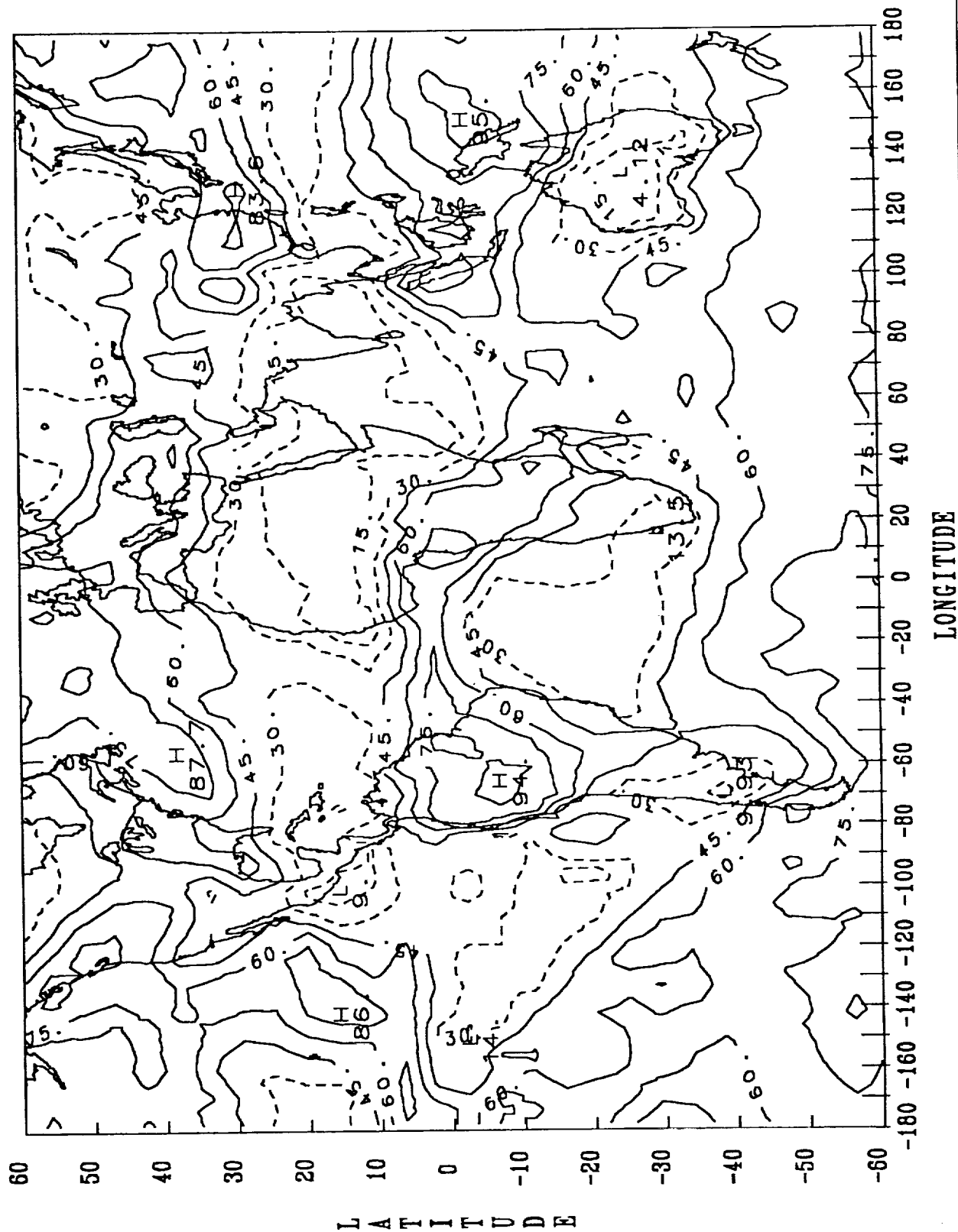
NIMBUS 7/TOTAL NOON CLOUD (%) JAN 1980



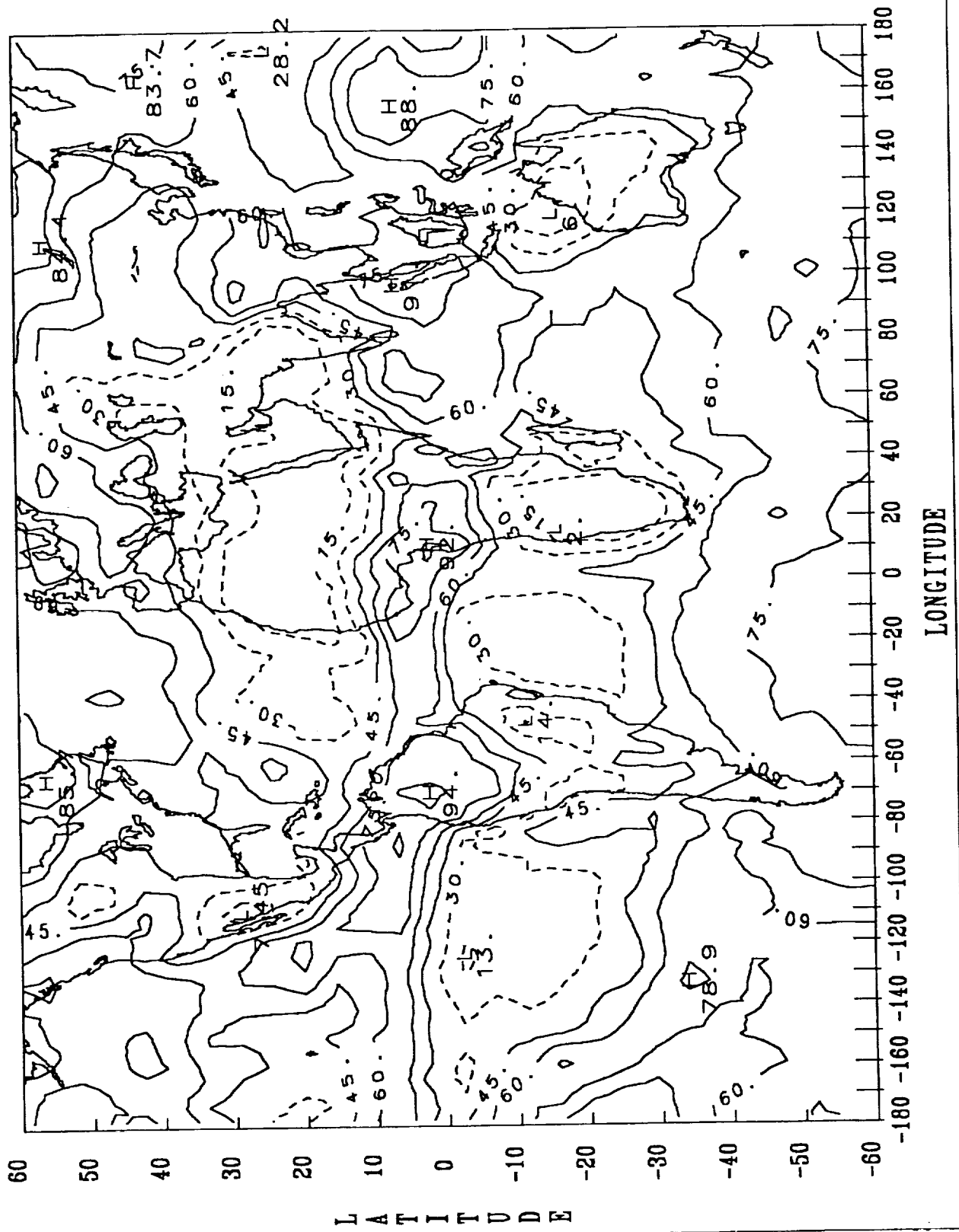
NIMBUS 7/TOTAL NOON CLOUD (%) FEB 1980



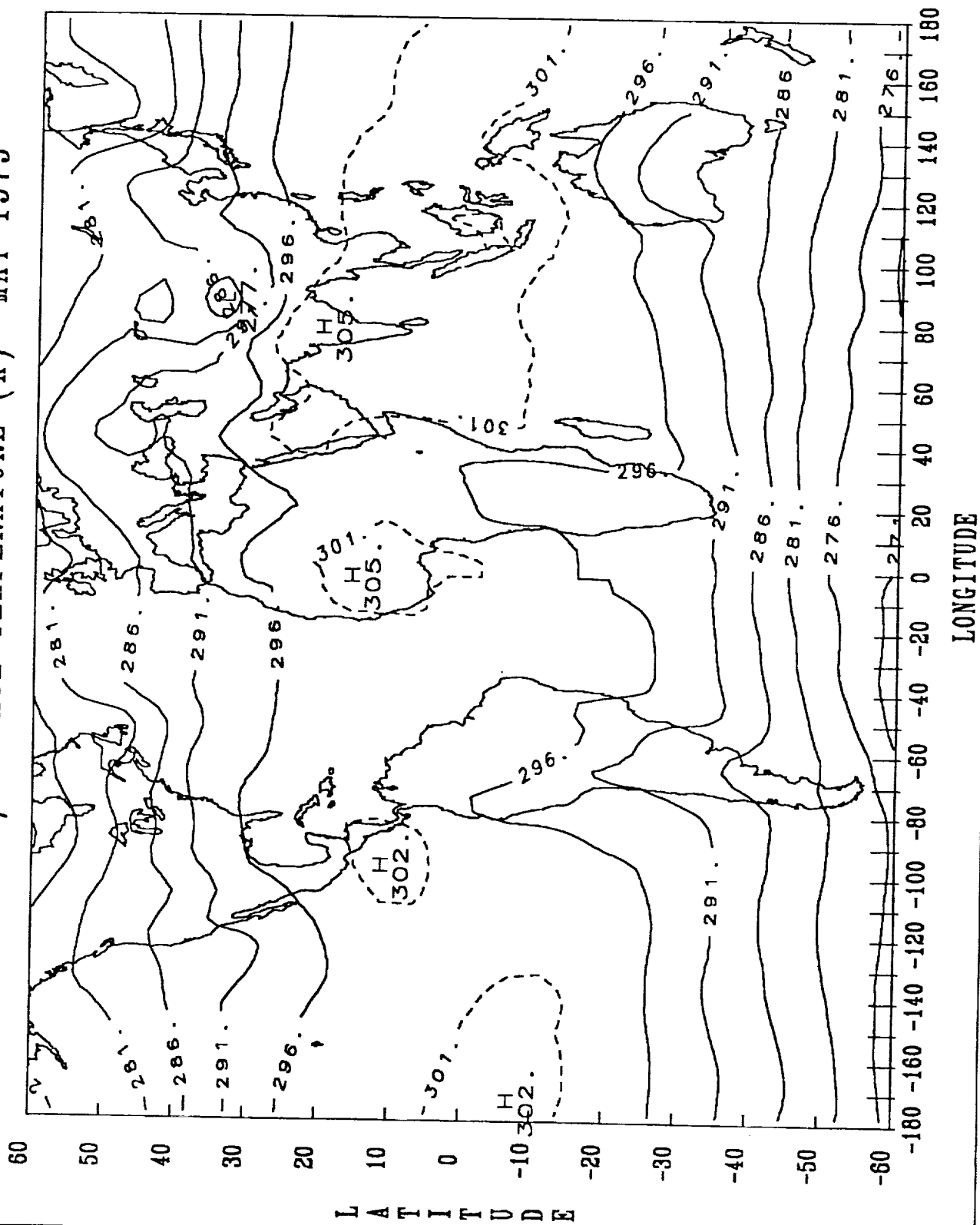
NIMBUS 7/TOTAL NOON CLOUD (%) MAR 1980



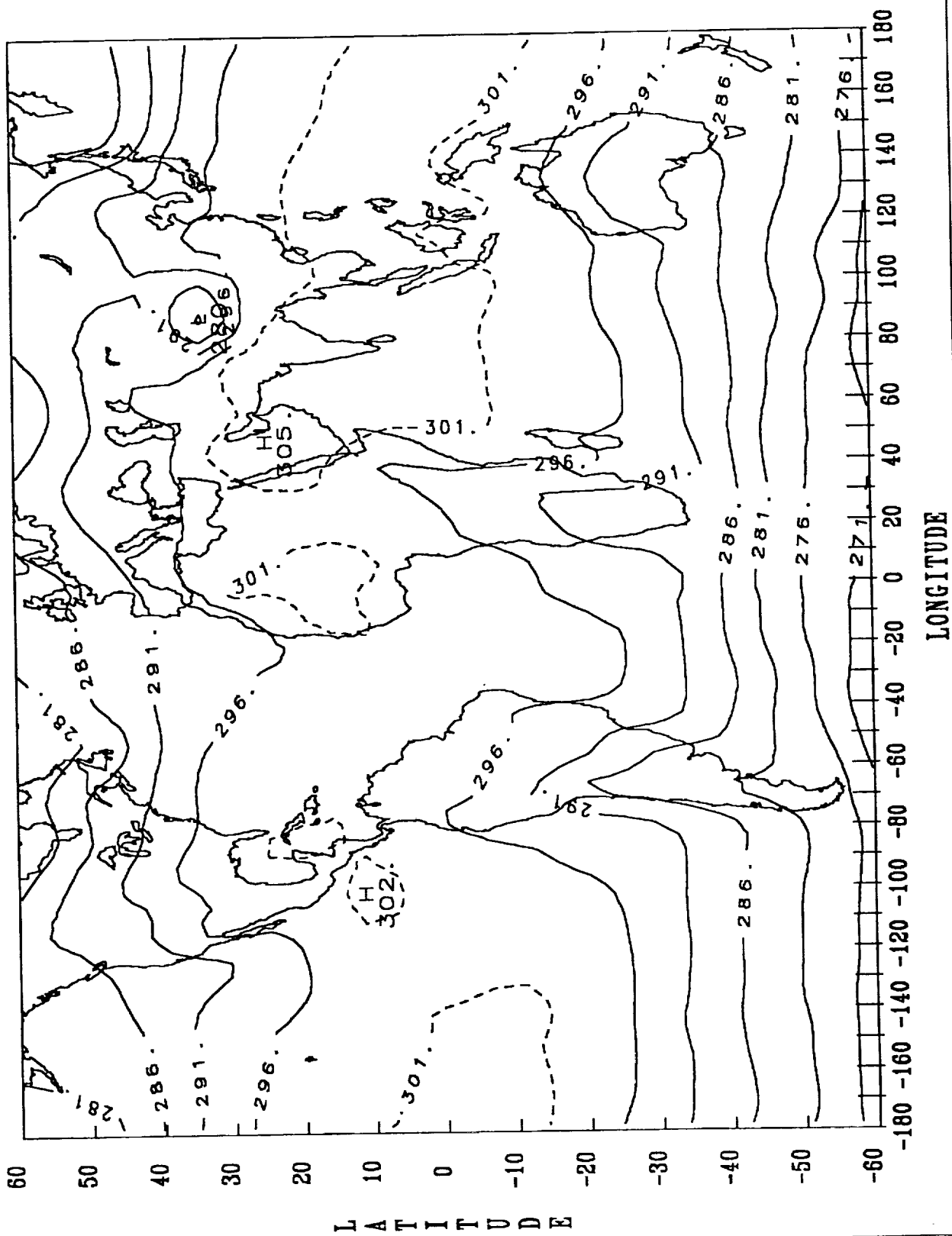
NIMBUS 7/TOTAL NOON CLOUD (%) MAY 1980



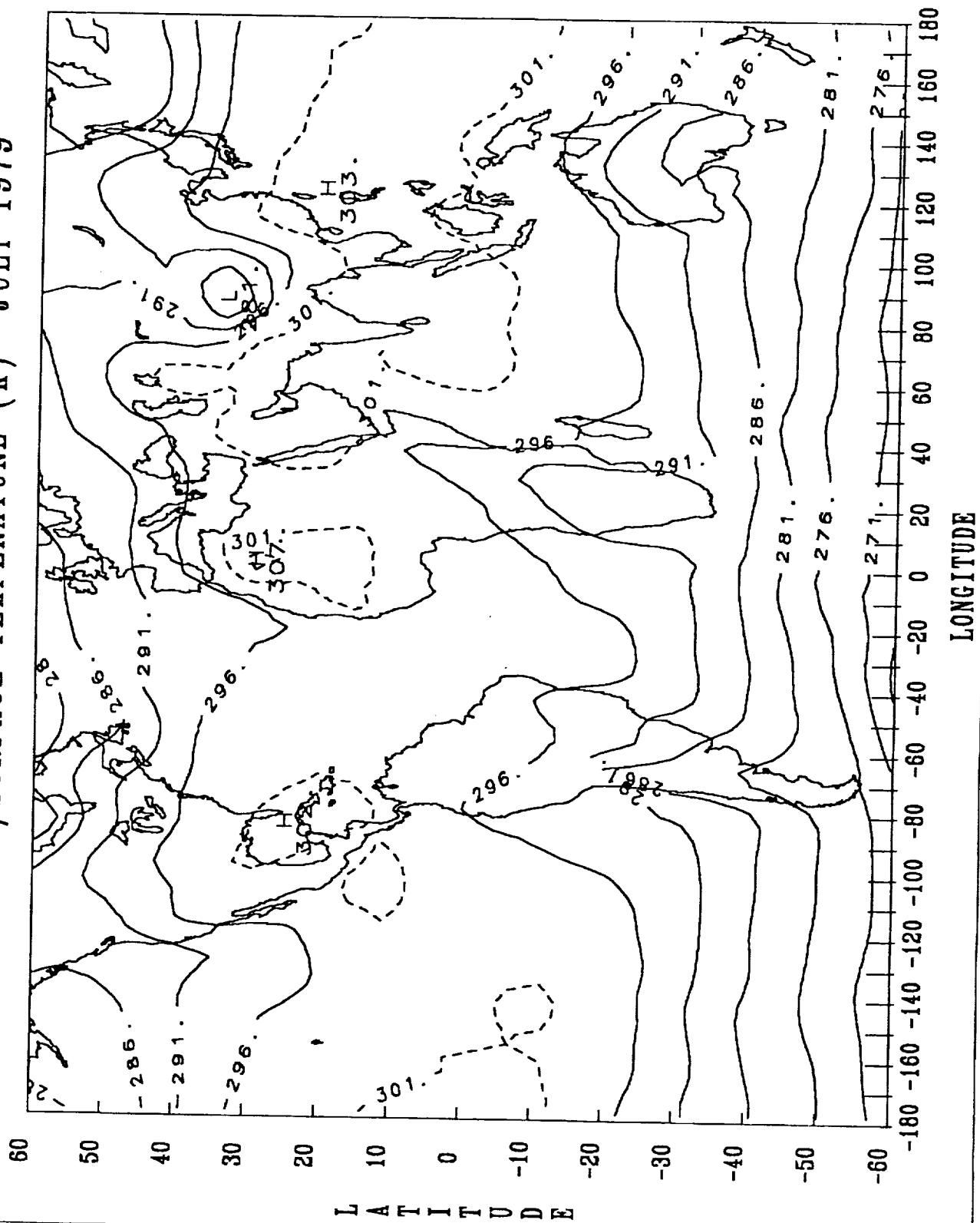
NIMBUS 7/SURFACE TEMPERATURE (K) MAY 1979



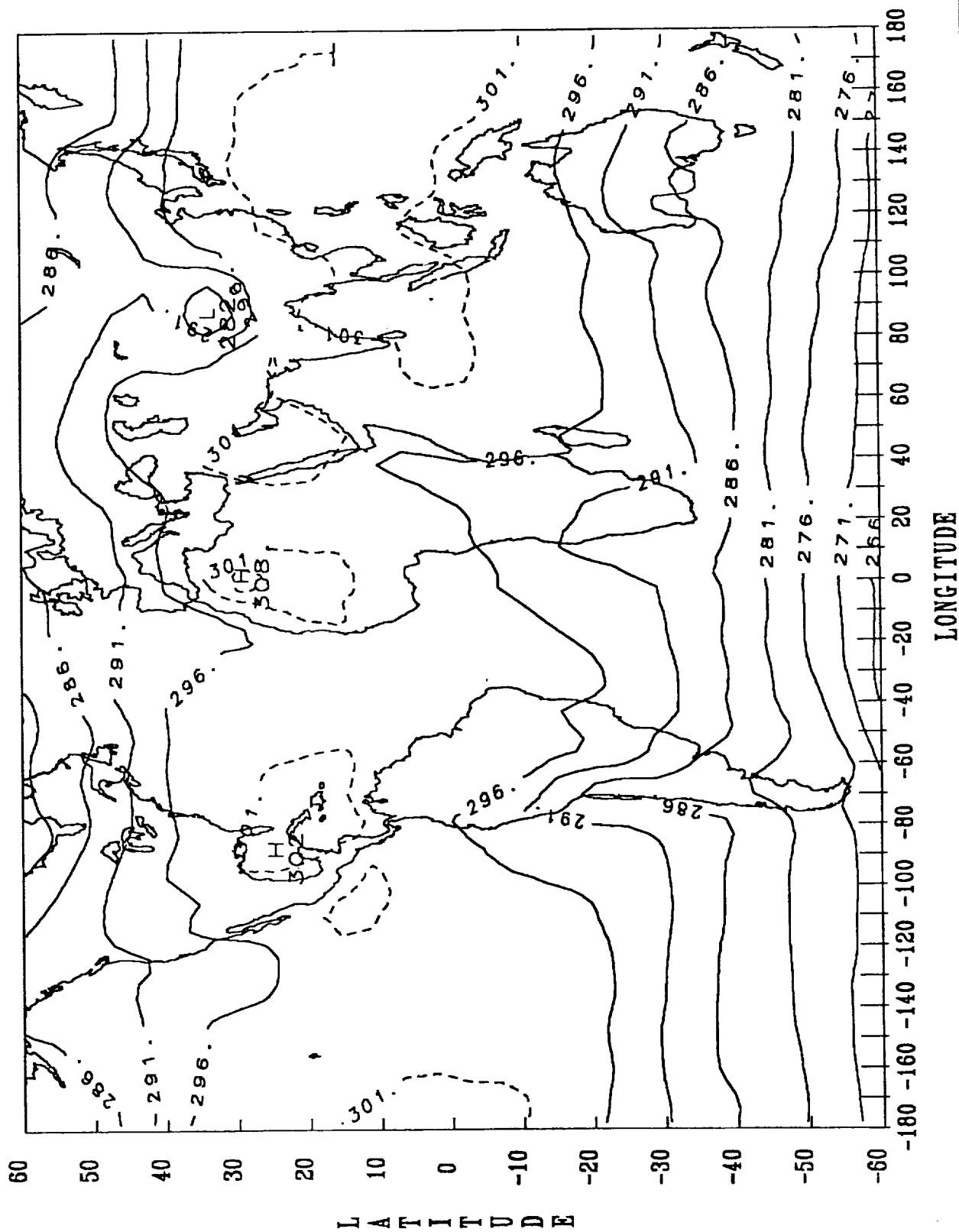
NIMBUS 7/SURFACE TEMPERATURE (K) JUNE 1979



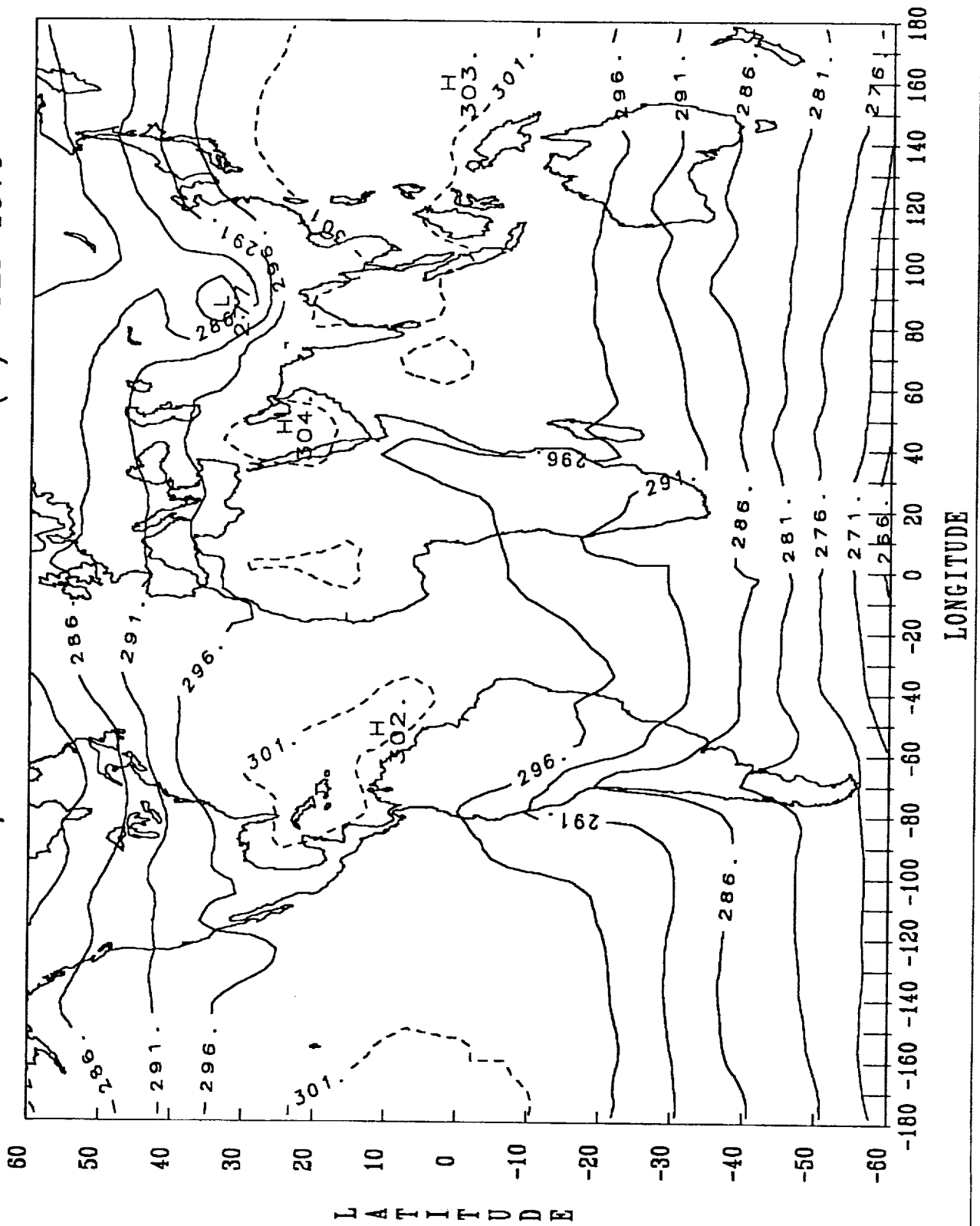
NIMBUS 7/SURFACE TEMPERATURE (K) JULY 1979



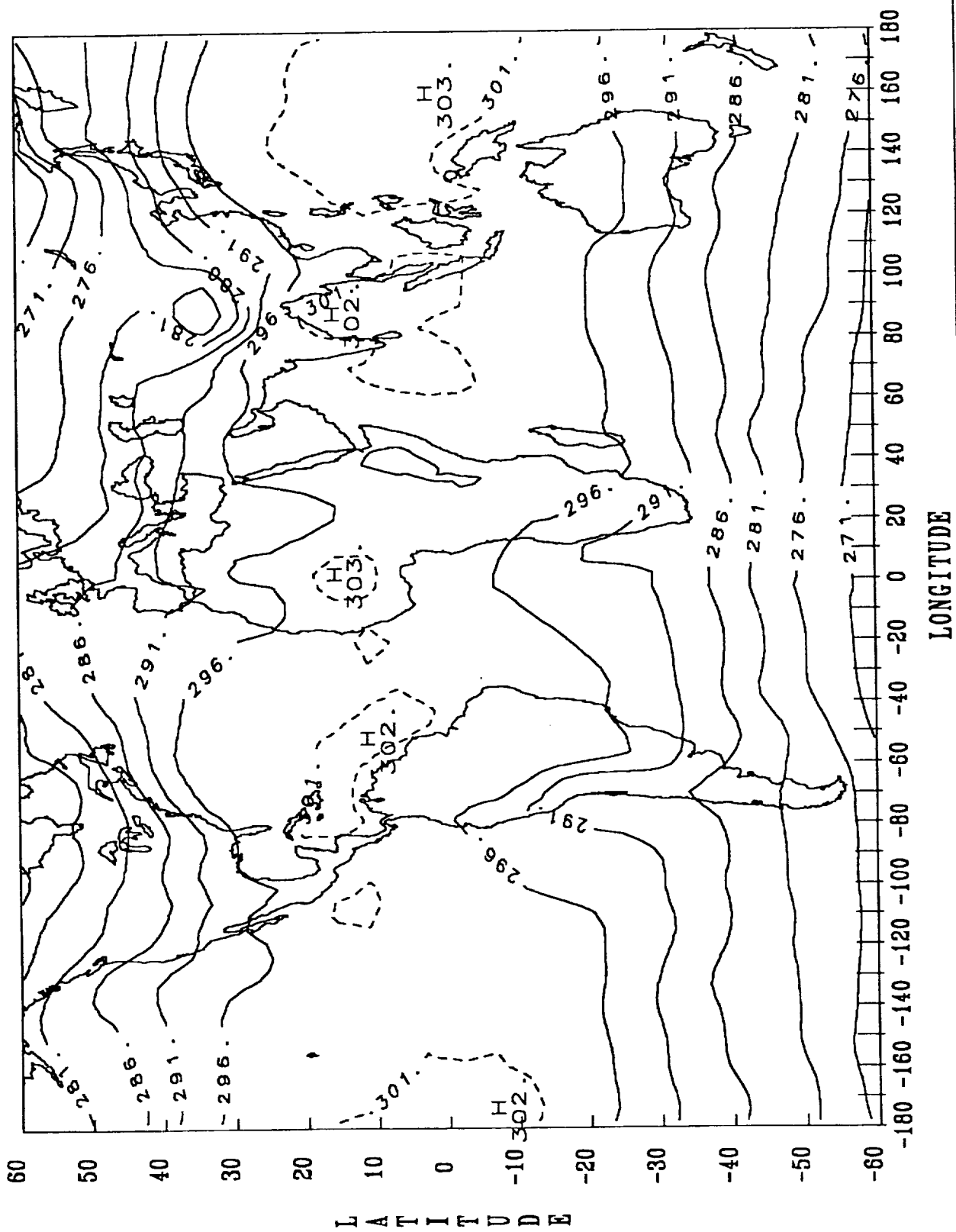
NIMBUS 7/SURFACE TEMPERATURE (K) AUG 1979



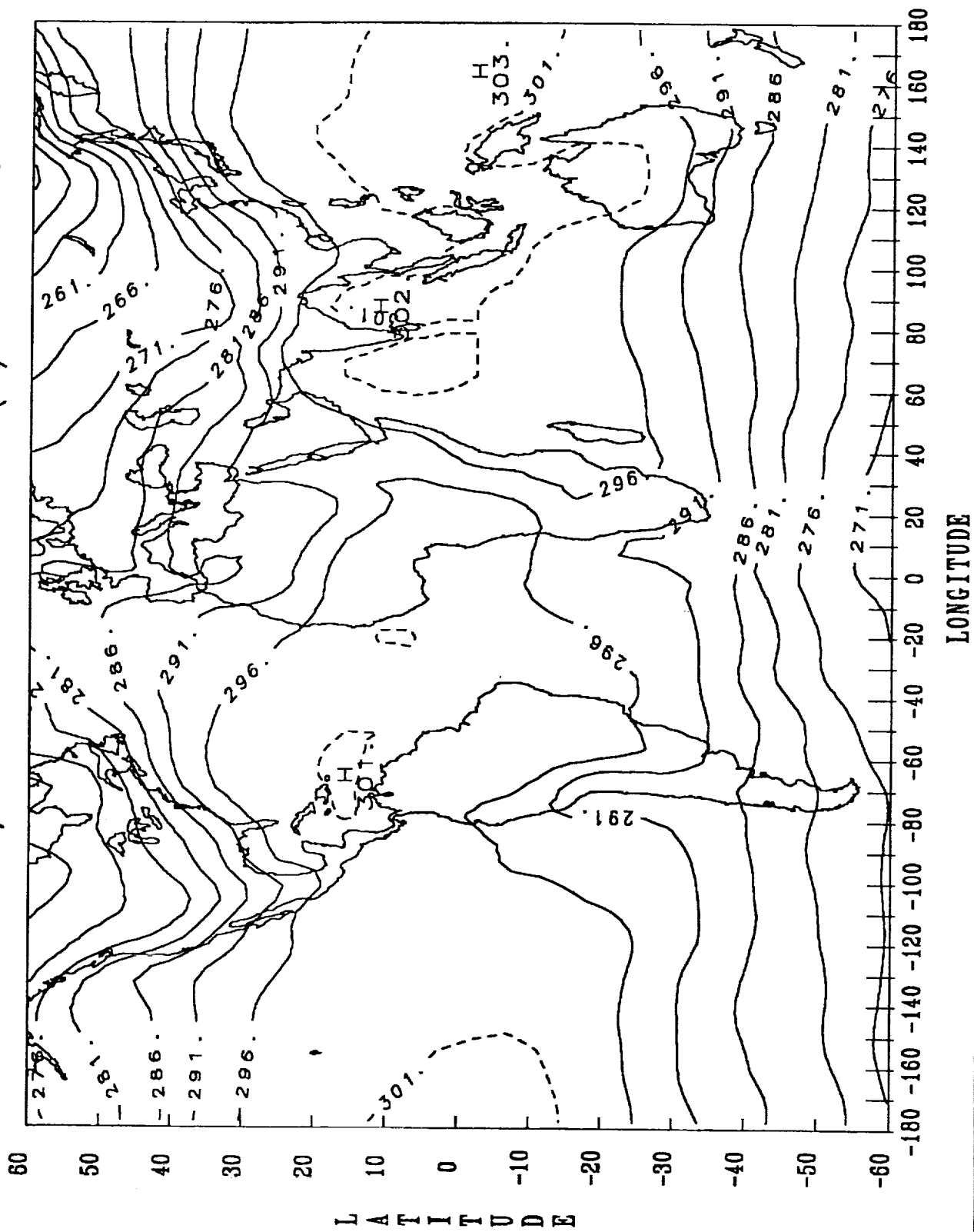
NIMBUS 7/SURFACE TEMPERATURE (K) SEP 1979



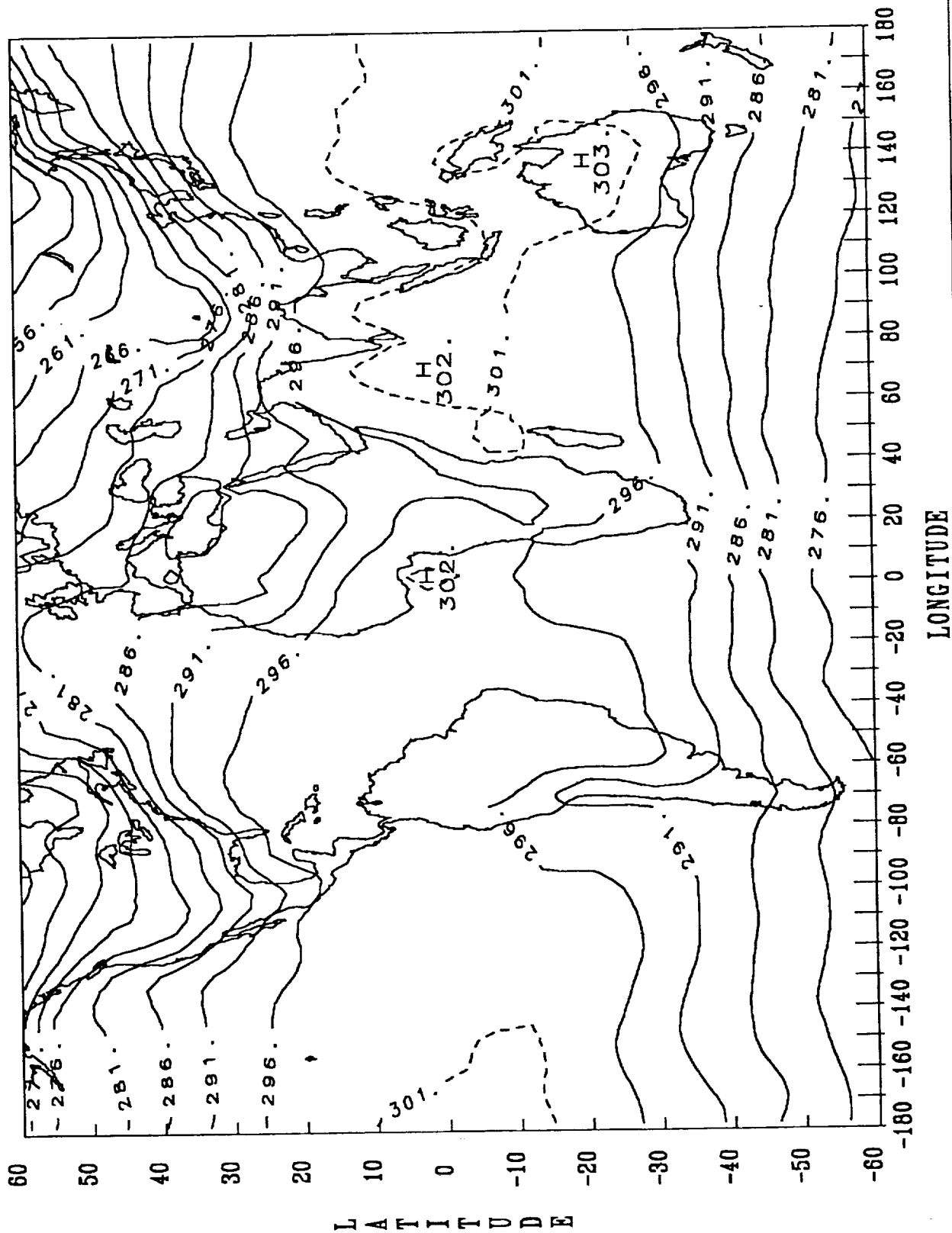
NIMBUS 7/SURFACE TEMPERATURE (K) OCT 1979



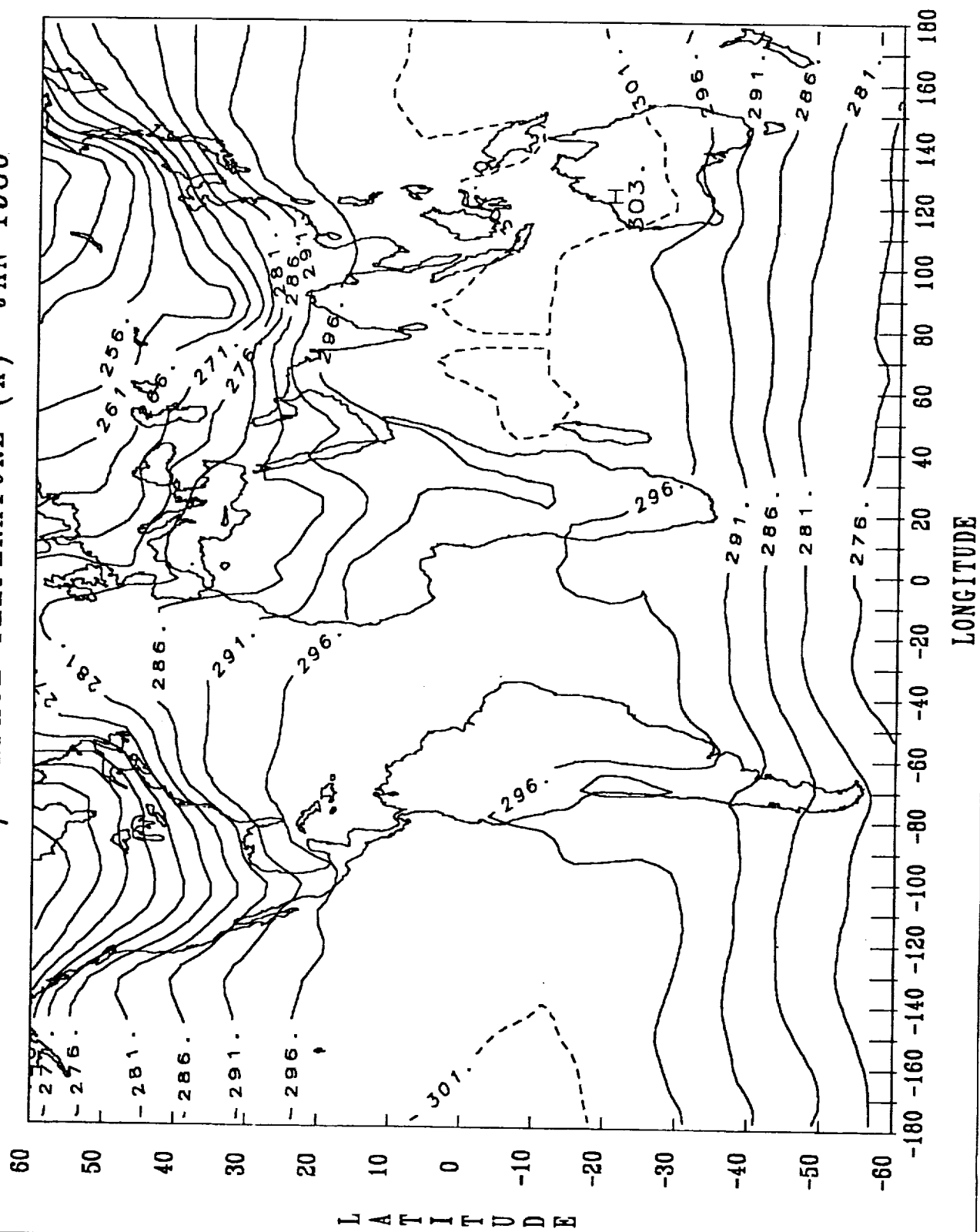
NIMBUS 7/SURFACE TEMPERATURE (K) NOV 1979



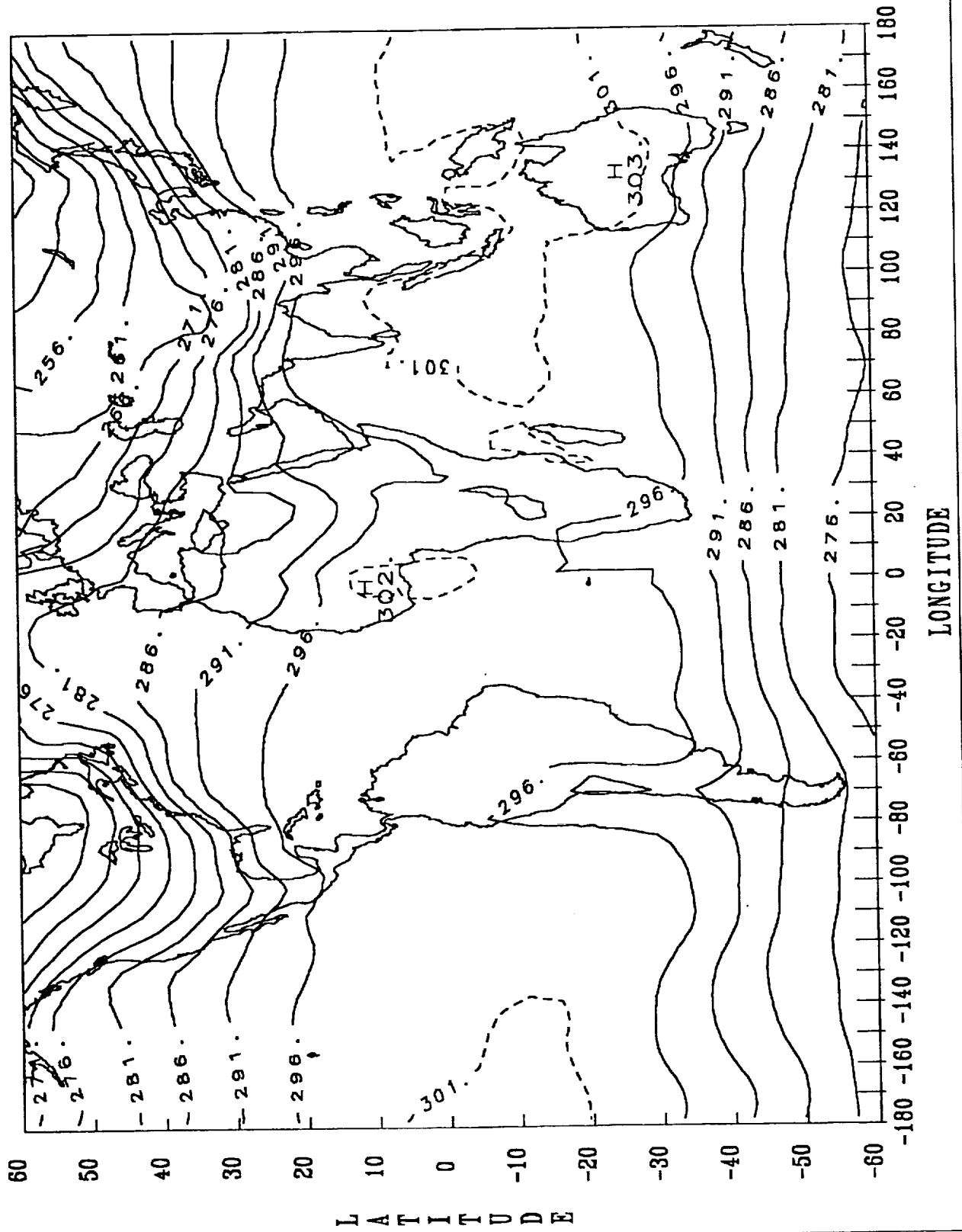
NIMBUS 7/SURFACE TEMPERATURE (K) DEC 1979



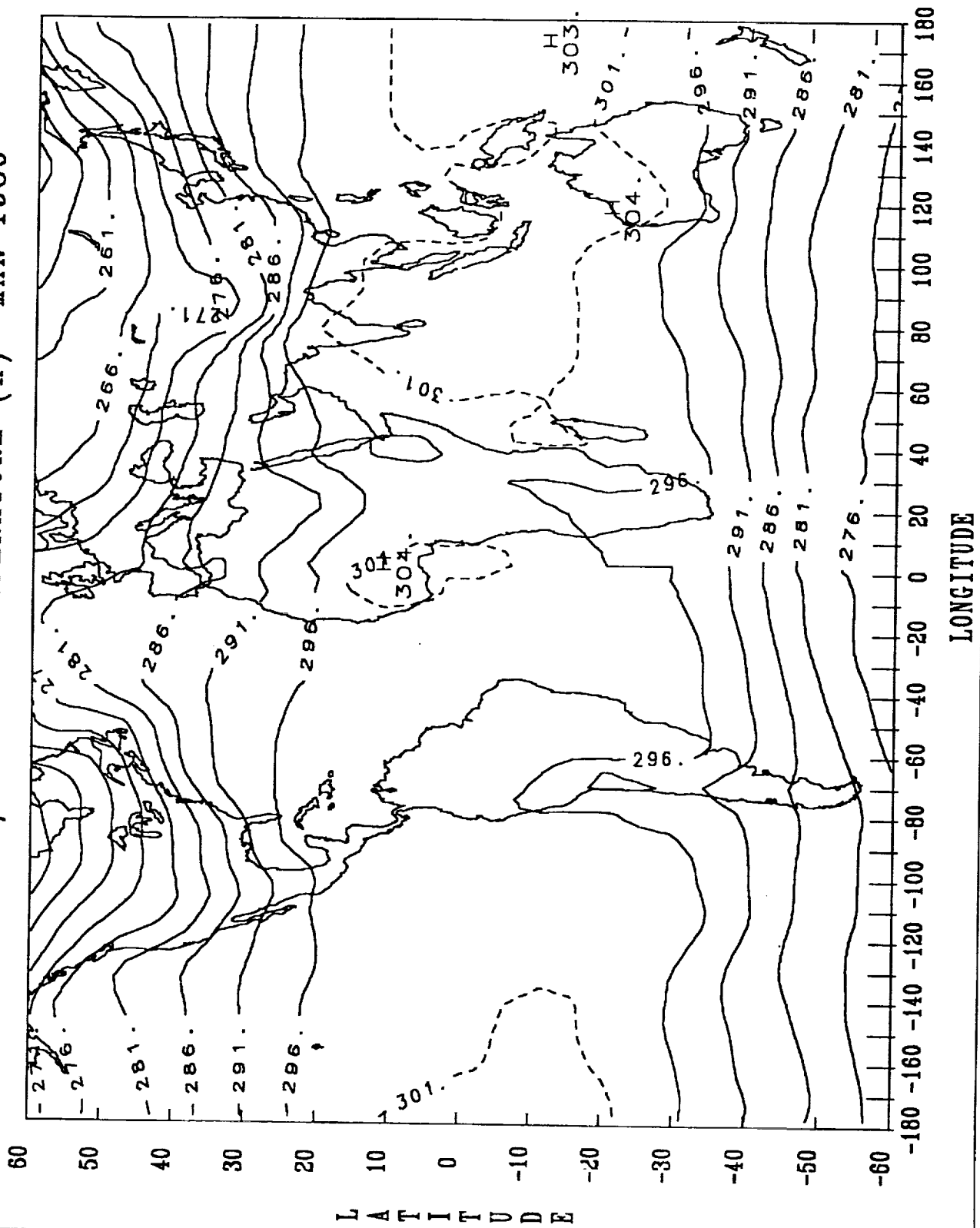
NIMBUS 7/SURFACE TEMPERATURE (K) JAN 1980



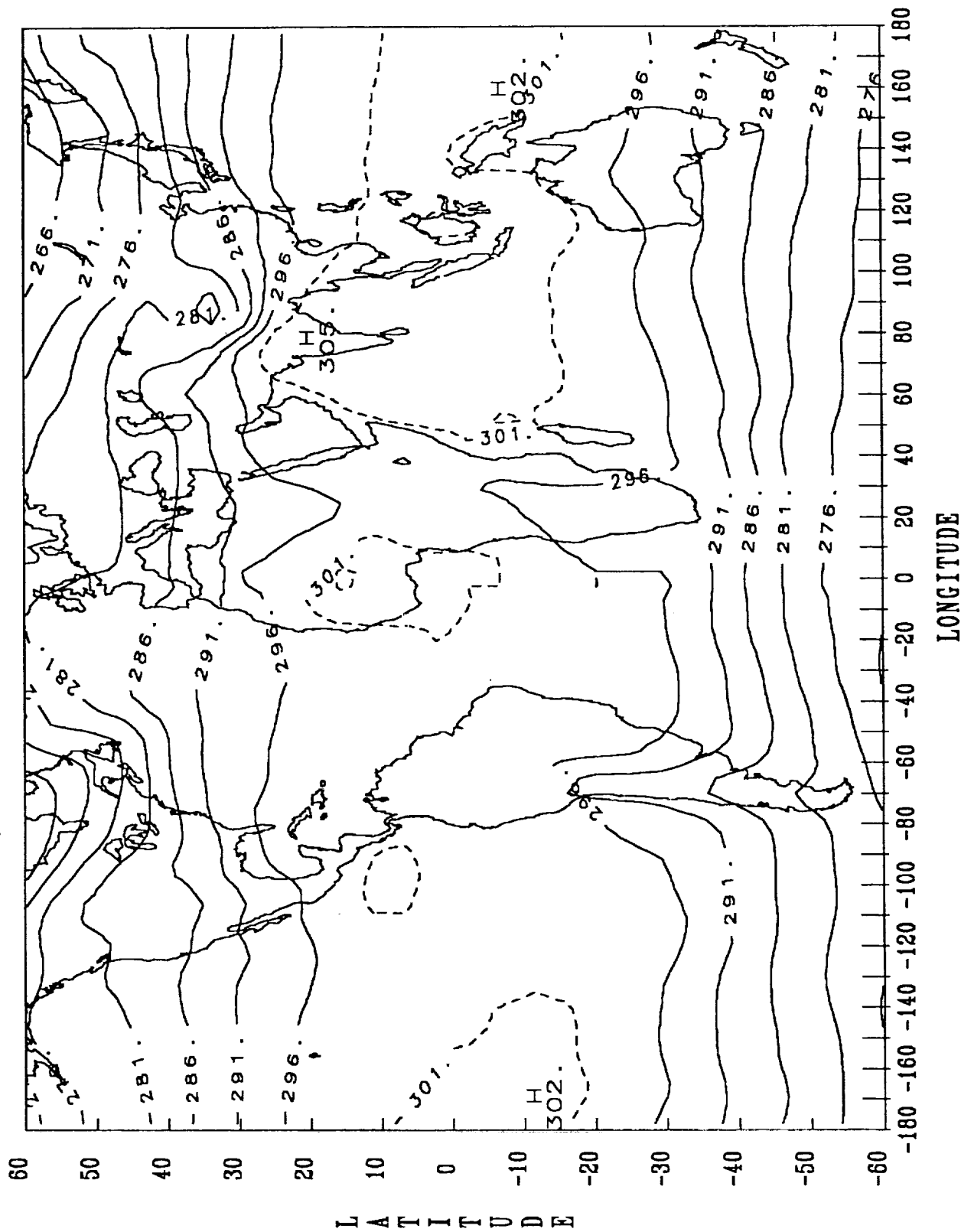
NIMBUS 7/SURFACE TEMPERATURE (K) FEB 1980



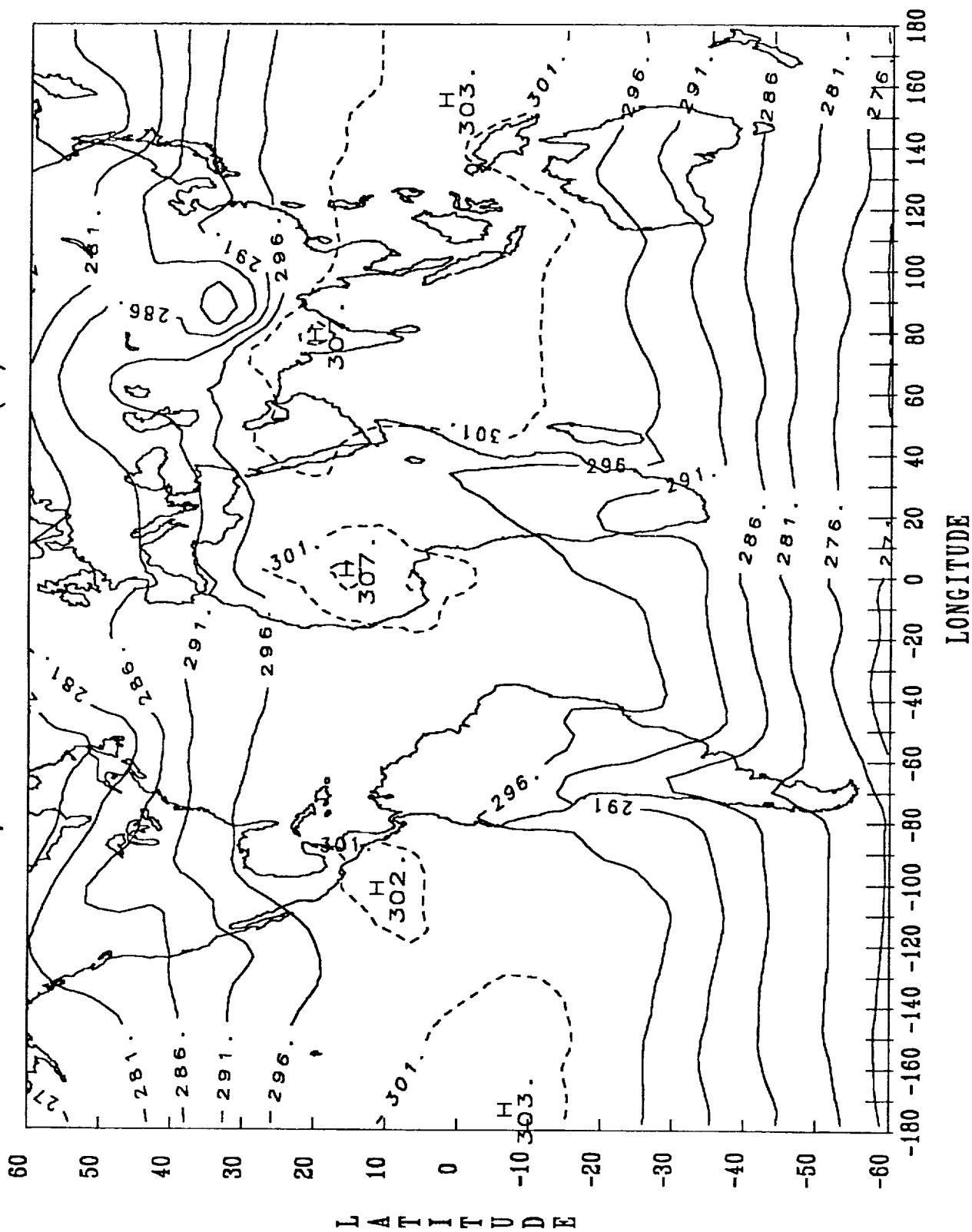
NIMBUS 7/SURFACE TEMPERATURE (K) MAR 1980



NIMBUS 7/SURFACE TEMPERATURE (K) APR 1980



NIMBUS 7/SURFACE TEMPERATURE (K) MAY 1980



9. ACRONYMS, INITIALS, AND ABBREVIATIONS

CF	Cloud Forcing
CF(LW)	cloud forcing (longwave)
CF(NR)	cloud forcing (net radiation)
CF(SW)	cloud forcing (shortwave)
ERB	Earth Radiation Budget
ERBE	Earth Radiation Budget Experiment
FGGE	First Global GARP Experiment
GARP	Global Atmospheric Research Program
IR	Infrared
ITCZ	Intertropical Convergence Zone
MLCE	Maximum Likelihood Cloud Estimation
MLE	Maximum Likelihood Estimation
NFOV	Narrow Field of View
NR	Net Radiation
OLR	Outgoing Longwave Radiation
THIR	Temperature Humidity Infrared Radiometer
TOA	Top of the Atmosphere
TOMS	Total Ozone Mapping Spectrometer
UV	Ultraviolet
WFOV	Wide Field of View

Report Documentation Page

1. Report No. NASA RP-1263		2. Government Accession No.		3. Recipient's Catalog No.	
4. Title and Subtitle Atlas of the Earth's Radiation Budget as Measured by Nimbus-7: May 1979 to May 1980				5. Report Date May 1991	
				6. Performing Organization Code 936	
7. Author(s) H. Lee Kyle, Richard R. Hucek, and Brenda J. Vallette				8. Performing Organization Report No. 91B00081	
				10. Work Unit No.	
9. Performing Organization Name and Address Space Data and Computing Division Goddard Space Flight Center Greenbelt, MD 20771				11. Contract or Grant No. NAS5-29373	
				13. Type of Report and Period Covered Reference Publication	
12. Sponsoring Agency Name and Address National Aeronautics and Space Administration Washington, DC 20546-0001				14. Sponsoring Agency Code	
15. Supplementary Notes H. Lee Kyle: Goddard Space Flight Center, Greenbelt, MD Richard R. Hucek and Brenda J. Vallette: Research and Data Systems Corporation, Greenbelt, MD					
16. Abstract This atlas describes the seasonal changes in the Earth's radiation budget for the 13-month period, May 1979 to May 1980. It helps to illustrate the strong feedback mechanisms by which the Earth's climate interacts with the top-of-the-atmosphere insolation to modify the energy that various regions absorb from the Sun. Cloud type and cloud amount, which are linked to the surface temperature and the regional climate, are key elements in this interaction. Annual, seasonal, and monthly maps of the albedo, outgoing longwave and net radiation, noontime cloud cover, and mean diurnal surface temperatures are presented. Annual and seasonal net cloud forcing maps are also given. All of the quantities were derived from Nimbus-7 satellite measurements except for the temperatures, which were used in the cloud detection algorithm and came originally from the Air Force 3-dimensional nephanalysis dataset. The seasonal changes are described. The interaction of clouds and the radiation budget is briefly discussed.					
17. Key Words (Suggested by Author(s)) Earth Radiation Budget, Nimbus-7, clouds and climate, Earth albedo, outgoing longwave radiation				18. Distribution Statement Unclassified - Unlimited Subject Category 47	
19. Security Classif. (of this report) Unclassified		20. Security Classif. (of this page) Unclassified		21. No. of pages 135	
				22. Price A07	

